DESIGN AND DEVELOPMENT OF ELECTROSPUN PIEZOELECTRIC NANOCOMPOSITE FOR SENSING APPLICATIONS

A Thesis Submitted in

Partial Fulfillment of the Requirements

for the Degree of

DOCTOR OF PHILOSOPHY

By

MUKESH KUMAR

(Roll No.176103016)

DEPARTMENT OF MECHANICAL ENGINEERING

INDIAN INSTITUTE OF TECHNOLOGY GUWAHATI

GUWAHATI (ASSAM)-781039

AUGUST 2023

Dedicated to my
beloved father Mr. Nunu Babu Singh,
and
mother Mrs. Nirmala Devi.

Certificate

This is to certify that the thesis entitled "**Design and Development of Electrospun Piezoelectric Nanocomposite for Sensing Applications**" being submitted by **Mr. Mukesh Kumar** to the Indian Institute of Technology, Guwahati, for the award of the degree of Doctor of Philosophy in Mechanical Engineering is a record of original bonafide research work carried out by him under my supervision and guidance. The thesis work, in my opinion, has reached the requisite standard fulfilling the requirements for the degree of Doctor of Philosophy.

The results contained in this thesis have not been submitted in part or full to any other University or Institute for the award of any degree or diploma.

Dr. Poonam Kumari

Associate Professor

Department of Mechanical Engineering

Indian Institute of Technology Guwahati

Guwahati - 781039

Declaration

I, Mukesh Kumar (Roll no: 176103016) declare that the present written submission is my thoughts in my own words. I have adequately cited and referenced the original sources, where other's ideas have been involved. I also declare that I have adhered to all principles of academic honesty and integrity and have neither fabricated nor falsified any idea/data/fact/source in my submission. I understand that any violation of the above will be cause for disciplinary action by the Institute and can also evoke penal action from the sources which have thus not been properly cited or from whom proper permission has not been taken when needed.

(Mukesh Kumar)

Date: Roll No. 176103016

Acknowledgements

First and foremost, I want to express my sincere gratitude toward my Ph.D. supervisor, Dr. Poonam Kumari, for providing me an opportunity to work under her supervision. I am grateful to her for her consistent guidance, motivation, patience, kindness and family support as well, over these years. She has always made available herself for discussions besides her busy schedules. Her enthusiasm, sublime work ethics, analytical abilities, and never-say-die attitude toward research and life as well, has natured my scientific skills and also inspired me immensely to work hard. I am proud to have her as my Ph.D. supervisor. Thank you, Ma'am, for all your help, advice, and support.

I want to thank my doctoral committee member, Prof. K. S. R. Krishna Murthy, Dr. Nelson Muthu , and Prof. D. Pamu, for their encouragement, insightful comments, and suggestions which have helped me to refine and widen my research from various perspectives. My sincere gratitude also goes to the Head of Department of Mechanical Engineering, Prof. K. S. R. Krishna Murthy, for providing all the resources needed for my research. I also thankful to all faculty and staff members of the Mechanical Engineering department who help me whenever I needed. Without their help, it would not have been possible to conduct my research. It is an honor for me to thank the Indian Institute of Technology Guwahati for giving me such an excellent opportunity for undergoing my research.

I gratefully acknowledge the Science and Engineering Research Board and NEWGEN IEDC, India for providing financial support through grant SB/WEA04/2019 and IEDC/2019-20/PK2 to support this research work. I am also thankful to the Ministry of Human Resource and Development (MHRD), Government of India for providing me financial support during my Ph.D. at IIT Guwahati.

I want to thank my seniors, Dr. Susanta Behera, Dr. Agyapal Singh, Dr. Sharnish Kar, and Dr. Sathish Kumar R. for their mentorship related to make things done and hand-holding whenever I got stuck during the research. I should also mention about Viwek, Abir, Nikhil, Vaishnavi, Vaibhav, Abhimanyu for their timely help, suggestions, and encouragements. It was fun to work with the PG students whose contributions showed new dimension to this research. I am indebted to my colleagues and friends, Pran, Mukesh, Krishan, Manjesh, Niranjan, and Abhinav who made this journey along with me creating a memorable campus life.

My special gratitude goes to my family for their role in my life. I offer my regards to my loving parents, Mr. Nunu Babu Singh and Mrs. Nirmala Devi, whose love, teachings, sacrifices, and blessings brought me this far. I am thankful to my elder sister Mrs. Rinku Devi and father-in-law, Mr. Ram Padarath Singh for supporting my parents and at instances taking my share of responsibilities. I am also grateful to my younger sister Guriya and Priti, and in-laws for their love and understanding and for motivating me to pursue my career.

I extend my sincere thank to my friends Chandan, Uttam, Santosh, Sanjeev, Pradeep and especially Ravi and Jainendra who helped me emotionally, financially, socially during the tough time of my life. Thanks for being what you are.

Last but not least, I am immensely grateful to my best friend and life partner, Laxmi Kumari who has been a constant inspiration, understating, and had faith in me which has been my greatest strength. I am truly thankful for having you in my life. My thesis acknowledgment would be incomplete without thanking my son, Devyut, whose smiling face always made me happy and inspired me. He has made our life wonderful. My parents, wife, son, sister, and in-laws are the backbone of my happiness, and I dedicate my thesis to them.

Finally, I thank God for always being with me.

Mukesh Kumar

Abstract

Piezoelectric material based sensor, actuator are widely used in many engineering fields such as aerospace, medical, marine, consumer sports, etc. Many research groups have been extensively studying piezoelectric based nanofiber mats over the years due to their higher sensing capability. Flexible piezoelectronics are the key components in various micro-, nano-scale energy harvesting devices, structural health monitoring, and medical devices. A wide range of devices have been developed specifically for energy harvesting applications. Moreover, these devices can be used to power small electronic devices such as sensors, capacitors, light-emitting diodes, watches, etc. Piezoelectric materials such as lead zirconate titanate PZT-5A and PZT-5H are highly brittle due to which complex shapes, robust stringent loading, and boundaries condition limits their application for developing nano or microdevices for sensing or actuation purpose. Hence, piezoelectric polymer-ceramic based nanofibers are better option for the sensing and energy harvesting applications. The sensitivity of nanofiber composite mats depend upon the manufacturing/fabrication method. Fiber mats can be manufactured using solution casting, thermal evaporation, spin coating, hydrothermal, and electrospinning, etc. Electrospinning is the most suitable fabrication metod due to its ability to fabricate nanostructures with novel properties such as small diameter, long length, diversified composition, high surface area to volume ratio, inter/intra fibrous porosity, flexibility in surface functionalities, and self poling. Electrospun nanofibers have been used in various areas such as tissue engineering, wound dressing, filtration, drug delivery system, desalination, protective clothing fabrication, optical electronics, personal care, sound absorption, and biosensors. The sensing and actuating capacity of these fibers significantly depend on various parameters, which affect the morphology of fabricated nanofibers. The aim of this research is to develop P(VDF-TrFE) based flexible piezoelectric mats for energy harvesting and sensing applications. Since,

pure P(VDF-TrFE) based mats have low power output. Some piezoceramic nano particles such as ZnO, $BaTiO_3$, TiO_2 are added to enhance the power output of the electrospun mats. P(VDF-TrFE)/ZnO nanofiber membranes are synthesized with optimizing the electrospinning parameter. Electrospun PVDF/$BaTiO_3$ functionally graded webs are fabricated for the energy harvesting application. Further, hybrid nanocomposite mats are synthesized and incorporated them as a wearable device. P(VDF-TrFE)/TiO_2 based hybrid nanogenerator comprised of piezoelectric and triboelectric nanogenerator are also designed for the energy harvesting and impact sensor application. The optimization of process parameter (applied voltage, flow rate, spinning distance, shape of spinneret), solution parameter (molecular weight, polymer concentration, viscosity, conductivity), and ambient parameter (humidity, temperature, and type of atmosphere), which affect the nanofiber power output are also studied. Electrospun nanofiber composites are then investigated for their energy capturing and sensing capability by varying the matrix and reinforcing fillers concentration. Subsequently, the surface morphology, mechanical behavior, crystallinity, fraction of beta phase, thermal stability, rheological properties, storage modulus, loss modulus, damping factor and piezoelectric performance of various fiber composite have been analyzed. Piezoelectric nanogenerator (PENG) devices are designed using nanofiber mats as an active layer placed between the top and bottom electrodes for energy harvesting and sensing applications. These devices are subjected to pressing, bending, tapping, and impact load and output is recorded using digital storage oscilloscope (DSO). These devices can be used as biomechanical sensors, impact sensors, and energy harvesting applications. The present research output can be basis for futuristic development of wearable medical and energy harvesting devices.

Contents

List of Figures

List of Tables

List of Abbreviation

DMF = Dimethylformamide
ACE = Acetone
PVDF = Poly(vinylidene-fluoride)
P(VDF-TrFE) = Poly(vinylidene-trifluoroethylene)
ZnO = Zinc oxide
$BaTiO_2$ = Barium titanate
TiO_2 = Titanium oxide
PDMS = Polydimethylsiloxane
FESEM = Field emission scanning electron microscopy
EDX = Energy-dispersive X-ray analysis
AFM = Atomic force microscopy
XRD = X-ray diffraction test
ATR = Attenuated total reflectance
FTIR = Fourier transform infrared spectroscopy
DSC = Differential scanning calorimetry
UTM = Universal testing machine
XPS = X-ray photoelectron spectroscopy
BET = Brunauer-Emmett-Teller
DMA = Dynamic mechanical analysis
TGA = Thermo-gravimetric analysis
RSM = Response surface methodology
ANOVA = Analysis of variance
DSO = Digital storage oscilloscope

Chapter 1

INTRODUCTION

1.1 PREFACE

Advancement in material sciences has delivered multi-functional materials with characteristics of superior flexibility, drability, mechanical and certain other physical properties such as pressure, strain, temperature, voltage, temperature sensitivity, etc. Intelligent structural systems can be created by efficiently integrating smart materials with traditional structures, demonstrating the versatility of such materials. The development of piezoelectric fiber reinforced composites (PFRC) has focused on achieving high strength, flexibility to adapt to curved surfaces, and durability, while also leveraging their diverse piezoelectric properties. Piezoelectric materials are among the most popular and widely utilized functional materials for converting mechanical energy to electrical energy and vice versa. Piezoelectric materials can be classified into two main categories: lead-containing and lead-free materials. Lead-containing includes materials such as lead zirconate titanate (PZT), lead titanate ($PbTiO_3$), and various chemically modified versions of these materials, demonstrate superior piezoelectric performance. Although, The utilization of lead in these materials poses environmental and biological concerns, thereby limiting their applications. This has led to the exploration and development of various types of lead-free piezoelectric materials, including zinc oxide (ZnO), barium titanate ($BaTiO_3$), titanium oxide (TiO_2), polyvinylidene fluoride (PVDF), poly(vinylidene fluoride) and its copolymers with trifluoroethylene P(VDF-TrFE). These materials offer several benefits such as strong piezoelectric properties, straightforward synthesis, cost-effective production, simple structure, and sustainability in mass production for various applications. As a result, they present a promising pathway to gradually replace all lead-containing

piezoelectric materials. During the last decade, there has been remarkable advancement in the research and development of sensors and energy harvesters based on piezoelectric technology. The ability of piezoelectric energy harvesters to capture and transform ambient mechanical energy into electrical energy, through the use of nanometer-scale materials, has demonstrated considerable potential. Piezoelectric energy harvesters are an eco-friendly alternative to conventional batteries, capable of sustaining electrical energy for longer periods. Therefore, they have been recognized as a crucial element for energy conversion, wearable device, and sensing applications. Nonetheless, these materials have not been extensively employed specifically in situations involving wearable applications. To make flexible electronic devices, it is necessary to develop flexible nanocomposite mats. These mats can be produced using various methods, including Layer-by-Layer (LbL) Assembly, sol-gel process, chemical vapor deposition, spin coating, solution casting, and electrospinning. Among these techniques, electrospinning is particularly suitable for producing flexible nanofiber composite mats that can be used in wearable applications. The electrospinning method offers significant advantages, including the production of fibers with high aspect ratios and large surface area to volume ratios, making it ideal for applications such as energy storage, filtration, and tissue engineering. Additionally, this method is highly versatile and can be used with a diverse range of polymers and nanofillers. Another key advantage of electrospinning is its scalability, as the process can be easily adapted for industrial production.

The objective of this study is to examine how the addition of three distinct fine fillers to P(VDF-TrFE) impacts the structure and characteristics of electrospun composite nanofiber membranes for energy harvesting and wearable applications. The dissertation includes a) synthesis and characterization of electrospun P(VDF-TrFE)/ZnO nano mats as biomechanical energy harvester, b) optimizing the electrospinning parameters using Box-Behnken design for the better piezoelectric performance, c) development of electrospun functionally graded PVDF/$BaTiO_3$ mats for the energy scavenging applications, d) design and development of three phase P(VDF-TrFE)/ZnO/TiO_2 nanocomposite for the wearable applications and analyse the influence of nanofillers, and e) P(VDF-TrFE)/TiO_2/PDMS based piezo-triboelectric hybrid nanogenerator for the wearable and energy harvesting applications.

The relevent literature is extensively reviewed of various process parameters of electrospinning method, for the enrgy harvesting, and werable devices applications is preented in the next chapter. The objectives and organization of this work is describe in the next chapter and the motive behind this work can be clearly reasoned from the following discussions.

1.2 PIEZOELECTRICITY

This section provides a review of the history and fundamental scientific concepts related to piezoelectricity, which serve as the foundation for the current work.

1.2.1 History of Piezoelectricity

In 1880, Pierre and Jacques Curie were the first to investigate the phenomenon of piezoelectricity [7]. Through their experiments with various crystals, including quartz, tourmaline, cane sugar, Rochelle salt, and topaz, they observed that these materials generated a surface charge when subjected to mechanical stress. Upon its discovery, the scientific community recognized the importance of this phenomenon and gave it the name "piezoelectricity," derived from the Greek word "piezo," which means to "press". Thus, the term describes the generation of electricity through the application of pressure. While the discovery of piezoelectricity is attributed to the Curie brothers, they did not report on the converse piezoelectric effect. In 1881, however, Gabriel Lippmann used thermodynamics principles and mathematical calculations to predict that applying a voltage difference across a piezoelectric crystal could cause it to undergo strain [8]. Piezoelectric crystals were deemed a valid scientific pursuit before World War I, and within the following three decades, research yielded significant findings. These included the recognition of the asymmetric nature of piezoelectric crystals, the capacity for reversible exchange of mechanical and electrical energy using these materials, and the application of thermodynamics in describing various aspects of piezoelectricity. During World War I, Paul Langevin of France developed the first engineering application of piezoelectric materials by fabricating a mosaic of thin quartz crystals that he then affixed between two steel plates acting as electrodes. The system's resonance frequency was roughly 50 KHz and its purpose was to transmit an ultrasonic signal into water while tracking the duration of time it

took for the reflected sound wave to return to the water surface. The pioneering sonar technology utilized piezoelectric materials to measure ocean depths, making it the first of its kind. In the years between World War I and II, advancements to sonar technology were made, and the application of piezoelectric crystals was expanded. For instance, quartz crystals were utilized to develop frequency stabilizers for vacuum tube oscillators [9]. During this time period, ultrasonic transducers that relied on piezoelectric crystals were also utilized for material property measurements. It is worth noting that numerous conventional applications of piezoelectric materials, including transducers, accelerometers, and microphones, were initially developed during this era. Throughout World War II, considerable research on piezoelectric materials was conducted by different research group, leading to the creation of piezo ceramics and the synthesis of materials with exceptionally high dielectric properties, which were utilized in capacitors. These investigations ultimately resulted in the invention of potent sonar equipment, sensitive headphones, ceramic phono cartridges, and piezo-ignition systems [9].

1.2.2 Mechanism of Piezoelectricity

Piezoelectricity in solid materials is closely connected to their electric dipole. This dipole may be created by molecular groups or induced by ions occupying crystal lattice sites that have an uneven distribution of charges. By adding up the dipole moments per unit volume of the crystallographic unit cell, the dipole density can be determined [10]. Since each dipole is a vector, the dipole density P is a vector field. Dipoles in close proximity to each other tend to be arranged in Weiss domains, which are generally randomly oriented but can be aligned by poling, where a strong electric field is applied through the material, often at elevated temperatures. Although, not all materials are capable of being poled [11]. The application of mechanical stress can cause a change in the dipole density P. This change may occur due to the reconfiguration of the environment brought about by the dipole or due to the reorientation of molecular dipole moments. Piezoelectricity can appear in different strengths of polarization, and their directions may be determined by the orientation of P, the symmetry of the crystal, and the magnitude and direction of the applied mechanical stress. If a change in electric field extends between the units of surface charge density and crystal faces

are equal to the units of polarization, P will change. Piezoelectricity is the result of change in the dipole density in a bulk material.

1.3 PIEZOELECTRIC MATERIALS

There are over two hundred piezoelectric materials available for energy harvesting purposes. Some common examples of such materials include quartz, barium titanate (BT), lead titanate (PT), bismuth sodium titanate (BNT), lead zirconate titanate (PZT), Aluminum nitride (AlN), lithium niobate ($LiNbO_3$), poly(vinylidene fluoride trifluoroethylene) P(VDF-TrFE), and polyvinyl fluoride (PVF), among others. Initially, the BT ceramic was identified as a piezoelectric material, and currently, PZT is the preferred choice for piezoelectric energy harvesting applications. Although piezoelectric ceramics are brittle, they exhibit superior electromechanical properties when compared to piezoelectric polymers [12]. Alternatives to PZT are gaining more attention due to the emergence of new property requirements such as lightweight, good flexibility, and low toxicity. One such alternative is sodium potassium niobate, which possesses similar properties to PZT but without lead. Piezoelectric materials are categorized into three types, namely, inorganic, organic, and composites, which are described in greater detail below.

1.3.1 Inorganic Piezoelectric Materials

Single crystal ceramic materials are typically anisotropic in nature, meaning that their properties vary with direction. Many of these materials exhibit piezoelectricity, such as quartz (SiO_2), lithium niobate ($LiNbO_3$), lithium tantalite ($LiTaO_3$), zinc oxide (ZnO), barium titanate ($BaTiO_3$) lithium sulfate monohydrate, and Rochelle salt. They offer various benefits in applications such as frequency-stabilized oscillators in watches and radars, and surface acoustic wave devices in television filters, sensor, transducer, and analog signal correlators [13]. The Perovskite family, which encompasses piezoelectric ceramics that possess the Perovskite structure, represents the largest group of piezoelectric ceramics. This category includes barium titanate ($BaTiO_3$ or BT), lead titanate ($PbTiO_3$ or PT), lead zirconate titanate ($Pb(Zr_xTi_{1-x})O_3$ or PZT), and lead magnesium niobate ($Pb(Mg_{1/3}Nb_{2/3})O_3$ or PMN) [13]. Piezoelectric ceramics exhibit strong piezoelectric effect

and possess a high dielectric constant. However, they tend to have a low mechanical quality factor, low stability, and power loss. Consequently, they are well-suited for use in power transducers and broadband filters, but not recommended for applications that require high stability and frequency. In contrast, quartz crystal displays a weaker piezoelectric effect and lower dielectric constant, but offers a high mechanical quality factor and excellent stability. Consequently, it is suitable for high frequency applications such as frequency control standard vibrators, narrow band filters, and high-temperature ultrasonic transducers. However, their size availability is limited due to cutting type restrictions.

1.3.2 Organic Piezoelectric Materials

In 1969, Kawai reported the first observation of piezoelectric behavior in polymers, which was attributed to a specific crystalline structure that formed during the solidification of the polymers from the melt [14]. Piezoelectric polymers occupy specialized areas where single crystals and ceramics are not capable of performing effectively. Typically, the piezoelectric strain constant (d_{31}) of piezoelectric polymers is lower than that of piezoelectric ceramics. However, the piezoelectric stress constants (g_{31}) of piezoelectric polymers are significantly higher than those of piezoelectric ceramics. Piezoelectric polymers are advantageous for various applications, such as in sensors, medical devices, and underwater equipment, due to their exceptional properties including high strength and impact resistance, low elastic stiffness and density, low dielectric constant, high voltage sensitivity, and low acoustic and mechanical impedance. They also exhibit high dielectric breakdown and operating field strength, further enhancing their usefulness. Furthermore, compared to their ceramic counterparts, piezoelectric polymers provide more processing flexibility, allowing for the fabrication of large film areas that can be cut and shaped into various forms. These polymers enable the placement of patterned electrodes on the film's surface and the selective poling of specific areas [15]. While several polymers, including polystyrene, polypropylene, polyvinyl acetate, poly(methyl methacrylate), and odd-numbered nylons such as Nylon-11, exhibit piezoelectric characteristics, the most prominent piezoelectricity has only been observed in polyvinylidene fluoride (PVDF) and its copolymers, such as poly(vinylidene fluoride-trifluoroethylene) copolymer or P(VDF-TrFE). PVDF is composed of a

chain of carbon atoms that are linked to alternating hydrogen and fluorine units, forming repetitive units (-CH_2-CF_2-). The way the chains are arranged determines the type of crystalline phase of PVDF. There are four different phases: α or δ (TGTG'), β (TTTT), and γ (TTTGTTTG') (T-trans, G-gauche+, G'-gauche). The -phase of PVDF exhibits piezoelectricity due to its spontaneous polarization. On the other hand, the α and γ phases, which are non-piezoelectric, can be converted into the piezoelectric β-phase through poling under high electric fields or mechanical stretching, respectively [13]. Additionally, the δ phase is a polar version of the α phase [16]. The piezoelectric properties of PVDF are a result of the attraction and repulsion forces between the long-chain molecules when applied to an electric field. The dipole polarization of PVDF is further intensified by stretching and poling thin polymer sheets, which induces the formation of the β phase in PVDF. Piezoelectric polymers, including PVDF, are commonly used in applications such as ultrasonic hydrophones [17], sensor [18], actuator [19], and directional microphones [20]. More information on these applications will be provided in the next chapter.

1.3.3 Piezoelectric Composites

Piezoelectric composites that combine piezoelectric ceramics and polymers are highly promising, as their properties can be customized to achieve desirable characteristics such as high coupling factors, low acoustic impedance, good mechanical flexibility, broader transducer bandwidth, and low mechanical quality factor. These features make them particularly useful in applications such as underwater sonar and medical diagnostic ultrasonic transducers [21, 22]. Further details on PVDF-based composites will be discussed in the next chapter.

1.4 GENERAL OVERVIEW OF NANOCOMPOSITES

In this section, fundamental aspects of nanocomposites will be presented. The discussion will begin with a review of nanoparticles and nanofibers, which are commonly used as dispersed phases in nanocomposites. Next, the key features of nanocomposites will be compared to those of conventional composites, and their classifications will be described.

1.4.1 Nanoparticles

A nanoparticle can be defined as the smallest unit of a composite material, whether it be a single particle, a cluster of particles, or remnants of agglomerates. However, in practice, complete separation of clusters or agglomerates into single particles is rarely achieved, and they still exhibit motion within the matrix of the composite. Particles can be classified based on their diameters or equivalent sizes. Coarse particles have diameters in the range of 2,500 to 10,000 nm, fine particles range from 100 to 2,500 nm, and ultrafine particles (nanoparticles) range from 1 to 100 nm, respectively as suggested by Buzea et al. in 2007 [23]. It should be noted that nanoparticles are not necessarily equiaxial and should have at least one dimension in the range of 1 to 10 nm with a narrow size distribution. Nanopowders are typically composed of agglomerated nanoparticles or nanoclusters [24].

Nanoparticles have garnered significant scientific interest due to their ability to bridge the gap between atomic/molecular structures and bulk materials. While bulk materials maintain relatively invariant physical properties regardless of size, size-dependent properties are frequently observed at the nanoscale. Consequently, the properties of materials can change when their sizes approach the nanoscale and the percentage of atoms on the material surface becomes significant. In bulk materials larger than one micron, the percentage of atoms on the surface is typically negligible when compared to the number of atoms in the bulk of the material. However, the large surface area of nanoparticles is responsible for many unexpected properties they exhibit. For instance, due to their small size, nanoparticles can restrict their electrons and produce quantum effects, leading to unexpected optical properties.

Numerous types of nanoparticles with various properties, including metal, dielectric, and semiconductor nanoparticles, as well as semi-solid and soft nanoparticles, and hybrid structures such as core-shell nanoparticles, have been produced and investigated for their potential uses in biomedical, optical, electronic, and mechanical applications.

Nanoparticles with semiconductor properties are commonly referred to as quantum dots if their size is less than 10 nm, which allows for the quantization of electronic energy levels [25]. These

quantum dots find applications in biomedical fields, such as drug carriers or imaging agents. On the other hand, liposomes are typical semi-solid nanoparticles that have been extensively used as delivery systems for anticancer drugs and vaccines in various clinical settings [26]. Janus nanoparticles possess hydrophilic and hydrophobic properties on two distinct halves, making them highly efficient for stabilizing emulsions. These nanoparticles can spontaneously assemble at the interface of water and oil and serve as solid surfactants [27]. Furthermore, nanoparticles exhibit beneficial properties for everyday products, including self-cleaning surfaces in materials that incorporate titanium dioxide nanoparticles, enhanced UV blocking capabilities through the use of zinc oxide nanoparticles in sunscreen lotion preparation and smart and functional clothing coated with nanoparticles [28]. The field of micromeritics encompasses the various shapes and surface morphologies of nanoparticles, ranging from spheres, rods, fibers to cups, among others. Nanospheres, nanoreefs, and nanoboxes, among other shapes, may spontaneously form during synthesis due to templating or directing agents such as miscellar emulsions or anodized alumina pores, or from the inherent crystallographic growth patterns of the materials. Certain morphologies of nanoparticles can serve specific purposes, such as the utilization of long carbon nanotubes for connecting electrical junctions. Amorphous particles typically assume a spherical shape due to their microstructural isotropy, while the shape of anisotropic microcrystalline whiskers corresponds to their unique crystal habit.

1.4.2 Nanofibers

Nanofibers are fibers with a diameter below 100 nm, and electrospun fibers, for example, have an average diameter ranging from 100 nm to 500 nm [29]. Like nanoparticles, nanofibers possess a high specific surface area (about a thousand times greater than that of a human hair) and thus have similar potential applications in nanocatalysis, tissue scaffolds, protective clothing, filtration, and nano-electronics [30]. Additionally, their almost infinite aspect ratio for continuous fibers makes them highly attractive for mechanical reinforcement in nanocomposites. Nanofibers have generated considerable interest due to their high specific surface area, strength, stiffness, and the ability to produce defect-free three-dimensional structures [29]. Polymer nanofibers with diameters of 100 nm, for example, possess an exceptionally high specific surface area. Nanofibers have numerous

potential applications in aerospace, protective clothing, filtration, electronic devices, tissue engineering, biomedical, and sensors [31, 32]. Nanofiber mats have even been utilized as drug carriers in drug delivery systems [33].

1.4.2.1 Fabrication method

Several techniques are available for the fabrication of nanofibers, such as splitting of bicomponent fibers, physical drawing, flash-spinning, meltblowing, solvent dispersion, centrifugal spinning, hydrothermal, self-assembly, phase separation, and template synthesis, and electrospinning.

Electrospinning is a commonly used method for the fabrication of ultrafine fibers by applying high voltage to a polymer solution or melt. The voltage stretches the solution, leading to the formation of nanofibers with diameters ranging from tens of nanometers to a few micrometers. These fibers are then collected on a grounded surface and can be used for various applications.

Meltblowing is a process in which a polymer is melted and passed through a tiny nozzle while a high-velocity air stream blows the extruded polymer. This results in the creation of microfibers and nanofibers, which can be used for various applications.

Centrifugal spinning is a technique used to generate nanofibers that employs a rotating spinneret. In this method, a polymer solution is loaded into the spinneret, and the rotation of the spinneret generates centrifugal force, ejecting the solution out of the spinneret and resulting in the formation of nanofibers. These fibers are then collected on a grounded surface for further use.

Self-assembly is a method used to create nanofibers by arranging molecules or nanoparticles into a predetermined structure via physical or chemical interactions. This technique results in the formation of nanofibers that have unique properties and can be utilized for various applications.

Phase separation is a process used to generate nanofibers by separating two immiscible polymers into separate phases. This separation leads to the formation of nanofibers at the interface between the two phases, which can be utilized for various applications.

Template synthesis is a method for creating aligned nanofibers with controlled dimensions by using a porous template to direct their growth. In this technique, the template guides the formation of nanofibers, resulting in fibers that are oriented in a specific direction and have a consistent size.

This process can be used for a variety of applications. The selection of the appropriate fabrication technique for nanofibers is dependent on the intended application and desired properties of the fibers. Various methods are available, each with its advantages and limitations, and the choice of technique should be made based on the specific needs of the application.

1.4.3 Nanocomposites

A solid material that contains multiple phases, with at least one phase having a dimension of less than 100 nm or a structure with nano-scale repeating distances between phases, is referred to as a nanocomposite [34]. The properties of nanocomposites, including optical, electrical, thermal, mechanical, electrochemical, and catalytic, differ significantly from those of their constituent materials due to their high specific surface area, which enhances chemical reactivity and stiffening, and quantum effects, which result in new optical, electrical, and magnetic properties [35]. It has been summarized that as the dimension of nano-scale phases decreases, the following effects occur: dimensions below 100 nm lead to superparamagnetism, mechanical strengthening, or limit matrix dislocation movement; dimensions below 50 nm change the refractive index; dimensions below 20 nm soften a hard magnetic material, and dimensions below 5 nm result in catalytic activity [36].

The unique characteristic of nanocomposites that distinguishes them from traditional composites is their extremely high surface area to volume ratio of the dispersed phases and their remarkably high aspect ratio. The dispersed phase may of of nano-sized minerals, fibers/whiskers (such as spun fibers, or nanocellulose), or sheets. The specific interfacial area between the dispersed phase and matrix in nanocomposites can be significantly higher as compared to conventional composites, resulting in significant changes in their properties. The properties of polymer nanocomposite is related to the chain mobility, chain configuration, thermoset cure level, interfacial chemistry, and degree of crystallinity. The specific interfacial area enables even a small quantity of nano-scale reinforcement to produce a notable enhancement in the properties of the composites.

1.4.4 Classification of Nanocomposites

Nanocomposites can be divided into various categories based on the matrix material, such as ceramic-matrix, metal-matrix, and polymer-matrix nanocomposites. A summary of each is provided

below.

1.4.4.1 Ceramic-matrix nanocomposites

Nanocomposites that have a ceramic matrix are a type of composite material. They are strengthened by incorporating nano-sized particles into the ceramic matrix. The addition of these particles can augment the mechanical, thermal, and electrical properties of the ceramic matrix, and also enhance its toughness and ductility. The nanoparticles used to reinforce the ceramic matrix may vary and include carbides, nitrides, oxides, and carbon-based materials. Ceramic-matrix nanocomposites are highly promising for various applications, including biomedical, energy, and aerospace, owing to their exceptional properties.

1.4.4.2 Metal-matrix nanocomposites

Metal-matrix nanocomposites comprise a metallic matrix (e.g., aluminum, copper, or titanium) reinforced with nanoparticles or fibers of a different material (e.g., carbon, ceramic, or polymers) [37]. This combination allows them to exhibit superior mechanical, thermal, and electrical properties by blending the strength and stiffness of the reinforcing material with the ductility and toughness of the metallic matrix. As a result of their distinct properties, they hold promise for numerous industries, including aerospace, automotive, electronics, and biomedical [38, 39, 40].

1.4.4.3 Polymer-matrix nanocomposites

Polymer nanocomposites are a type of composite materials that involve the dispersion of inorganic nanoparticles throughout an organic polymer matrix, resulting in enhanced performance properties [41]. Polymer nanocomposites consist of two main components: the polymer matrix and the nano-fillers. By incorporating nano-fillers into the polymer matrix, the benefits of both materials can be combined. The classification of polymer nanocomposites can be based on the the dimensions of the nanomaterials, morphology of the resulting polymer nanocomposites, the thermal response, and the polymer class. There are several methods for preparing polymer nanocomposites, with the most popular being solution dispersion, in situ polymerization, melt extrusion, spin coating, and electrospinning [42]. Polymer nanocomposites exhibit outstanding properties such as high

magnetic efficiency, electrical conductivity, and resistance to barriers. Polymer nanocomposites present numerous advantages including increased stiffness, enhanced fire resistance, improved thermal and dimensional stability, positive optical properties, and an improved barrier effect. These features make polymer nanocomposites applicable in multiple state-of-the-art industries, such as medical [43], electrical [44], actuator [45], sensor [46], and environmental sectors [47].

1.5 APPLICATION OF ELECTROSPUN MAT

Electrospun mats possess distinctive characteristics, such as high surface area-to-volume ratio, high porosity, and adjustable morphology, which render them highly versatile for application across diverse fields. Some of the typical applications in specific domain of engineering are as follows:

Tissue engineering: The ability of electrospun mats to mimic the extracellular matrix of tissues and create a conducive environment for cell proliferation makes them a suitable option as scaffolds for tissue engineering purposes. These mats can be used to facilitate wound healing, bone regeneration, and nerve regeneration, among other tissue engineering applications [48].

Drug delivery: The medical industry has shown interest in finding the most practical method of drug delivery, which has led to a focus on nanofibers as the ideal drug delivery carriers. Nanofibers fabricated through electrospinning have been found to be highly compatible with drug loading, allowing for a wide range of drugs to be loaded onto them [49].

Filtration: Electrospun mats are well-suited for filtration purposes owing to their high porosity and small pore size, which makes them suitable candidate for filtering air and water and separating minute particles. These mats can be employed in various filtration applications [50].

Energy storage: The high surface area and porosity of electrospun mats make them a viable option as electrodes for energy storage devices, including supercapacitors and batteries. This is because electrospun mats possess characteristics that are beneficial for such applications [51].

Sensors: electrospun mats can be applied as sensors for a range of applications, including gas and biosensing, as well as environmental monitoring. This is because electrospun mats exhibit properties that make them well-suited for detecting changes in their surroundings [52].

The distinctive characteristics of electrospun mats enable them to have a wide range of appli-

cations, making them a promising material for a variety of engineering applications. In summary, electrospun mats possess properties that make them a versatile and useful material for numerous purposes.

1.6 MOTIVATION

Application of the nanofiber composite membranes in real world is obviously inevitable. Further, enlarging scope for development of the piezoelectric fiber reinforced composite and structures in engineering domains has directed the evolution of theories based on the various surface morphology. Piezoelectric materials have the potential to be utilized in various practical applications and hold great promise for future use. Ambient sources of vibrational and kinetic energy, such as those present in wind or water waves, or machinery vibrations, are abundant and could serve as potential sources of energy to be harvested by piezoelectric materials. Piezoelectric conversion of energy from these sources holds potential for providing an alternative source of clean energy. For MEMS devices and sensors, batteries can be a hindrance due to their bulkiness and need for frequent replacement. However, piezoelectric materials offer a solution by enabling the development of self-powered wireless sensing devices that do not require batteries and can be placed in remote locations. This is further motivated by the wide range of frequency applications, low surface potential of certain piezoelectric materials, or minor imperfections in the bonding between components, whose effects need to be predicted very precisely.

Chapter 2

LITERATURE REVIEW

In this chapter, a detailed literature review has been presented on different process, solution, and ambient parameters of the electrospinning method for the fabrication of electropun nanocomposite and functionally graded (FG) mats in Sec. 2.1. Further, the brief survey of literature has been presented for the different nanocomposite system based self-powered sensor as energy harvesting and wearble applications in Sec. 2.2. The objectives of this work are outlined in Sec. 2.3 and organization of the thesis is described in Sec. 2.4.

2.1 LITERATURE REVIEW FOR ELECTROSPINNING

Nanotechnology is an emerging field that has been recognized as a significant scientific and commercial enterprise with worldwide economic advantages. As understanding of nanomaterial manufacturing techniques continues to grow, research teams worldwide are increasingly concentrating on developing nanomaterials for diverse applications. Among the many techniques documented in the literature, electrospinning has garnered considerable attention due to its capacity for producing nanostructures with distinctive features such as high surface area and inter/intra fibrous porosity. Electrospinning has been the most extensively employed technique in the late 20th century (1990s) and early 21st century (2000) [53]. Since its initial utilization in the early 20th century (1900) by Cooley [54], substantial enhancements have been made in instrument design, materials employed, and produced nanomaterials. Numerous operational parameters influence the fabrication of nanofibers using electrospinning. This review presents an outline of the electrospinning (applied voltage, flight distance, flow rate, and needle diameter), solution (concentration, viscos-

ity, solvent and solution conductivity), and ambient (humidity and temperature) parameters that impact nanofiber fabrication and the applications of nanofiber mat.

2.1.1 Influence of Parameters on Electrospinning

Numerous factors, which significantly affect the electrospinnning process. These factors can be categorized as operating parameters, solution parameters, and ambient parameters. The operating parameters include the applied voltage, flight distance, flow rate, and needle diameter. The solution parameters include the concentration of polymer, viscosity, solvent and solution conductivity. The ambient parameters include the temperature and humidity. The smoothness and absence of beads in electrospun fibers are directly influenced by these parameters. Thus, to enhance comprehension of the electrospinning process and synthesis of polymeric nanofibers, it is crucial to have a comprehensive understanding of the effect of all these governing factors. The affecting parameters are presented here in details.

***(i)* Effect of applied voltage**

In general, it is widely recognized that applying an electric current from a high-voltage power source to a solution through a metallic needle can lead to the deformation of a spherical droplet into a Taylor cone shape, resulting in the formation of ultrafine nanofibers at a particular critical voltage [1]. The critical voltage required for this process varies depending on the type of polymer used. The reason for the generation of smaller nanofibers with an increase in voltage can be attributed to the stretching of the polymer solution due to charge repulsion within the polymer jet [55]. Beyond the critical voltage, an increase in the applied voltage will cause the formation of either beads or beaded nanofibers. The increase in diameter and formation of these beads or beaded nanofibers can be attributed to a reduction in the size of the Taylor cone and an increase in the velocity of the jet for the same flow rate. Deitzel et al. studied on poly(ethylene oxide) (PEO)/water and observed bead formation as the applied voltage increased, which was later supported by similar findings reported by Meechaisue et al. and Zong et al. [56]. Additionally, an increase in the diameter of nanofibers was noted with a rise in applied voltage, which was attributed to the extension of the jet length as a result of the applied voltage as shown in Fig. 2.1 (a-f) [57]. Gu et al. [58] conducted

research on the electrospinning of polyacrylonitrile (PVA) nanofibers and concluded that altering the voltage had no significant impact on the diameter of the fibers. Reneeker and Chun investigated the electrospinning of polyethylene oxide nanofibers and observed that high voltage did not have a notable effect on the fiber [59]. Gee et al. [60] presented that the contribution of voltage to the formation of the phase in PVDF was minimal, and the average fraction of β phase was relatively similar across different applied voltages. ***(ii)*** **Effect of flow rate**

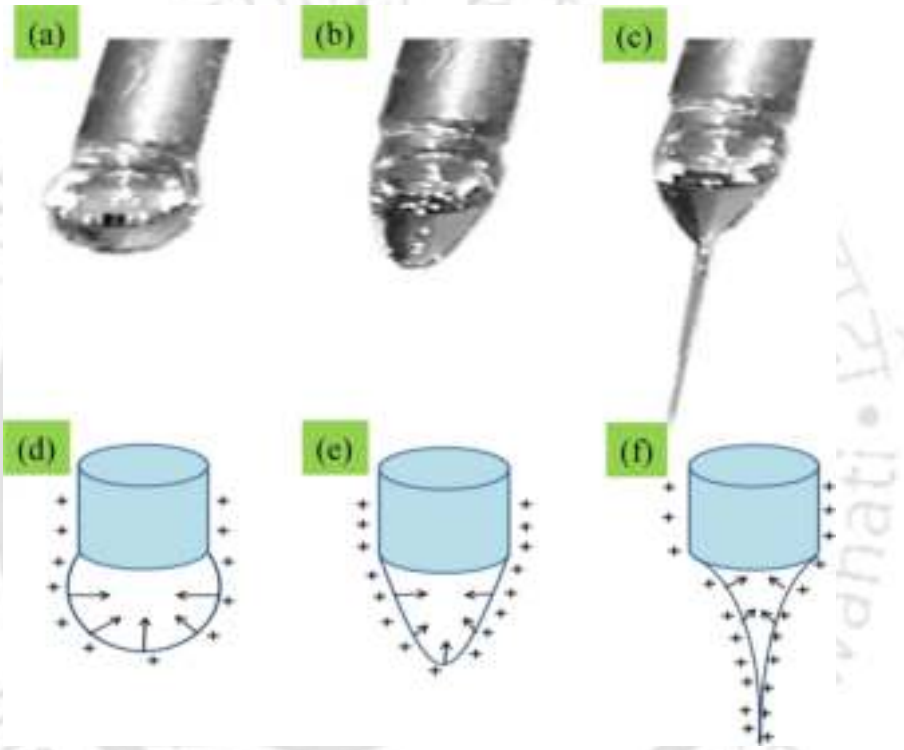

Fig. 2.1: Effect of increasing applied voltage on (a-c) three stage deformation of the polyvinylpyrrolidone droplet and effect (d-f) of charges on polymeric droplets [1].

The morphology of electrospun nanofibers is determined by the flow of the polymeric solution through the metallic needle tip. A critical flow rate for a particular polymeric solution can result in the production of uniform, beadless nanofibers. However, this critical value varies depending on the polymer system. The increase of flow rate beyond the critical value can lead to the formation of beads, as was observed in the case of polystyrene, where bead formation occurred when the flow rate was increased to 0.10 mL/min. By contrast, reducing the flow rate to 0.07 mL/min resulted in the formation of bead-free nanofibers. If the flow rate is increased beyond a critical value, it can result in an increase in pore size and fiber diameter, as well as bead formation,

which is caused by incomplete drying of the nanofiber jet during its flight between the needle tip and metallic collector [61]. Given that the nanofiber formation and diameter are influenced by changes in the flow rate, it is preferable to use a minimum flow rate to maintain a balance between the leaving polymeric solution and the replacement of that solution with a new one during jet formation [61, 62]. The different fiber jet, semi-spherical, and unspun droplets are shown in Fig. 2.2(a-e). Using a minimum flow rate can facilitate the creation of a stable jet cone, and in some cases, a receded jet (a jet that emerges directly from the inside of the needle with no visible droplet or cone). However, receded jets are unstable and are consistently replaced by cone jets during the electrospinning process. Consequently, nanofibers with a broad range of diameters are produced due to this phenomenon as shown in Fig. 2.2f [2]. In some instances, it has been presented in the literature that, aside from the formation of beads, ribbon-shaped defects [61] and unspun droplets (Fig. 2.2g) may occur when the flow rate is raised [2]. The production of beads and ribbon-like structures with an increased flow rate was largely attributed to the solvent not evaporating and the solution not being adequately stretched during the journey between the needle tip and metal collector. This same effect may also be due to an increase in nanofiber diameter as the flow rate increases [63]. It has been suggested that the existence of unspun droplets can be ascribed to the effect of gravitational force [2]. Furthermore, the surface charge density is another crucial factor that can induce defects in the nanofiber architecture. Even slight alterations in the surface charge density may impact the surface morphology of the nanofibers. Theron et al. conducted a study on various polymers, including PEO, polyacrylic acid (PAA), polyvinyl alcohol, (PVA), polyurethane (PU), and polycaprolactone (PCL) to investigate the relationship between flow rate and electric current. They found that an increase in flow rate was directly linked to an increase in electric current and reduced the surface charge density. For PEO, the researchers observed that an increase in flow rate led to a decrease in surface charge density while increasing the electric current. When surface charge density decreases, electrospun nanofibers can merge during their flight to the collector, resulting in the formation of garlands [64, 65]. Wu et al. [66] studied on various parameter for continuous electrospinning of polyacrylonitrile nanofiber yarn and found the variation of flow rate have significant effect on the diameter of nanofiber.

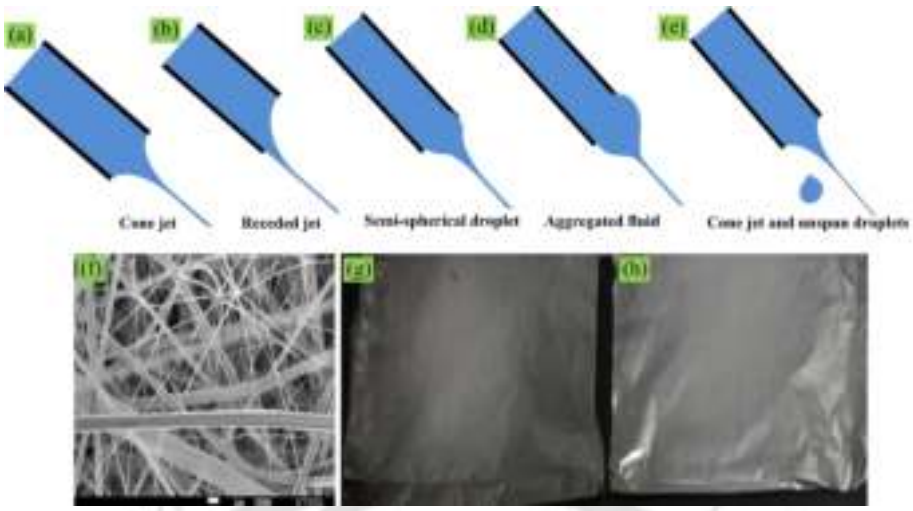

Fig. 2.2: Formation of (a-e) several jets with increasing flow rate [2] of nylon 6, SEM image of (f) nanofibers with wide diameter ranges (g) digital image of unspun droplet, (h) spun fibers of chitosan deposited on aluminum foil.

(iii) Effect of flight distance

The morphology of electrospun nanofibers is significantly influenced by the distance between the needle tip and the collector, which, like the applied voltage, viscosity, and flow rate, is subject to variation depending on the polymer system. Due to factors such as deposition time, evaporation rate, and whipping or instability interval, the nanofiber morphology can be easily altered by the distance between the needle tip and collector [67]. In order to produce electrospun nanofibers with a smooth and uniform morphology, it is essential to maintain a critical distance, as any deviation from this distance can impact the nanofiber's morphology [68]. Nazari et al. [69] studied on PLA/PEG melt electrospun fibers and found that spinning distance 10 cm is preferred to maintain smooth fabrication of uniform non-woven fiber. Several research groups have investigated the influence of distance between the needle tip and the collector, and their findings suggest that a small distance leads to the formation of defective and large-diameter nanofibers, while increasing the distance reduces the nanofiber diameter [57, 67, 70]. Although, there are instances where the nanofiber morphology remains unaffected by changes in the distance between the needle tip and collector [71].

(iv) Effect of concentration and viscosity

The electrospinning process is dependent on the phenomenon of a charged jet being stretched in a uniaxial direction. Altering the concentration of the polymeric solution has a notable impact on

the stretching of the charged jet. When the polymeric solution concentration is low, the electric field and surface tension cause the intertwined polymer chains to break into smaller fragments before reaching the collector, as observed in studies [72, 73]. Beads or beaded nanofibers are formed as a result of these fragments. If the concentration of the polymeric solution is increased, the viscosity rises, and the chain entanglement among the polymer chains increases. These chain entanglements overcome surface tension, leading to the formation of uniform, beadless electrospun nanofibers. However, if the concentration exceeds a critical value, the flow of the solution through the needle tip is impeded, causing the polymer solution to dry at the metallic needle's tip and block it. This ultimately results in defective or beaded nanofibers, as observed in studies conducted by [72]. As the viscosity of the solution alters, there is a remarkable alteration in the shape of the beads, progressing from a circular droplet-like structure (for solutions with low viscosity) to an elongated droplet or ellipse and then to smooth fibers (for solutions with adequate viscosity). This transformation is depicted in Fig. 2.3(a-d) [2]. Fong et al. [5] also found a similar phenomenon while varying the viscosity of PEO during electrospinning, as seen in Fig. 2.3(e-h). Zong et al. [74]

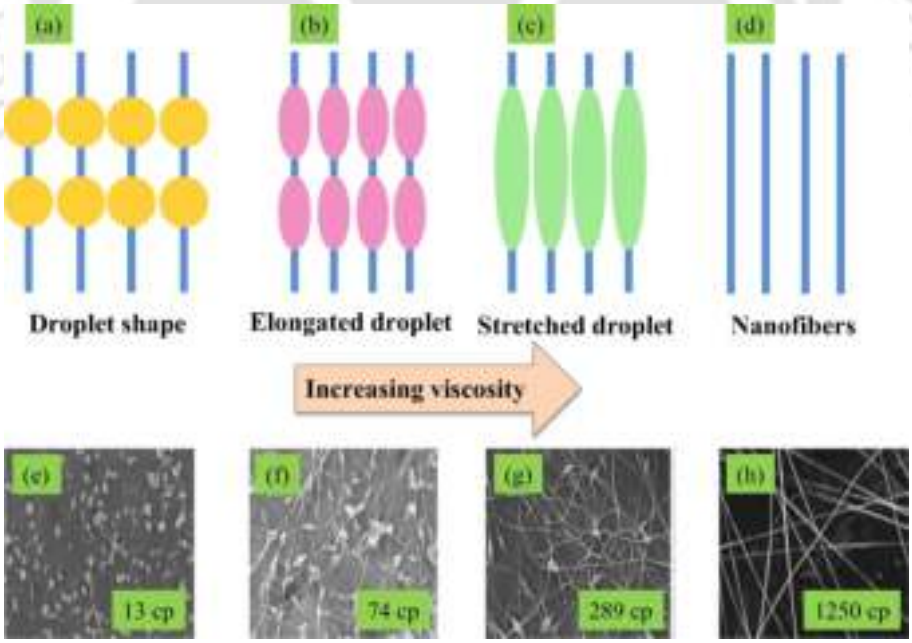

Fig. 2.3: Surface morphology of spun PEO nanofibers changes with viscosity (ad) schematic and (eh) FESEM images [3, 4, 5].

observed a comparable effect while examining PDLA poly(d,l-lactic acid) and PLLA poly(l-lactic acid), indicating that the shape of the beads is impacted by viscosity. Doshi et al. [75] reported

that the concentration/viscosity has an influence on the morphology of nanofibers, stating that the optimal viscosity range for generating electrospun nanofibers from PEO is between 800 and 4000 cp. Aside from the work of Doshi et al. [75], a study using a polyacrylonitrile (PAN) polymer solution demonstrated that maintaining the solution viscosity within 1.7 to 215 cp range produced smooth electrospun nanofibers. Therefore, it can be concluded that, in addition to controlling the electrospinning parameters, identifying the critical concentration/viscosity value is crucial to obtaining nanofibers without beads [57].

***(v)* Effect of solution conductivity**

Solution conductivity does not only influence the Taylor cone formation, but it also control the doameter of nanofibers. A solution with poorer conductivity will prevent electrospinning since the surface of the droplet won't be charged enough to create a Taylor cone. The Taylor cone will form when the conductivity of the solution is increased to a critical level, which will also result in a reduction in the diameter of the fibre [76]. Increasing the conductivity above the critical value will once more prevent the development of Taylor cones and electrospinning. The full electrospinning procedure could be considered in order to explain this phenomena. The process of electrospinning relies on the interaction between the charges present on the fluid's surface and the external electric field. The Coulomb force and the force generated by the electric field are crucial factors in this process. The creation of the Taylor cone, on the other hand, is mainly determined by the electrostatic force produced by the surface charges generated by the applied electric field. This force is induced by the component of the field, which is tangential to the fluid surface. If a dielectric polymer solution is ideal, it will not contain sufficient charges in the solution to move onto the fluid surface. Consequently, the electrostatic force that arises from the applied electric field will not be strong enough to create a Taylor cone and start the electrospinning process. On the other hand, a solution of conductive polymer will contain enough free charges to move onto the fluid surface, allowing the formation of a Taylor cone and start the electrospinning process. By incorporating an appropriate salt into a polymer solution, the solution's conductivity can be regulated. The addition of salt has two impacts on the electrospinning process: (i) it boosts the number of ions present in the polymer solution, which heightens the fluid's surface charge

density as well as the electrostatic force induced by the applied electric field, and (ii) it elevates the conductivity of the polymer solution, which lowers the tangential electric field along the fluid surface. However, as the solution's conductivity increases and the tangential electric field along the fluid surface is significantly reduced, the electrostatic force along the surface of the fluid weakens, leading to an adverse effect on the formation of the Taylor cone. The extension and thinning of the straight jet section are influenced by both Coulomb and electrostatic forces. The length of this portion, as well as the behavior of the whipping jet region, plays a vital role in determining the diameter of the resultant nanofibers. The presence of surface charges in the whipping region leads to stretching, which causes the fluid jet to be drawn into the nanoscale [77]. Several research teams have examined how the addition of salt impacts the diameter of nanofibers. Zong et al. [74] explored how various salts (KH_2PO_4, NaH_2PO_4, and NaCl in 1% w/v) affected the diameter of poly(d,l-lactic acid) (PDLLA) nanofibers. They found that after introducing the salt to the polymer solution individually, the resulting nanofibers were not only smooth and bead-free but also had a smaller diameter than the pristine nanofibers. Choi et al. [78] reported a similar finding when they added a small quantity of benzyl trialkylammonium chlorides to a solution of poly(3-hydroxybutyrate-co-3-hydroxyvalerate); the mean diameter of the resulting nanofibers decreased to 1.0 m.

***(vi)* Effect of solvent**

The choice of solvent is a critical factor in achieving smooth and bead-free electrospun nanofibers. Two factors need to be considered when selecting a solvent. Firstly, the solvent should be capable of completely dissolving the polymer used in the electrospinning process. Secondly, the solvent should possess a moderate boiling point, which indicates its volatility. Typically, solvents with high volatility are preferred because they facilitate the rapid evaporation of the solvent from the nanofibers during their flight from the needle tip to the collector. Although, solvents with extremely low boiling points and high evaporation rates should be avoided as they can cause the jet to dry up at the needle tip, leading to blockage of the needle and hindering the electrospinning process. Likewise, solvents with low volatility are also undesirable as their high boiling points hinder the drying of the solvent during the flight of the nanofiber jet. The accumulation of solvent-laden nanofibers on the collector can result in the formation of beaded nanofibers [55, 79]. Kanani and

Bahrami studied the influence of the solvent on the surface morphology of nanofibers and found that similar to applied voltage, the solvent also affects the polymer system [80]. Similar objervation is also found by Fong et al. [5]. In addition, the solvent is a critical factor in producing highly porous nanofibers. This can be achieved by dissolving the polymer in two solvents, with one of the solvents acting as a non-solvent. The varying evaporation rates of the solvent and non-solvent cause phase separation, resulting in the fabrication of highly porous electrospun nanofibers [55]. Megelski et al. [61] varied the ratio of tetrahydrofuran (THF) and dimethylformamide (DMF) to prepare porous nanofibers. Along with the volatility of the solvent, its conductivity and dipole moment are also critical factors. To investigate these effects, Jarusuwannapoom et al. [81] studied over 18 solvents and found that only five solvents, including ethyl acetate, DMF, THF, methyl ethyl ketone, and 1,2-dichloroethane, were suitable for electrospinning a polystyrene polymeric solution due to their comparatively higher conductivity and dipole moment values.

***(vii)* Effect of humidity and temperature**

In addition to the electrospinning and solution parameters, there have been recent findings that indicate environmental conditions such as relative humidity and temperature can also affect the surface morphology and diameter of nanofibers, as reported by different research groups [82, 83]. The solidification process of the charged jet, which affects the diameter of nanofibers, is influenced by humidity. It should be noted, however, that this effect is contingent upon the chemical properties of the polymer. Pelipenko et al. [83] explored how changes in humidity impacted the diameter of nanofibers made from PVA, PEO, and a blend of PVA/hyaluronic acid (HA) or PEO/chitosan (CS) solutions. Their findings indicated that as humidity levels increased from 4% to 60%, the diameter of the nanofibers decreased from 667 nm to 161 nm (PVA) and 252 nm to 75 nm (PEO). The blend solution experienced an even greater decrease in diameter. Specifically, when humidity levels were increased from 4% to 50%, the diameter of the nanofibers decreased from 231 nm to 46 nm for both PVA/HA and PEO/CS blends. However, when humidity levels increased further, bead fiber formation occurred for the individual polymers and electrospinning was difficult for the blends [83]. Park et al. [84] reported a reduction in the diameter of PEO nanofibers as humidity levels increase. Additionally, when a binary solvent system is utilized, humidity is a critical factor

in the development of porous nanofibers. Bae et al. [6] employed PMMA and a binary solvent system consisting of dichloromethane (DCM) and dimethylformamide (DMF) in an 8:2 ratio to generate highly porous nanofiber membranes. The formation of pores was attributed to the different evaporation rates at which the solvents evaporate, with the more volatile solvent (DCM) evaporating more quickly than the less volatile solvent (DMF) while the fibers were in flight towards the collector (Fig. 2.4). The different evaporation rates of the two solvents result in a cooling

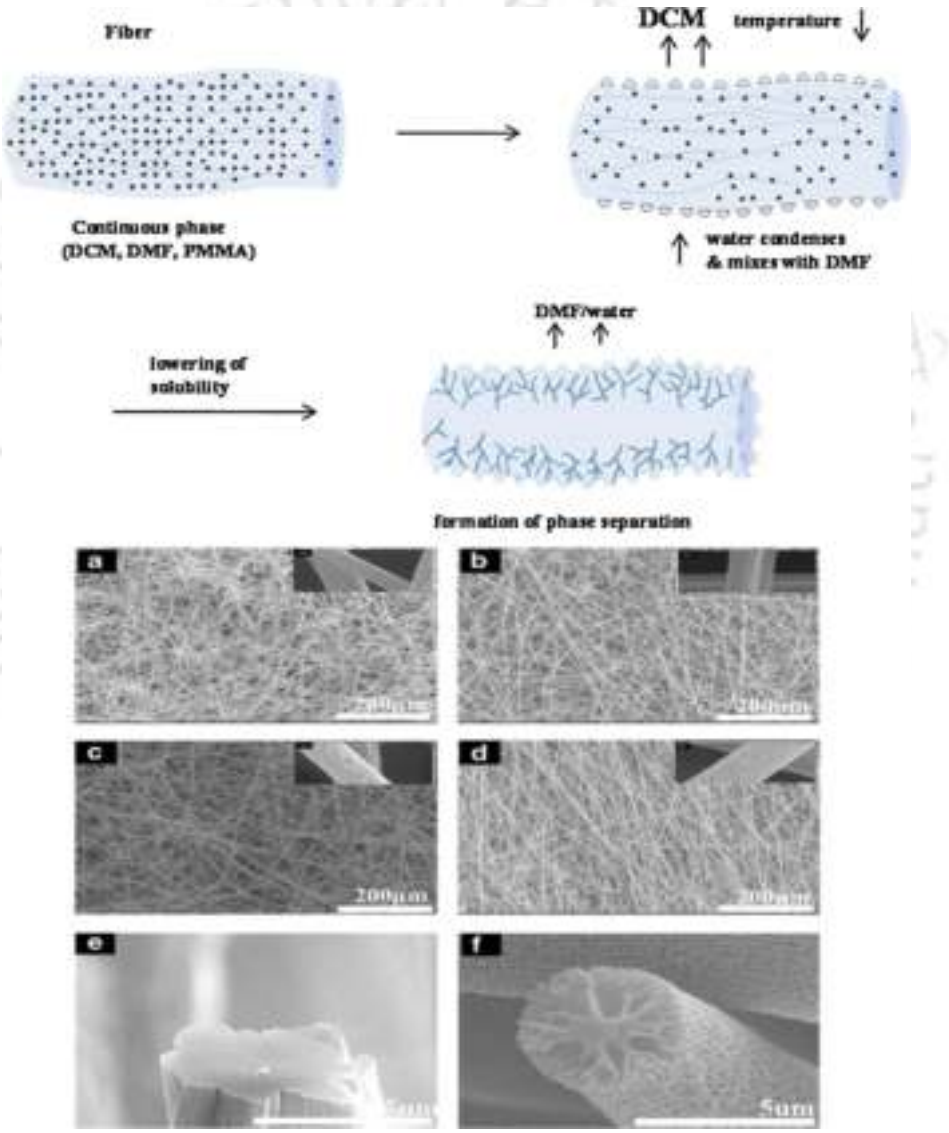

Fig. 2.4: Schematic diagram for creation of pores in electrospun fibers and FESEM images of PMMA fibers with various humidity level: (a) 15-25%, (b) 26-40%, (c) 41-55%, (d) 56-70%, and cross-section of (e) nonporous fiber, and (f) porous fiber [6].

effect similar to perspiration, which leads to the condensation of water vapor into droplets. This phenomenon is similar to what occurs during cloudy weather or fog. The droplets subsequently

settle on the fibers, and as water is miscible with DMF, the two solvents mix together on both the inner and outer surfaces of the fibers. Bae et al. [6] fabricated the porous PMMA electrospun fibers with the complete evaporation of solvents and water droplets from the fibers as shown in Fig. 2.4. Temperature has two contrasting effects on the average diameter of nanofibers: first, it enhances the rate of solvent evaporation, and second, it reduces the viscosity of the solution. These opposing mechanisms ultimately result in a decrease in the average fiber diameter. A similar finding was reported by De Vrieze et al. [85], where cellulose acetate (CA) and polyvinylpyrrolidone (PVP) were employed.

2.2 LITERATURE REVIEW ON P(VDF-TrFE) BASED NANOCOMPOSITE SYSTEM AS ENERGY HARVESTING AND SENSING APPLICATIONS

In this section, energy harvesting and sensing applications have been discussed as a means of supplementing our energy requirements. This discussion will center on energy harvesting and wearable devices that utilize piezoelectric materials. First, there will be a brief overview of piezoelectric materials, followed by a focus on PVDF polymer and its copolymer P(VDF-TrFE). The process of electrospinning, which is commonly utilized to manufacture flexible P(VDF-TrFE) membranes, is discussed, and extended to work on P(VDF-TrFE) matrix composites that incorporate various types of filler.

2.2.1 Material Characterization of P(VDF-TrFE)/ZnO Mats as a Self-powered Sensor Through Optimazation of Process Parameters

Electrospun nanofiber mats are the active area for the sensing and energy harvesting applications. Some major fabrication process are used to synthesized the nanofiber membranes as per the applications. The various techniques are generally employed to produce nanofiber, which are as follows; splitting of bicomponent fibers, melt-blowing, physical drawing, flash-spinning, phase separation, self-assembling, solution casting, spin coating, hydrothermal, and electrospinning. The electrospinning process is one of the most commonly used technique for the fabrication of nanofiber composite mats with an exceptionally uniform diameter, long length and diversified composition [86]. In this direction, Mokhtari et al. [87] studied the effect of different fillers for energy harvesting application

using PVDF polymer. ZnO filler (18 wt.%) was incorporated into the polymer and piezo output was recorded from peak to peak voltage 1.1 V after applying free fall load on the device. Zhang et al. [88] fabricated nanocomposite PVDF/$BiCl_3$/ZnO film structure using electrospinning method and the filler concentration was taken in weight percentage. Jiang et al. [89] synthesized PVDF/$BaTiO_3$ nanocomposite films by electrospinning method for tactile sensor applications, with the $BaTiO_3$ content added as a weight percentage. P(VDF-TrFE)/ZnO composite films were electrospun for a surface acoustic device with ZnO content added as a weight percentage by Augustine et al. [90]. Recently, Sahoo et al. [91] fabricated the flexible Fe-doped ZnO/P(VDF-TrFE) nanocomposite film through solution casting. It has been found that the piezoelectric output of the composite film is enhanced as compared to pure P(VDF-TrFE). Pan et al. [92, 93, 94] used near-field electrospinning to fabricate hollow PVDF fiber tubes and PMLG/PVDF composite films to improve their energy harvesting and spider silk to scavenge energy. Erdem et al. [95] made PVDF fiber mats and PVDF/ZnO composite pellets using electrospinning and performed the electromechanical characterization. Meyers et al. [96] designed P(VDF-TrFE)/ZnO interdigitated transducer, which was used for their actuation and sensing of Lamb waves for detecting simulated damage in pipes and metallic plates. Kim et al. [97] constructed resistive random access memory devices (ReRAM) based on P(VDF-TrFE)/ZnO nanocomposite film, was fabricated using spin coating. Zhang et al. [98] prepared ZnO-Ag/P(VDF-TrFE-CTFE) based composite and Silver (Ag) coated ZnO nanoparticles through solution casting and reflux method. Jie et al. [99] also found that P(VDF-TrFE)/ZnO flexible piezoelectric nanogenerator (PENG) has high electrical output compared to P(VDF-TrFE) fiber. The film was prepared by spin coating technique. Similar observations also have been made by various researchers [100, 101, 102, 103, 104, 105]. Mohammad et al. [106] fabricated the electrospun nanofibers made of PVDF-ZnO wherein PVDF acts as a matrix and ZnO as nanoparticles. Four weight percentages of ZnO nanoparticles were considered 7, 12, 15, and 18%. However, only two samples, which had 0 and 15% were presented for discussion, whereas many samples were not discussed in detail. Recently, Soheil Mansouri et al. [107] studied the effect of ZnO nanoparticles in PVDF electrospun mats for environmental energy harvesting. Initially, they have taken three weight percentages 7, 12, and 18%. In this case, fibers were not electrospun (only spraying) for 12

and 18% weight percentage. The results are presented only for 7% ZnO concentration. The present review clearly indicates that no in-depth/detailed results are available about the optimum value of ZnO weight percentage into P(VDF-TrFE) solution for maximum piezoelectric output. Although, the effect of various parameters is to be needed to study for the higher piezoelectric output of electrospun nanocomposite based nanogenerators.

2.2.2 Electrospun Functionally Graded Mat Based Nanogenerator

The different reinforced nanoparticles have drawn the attention of researcher to increase the energy harvesting capability of the PENG device. Barium titanate ($BaTiO_3$) have been used recently for energy harvesting due to its high piezoelectric, dielectric properties, and its environmental friendliness [108]. However, it is brittle in nature and easily breaks during the operating process, which restrict its use in self-powered wearable device. To address this issue, various studies have shown that mixing nanoparticles (NPs) and polymers to create flexible piezoelectric nanocomposites is highly effective. Recently, a trilayer flexible piezoelectric nanogenerator made of surface-modified graphene and PVDF/$BaTiO_3$ nanocomposites was prepared by Yaqoob et al. [109] using spray coating. In this work, stacking of three layers is accomplished by fabricating separate layers and placed on each other manually. Jiang et al. [89] reported the fabrication of PVDF/$BaTiO_3$ nanocomposite film using electrospinning for the application of flexible tactile pressure sensor wherein, $BaTiO_3$ filler was added 5, 10 and 20 wt.%. Here, nanocomposite is fabricated at fixed concentration of matrix and varying with $BaTiO_3$ content. However, the effect of multiple layers was not studied. Guo et al. [110] fabricated PVDF/$BaTiO_3$ NW nanocomposite fiber based wireless piezoelectric device used in human motion monitoring. Pereira et al. [111] synthesized P(VDF-TrFE)/$BaTiO_3$ nanocomposite film using spin coating for energy harvesting application and also studied the effect of filler size and content. Wang et al. [112] fabricated P(VDF-TrFE)/$BaTiO_3$ based piezoelectric functionally graded structures using spin coating followed by hot press technique and further used for energy harvesting application. Maximum piezoelectric output of 120 mV is reported in the literature. It is observe that functionally graded PVDF/$BaTiO_3$ based nanocomposite fabricated through electrospinning approach is not investigated.

2.2.3 Self-powered Flexible P(VDF-TrFE)/ZnO/TiO_2 Hybrid Composite Based Wearable Device

The only material used initially for nanogenerators and sensor applications was piezoelectric ceramic. The limitations of ceramics, such as high-temperature synthesis and brittleness, led to the development of polymer-based PENGs. Again, the piezoresponse of pure polymer-based PENGs is considerably below that of ceramic-based PENGs. Composites based on polymer/ceramic materials have been studied over the past decade extensively due to their high piezoelectric response and flexibility compared to pure polymers [113, 114]. Zhang et al. [88] prepared PVDF/$BiCl_3$/ZnO nanofiber by electrospinning method used in PENGs and reported piezoelectric output of 12 V. Faraz et al. [115] designed piezoelectric nanogenerators based on PVDF/rGO/MoS_2 composite mats fabricated by solution casting method. The maximum voltage is obtained 2.4 V by subjecting a constant pressure of 15 kPa on the device. Amith et al. [116] synthesized PVDF/Cloisite-30B clay based three phase composite using far-field electrospinning method and the prepared composite was used as an active layer in an energy harvesting device. Piezoelectric voltage was found to be as maximum as 4.74 V even after incorporation of optimization tool Taguchi's L9 orthogonal array. Karan et al. [117] fabricated PENG devices based on Fe-dopped reduced graphene oxide (Fe-RGO)/PVDF nanocomposite mats by solution casting method. The PENG device was subjected to finger tapping to extract 5.1V energy as piezo output. PZT/MWCNT/PVDF based three phase composite mats were synthesized using tape casting technique for the energy storage applications by Pal et al. [118]. The maximum electrical voltage was 20 V under the load application of finger tapping on the nanofiber mat surface. The piezoelectric output of P(VDF-TrFE)/ZnO/MgO composite films based energy harvester was recorded 1.89 V, which was reported by Arunguvai et al. [119]. This voltage was generated by a thin film vibration energy harvester based on a composite cantilever model at a resonance frequency of 56 Hz. PVDF-HFP/$BaTiO_3$/h-BN three phase composite mats were fabricated by solution casting and then electrical poling was carried out for obtaining the greater piezoelectric output. This study was conducted by Ponnamma et al. [120] with varying frequencies and the maximum electrical voltage was obtained to be 2.4 V. So far, no research has been reported on P(VDF-TrFE)/ZnO/TiO_2 nanocomposite films incorporated as an

active layer in PENG devices for energy scavenging applications.

2.2.4 P(VDF-TrFE)/TiO_2 Based Piezo-triboelectric Hybrid Nanogenerator

Triboelectric nanogenerators are another option for creating self-powered devices owing to their relatively high output and ease of fabrication compared to piezoelectric nanogenerators. A triboelectric nanogenerator is based on the principle of contact electrification, while a piezoelectric nanogenerator harvests vibration energy through constant touching, vibrating, and bending. It is therefore highly desirable to fabricate multi-mechanism based nanogenerators that use both piezoelectric and triboelectric nanogenerators to miniaturize the system and obtain high voltage. Sahatiya et al. [121] used few layer MoS_2 grown on cellulose paper followed by the deposition of PVDF nanofiber to fabricate hybrid nanogenerator comprised of piezoelectric and triboelectric nanogenerator for energy harvesting applications. The piezoelectric output recorded as voltage peak to peak 50 V, current of 30 nA and later this enrgy is utilised in powering the LED bulb. Wang et al. [122] investigated the performance of hybrid nanogenerator based on P(VDF-TrFE) and PDMS/MWCNTs in a wearable device. The hybrid nanogenerator was capable of generating a maximum voltage of 25 V. The d-arched hybrid nanogenerator was designed by Zhu et al. [123] and demonstrated as self-powered vibration sensor with peak to peak voltage of 20 V. The combined effect of both piezoelectric and triboelectric output enabled the hybrid nanogenerator to generate more voltage output than pure nanogenerator. The designed HNG can be used for powering the LED bulb with human finger tapping without the need of external power source. Very few works are reported on fabricating hybrid nanogenerators based on nanomaterials with different configurations.

2.3 OBJECTIVES OF THE PRESENT WORK

Based on the extensive literature survey, the following objectives are framed for the present work in the thesis. Broadly, the objectives include, (i) Development of self-powered sensor device based on P(VDF-TrFE)/ZnO composite mats, (ii) Extend the process for the electrospun functionally graded PVDF/$BaTiO_3$ mats, (iii) Present a hybrid P(VDF-TrFE)/ZnO/TiO_2 nanocomposite films

which is employed as wearable device and study the response of a hybrid composite under finger tapping load, and (iv) Further, flexible Piezo-triboelectric hybrid nanogenerator is preented as a werable device. The objectives specifically addressed are as follows:

1. To fabricate P(VDF-TrFE)/ZnO based aligned flexible piezoelectric nanofiber using electrospinning method.
2. To investigate the mechanical, thermal, rheological, and piezoelectric performance of P(VDF-TrFE)/ZnO composites.
3. To optimize the process parameters to get the maximum piezoelectric output for the nanogenerator application
4. To fabricate and investigate the performance of five layered functionally graded PVDF/$BaTiO_3$ mats.
5. To fabricate and investigate the performance of P(VDF-TrFE)/ZnO/TiO_2 fiber mats for wearable applications.
6. To fabricate P(VDF-TrFE)/TiO_2 based piezo-triboelectric hybrid nanogenerator for energy harvesting applications.

2.4 ORGANISATION OF THE THESIS

The complete work presented in this thesis has been organized into eight chapters. The motivation behind the presently conducted research is presented in Chapter 1. An overview has been presented of piezoelectric materials and structures and the engineering characteristics of the electrospun nanocomposite mat by virtue of which they impart structural advantage and aesthetics. Smart materials such as piezoelectric materials have been used for the sensing and energy harvesting applications. Various piezoelectric materials have been discussed and the mechanics of certain important smart piezoelectricity structures have been explained. The various fabrication methods of the piezoelectric fiber reinforce composite has been briefly discussed. The chapter highlights

the need to develop sensor devices based on the unique properties of electrospun mats, which is apparent from the attraction towards the potential of smart materials.

In the Chapter 2 literature survey for the synthesis and present status of electrospun mat based sensor device as a energy harvesting and wearable device have been conducted. The parameters associated with the electrospinning method have also been reviewed emphasizing on the fabrication of nanocomposite films. Based on the extensive literature review, the proposed objectives of the present work are framed. An overview of the contents of the remaining six chapters is presented below.

Chapter 3 presents an experimental analysis for the P(VDF-TrFE)/ZnO nanocomposite mats fabrication using electrospinning method. The surface morphology, crystalline structure analysis, rheological study, mechanical characterization, and thermal stability test are carried out using FESEM, XRD, FTIR, DSC, UTM, and TGA. Further, the piezoelectric performance of the device is tested for the prepared nanocomposite film and the effect of electrospinning parameters are analysed.

In Chapter 4, P(VDF-TrFE)/ZnO nanocomposites are fabricated with different process parameters. the experiments are conducted as per the statistical approach design of experiment (DOE). In this analysis, 3 factors and 3 levels are incorporated which have impact on the outcome. Box-Behnken that involves fitting a quadratic model to the response variable in order to optimize it. The various test has been conducted to characterize the fabricated electrospun mats. Further, piezoelectric nanogenerator is prepared using the fabricated mats and used as a self-powered sensor. The process parameters are optimized for the piezoelectric performance of the nanocomposite films and new benchmark results are presented.

In Chapter 5, the electrospinning method is extended to fabricate functionally graded PVDF/$BaTiO_3$ mats. For the first time from the conducted experimental study, the electrospun PVDF/$BaTiO_3$ functionally graded film based results are reported for piezoelectric output. The prepared electrospun mat is used as an active layer in the flexible nanogenerator device. The functionally graded PVDF/$BaTiO_3$ film is optimized for the better performance of piezoelectric output.

Chapter 6 presents a design and fabrication of self-powered flexible P(VDF-TrFE)/ZnO/TiO_2 hy-

brid fiber mats as nanogenerator for wearable applications. The hybrid composite is fabricated with varying the TiO_2 content and its influence is studied on the crystalline structure, mechanical properties, and viscoelastic behaviour. Apart from new benchmark results presented for the hybrid nanocomposite film, the nanoparticles concentration and their influence on the piezoelectric performance are studied.

In Chapter 7, P(VDF-TrFE)/TiO_2/PDMS based piezo-triboelectric hybrid nanogenerator is investigated for piezoelectric output. The piezoelectric output obtained from the nanogenerator device is used to power the LED bulb and small electronic device.

Finally, the major conclusions of this work and suggestions for future research are summarized in Chapter 8.

Chapter 3

Material characterization and piezoelectric performance of P(VDF-TrFE)/ZnO nanocomposite

3.1 INTRODUCTION

In this chapter, piezoelectric nanogenerators (PENGs) based on P(VDF-TrFE)/ZnO nanofiber composite thin film is developed using electrospinning method. The P(VDF-TrFE) nanofiber and P(VDF-TrFE)/ZnO nanocomposites are synthesiszed to be used as an active layer in the flexible device. The comprehensive work has been reported conclusively on the effect of nanofiller addition relative to solvent (DMF) and solute P(VDF-TrFE) polymer. ZnO nanoparticles with 18% (w/w) and 18% (w/v) concentrations have been dispersed in the prepared P(VDF-TrFE) solution. The material system, synthesis of nanocomposite films, and PENGs device are presented in Sec. 3.2. The P(VDF-TrFE)/ZnO nanocomposite films are synthesized using electrospinning method, wherein, P(VDF-TrFE) as a flexible matrix and ZnO as reinforcing materials are used. The PENG device fabrication is accomplished using three layers including piezoactive P(VDF-TrFE)/ZnO layer and two electrode layers. In Sec. 3.3, the behaviour of electrospun nanocomposite mats are discussed. In this section, surface morphology, diameter distribution, elemental analysis, presence of β phase, thermal stability, mechanical properties and crystallinity are investigated. These investigations are carried out using the following instruments: field emission scanning electron microscopy (FE-SEM), atomic force microscopy (AFM), energy dispersive X-ray analysis (EDX), X-ray diffraction (XRD), fourier transform infrared (FTIR), thermogravimetric analysis (TGA), 5kN electromechanical universal testing machine and differential scanning calorimetry (DSC). The viscosity, dynamic

modulus, and damping factor of the blended solution are measured using rheometer. Finally, PENG devices have been fabricated and its performance is evaluated in terms of their voltage output and current. The piezoelectric nanogenerators (PENGs) are subjected to pressing, bending and tapping by human hand for getting electrical output. These devices are sensitive towards the manual activities. The piezoelectric output of the PENGs is enhanced from 704 mV to 1.15 V and 4 μA to 5.2 μA. It is observed that the addition of ZnO nanoparticles into the P(VDF-TrFE) nanofiber made the composite film more active and sensitive. It can be used for energy harvesting applications.

3.2 ELECTROSPUN MAT FABRICATION

3.2.1 Material System

P(VDF-TrFE) copolymer is purchased for electrospinning in this work because of its ease in controlling the process parameters. P(VDF-TrFE) pellets are purchase from Sigma-Aldrich with 75 percent VDF and 25 percent TrFE. The average molecular weight (Mw) of P(VDF-TrFE) is 300 kg/mol. N,N Dimethylformamide (DMF) with anhydrous 98%, molecular weight (73.09 g/mol) is procured from Sigma-Aldrich. Sigma Aldrich supplied zinc oxide (ZnO) nanopowder with a molecular weight of 81.39 g/mol. No treatment has been performed with the chemicals before use in electrospinning.

3.2.2 Electrospinning for Fabrication of P(VDF-TrFE) and ZnO Nanofibers

The nanofiber unit supplied by E-spin Nanotech (Model-SUPER ES-2, India) is employed for electrospinning operation. In order to prepare polymer solution, 18% (w/v) concentration of P(VDF-TrFE) pellets are dispersed in the solvent of dimethylformamide (DMF) and acetone with a proportion of 8:2 (vol/vol) in a beaker. The homogeneous solution is obtained by stirring it for 4 h at 40°C and 600 r.p.m. The other two solutions are prepared for ZnO reinforced nanocomposite. In comparison with P(VDF-TrFE) polymer and DMF solvent, ZnO nanopowder at 18% (w/w) and 18% (w/v) concentrations are incorporated with P(VDF-TrFE) solution and then sonicated for 30 minutes. The solutions are subsequently stirred for 2 h at 40°C resulting in a white-coloured homogeneous solution, which can be used to fabricate P(VDF-TrFE) nanofiber and their composite. The

plastic syringe with an inner diameter of 13.08 cm is filled with the obtained homogeneous solution. The metallic needle attached to the syringe is placed on the syringe pump and used as a spinneret. The high voltage source is connected to the needle through the alligator clip. The rotating drum collector with 90 mm diameter is deployed for deposition of an electrified fiber jet and located 13 cm apart from the metallic needle tip. The drum collector is driven with an angular velocity of 178 rad/s during the accumulation of nanofibers. The process parameters are coordinated with the solution to start the electrospinning process as follows: the flow rate of the solution is 15 µl/min, the applied voltage is 21 kV, and the chamber temperature is set at 30°C. All parameters are kept constant for the P(VDF-TrFE) nanofiber and P(VDF-TrFE)/ZnO nanocomposite. All three films are collected on a drum collector for 60 min.

3.2.3 Preparation of Piezoelectric Nanogenerator (PENG) Devices

The P(VDF-TrFE) nanofibers and their composite are collected on an aluminium substrate, wrapped on the collector. This substrate is used as one of the electrodes in an energy harvesting device. P(VDF-TrFE) nanofiber and P(VDF-TrFE)/ZnO composite are used in self-powered PENG, which is having a 6 cm^2 active functional area. Aluminium foil attached to the fiber structure functions as a top electrode, while copper tape serves as a bottom electrode. These electrodes are used to be part of an electric circuit to measure the electrical output of PENG device. For proper electrical connection, carbon tape with both sides adhesive are used on both ends of the fiber web. Further, PENGs are covered with polyimide tape to make protection from the surrounding noise. The schematic diagram of electrospinning, piezoelectric fabrication device and actual image of PENG is shown in Fig. 3.1.

3.2.4 Material Characterization

The image analysis is performed using field emission scanning electron microscopy (FESEM) (model: Sigma 300, make: Zeiss) to study the surface morphology and fiber distribution of electrospun P(VDF-TrFE) fibers and their composite. The FESEM images are used to calculate the fiber diameter using image analysis software. The image analysis software is used to compute the surface area to volume ratio of non-woven webs using a FESEM image. Atomic force microscopy (AFM)

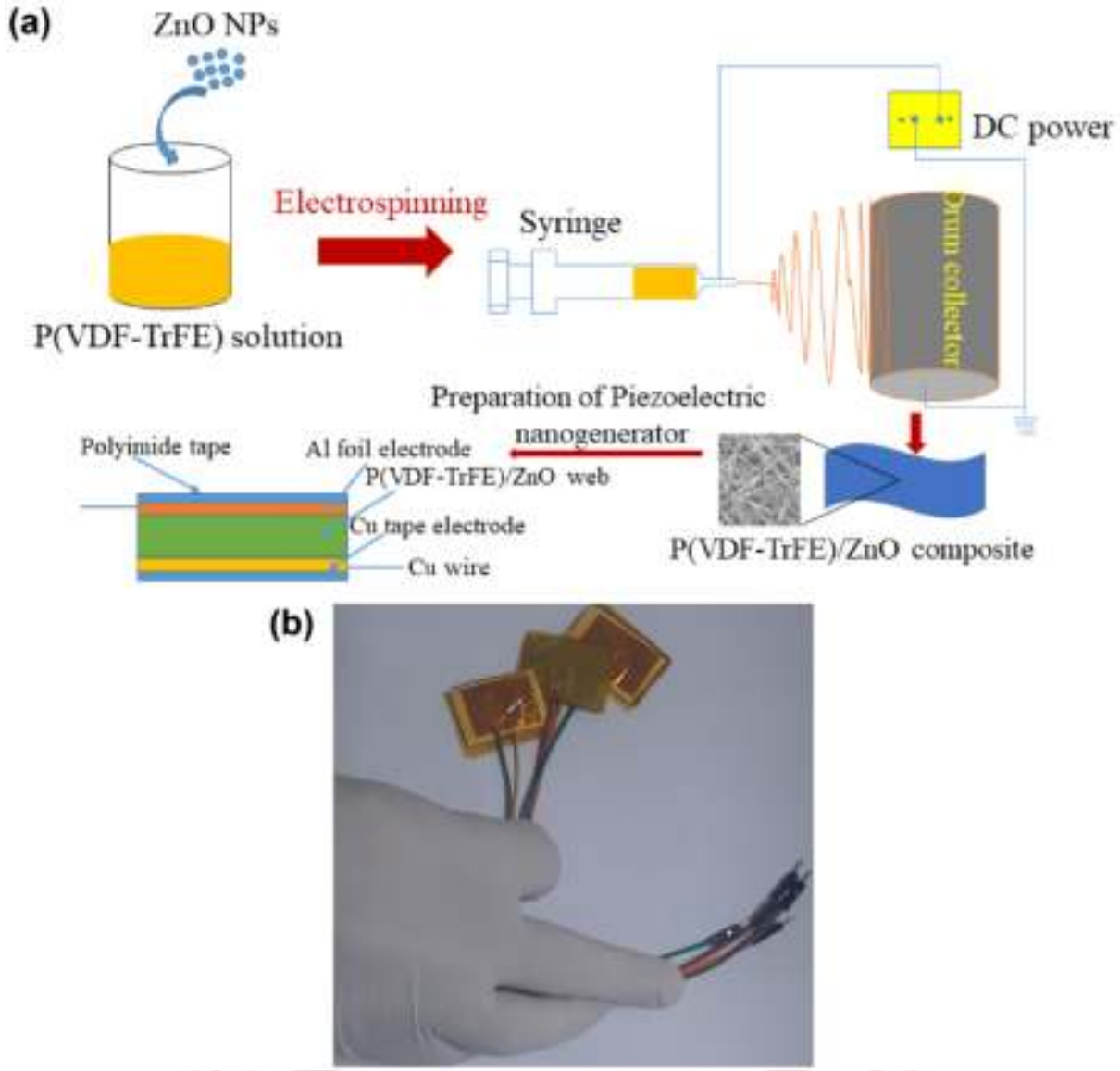

Fig. 3.1: Schematic diagram of (a) electrospinning and PENG device and (b) actual photo of PENG.

MFP-3D-BIO is used for imaging a sample and its topography for phase and amplitude images. The rheological behavior of neat P(VDF-TrFE) and P(VDF-TrFE)/ZnO blended solution is carried out using Physica MCR 101 rheometer (Anton Paar) with 1° cone angle and 25 mm diameter of cone and parallel plates. The viscosity and dynamic modulus test are performed at 25°C and 50°C, a gap of 0.1 mm, and the strain is fixed at 1%. The storage, loss modulus (G', G") and damping factor are evaluated with varying frequencies for 10 minutes. The element characterization of film structures is evaluated using energy dispersive X-ray (EDX) analysis (model: Gemini 500 FESEM, make: Zeiss). X-ray diffraction (XRD) (Rigaku, Japan model: Smart lab) pattern is obtained

on a diffractometer using Cu-Kα radiation (λ = 1.54Å) at room temperature. The samples are examined in the range of 2θ from 10° to 60° at a rate of 5 degree/minute. Fourier transform infrared (FTIR) (PerkinElmer, Singapore; model: Spectrum two) spectra of P(VDF-TrFE) fibers and P(VDF-TrFE)/ZnO composite films are collected on a Bruker spectrometer using an attenuated total reflection (ATR) mode in the range 400-3500 cm^{-1}. The nanofiber samples are heated from 20°C to 225°C in argon atmosphere for differential scanning calorimetry (DSC) analysis (model: STA449F3A00, maker: Netzsch). The thermogravimetric analysis (TGA) is carried out using the Netzsch STA449F3A00 apparatus operating from 20°C to 700°C, for the determination of thermal stability of the samples. The films are placed in alumina pan sample holders and the analysis are performed with a heating rate of 10°C/min under argon atmosphere. Electrospun nanofiber composites are tested under a 5kN electromechanical universal testing machine (model: Z005TN Proline, make: ZwickRoell) at a strain rate of 5 mm/min for their mechanical properties. This test is conducted under the application of load cell 100 N. Digital micrometre (Mitutoyo 293-240-30) is used to measure the thickness of electrospun nanofibers. Digital oscilloscope (GwINSTEK GDS-1102-U) is deployed to measure the voltage of P(VDF-TrFE) fibers and its composites based PENG with a working area of 6 cm^2. The PENGs device is subjected to bending, pressing and tapping by a human finger to obtain the piezoelectric output.

3.3 RESULTS AND DISCUSSIONS

3.3.1 Surface Morphology Analysis of Fabricated Films

The electrospun nanofibers are collected on rotating drum collectors by horizontal electrospinning. All three samples are fabricated as beads-free. The surface morphology and diameter distribution of P(VDF-TrFE)/ZnO fiber composite are illustrated in Fig. 3.2 (a-f). The diameter of nanofiber is measured 180.29 nm and the diameter for P(VDF-TrFE)/ZnO composite is calculated to be 168.69 nm and 196 nm. The diameter of the composite reduced by introducing ZnO nanopowder due to the increase in conductivity of the solution. However, the diameter increased for the sample which is fabricated at 18% w/w concentration of nanofiller.

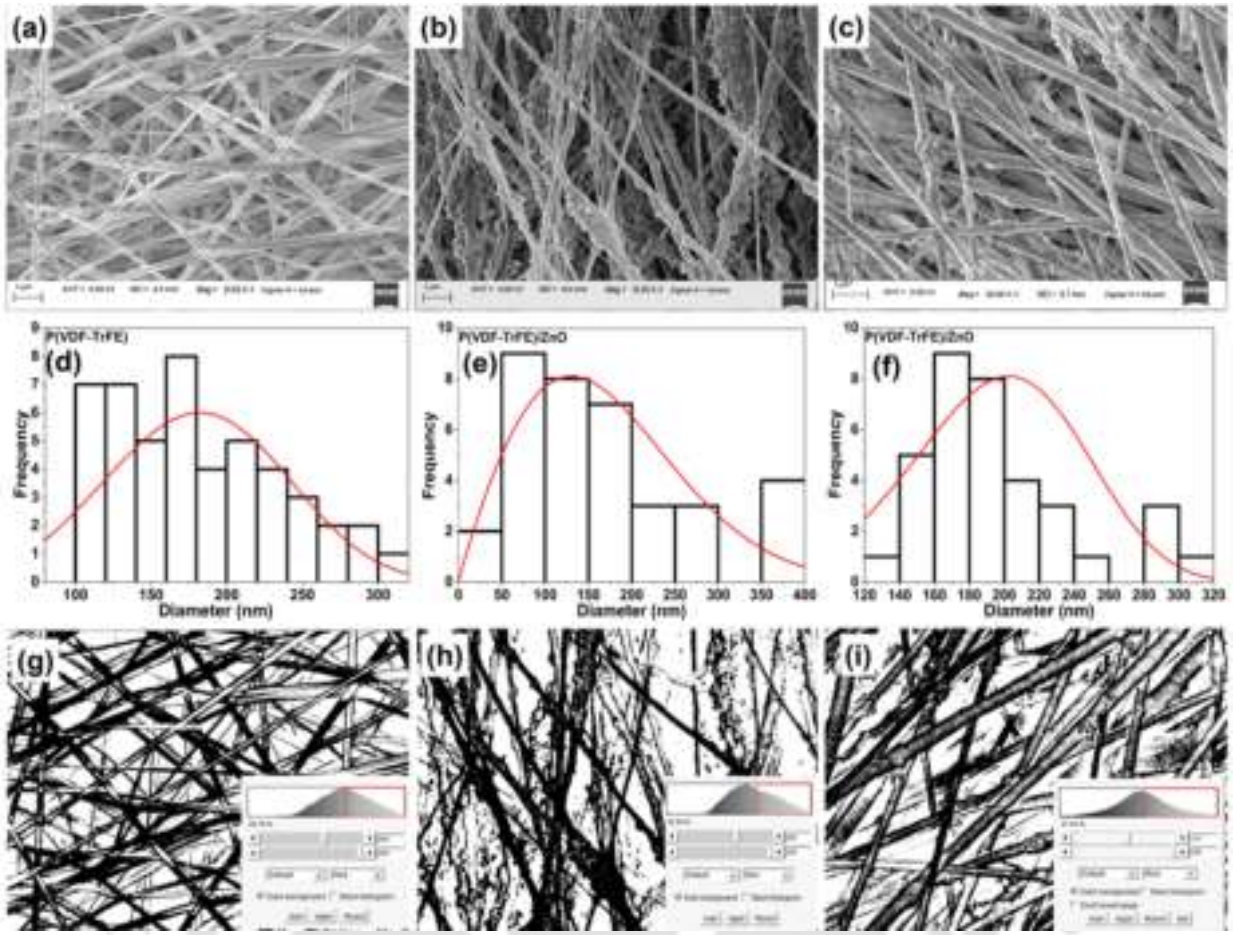

Fig. 3.2: FESEM image of (a) P(VDF-TrFE) fiber, (b) P(VDF-TrFE)/ZnO composite (18% w/v concentration of filler with respect (w.r) to DMF, (c) P(VDF-TrFE)/ZnO composite (18% w/w concetration of filler w.r to P(VDF-TrFE), (d,e,f) diameter distribution of nanofiber composite, (g,h,i) surface area to volume ratio of P(VDF-TrFE)fiber and P(VDF-TrFE)/ZnO composite fabricated at 18% w/v and 18% w/w of filler.

3.3.2 Calculation of Fiber Surface Area to Material Volume Ratio

The fiber surface area to material volume ratio of P(VDF-TrFE) nanofiber and P(VDF-TrFE)/ZnO nanocomposite is calculated utilizing FESEM images. The fiber surface area and material volume of the non-woven structures are analyzed using image analysis software. This calculation is executed in the threshold mode of the image software in Fig. 3.2 (g-i).

Area covered by image (A_I) = 14.421μm×9.746μm = 140.55 μm^2

Fiber occupied area in image (A_P) = 48.76% = 68.53 μm^2

Average diameter of fibers (D) = 180.29 nm = 0.18092 μm

Fiber length on average in image (L) = A_P/D = 378.79 μm

Surface area of fibers (S.A) = $2\pi rL = \pi DL = 215.19\ \mu m^2$

Volume of fibers (cylinder) = $\frac{\pi}{4} \times (D^2L) = 9.73\ \mu m^3$

Surface -to- volume ratio = 22.12×10^6

Similarly, the fiber surface area to material volume ratio for the P(VDF-TrFE)/ZnO nanocomposite fabricated at 18% w/v and 18% w/w concentration of filler is calculated to be 20.39×10^6 and 23.71×10^6, which indicates that the fiber surface-to- material volume ratio increased after the addition of ZnO nanoparticles (wt/wt) and decreased when 18% (wt/vol) filler is added.

3.3.3 Atomic Force Microscopy (AFM) Analysis

The atomic force microscopy analysis is carried out for the P(VDF-TrFE) nanofiber and P(VDF-TrFE)/ZnO nanocomposite, as shown in Fig. 3.3. The height, amplitude, and phase images of the nanofiber composites are presented in Fig. 3.3. This study evaluated P(VDF-TrFE) fibers and P(VDF-TrFE)/ZnO nanocomposite films for roughness. Our result revealed that the average roughness for P(VDF-TrFE) fiber are 161 nm, 122.63 nm for the P(VDF-TrFE)/ZnO film prepared at 18% w/v (ZnO), and 259 nm for the P(VDF-TrFE)/ZnO film structure prepared with 18% w/w filler. It is observed that the nanocomposite film made of P(VDF-TrFE)/ZnO is having more rough surfaces than P(VDF-TrFE) nanofiber film. The increase in roughness of film structure could be attributed to the proper dispersion of ZnO nanofiller in a polymer solution.

3.3.4 Energy-Dispersive X-ray Analysis (EDX)

The elemental analysis of P(VDF-TrFE)/ZnO nanocomposite membranes fabricated under different conditions are performed using the energy and intensity distribution of X-ray signals generated by the electron beam. The element analysis is conducted for the Carbon (C), Fluorine (F), Zinc (Zn), and Oxygen (O) atoms. The elemental and their atomic weight percentage analysis of the synthesized film structure is shown in Fig. 3.4. The EDX spectra can be expressed in both semi-quantitative and semi-qualitative analysis. The C element is studied to be found in the film at 56.31%, 45.36%, and 49.10%. The F element is evaluated to be found in the film at 43.69%, 27.97%, and 39.42%. The O element is investigated to be found in the last two films at 15.02% and 7.91%. The Zn element is studied to be found in the film at 11.65% and 3.57%. Some sharp peaks are

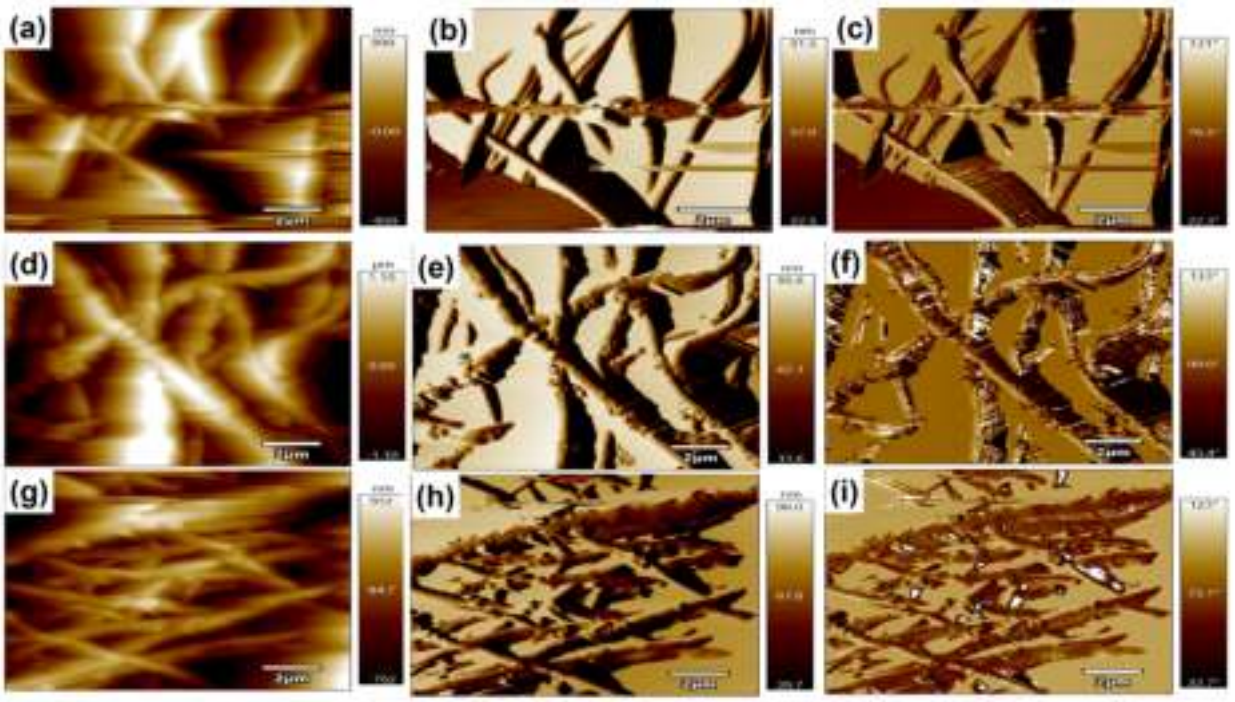

Fig. 3.3: Topography map of (a,d,g) P(VDF-TrFE)/ZnO film (0, 18% w/v, 18% w/w filler) for height image, (b,e,h) amplitude image of P(VDF-TrFE)/ZnO film (0, 18% w/v, 18% w/w filler) (c,f,i) phase image of P(VDF-TrFE)/ZnO film (0, 18% w/v, 18% w/w filler concentration).

present in the EDX spectra of P(VDF-TrFE)/ZnO nanocomposites, as well as neat P(VDF-TrFE) membranes. These peaks correspond to the elements carbon (K_α radiation with 0.277 keV) and fluorine (K_α radiation with 0.677 keV). As a consequence of the incorporation of ZnO nanoparticles into P(VDF-TrFE) nanocomposite membranes, additional peaks were observed at energy levels 1.01 keV (L_α), 8.63 keV (K_α), and 9.5 keV ($K\beta$), which are related to the zinc element.

3.3.5 Rheological Behavior Analysis

The rheological analysis is essential before fabricating the nanofiber composite film by the electrospinning technique. Viscosity is a prime factor in this fabrication technique and could affect the fabrication process. Rheology analysis is used to study the effect of viscosity, storage modulus, loss modulus, and damping factor of a homogeneous solution. The blended solution's viscosity, dynamic modulus, and damping factor are shown in Fig. 3.5. The viscosity for the all-prepared solution decreased as the shear rate increased, which shows the thinning behavior of the solution, while viscosity increased with the addition of ZnO filler. The solution obtained for the P(VDF-TrFE)/ZnO at 18% w/w concentration showed greater viscosity than the other two solutions. The

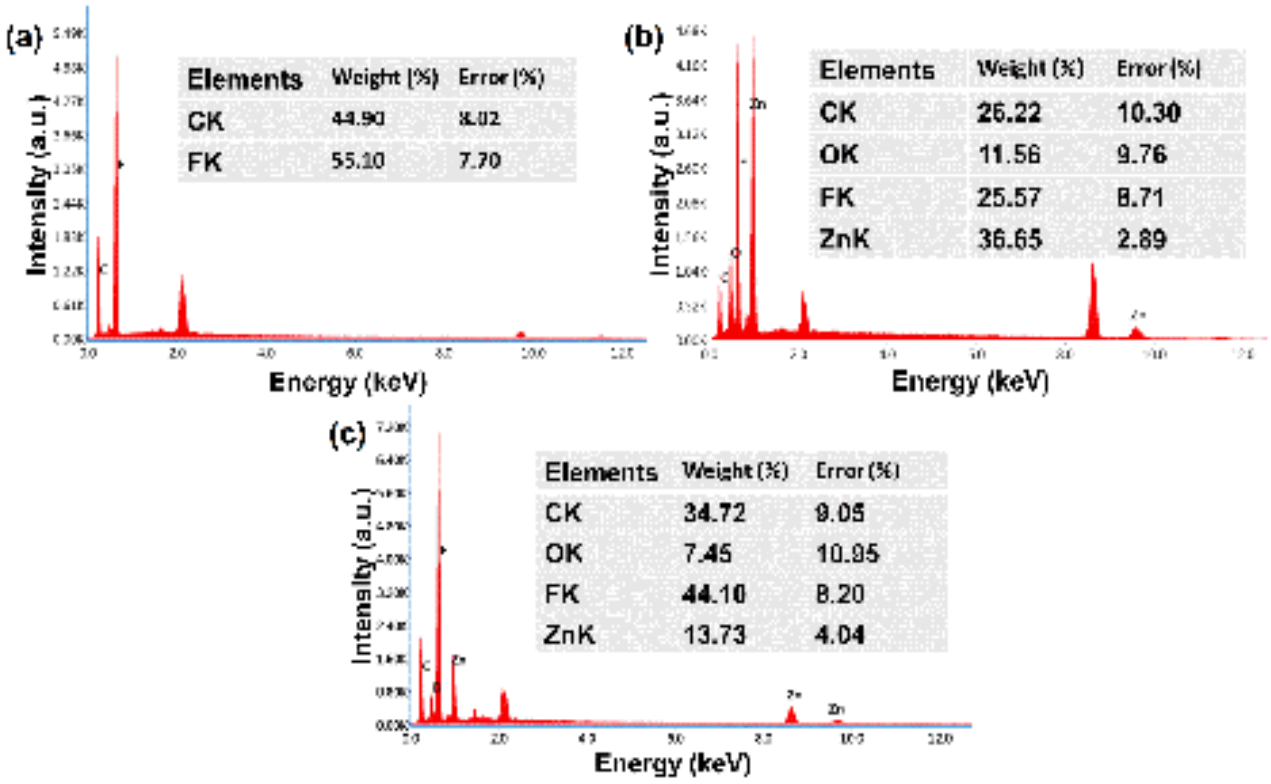

Fig. 3.4: EDX spectra of P(VDF-TrFE)/ZnO nanocomposite film (a) 0 wt.% (b) 18% wt/vol and (c) 18% wt/wt nanofiller.

dispersion of the nanofiller improves the storage and loss modulus of the blended solution while reducing the damping factor. The dynamic moduli of the solution prepared for P(VDF-TrFE)/ZnO at 18% w/v showed higher as the frequency increased. The increased viscosity of the solution may have resulted from proper dispersion of the nanofiller in pure P(VDF-TrFE) solution. The increase in dynamic moduli of the obtained P(VDF-TrFE)/ZnO solution at 18% w/v concentration of filler in a higher frequency range can be attributed to the thinning behavior of the solution. The damping factor of P(VDF-TrFE)/ZnO solution significantly decreased with the addition of nanofiller, while the P(VDF-TrFE) solution damping factor increased.

3.3.6 XRD Analysis

The X-ray diffraction test (XRD) is evaluated in order to confirm the formation of beta phase crystal structure and ZnO nanopowder presence in the nanofiber composite. In the XRD pattern, it is shown that the beta phase of synthesized nanocomposite film is at $2\theta = 20°$ (110) [124] as shown in Fig. 3.6. The diffraction peaks of ZnO nanopowder appeared at a 2θ value of 31.77°,

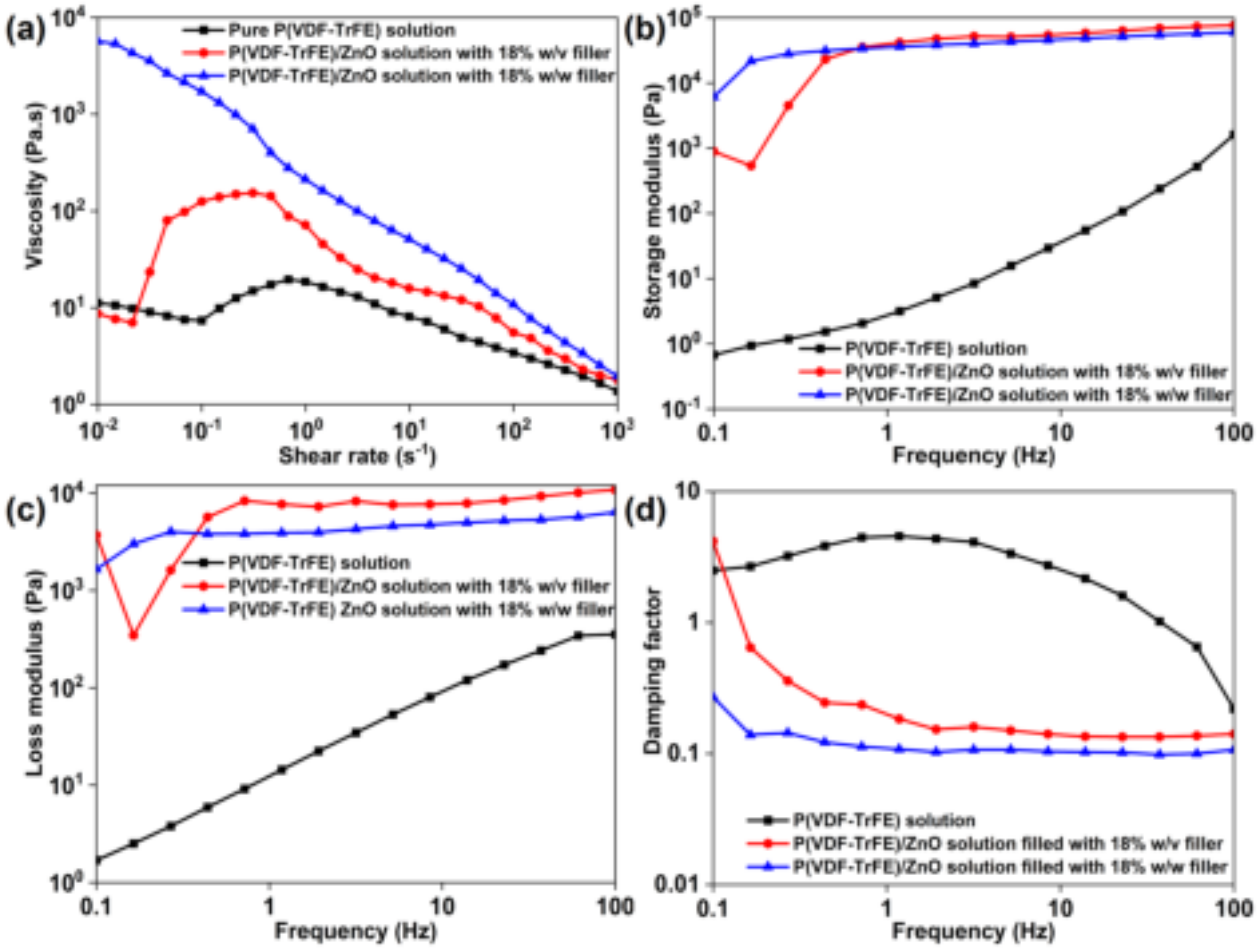

Fig. 3.5: Rheological study of various blended solutions (a) viscosity, (b) storage modulus, (c) loss modulus, and (d) damping factor.

34.46°, 36.25°, 47.55°, 56.61° and 62.98° [125] as shown in Fig. 3.6. Moreover, the matrix phase is not altered after the addition of ZnO filler. The aluminium peaks are found at 38.44° and 44.83° in fiber composite film as per JCPDS card no. 001-1176. The crystallinity is determined from the ratio of the integrated area of the crystal peak to the total area (crystalline and amorphous part) in the XRD pattern. The percentage crystallinity of fabricated film is calculated using the Ruland-Vonk method [126] as per the equation.

$$\text{Crystallinity}(\%) = \frac{A_{cr}}{A_{cr} + A_{am}} \times 100 \tag{3.1}$$

Where A_{cr} is the integrated area of the crystalline part, and A_{am} is the area of the amorphous zone. The crystallinity index of the pure P(VDF-TrFE) fiber, P(VDF-TrFE)/ZnO composite (18% w//v filler) and P(VDF-TrFE)/ZnO film (18% w/w filler) is obtained to be 23.12, 21.74 and 17.06% respectively. The XRD pattern of ZnO powder is illustrated in Fig. 3.6. The all peaks are indexed

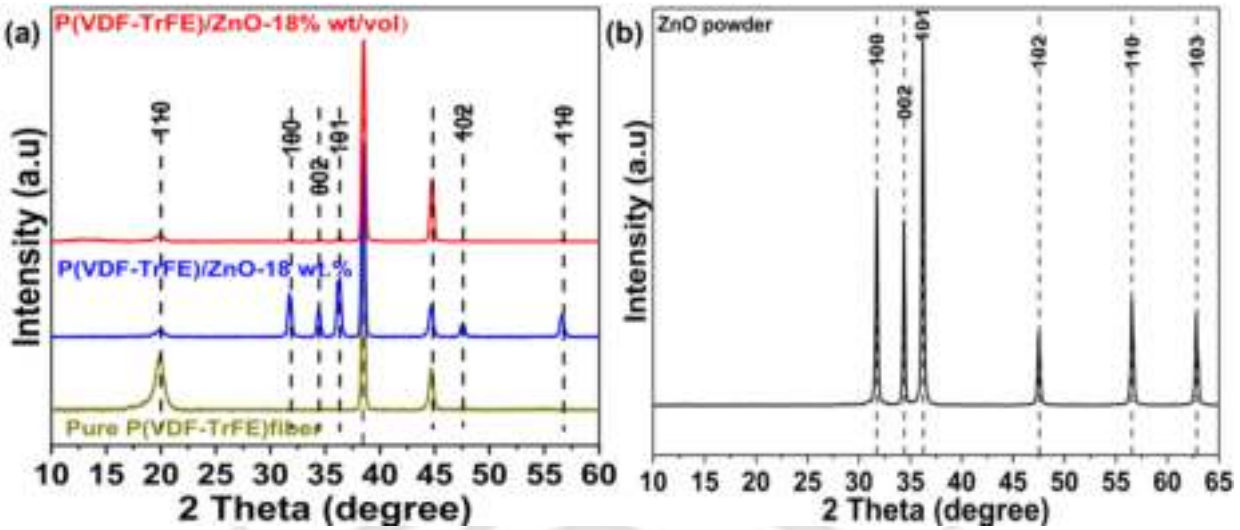

Fig. 3.6: XRD pattern of electrospun (a) P(VDF-TrFE) nanofiber, (b) nanocomposite fabricated at 18% w/v filler concentration, (c) nanocomposite synthesized at 18% w/w filler concentration, and (d) ZnO powder.

to the zincite phase of ZnO according to the JCPDS card no. 00-005-0664. The same diffraction peaks of ZnO nanoparticle is observed as in P(VDF-TrFE)/ZnO nanofiber composite film. The observed peaks are not associated with other phases of ZnO or impurities, suggesting the purity of the ZnO obtained is high. The all peaks of ZnO nanoparticles showed very strong peak, which indicate that excellent crystallinity.

3.3.7 Fourier Transforms Infrared Spectroscopy (FTIR) Analysis

The crystal structures of the fabricated nanocomposite are examined by FTIR spectroscopy in ATR mode. The comparison for FTIR spectra of electrospun P(VDF-TrFE) and ZnO reinforced composite is shown in Fig. 3.7. The large parts of the polymer chain skeleton and its functional groups oscillate, leading to the observed pattern. The characteristic vibrational mode can distinguish between the different phases in P(VDFTrFE) polymer. Most of the infrared active vibrations for the copolymer mainly occur between 600 and 1500 cm^{-1}. The characteristics peaks at 842, 880, 1118.93, 1173.79, 1283, and 1400 cm^{-1} correspond to the electroactive β phase crystal structure of P(VDF-TrFE)/ZnO fiber composite [127]. The absorption peaks appear at 842 cm^{-1} and 1288 cm^{-1} due to symmetrical tensile vibrations of -CF_2 and C-C, while the absorption peak at 1400 cm^{-1} is due to the -CH_2 swing anti-symmetric stretching of C-C. The peak intensity corresponding

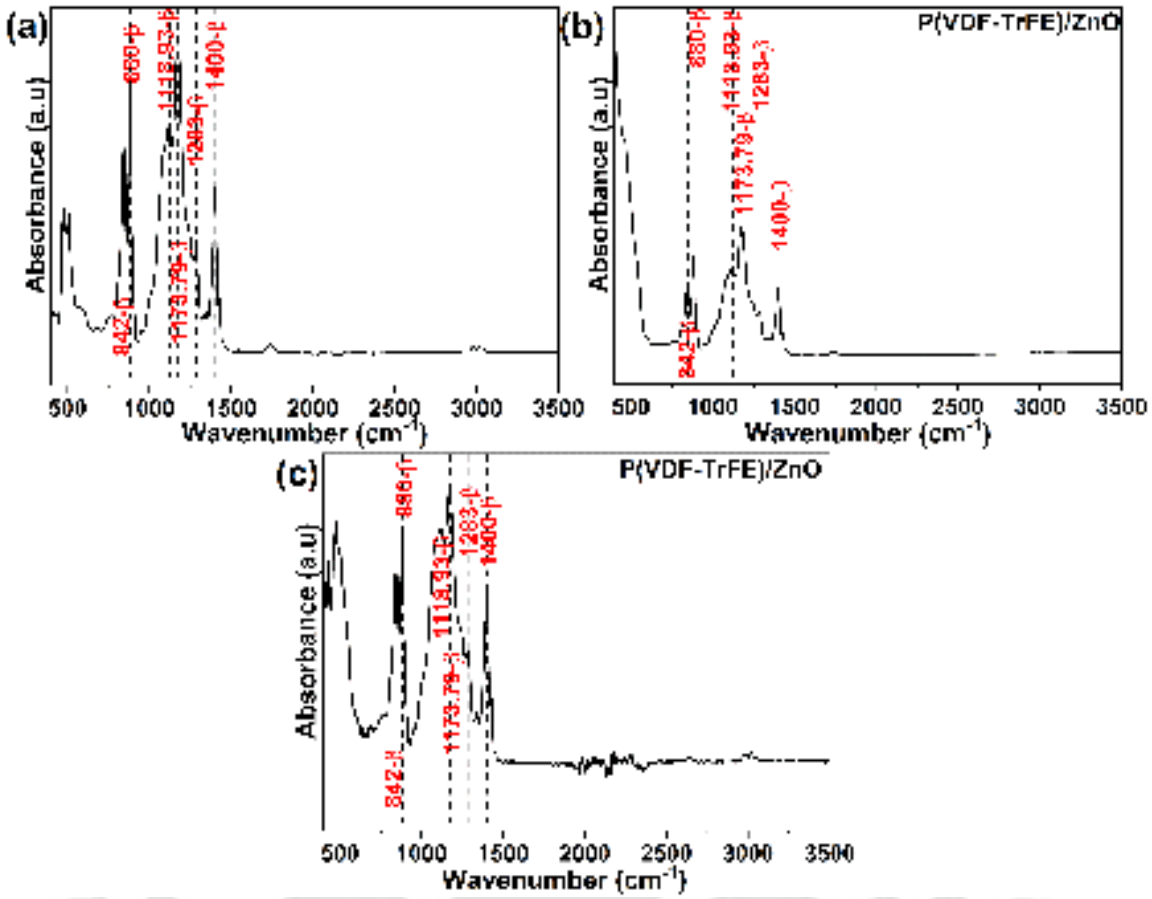

Fig. 3.7: FTIR analysis of (a) P(VDF-TrFE) fiber and (b,c) P(VDF-TrFE)/ZnO fiber composites fabricated at different electrospinning conditions.

to the beta phase is decreased of composite film fabricated with 18% w/v ZnO filler, while the peak intensity of nanocomposite film synthesized with 18% w/w filler is increased compared to pure P(PVDF-TrFE) nanofiber. Moreover, the addition of ZnO nanopowder did not significantly alter any of the polymer matrix's characteristic vibration bands. The fraction of the beta phase can be determined by applying the following mathematical relation:

$$F(\beta) = \frac{A_\beta}{A_\beta + 1.26A_\alpha} \tag{3.2}$$

The F(β) value for electrospun P(VDF-TrFE) nanofiber and P(VDF-TrFE)/ZnO composite at 18% w/v with respect to DMF and P(VDF-TrFE)/ZnO composite at 18% w/w concentration relative to polymer is 77.47%, 75.83% and 80.88%. The F(β) significantly increased with the dispersion of ZnO nanofiller due to an increase in interfacial interaction between ZnO nanoparticles and P(VDF-TrFE) [128, 129, 130]. Where A_α corresponds to the absorption coefficient associated with 760

cm^{-1} phase α , A_β is the absorption coefficient corresponding to wavelength 840 cm^{-1} of phase β, $k_\alpha = 6.1\times10^4$ is the absorption coefficient at wavenumber 760 cm^{-1}, and k_β is the absorption coefficient at wavenumber 840 cm^{-1} [131, 132].

3.3.8 Mechanical Testing of P(VDF-TrFE) and ZnO Reinforced Nanocomposite

The stress versus strain curves of P(VDF-TrFE) nanofiber and P(VDF-TrFE)/ZnO fiber composite are shown in Fig. 3.8. The dimension of the tested nanofiber composite sample are taken as gauge length of 40 mm, width 20 mm, and 10 mm length is placed in the top and bottom jaw of the instrument. The uniaxial tensile stress-strain test is carried out at room temperature with a strain

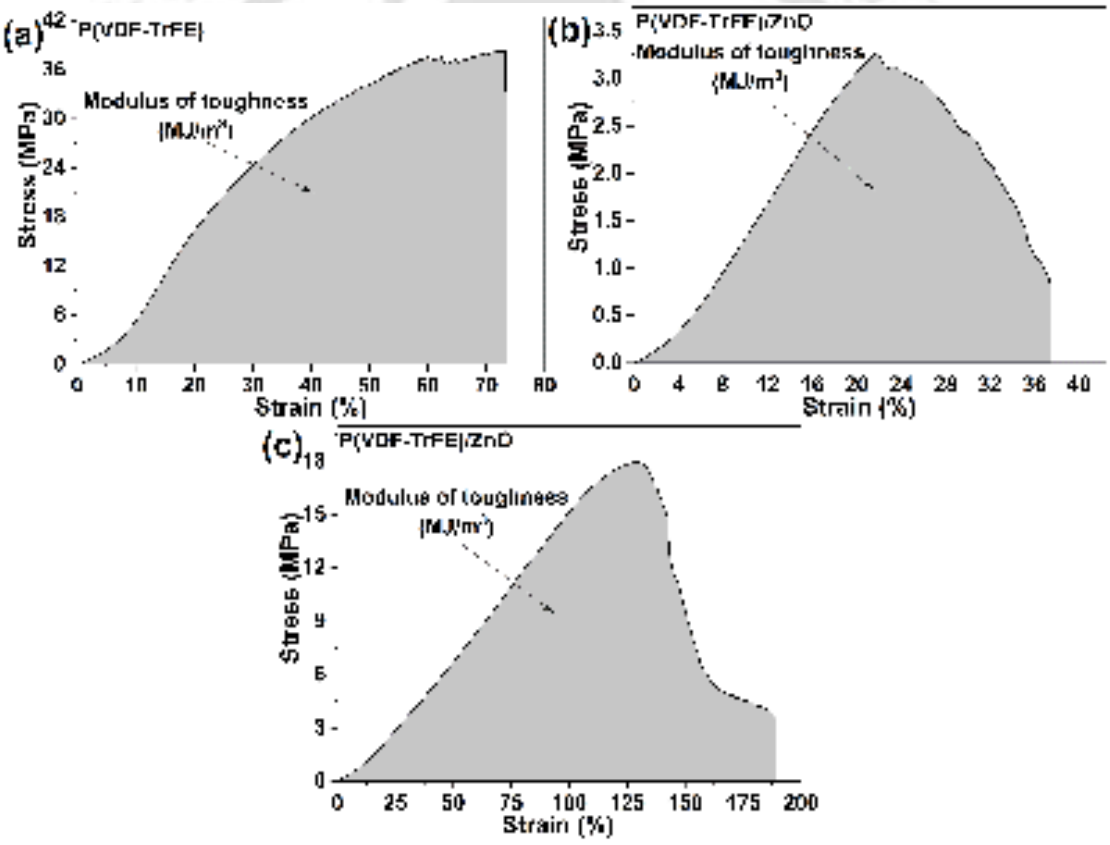

Fig. 3.8: Tensile mechanical test of nanofiber composite prepared at different concentration of nanofiller (a) 0% w/v (b) 18% w/v (c) 18% w/w.

rate of 5 mm/minute. The strain(%) and resultant load are recorded till the film specimen fractured. The stress, strain, Young's modulus and modulus of the toughness of the fabricated film are listed in Table 3.1. P(VDF-TrFE) nanofiber showed more stress, strain, and Young's modulus than P(VDF-TrFE)/ZnO fabricated at 18% w/v. However, the nanocomposite prepared at 18% w/w

concentration of filler exhibited more strain than P(VDF-TrFE) nanofiber and P(VDF-TrFE)/ZnO composite (18% w/v filler). The decrease in mechanical strength of P(VDF-TrFE)/ZnO fiber composite may be due to the not effective dispersion of ZnO nanopowder in the prepared P(VDF-TrFE) solution. The accumulation of Zno nanofiller generally occurs at higher concentrations, which leads to weak bonding between the polymer and ZnO nanoparticles. The result revealed that the mechanical properties of the film are decreased with increase in filler content. The nanocomposite film therefore exhibited lesser mechanical properties at higher filler content. Modulus of toughness is calculated by using the area under stress versus strain curve till the fracture point. The modulus of toughness of P(VDF-TrFE) fiber is calculated to be 17.87 MJ, while for the P(VDF-TrFE)/ZnO composite synthesized at 18% by volume and 18% by weight filler content has 0.70 MJ and 17.06 MJ respectively. Results state that modulus of toughness for the composite film is declined with the addition of ZnO nanoparticles at higher concentration. As discussed earlier, this result is consistent with other mechanical properties.

Table 3.1: Mechanical properties of fiber composite at different concentration of nanofiller.

Sl. no.	Sample	Stress (MPa)	Strain (%)	Young's modulus (MPa)	Modulus of toughness (MJ/m^3)
1	P(VDF-TrFE)	38.30	73.39	36.97	16.87
2	P(VDF-TrFE)/ZnO-18 vol.%	3.27	37.51	16.47	0.70
3	P(VDF-TrFE)/ZnO-18 wt.%	17.96	189.04	15.76	17.06

3.3.9 Differential Scanning Calorimetry Analysis

Polymer's crystallinity is one of its most important properties that determine physical characteristics such as mechanical stability and degradation resistance. It can also be used to study the crystal phases of P(VDF-TrFE) and its copolymers. Temperature versus heat flow has been plotted in the DSC curve as shown in Fig. 3.9a. This analysis is performed for the P(VDF-TrFE) nanofiber and P(VDF-TrFE)/ZnO nanocomposite. The first peak in the graph illustrates the phase transition from ferroelectric to paraelectric of pure P(VDF-TrFE) fiber and P(VDF-TrFE)/ZnO

nanocomposite at 108, 109 and 107.5°C, respectively. The second peak of the plot reveals the melting of crystalline phase in nanofiber composites. The percentage crystallinity of the film can be obtained using this equation [133]:

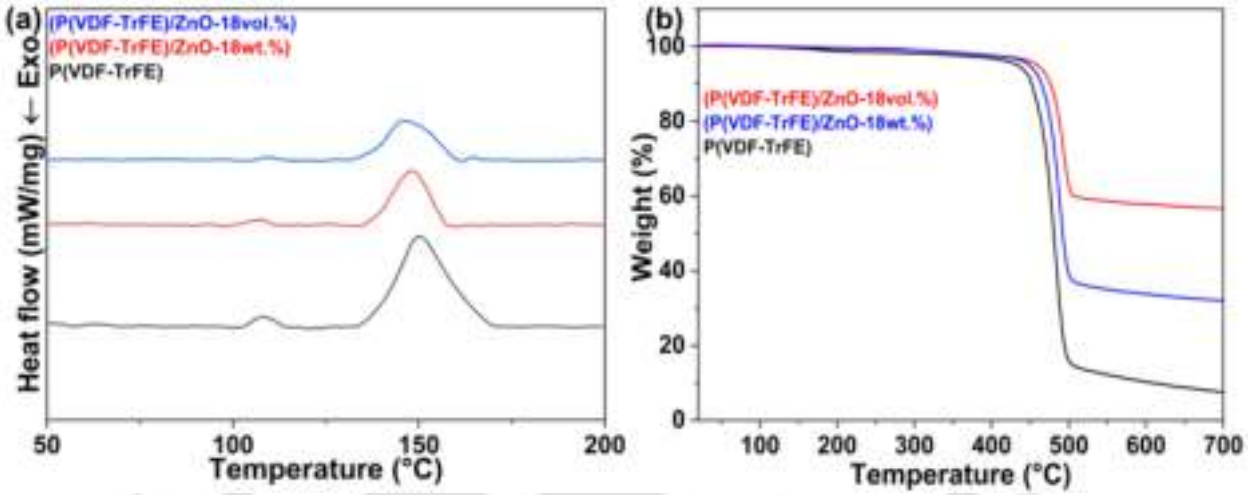

Fig. 3.9: (a) DSC curve and (b) TGA analysis of fabricated films.

$$X_C = \frac{\Delta H_f}{\Delta H_f^\star \times (1 - \frac{filler(wt.\%)}{100})} \times 100 \tag{3.3}$$

Where X_C is percentage crystallinity, ΔH_f is melting enthalpy and $\Delta H_f^\star = 104.6$ J/g presents the enthalpy for the P(VDF-TrFE) copolymer at 100% crystallinity [134]. The melting temperature of P(VDF-TrFE) and P(VDF-TrFE)/ZnO film is found to be measured 150°C, 146.48°C and 147.4°C, respectively. The crystallinity of the film is calculated to be 19.62, 20.92 and 19.93%, respectively. Results found that increasing the concentration of nanofiller to 18% w/v reduced the percentage crystallinity, while the nanocomposite fabricated with ZnO (18 wt.%) showed more crystalline compared to film synthesized using ZnO (18 vol.%). The reduced percentage crystallinity could be attributed to the accumulation effect of nanofiller. The crystallinity index obtained using XRD pattern is greater compared to DSC curve. The comparison of crystallinity calculated using DSC and XRD study is shown in Table 3.2.

3.3.10 Thermal Gravimetric Analysis (TGA)

The temperature versus weight (%) presents TGA thermograms, which is shown in Fig. 3.9b. TGA analysis is conducted with the same equipment where DSC analysis was performed. This

Table 3.2: Crystallinity index comparison of fiber composite at different concentration of nanofiller.

Sl. no.	Nano composite film	Crystallinity(%)		Change(%)
		DSC curve	XRD pattern	
1	P(VDF-TrFE) fiber	19.62	23.11	3.49
2	P(VDF-TrFE)/ZnO film (ZnO-18 vol.%)	20.92	21.74	0.82
3	P(VDF-TrFE)/ZnO film (ZnO-18 wt.%)	19.93	17.06	2.87

analysis is recorded from 20°C to 700°C with a heating speed of 10°C/min. Fig. 3.9b indicates that each nanofiber composite film is decomposed in one step, as seen by the TGA traces. Pure nanofiber is almost thermally stable till 420.5°C, then sudden degrading starts to 502°C. The shifting of degradation temperature range can be seen in Fig. 3.9b with the addition of ZnO filler in matrix. P(VDF-TrFE)/ZnO composite showed greater thermal stability with ZnO nanofiller as compared to the pristine nanofiber film. The residue mass of the fabricated film is analyzed using TGA thermograms. The residue mass of 7.6% is found on pristine P(VDF-TrFE) nanofiber, while 56.67% is found on P(VDF-TrFE)/ZnO film made with ZnO-18% by vol and 32.0% are found on P(VDF-TrFE)/ZnO film membrane fabricated using ZnO filler 18% by weight. Our result suggests that the presence of ZnO nanoparticles significantly affects residual mass and decomposition of matrix in nanocomposite film. These findings conclude that the fabricated nanofiber composite film can be used in a thermally stable zone for mechanical energy harvesting applications.

3.3.11 Device Testing and its Analysis

The schematic structure of PENG and voltage output generated by finger tapping, pressing, and bending in PENG device based on P(VDF-TrFE) and P(VDF-TrFE)/ZnO films are illustrated in Fig. 3.10. The small part of P(VDF-TrFE) and P(VDF-TrFE)/ZnO web with an effective area of 6 cm^2 are placed between two electrodes. The copper wires are connected to the electrodes through their terminals. The PENGs devices are subjected to load in the form of repeated soft tapping, bending and pressing by a human hand and then recorded their piezoelectric output using DSO.

Based on the results of the tests, the peak to peak electrical voltages for the P(VDF-TrFE) based PENG is 768 mV, 704 mV and 712 mV after they are bent, pressed, and tapped manually. The P(VDF-TrFE)/ZnO based PENG (fabricated at 18% w/v filler) exhibited 528 mV, 592 mV and 376 mV after applying the same load. While the voltage output for P(VDF-TrFE)/ZnO based PENG (fabricated at 18% w/w filler) are 840 mV, 744 mV and 1.15 V for the same loading condition. The current output is measured for P(VDF-TrFE) fiber and P(VDF-TrFE)/ZnO film fabricated at 18% w/v and 18% w/w are 4.8 μA, 4 μA, and 5.2 μA. The piezoelectric output of fabricated film is listed in Table 3.3. The higher piezoelectric output is found for the PENG device, which is fabricated at 18% w/w concentration of nanofiller. The roughness and fraction of the β phase are increased for this sample (18% w/w) as data obtained from the AFM and FTIR analysis, which support the higher piezoelectric output and good agreement with the reported results [135]. That could be accredited to the piezoelectric properties of ZnO nanofiller. Nanocomposite films fabricated with a greater amount of filler might not have strong interfacial interactions between filler and polymer, and solution agglomeration can also be observed with a higher amount of filler. This effect is possibly caused by the decrease in piezoelectric output over the film having a filler concentration of 18% w/v.

Table 3.3: Piezoelectric output of fiber composite at different concentration of nanofiller.

Sl. no.	Devices	Bending (mV)	Pressing (mV)	Softly tapping
1	P(VDF-TrFE)	768	704	712 mV
2	P(VDF-TrFE)/ZnO (18% w/v)	528	592	376 mV
3	P(VDF-TrFE)/ZnO (18% w/w)	840	744	1.15 V

3.4 SUMMARY

In this work, P(VDF-TrFE) nanofiber and P(VDF-TrFE)/ZnO nanocomposites are fabricated by means of electrospinning method. The ZnO nanofiller is dispersed with higher content in the different polymeric P(VDF-TrFE) solution. The effect of ZnO nanoparticles on average diameter, beta

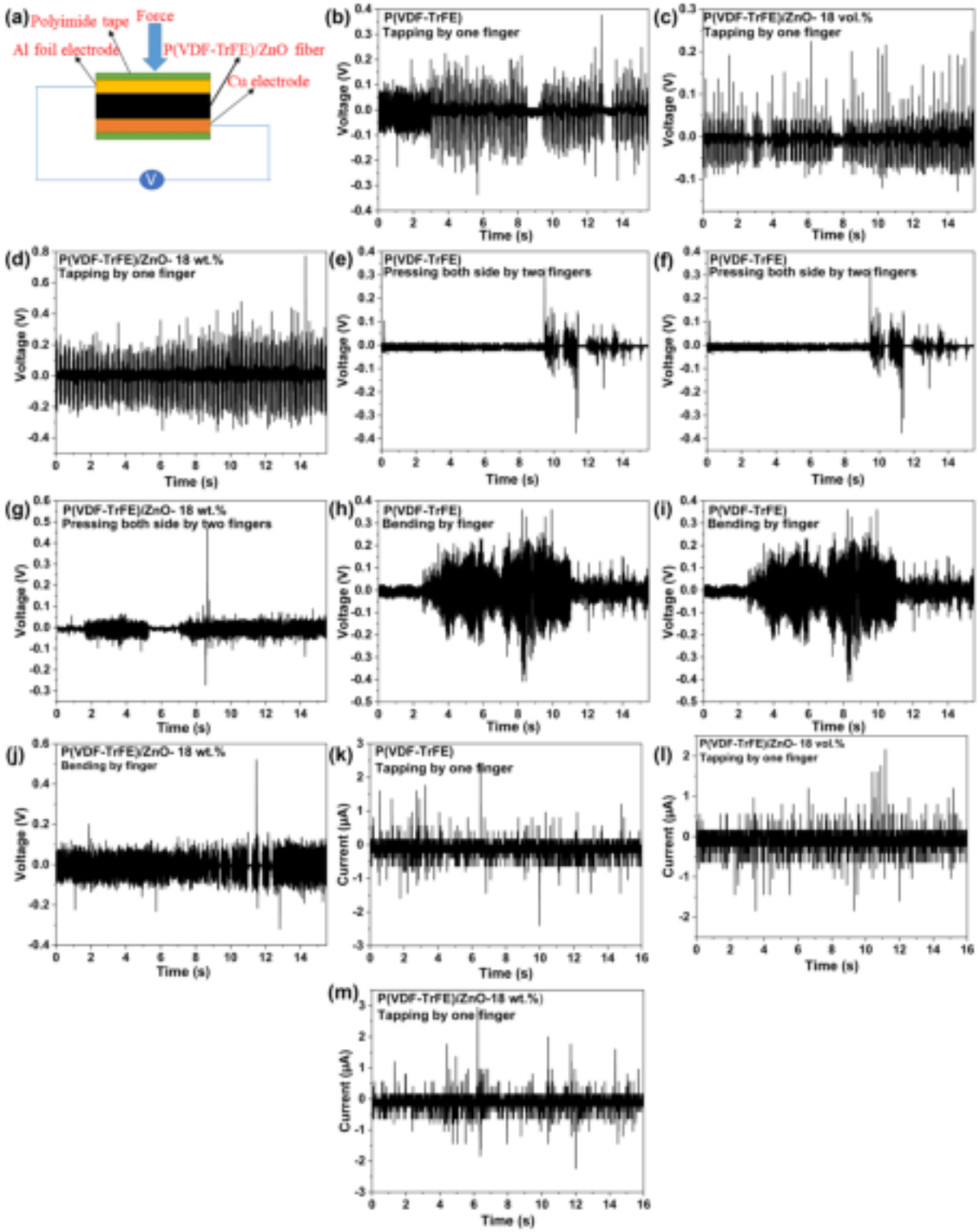

Fig. 3.10: (a) Schematic diagram of PENG, (b,e,h) voltage generated by finger tapping, pressing and bending in P(VDF-TrFE) based PENG, (c,f,i) voltage generated by finger tapping, pressing and bending in P(VDF-TrFE)/ZnO (18 vol.%) based PENG, (d,g,j) voltage generated by finger tapping, pressing and bending in P(VDF-TrFE)/ZnO (18 wt.%) based PENG (k,l,m) current generated in tapping mode.

phase crystalline structure, stress, strain, Young's modulus, and the output of the PENG devices are investigated. The structural characterization has been carried out for the surface morphology, elemental composition and confirm the presence of crystalline structure in the fabricated samples. This charcterization is accomplished by the FESEM, EDX, XRD and FTIR tests. The mechanical characterization is conducted using UTM test in the tensile mode. Further, the piezoelectric responses have been recorded employing the piezoelectric nanogenerator subjected to different manual activities including bending, pressing, and tapping. This PENG device with enhanced piezoelectric output that energy harvests may provide simple, cost-effective, useful, and flexible access to self-powering for many microelectronic devices. This study reveals the following conclusions:

(i) Higher content of ZnO nanoparticles on the nanofiber mat result in agglomeration. It further reduces surface area to volume ratio causes to reduce the efficiency of energy harvesting device.

(ii) The fraction of β phase and roughness increased with the dispersion of nanoparticles as confirmed from the FTIR and AFM test.

(iii) The viscosity, dynamic moduli of the solution are substantially enhanced with the inclusion of ZnO nanopowder while damping factor is reduced.

(iv) ZnO with higher concentration significantly affect the fiber diameter, β phase crystalline structure, stress, strain, Young's modulus, and the piezoelectric output of the PENG device.

(v) The findings of this study indicated that the film fabricated using the nanofiller concentration relative to the polymer is more suited for energy harvesting applications.

(vi) The piezoelectric nanogenerator under softly tapping generates more power output as compared to pressing and bending.

Chapter 4

Optimizing process parameters for P(VDF-TrFE)/ZnO nanofiber composite as self-powered sensor

4.1 INTRODUCTION

In this chapter, P(VDF-TrFE)/ZnO based electrospun nanofiber composites have been developed through electrospinning to cater the need of self-powered small wearable devices. Even though after huge work in this field, real-time commercial applications are very less because pure PVDF based electrospun mats have very low electrical outputs. In this work, an effort is made to enhance the voltage output of the P(VDF-TrFE) based nanomats by adding ZnO nanoparticles into the viscous solution. The materials, fabrication of nanocomposite films as per the DOE, energy harvesting device, and characterization through various instruments are presented in Sec. 4.2. The fiber composites have been made with the fixed ratio of dimethylformamide, acetone, matrix concentration, and different percentage concentration of ZnO nanopowder. The main operating parameters, namely applied voltage, flow rate, and concentration of reinforcing component are optimized using the response surface method of statistical design of experiments (DOE). A three-level factorial design based on Box-Behnken RSM technique is incorporated to design the experiment (DOE), and the corresponding experimental plan is carried out. The composite films are synthesized employing the process parameters to validate the model obtained from design of experiment (DOE). In addition, three more experiments are performed by varying the same parameters just before and after the optimum value to ensure that the maximum pieoelectric output is achieved with the same parameters obtained from DOE. In Sec. 4.3, the study of electrospun nanocomposite mats are presented

in detail. It focuses on surface morphology, elemental analysis, percentage crystallinity, crystalline structure, β phase variation, and mechanical properties. These studies are accomplished using the various instruments. Further, surface area to volume ratio, rhelogical behaviour of blended solution, and dynamic modulus of nano mats are investigated using Brunauer-Emmett-Teller (BET), rheological test, and DMA analysis, respectively. The electrical output of the piezoelectric nanogenerators (PENGs) have been measured using digital storage oscilloscope under various loading conditions at room temperature. A systematic and detailed analysis is conducted to assess the effect of ZnO nanoparticles. It has been observed that voltage output increases with the increment of ZnO weight percentage up to 10 and then decreases. The piezoelectric voltage and current of the piezoelectric nanogenerator device based on fiber composite is found 2.52 V and 20.8 μA whereas 0.82 V and 12.8 μA for the pristine P(VDF-TrFE) nanofiber under softly tapping loading condition. In the health and engineering fields, these results may open the door to the development of P(VDF-TrFE)/ZnO based nanomats and their use as sensors and actuators.

4.2 EXPERIMENTAL

4.2.1 Materials

P(VDF-TrFE) pellets (M_w = 300,000), Zinc oxide (ZnO) nanopowder (Average particle size = 100 nm, M_w = 81.39 g/mol), N,N-Dimethylformamide (DMF), and acetone (ACE) are procured from the Sigma Aldrich. Materials are used for electrospinning without further purification.

4.2.2 Fabrication of P(VDF-TrFE) and ZnO Nanofibers

P(VDF-TrFE) solution is prepared by combining P(VDF-TrFE) pellets (solute) into DMF/ acetone (solvent). In 3 ml of solvent, 2.1 ml of DMF is used, 0.9 ml of acetone, and 0.6 gm of P(VDF-TrFE) pellets are taken. For every sample, 20% (wt./vol.) of P(VDF-TrFE) pellets and 7/3 (vol/vol) % of DMF/acetone proportions are taken and stirred approximately 3 h at 50°C to get a white-colored homogeneous solution. Different weight percentage (0, 10, 20) of ZnO nanopowder are dissolved into the P(VDF-TrFE) solution. Further, three more ZnO concentrations (3, 7, and 9 wt.%) are incorporated with the matrix. The weight fraction of ZnO nanofiller can be determined

using the following equation:

$$\text{Wt.\% age of nanofiller} = \frac{W_{ZnO}}{W_{P(VDF-TrFE)} + W_{ZnO}} \times 100 \tag{4.1}$$

After that stirred solution has been placed inside the ultrasonic bath for 30 minutes. Later on, the solution is stirred for 1h to get a uniform homogeneous P(VDF-TrFE)/ZnO solution. This solution has been directly used to fill up the electrospinning apparatus syringe for preparing nanofibers. The various electrospinning parameters such as voltage, flow rate, and ZnO nanofiller concentration (wt.%) are investigated by taking different values as shown in Table 4.1. A syringe of 5 ml capacity under controlled chamber temperature 27°C is used to electrospun the fibers on the collectors. An electrospinning machine (E-SPIN NANOTECH Fig. 4.1) is used to draw fibers in a horizontal direction. For the present investigation, the syringe is placed horizontally with the needle (Fig. 4.1) and a cylindrical grounded collector is used. The high voltage source (12-18 kV) is connected

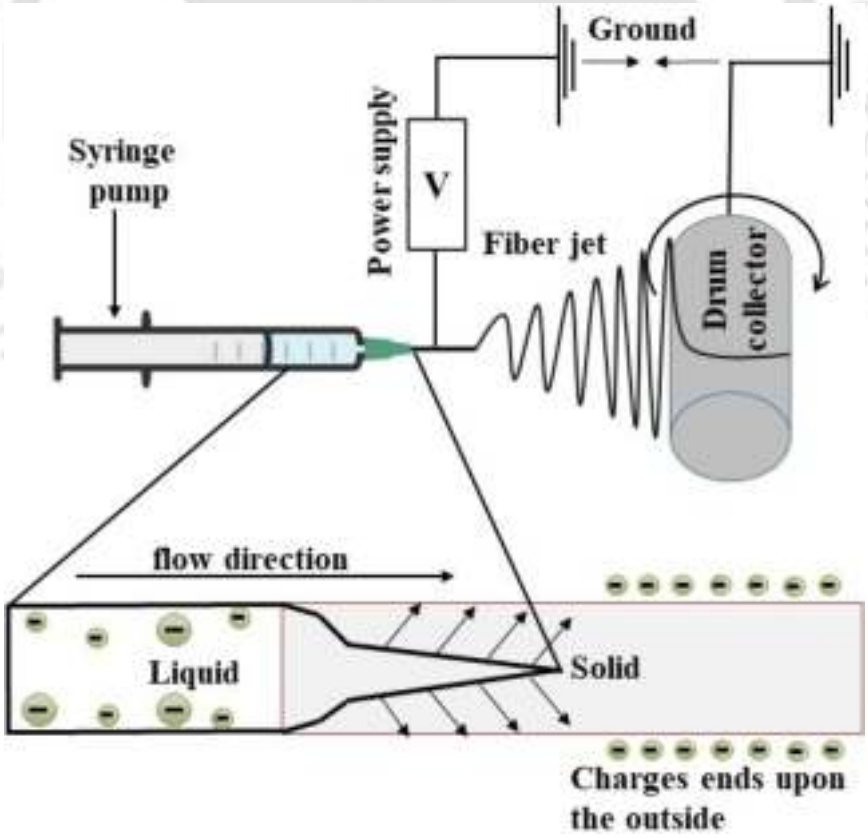

Fig. 4.1: Schematic diagram for the horizontal electrospun set-up.

to the needle tip through the alligator clip. The voltage-dependent Taylor cone is formed at the needle tip due to the electrostatic charge repulsion and surface tension of the solution. The

charged jet is ejected from the tip at a set voltage, and the fibers are deposited on the grounded collector. By following the above procedure, twenty (20) samples (electrospun mats) are prepared for investigation.

4.2.3 Design of Experiments

The piezoelectric response of fabricated nanocomposite is achieved by varying three variables. The electrospinning parameters, which is applied voltage (A), flow rate (F), and concentration of ZnO nanofiller (C), are selected from preliminary experiments. A statistical design of experiments (DOE) is carried out to analyze the impact of electrospinning parameters and its interactions on piezoelectric output. The electrospinning parameters with their levels are presented in Table 4.1. Twelve points are corresponding to the midpoints of the edges and five center nodes are considered for design feasibility and the fabrication limitation of electrospinning used in this work. The details of experiments based on the BoxBehnken approach with three input parameters and responses are summarized in Table 4.2.

Table 4.1: Electrospinning parameters and 3-level design of DOE.

		Levels		
Factor symbol	Electrospinning parameter	-1	0	+1
A	Voltage (kV)	12	15	18
F	Flow rate (µl/min)	8	12	16
C	ZnO (wt.%)	0	10	20
Constant Parameters				
Distance				12 cm
DMF:Acetone = 3:1	Speed of collector (rpm)			

4.2.4 Preparation of Energy Harvesting Devices

Electrospun mats have been cut into rectangular patches measuring 3.5 cm long and 2 cm wide for fabrication of piezoelectric nanogenerators (PENG) as shown in Fig. 4.2. Aluminium foil and copper tape with conductive adhesive tape are pasted at the bottom and top as electrodes, respectively.

Table 4.2: Electrospinning condition for the fabrication of nanofiber samples.

	Operating parameters			Output response
Exp. no. (or) Sample (SA) no.	Voltage (kV)	Flow rate (µl/min)	ZnO concentration (wt.%)	Piezoelectric output (V)
1	18	8	10	2.25
2	15	12	10	2.35
3	12	16	10	2.4
4	12	12	20	1.2
5	18	12	20	1.32
6	15	12	10	2.15
7	12	8	10	1.98
8	12	12	0	0.82
9	15	8	20	1.52
10	15	16	0	1.04
11	18	16	10	2.52
12	18	12	0	0.95
13	15	12	10	2.02
14	15	12	10	2.28
15	15	8	0	0.9
16	15	12	10	2.3
17	15	16	20	1.78

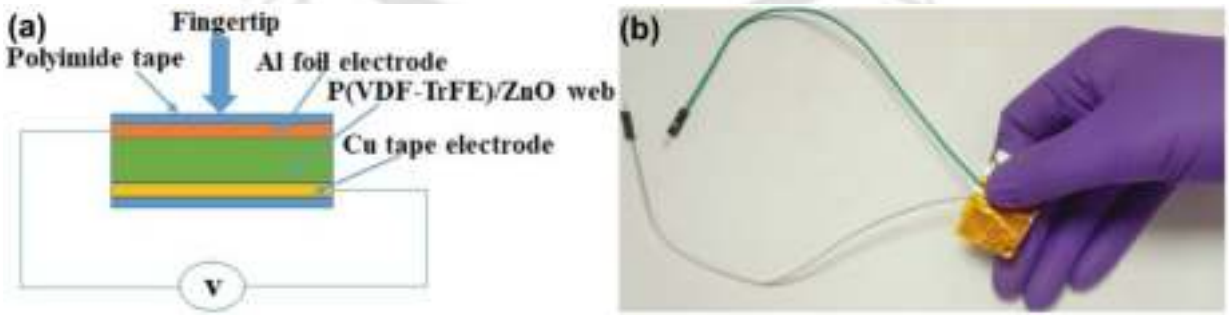

Fig. 4.2: Schematic view of the (a) PENG device and (b) showing an actual photo of PENG in hand.

The copper wires are connected to the electrodes for connecting digital storage oscilloscope (DSO) terminals. A polyimide tape is used to seal the whole PENG to make it safe from environmental

noises and get protected it from damage (Fig. 4.2).

4.2.5 Material Characterization

The field emission scanning electron microscopy (FESEM) image analysis has been carried out to probe the electrospun nanofibers microstructure and morphology (FESEM, model: JSM-7610F, JEOL Co.). This test is executed at an accelerated voltage of 15 kV. The average diameter of the nanofibers are calculated using image analysis software. The thickness of the electrospun web is measured using a digital micrometer (Mitutoyo 293-240-30 micrometer). XRD (X-ray diffraction) (model: Smartlab, make: Rigaku Technologies, Japan) of P(VDF-TrFE)/ZnO webs are conducted to know crystalline structure on a diffractometer using Cu-Kα radiation 1.54 Å. This test has been conducted for the samples having 2θ range of 10° to 60°. FTIR (Fourier Transform Infrared) spectra of P(VDF-TrFE)/ZnO samples are carried out by a spectrometer (model: Spectrum two, make: PerkinElmer, Singapore) with attenuated total reflection (ATR) mode over the wavenumber range of 400-2700 cm^{-1}. Differential scanning calorimetry (DSC) (model: STA449F3A00, make: Netzsch) test is performed in an argon atmosphere. The fabricated samples are heated from 25°C to 250°C at the rate of 10°C/min. Tensile tests are conducted using a 5kN Electromechanical universal testing machine (model: Z005TN Proline, make: ZwickRoell) at a 5 mm/min strain rate. XPS (Thermo Fisher Scientific Pvt. Ltd. UK, Model- K-Alpha) analysis has been carried out to acquire the chemical composition and bonding between the atoms of the nanofiber composite films. Brunauer-Emmett-Teller (BET) (Make: Quantachrome, Model: Autosorb-IQ MP) characterization has been carried out to determine the specific surface area of the membranes low temperature (77.35 K) using nitrogen adsorption isotherms measured over a range of relative pressures, from 0.05 to 0.3. Before conducting the test, the samples are degassed at 80°C for 3 h in the degas pot of the adsorption analyser. A dynamic mechanical analyzer (Physica MCR 702-Anton Paar) test is performed to measure the dynamic moduli of the electrospun neat P(VDF-TrFE) fiber and P(VDF-TrFE)/ZnO nanofiber composite membranes under the tensile mode on 40×10 mm^2 rectangular specimens (L×W). The analysis is performed at a frequency of 1 Hz and the temperature range from -84°C to 90°C at a heating rate of 8°C/min. The rheological properties of P(VDF-TrFE) and P(VDF-

TrFE)/ZnO blended solution are analyzed by means of a Physica MCR 301 rheometer (Anton Paar) with 1° cone angle and 50 mm diameter of cone and parallel plates. The test is performed at 40°C, a gap of 0.1 mm, and the strain is fixed at 1%. The storage and loss modulus (G', G") are evaluated with varying frequencies for 10 minutes.The voltage and current of (PENG) with an effective area of 7 cm^2 are measured using a digital oscilloscope (GDS-1102U-Gwin Instek Co.). The samples are tested using the softly tapping and softly bending at room condition (humidity of 56% and temperature of 27°C).

4.3 RESULTS AND DISCSSION

4.3.1 Morphology Analysis

Uniform, beadless, and aligned nanofibers mats are fabricated by setting the proper parameters as discussed in Table 4.2. FESEM technique is used to analyze the morphology and structure of the fabricated mats. Seventeen samples are fabricated as per the design of experiment model. Pure P(VDF-TrFE) nanofibers and its composites are fabricated with varying applied voltage of 12 to 18 kV. It is to be noted that electrospun nanofiber mats are successfully made at specific parameters as discussed in Table 4.2. Through a series of experiment, hence parameters are set for electrospinning the fiber. FESEM images of the fiber samples are presented in Fig. 4.3. Pure P(VDF-TrFE) nanofiber and P(VDF-TrFE)/ZnO mats are shown in Fig. 4.3. Sample-1 as shown in Fig. 4.3 indicates that uniform and smooth surfaces are developed for the P(VDF-TrFE) nanofiber. Defect-free mats for other samples are also formed as presented in Fig. 4.3. The average diameter of P(VDF-TrFE) nanofiber is 282.65 nm at a zero percent concentration of ZnO nanopowder. The average nanofiber diameter of nanocomposite samples increases with ZnO (10 wt.%) and then decreases for other samples. As the concentration of ZnO nanopowder increases, the conductivity of the solution increases. Therefore, the diameter of fiber gets decreased. The introduction of ZnO nanopowder to the piezoelectric polymeric solution could alter the optimal condition of the electrospinning process. For this, an optimization study is executed to get the appropriate parameters that are presented in Table 4.2.

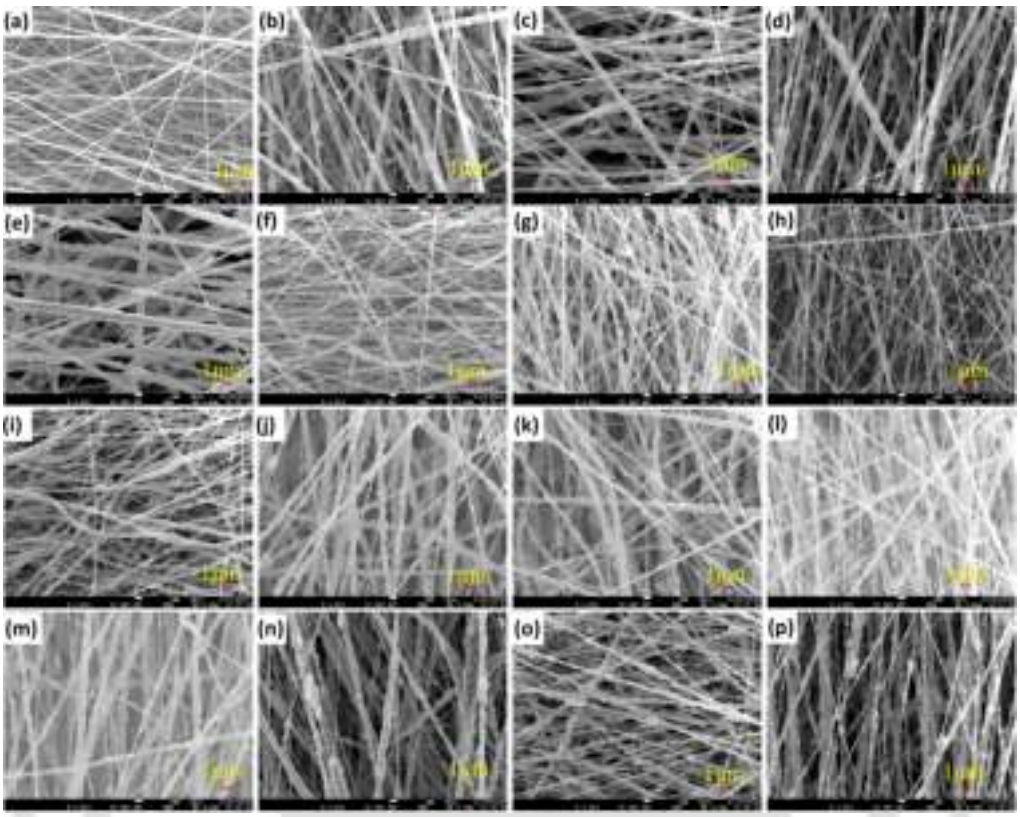

Fig. 4.3: FESEM image of (a) P(VDF-TrFE) nanofiber and (b-p) P(VDF-TrFE)/ZnO fiber composites at different operating conditions.

4.3.2 X-ray Diffraction Analysis

XRD tests are carried out for the all samples to verify the presence of ZnO nanoparticles in P(VDF-TrFE)/ZnO nanocomposite. Further, it is also used to identify the beta phase crystal structure. The diffraction peaks are observed at angle $2\theta = 20°$, which suggest the appearance of the beta phase in the nanocomposite (Fig. 4.4). This is required for better piezoelectric output for P(VDF-TrFE) [124]. The formation of ZnO nanoparticles are visible in Fig. 4.4 (represented by the green line). All the diffraction peaks of nanoparticles are identified at 2θ values of 31.77, 34.45, 36.27, 47.58, and 56.60 [125]. Their corresponding lattice planes are (100), (002), (101), (102), and (110), which confirms the presence of ZnO nanofiller in the nanocomposite. XRD results showed that the nanocomposite fabricated with 20 wt.% of ZnO have a weak diffraction peaks while for the other composite shows strong peaks for the beta crystalline phase. The higher percentage of ZnO nanoparticles (20%) do not alter the formation of the beta phase. ZnO has higher piezoelectric properties than P(VDF-TrFE) therefore, samples fabricated with higher concentration of ZnO are

not much affected by the flow rate at the given range.

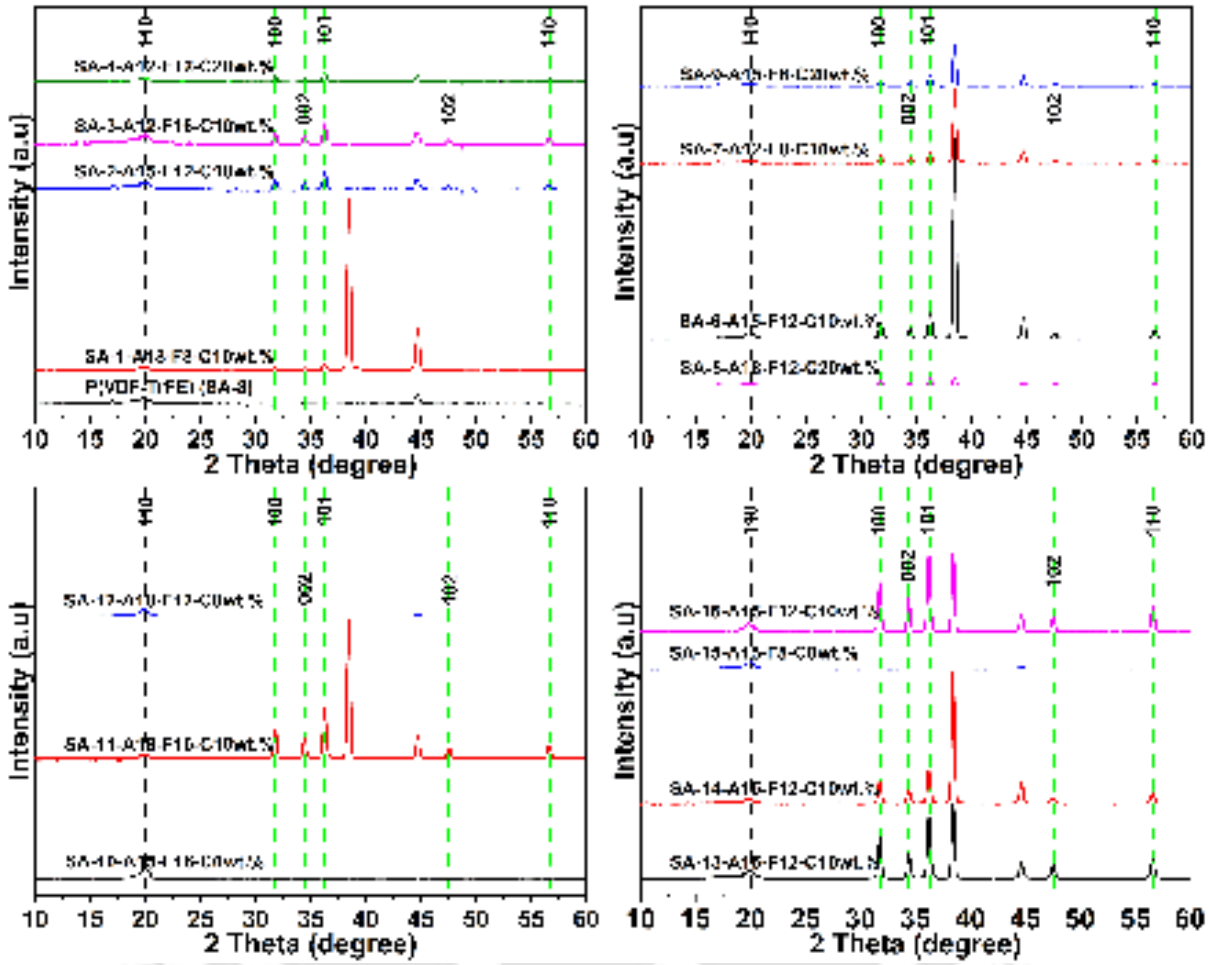

Fig. 4.4: XRD analysis of P(VDF-TrFE) and P(VDF-TrFE)/ZnO composite films fabricated at different operating condition.

4.3.3 Fourier Transforms Infrared Spectroscopy (FTIR) Analysis

FTIR spectroscopy test has been conducted to identify the crystalline beta phase of P(VDF-TrFE) fiber and their nanocomposite. Numerous peaks are observed for each type of copolymer conformation, as shown in Fig. 4.5. The scanned spectra indicates that the vibration bands at 473, 505, 845, 882, 1078, 1117, and 1400 cm^{-1} are responsible for the beta phase. These are corresponding to the presence of all-trans ferroelectric β phase of P(VDF-TrFE) (75/25) [127]. The intensity of the beta phase increases as the concentration of ZnO increases till 10 wt.%. It can be seen in Fig. 4.5 that the characteristic peak of the P(VDF-TrFE) nanocomposite is not significantly changed with increased concentration of ZnO nanopowder. The variation of the beta

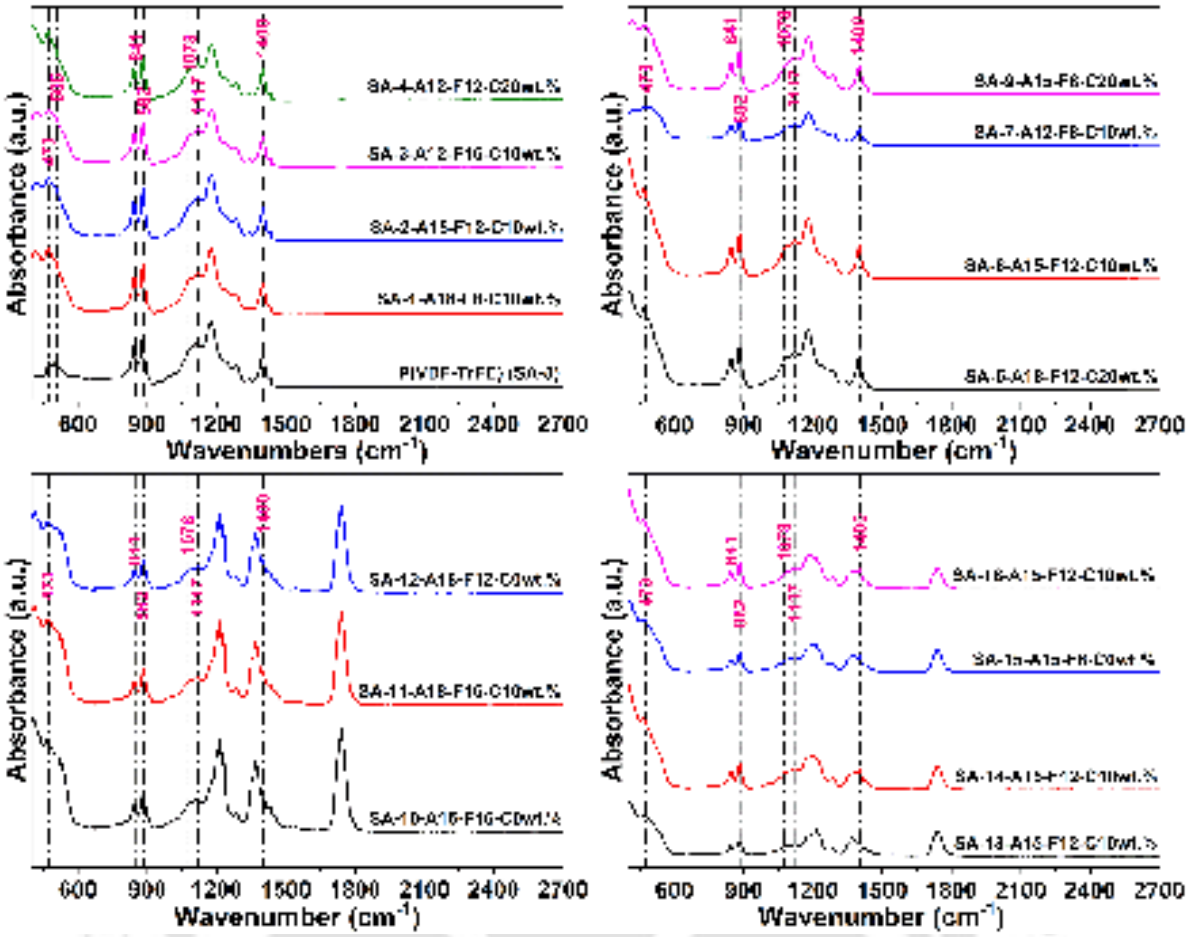

Fig. 4.5: FTIR analysis of P(VDF-TrFE) fiber and P(VDF-TrFE)/ZnO fiber composites fabricated at different electrospinning condition.

crystalline phase percentage of the film is shown in Fig. 4.6. The high electroactive β phase fraction is found at 10% concentration of ZnO filler.

4.3.4 Differential Scanning Calorimetry Analysis

Due to the limitation of slot availability for DSC spectra analysis, two samples (SA-1 and SA-8) are analyzed. The variation of heat flow with the temperature is shown in Fig. 4.7. The sum of the melting and phase transition enthalpy of nanocomposite mats are greater than the P(VDF-TrFE) nanofiber mat. The first peak tells about the transition phase from the ferroelectric to paraelectric of the neat P(VDF-TrFE) fiber and P(VDF-TrFE)/ZnO composite at 105.29°C and 108.18°C, respectively. The second peak at 146.29°C and 149.76°C corresponds to the melting point of the sample. The increase in melting peak temperature of nanocomposite mat can be attributed to the strong interaction between the matrix and ZnO nanofiller. The percentage crystallinity can be

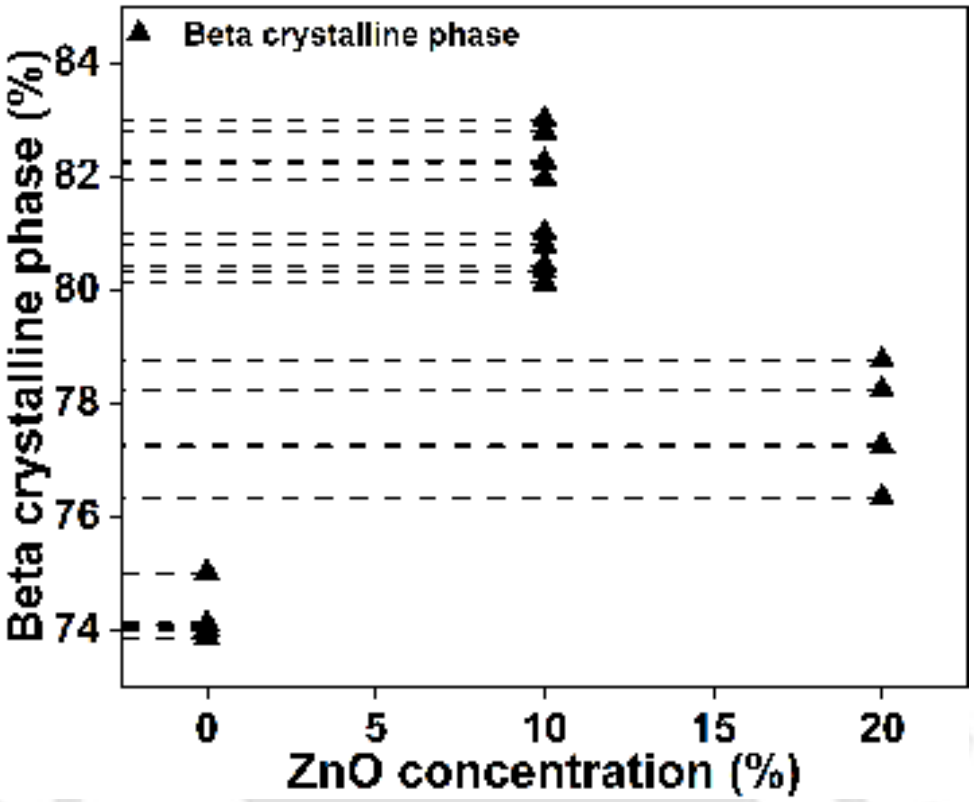

Fig. 4.6: Beta crystalline phase (%) showing at different concentrations of ZnO nanofiller.

calculated using the following equation [136].

$$X_C = \frac{\Delta H_f}{\Delta H_f^{\star} \times (1 - \frac{filler(wt.\%)}{100})} \times 100 \tag{4.2}$$

The percentage crystallinity for the P(VDF-TrFE) nanofiber and P(VDF-TrFE)/ZnO nanocomposite is 20.42% and 22.80%. Where ΔH_f is melting enthalpy for the nanofiber and composite. $\Delta H_f^{\star} = 104.6$ J/g is change in enthalpy for P(VDF-TrFE) copolymer at 100% crystallinity [134].

4.3.5 Tensile Test of P(VDF-TrFE)/ZnO Nanocomposite

The variation of stress versus strain for the pure P(VDF-TrFE) nanofiber and P(VDF-TrFE)/ZnO nanocomposites are presented in Fig. 4.8. The dimensions of the tested nanofiber composite are taken as length = 5 cm and width = 1.1 cm. Samples are stretched in the longitudinal direction. P(VDF-TrFE) nanofiber experienced more strain than P(VDF-TrFE)/ZnO. The supporting results are shown in Table 4.3. Strain in the fabricated samples decrease with the increase of ZnO nanofiller concentration compared to pure P(VDF-TrFE) and stress increases. It could be due to accumulation of the ZnO nanopowder in the viscous solution resulted in not perfect interaction with the

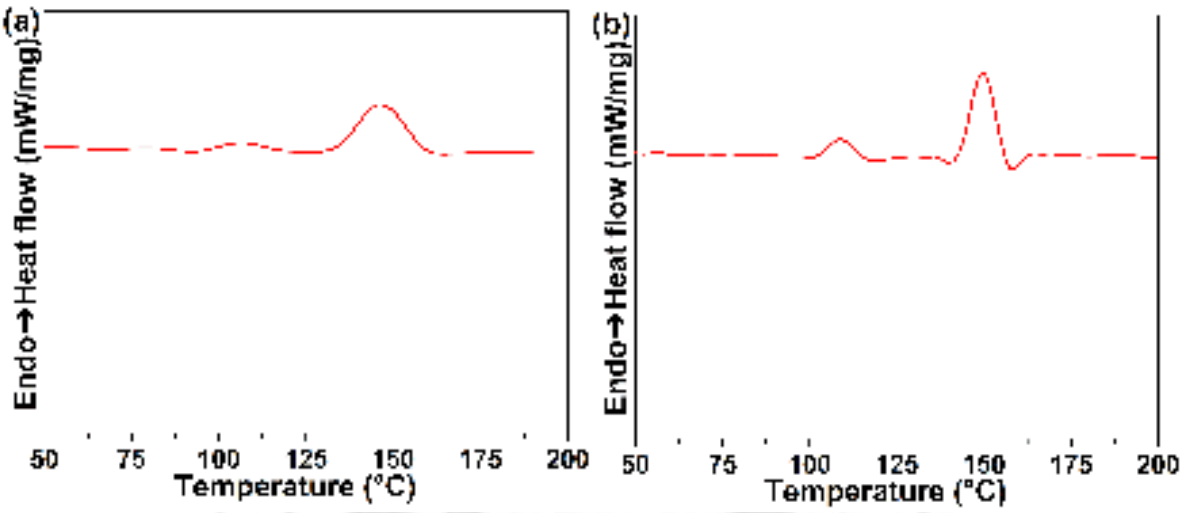

Fig. 4.7: DSC spectra analysis of P(VDF-TrFE) nanofiber and P(VDF-TrFE)/ZnO composite .

Table 4.3: Overview of the Mechanical Properties of P(VDF-TrFE) and P(VDF-TrFE)/ZnO at different condition.

Sample (SA) no.	Stress (MPa)	Strain (%)	Young's modulus (MPa)
SA-1	16.33	110	14.2
SA-2	17.31	105.85	15.1
SA-3	19	99.50	16
SA-4	14.58	62.77	12.8
SA-5	14.71	54.62	12
SA-6	17.54	103.23	14.9
SA-7	15.88	108.83	14
SA-8	11.51	129	8
SA-9	13.25	73	11
SA-10	12	130.64	8.1
SA-11	19.93	84.75	18
SA-12	9.81	124.36	7.89
SA-13	16.96	104.9	15
SA-14	17.1	104.7	14.8
SA-15	10.16	122.83	7.82
SA-16	17.30	104.55	14.75

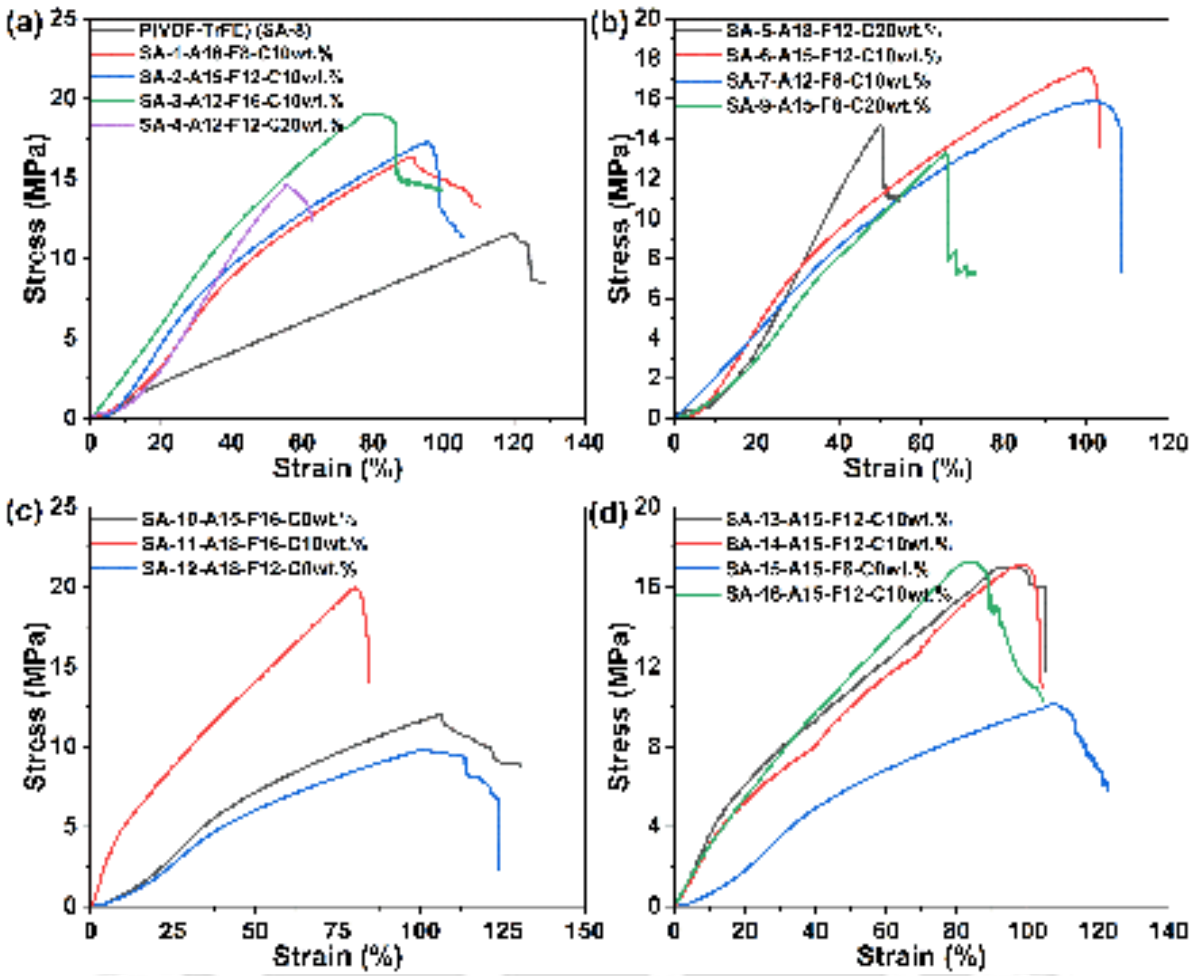

Fig. 4.8: Comparing tensile testing of the P(VDF-TrFE) fiber web and P(VDF-TrFE)/ZnO composites prepared at various electrospinning condition.

P(VDF-TrFE) nanofiber. Hence, P(VDF-TrFE)/ZnO composite exhibited less tensile strength at a 20 wt.% of ZnO nanopowder as compared to the mats fabricated with 10 wt.% ZnO nanoparticles. The fiber mats fabricated using ZnO shows less tensile strain than the pure P(VDF-TrFE) nanofiber. Young's modulus of the fabricated nanocomposite samples increases with the addition of ZnO filler than the P(VDF-TrFE) nanofiber. Hence, it should be noted that the stress and strain of samples are affected with the introduction of reinforcing nanoparticles and increasing flow rate. The sample exhibited a higher value of Young's modulus at higher flow rate and 10 wt.% of ZnO (Fig. 4.9). The flow rate and ZnO content significantly affect the mechanical properties of the fabricated nanofiber mats. The variation in stress, strain, and Young's modulus with nanofiller is shown in Fig. 4.9.

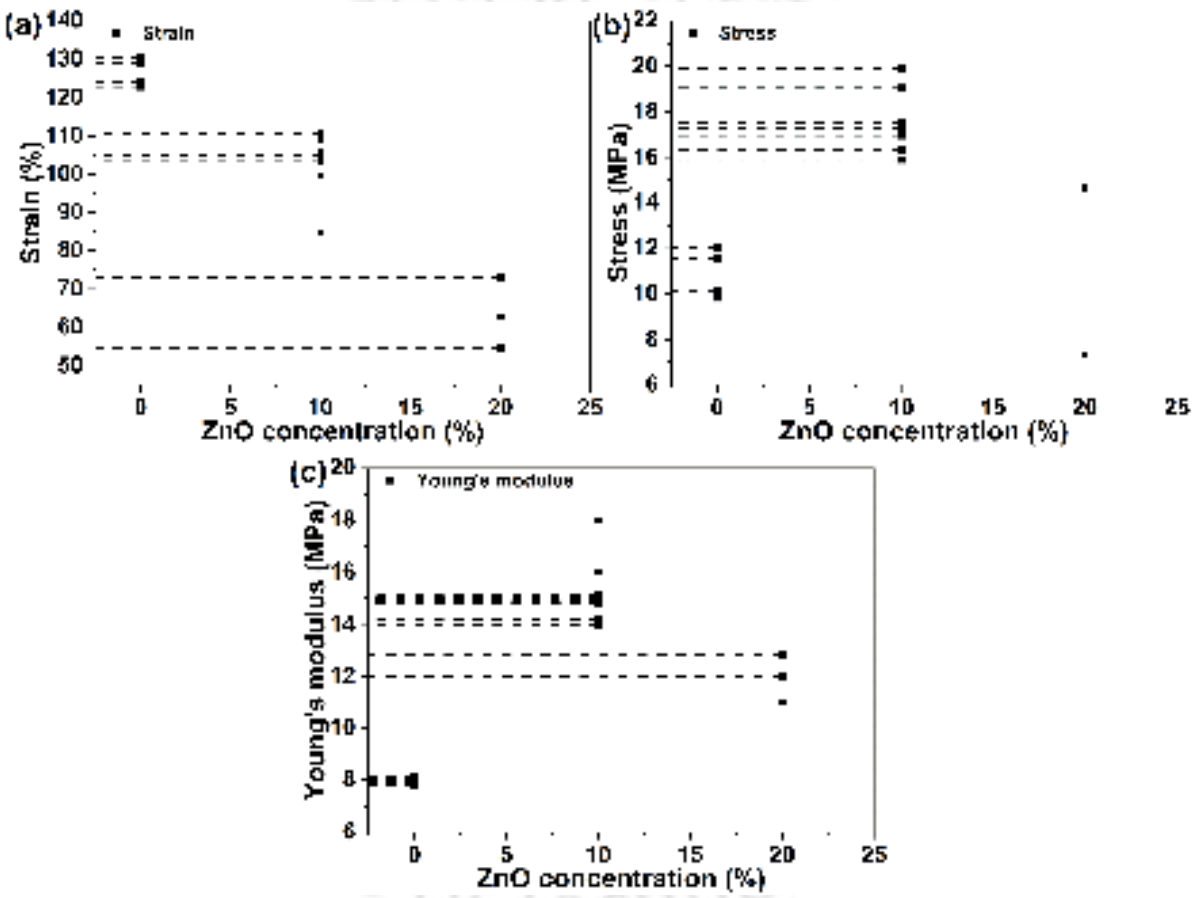

Fig. 4.9: A comparison of (a) strain, (b) stress, and (c) Young's modulus at a different level of ZnO nanofiller.

4.3.6 X-Ray Photoelectron Spectroscopy (XPS) Analysis

The XPS analysis has been carried out to obtain the atomic composition and chemical bonding in the prepared P(VDF-TrFE)/ZnO nanocomposite. The chemical composition of the film is evaluated as shown in Table 4.4. The full scanning XPS spectrum of a P(VDF-TrFE)/ZnO film grown at room temperature is presented in Fig. 4.10a. The elemental composition in P(VDF-TrFE)/ZnO film is evaluated using complete XPS spectra as F1s - (53.38%), C1s - (44.36%), $Zn2p_{3/2}$ - (.81%) and O1s - (1.45%) respectively. The core levels of Zn and O can be observed in Fig. 4.10 (d,e), respectively, in which the $Zn(2p_{3/2})$ peak is found at 1022.1 eV and the O (1s) peak is at 532.21 eV, these findings are in good agreement with the reported results [137]. The F1s and C1s spectra of nanocomposite film is shown in Fig. 4.10 (b,c) and their peak binding energies are 687.95 eV and 284.8 eV respectively [138]. The O1s and $Zn2p_{3/2}$ spectra are difficult to deconvolute owing to overlapping peaks. Although, They are important to evaluate the surface composition of the film.

Table 4.4: Elements detected using XPS spectra in atomic percentage of P(VDF-TrFE)/ZnO.

Sl. no.	Atom	Composition (%)
1	F1s	53.38
2	C1s	44.36
3	$Zn2p_{3/2}$	0.81
4	O1s	1.45

4.3.7 Brunauer-Emmett-Teller (BET)

The BET test is performed to evaluate the specific surface area of the fabricated film, which is fabricated at 0 and 10% (wt.%) concentration of ZnO nanofiller with the polymer as shown in Table 4.5. The nanofiber composite film has been cut into the smallest possible size and then placed in the cylindrical glass tube to conduct the test. The specific surface area obtained is 4.861 and 12.261 m^2/g for the P(VDF-TrFE) nanofiber (SA-8), P(VDF-TrFE)/ZnO nanocomposite film (SA-1) respectively. Results proved that the specific surface area of nanofiber composite increases with the increase in the concentration of ZnO nanofiller. Hence, it is believed that the higher surface area

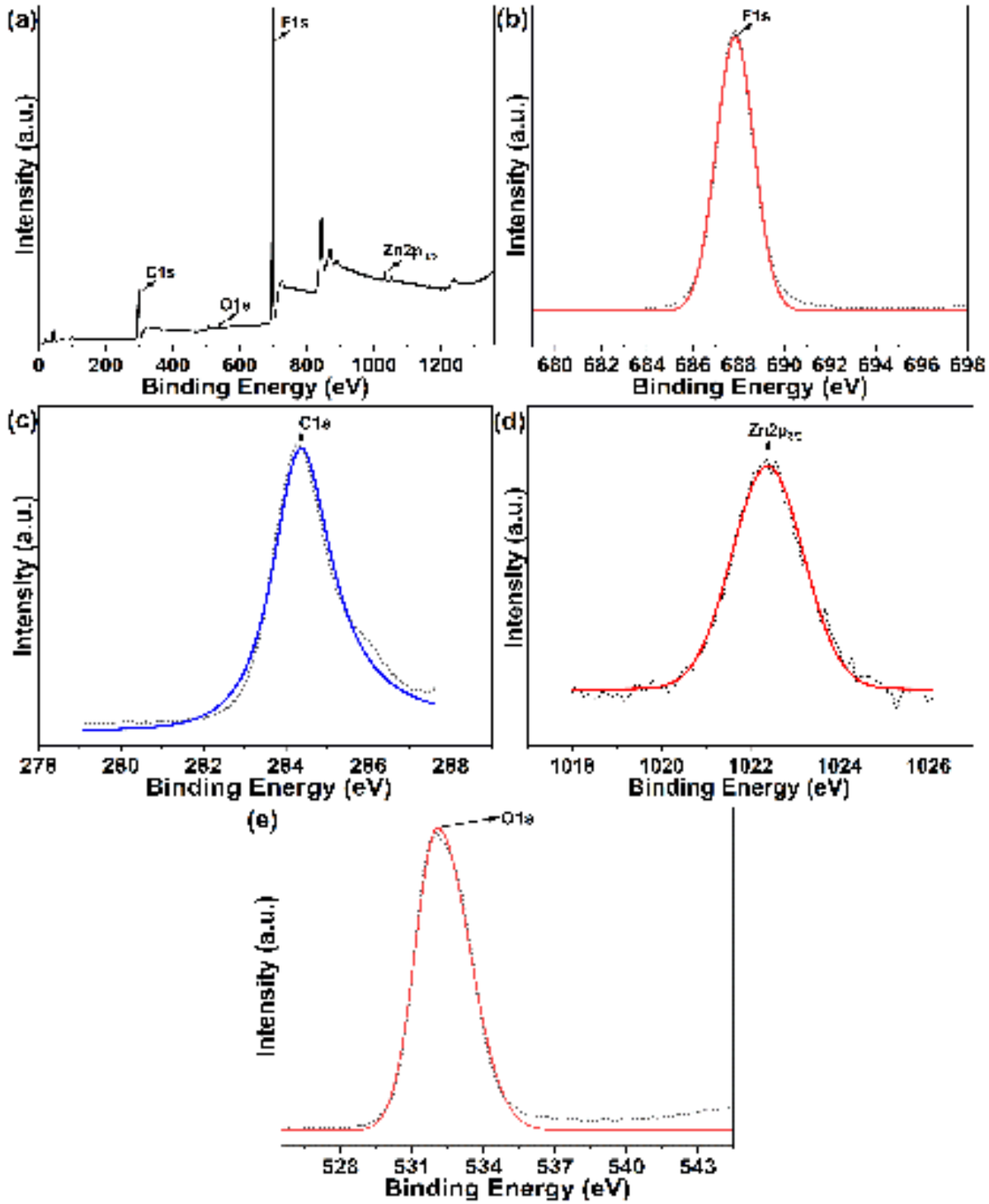

Fig. 4.10: XPS full survey scanning spectra of (a) P(VDF-TrFE)/ZnO nano composite film and high-resolution spectra of (b) F1s, (c) C1s, (d) $Zn2p_{3/2}$, and (e) O1s.

of P(VDF-TrFE)/ZnO nanocomposite film enhance the sensing capability. The piezoelectric output of a composite made of P(VDF-TrFE)/ZnO is greater than that of a pure fiber, which support the BET results. The increase in specific surface area enables the film to convert mechanical energy into more electrical output and increases its sensing ability.

Table 4.5: Specific surface area evaluation for the fabricated nanocomposite film using BET.

Sl. no.	Sample (SA) no.	Specific surface area (m^2/g)
1	SA-8	4.861
2	SA-1	12.261

4.3.8 Rheological Test

The rheological characterization of the P(VDF-TrFE) and P(VDF-TrFE)/ZnO viscous solution with 0 10, and 20% (wt/wt) concentration of ZnO filler is performed as shown in Fig. 4.11. In all polymeric solution sample, linear viscoelastic behaviour is observed with the dispersion of ZnO nanoparticles. The complex viscosity of the prepared homogeneous solution is evaluated. The polymeric solution prepared with 10 wt.% concentration of filler showed higher complex viscosity, storage modulus and loss modulus than any other polymeric solution. Although, the viscous solution prepared with 20 wt.% concentration of ZnO filler with the polymer showed greater storage and loss modulus than pure P(VDF-TrFE) solution. This could be attributed to the strong interaction between the ZnO filler and polymer matrix. Fig. 4.11a presents the decrease in viscosity of the solution with increasing frequency. Addition of filler and frequency increase lead to a significant increase in storage and loss modulus. Though, P(VDF-TrFE)/ZnO-10 wt.% solution showed higher storage and loss modulus than other viscous solution. P(VDF-TrFE) solution containing ZnO nanopowder enhanced moduli probably due to the proper dispersion of nanofiller in polymeric solution, which has lead to significant improvement in the rheological property of the solution.

4.3.9 Dynamic Mechanical Analysis (DMA)

The DMA test is used to evaluate the dynamic moduli of polymer based nanofiber composite film. The storage and loss modulus as functions of temperature are illustrated in Fig. 4.12.

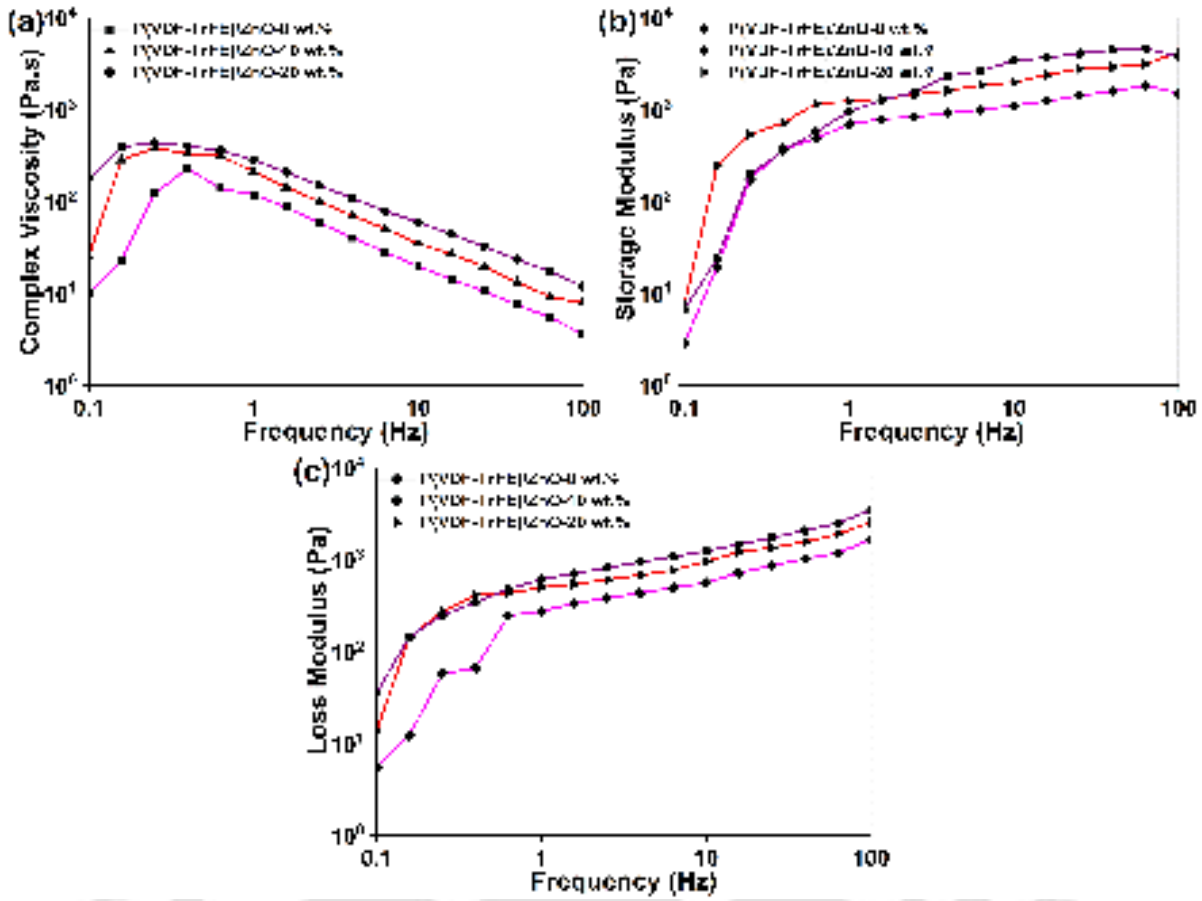

Fig. 4.11: Rheological behaviour of different viscous solution (a) complex viscosity, (b) storage modulus, and (c) loss modulus.

Nanofiller interactions with the polymer matrix in nanocomposites film can be studied with dynamic mechanical analysis [139]. The dynamic mechanical analysis has been done for the fabricated pure P(VDF-TrFE), P(VDF-TrFE)/ZnO-10 wt.% and P(VDF-TrFE)/ZnO-20 wt.% film as shown in Fig. 4.12. The storage and loss modulus decreases with increase in temperature as shown in Fig. 4.12 but not linearly. The storage modulus of the pure P(VDF-TrFE) film is observed less than the other two P(VDF-TrFE)/ZnO nanocomposites samples. The storage modulus increased with the introduction of ZnO nanofiller into the P(VDF-TrFE) film. This increase in storage modulus can be due to the reinforcing effect of ZnO nanofiller in the polymer matrix [140]. The loss modulus of P(VDF-TrFE)/ZnO nanocomposite film is greater than pure P(VDF-TrFE) nanofiber. The loss modulus of the prepared film decreases with the increase in temperature. The storage and loss modulus shows a higher value in the temperature from -80°C to -20°C and then rapidly reduced till 84°C.

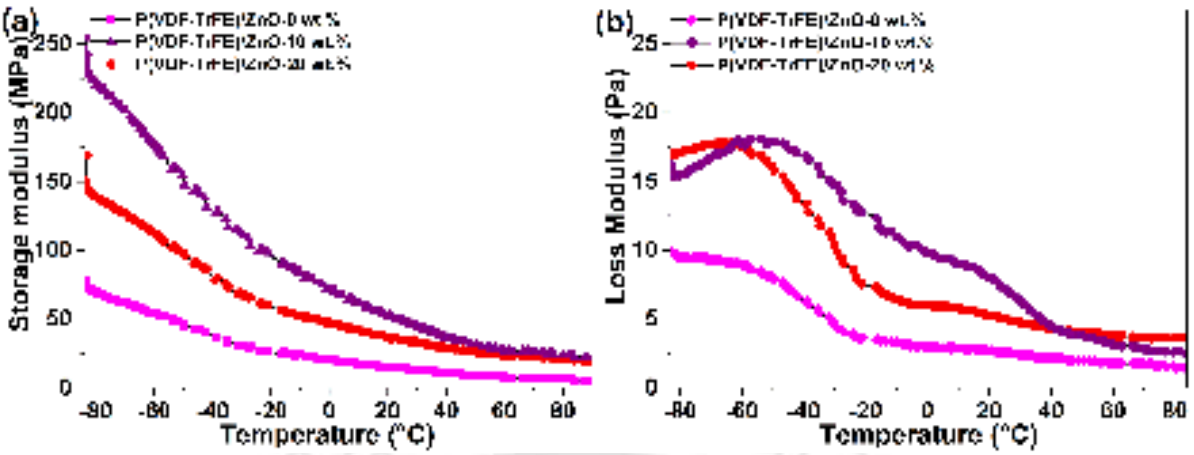

Fig. 4.12: Dynamic mechanical analysis of film for storage modulus and loss modulus versus temperature for a, b neat P(VDF-TrFE) fiber and P(VDF-TrFE) film with different concentrations of ZnO.

4.3.10 Modelling and Optimization

The methodology of model development and identification of an optimal design is presented in Fig. 4.13. BoxBehnken RSM technique is uesd to develop the model, which needs a smaller number of experiments to generate accurate response surfaces compared to normal factorial technique [141]. Here, five center nodes and twelve middle edge nodes points are required to fit the polynomial. Seventeen experiments are carried out to determine the influence of operating parameters (applied

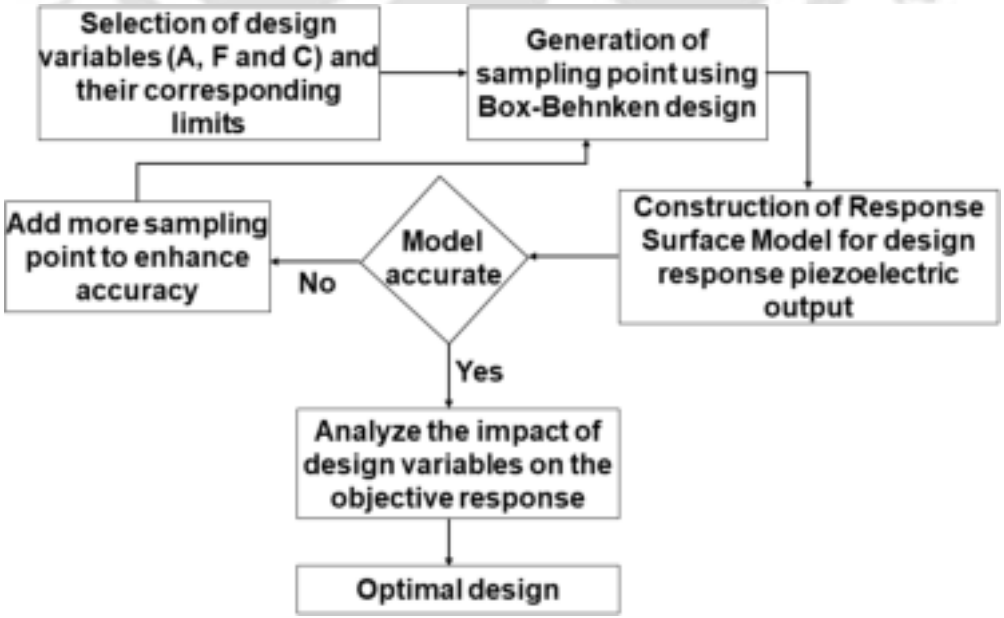

Fig. 4.13: Flow chart for the design optimization.

voltage, flow rate, and ZnO concentration) on piezoelectric output. Analysis of Variance (ANOVA)

study for the piezoelectric output has been discussed with the test for the model to be significant and for the lack of fit to be insignificant. F-value obtained through ANOVA study presents whether the generated model is relevent or not. P-value indicates the confidence level (or $\alpha = 0.05$) of the obtained model. The regression equation describes the correlation between the input parameters and the output parameter. The maximum piezoelectric output of the PENG device is produced after many test, which is discussed in details. The ANOVA study for the piezoelectric output is presented in Table 4.6. The probability (p-value<0.05) is termed significant for the preferred condition of the model. The coefficient of determination (R^2) for the piezoelectric output is 0.9672. This value indicates that the regression equation strongly correlates among the input parameters (i.e., applied voltage, flow rate, and ZnO concentration) with the output parameter (piezoelectric output). The impact of input parameters on the piezoelectric output (P_a) is described by the quadratic model. The quadratic model is presented as below.

$$\begin{aligned} P_a = & -1.15250 + 0.348333A - 0.155312F + 0.231125C \\ & -0.003125AF - 0.000083AC + 0.00075FC - 0.009444A^2 \\ & +0.009531F^2 - 0.010625C^2 \end{aligned} \tag{4.3}$$

Where A, F, and C present voltage, flow rate, and ZnO concentartion, respectively, in Eq. (4.3) presented by the model. The comparasion between the experimental and predicted (determined from the quadratic model as Eq. (4.3)) for the piezoelectric output values for different experiments is shown in Fig. 4.14. The experimental piezoelectric output values is in good agreement with the predicted values (Fig. 4.14) with minimal variation. The coefficient of determination (R^2) value for the developed quadratic model obtained using the regression equation is used to confirm the trial, provide 96.72% accuracy. After the ANOVA, an optimization study to maximize the piezoelectric output (keeping the operating parameters in the range) is conducted to obtain the optimum condition of operating parameters. The optimized operating parameters are 16 kV voltage, 16 µl/min, and 10 wt.% concentration of ZnO, predicting 2.53 V piezoelectric output. Three experiments are carried out to validate the ANOVA model; Exp. II: at optimum condition, Exps. I and III: parameters are randomly chosen within the range (Table 4.1). The experimental piezoelectric output

Table 4.6: ANOVA for piezoelectric output.

Source	Sum of Squares	DOF	Mean Square	F-value	p-value	% contribution
Model	5.64	9	0.6262	33.39	<0.0001	
A-voltage	0.0512	1	0.0512	2.73	0.1425**	0.91
F-flow rate	0.1485	1	0.1485	7.92	0.0260*	2.63
C-ZnO	0.5565	1	0.5565	29.68	0.0010*	9.86
AF	0.0056	1	0.0056	0.2999	0.6009**	0.10
AC	0.0000	1	0.0000	0.0013	0.9719**	0.0004
FC	0.0036	1	0.0036	0.1920	0.6745**	0.06
A^2	0.0304	1	0.0304	1.62	0.2435**	0.54
F^2	0.0979	1	0.0979	5.22	0.0562**	1.73
C^2	4.75	1	4.75	253.46	<0.0001*	84.17
Residual	0.1313	7	0.0188			
Lack of Fit	0.0595	3	0.0198	1.10	0.4449**	

Note: * Significant (p-value <.05), ** Not Significant (p-value >.05), $R^2 = 0.9672$.

values are compared with predicted results (calculated from the regression Eq. (4.3)), as presented in Table 4.7. Based on the three validation tests, an error of 8.28% (maximum) is observed, suggesting

Table 4.7: Validation tests comparing predicted and experimental piezoelectric output values.

	Input parameters			Response		
	Voltage (kV)	Flow rate (µl/min)	ZnO (wt.%)	Predicted P_a (V)	Experimental P_a (V)	Error %
EXP I	14	10	7	1.98	2.11	6.56
EXP II	16	16	9	2.39	2.55	6.85
EXP III	16	13	3	1.57	1.70	8.28

that the proposed ANOVA model is feasible. The percentage contribution of each input parameters (linear and non-linear) on piezoelectric output with the individual and combined parameters is shown in Fig. 4.15. The combined influence of voltage (A and A^2) on piezoelectric output is 1.45%

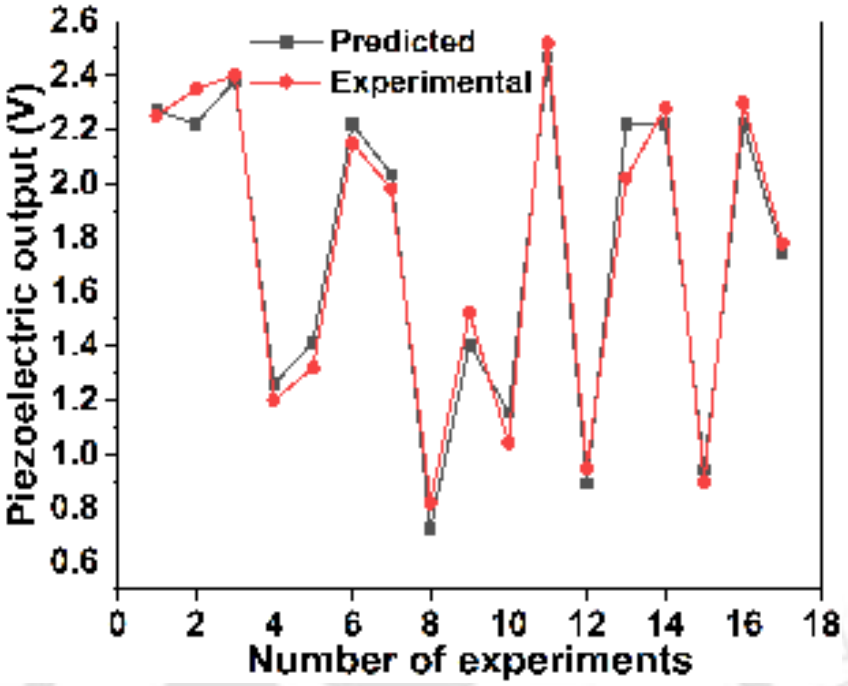

Fig. 4.14: Variation between predicted and experimental piezoelectric output values for the different experiments.

(Fig. 4.15). The impact of change in voltage, while keeping other parameters constant, is shown in

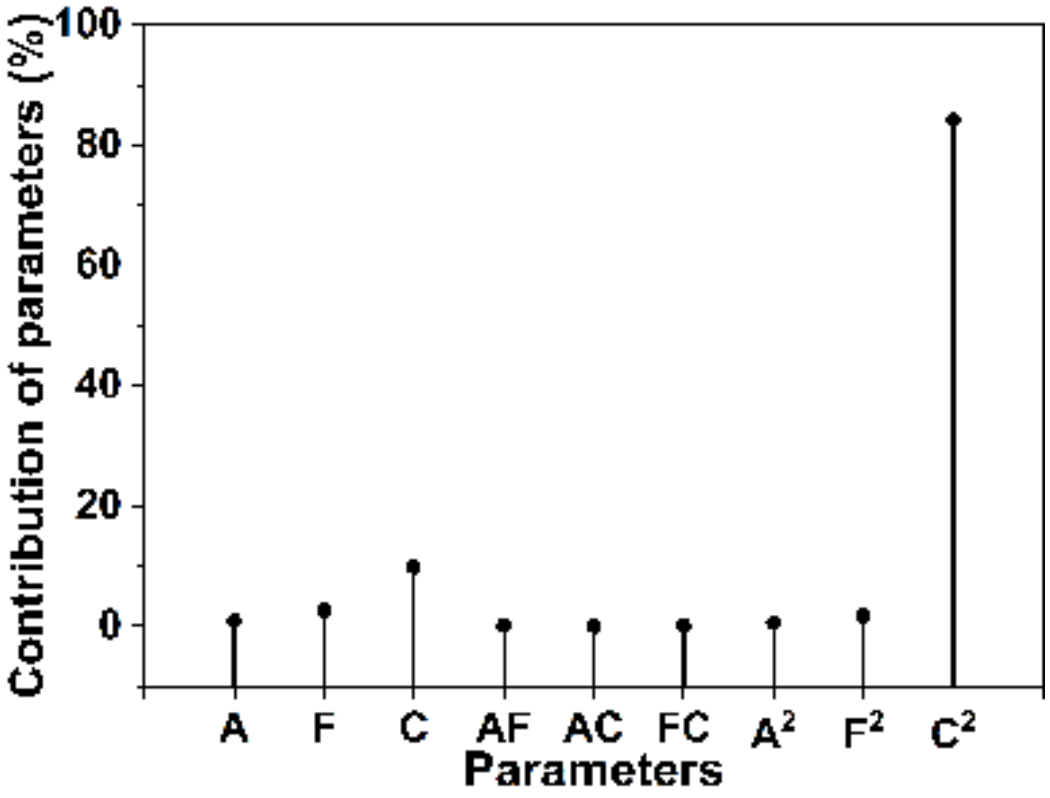

Fig. 4.15: Percentage contribution of operating parameters on piezoelectric output.

Fig. 4.16a. In response to an increase in applied voltage, electrospun mats produce more piezoelectric output. The possible reason may be the polarization of the fiber membranes with the higher applied voltage. The combined contribution of flow rate (F, F^2) on the piezoelectric output is 4.36% (Fig. 4.15). The impact of change in flow rate, while keeping other parameters constant, is shown in Fig. 4.16b. An increase in flow rate leads to an increase in piezoelectric performances. The increase in piezoelectric performance may be due to thicker nanocomposite mat. The combined impact of ZnO concentration (C and C^2) on piezoelectric output is 94.03% (Fig. 4.15). The influence of change in ZnO concentration, while keeping other parameters constant, is shown in Fig. 4.16c. As the ZnO

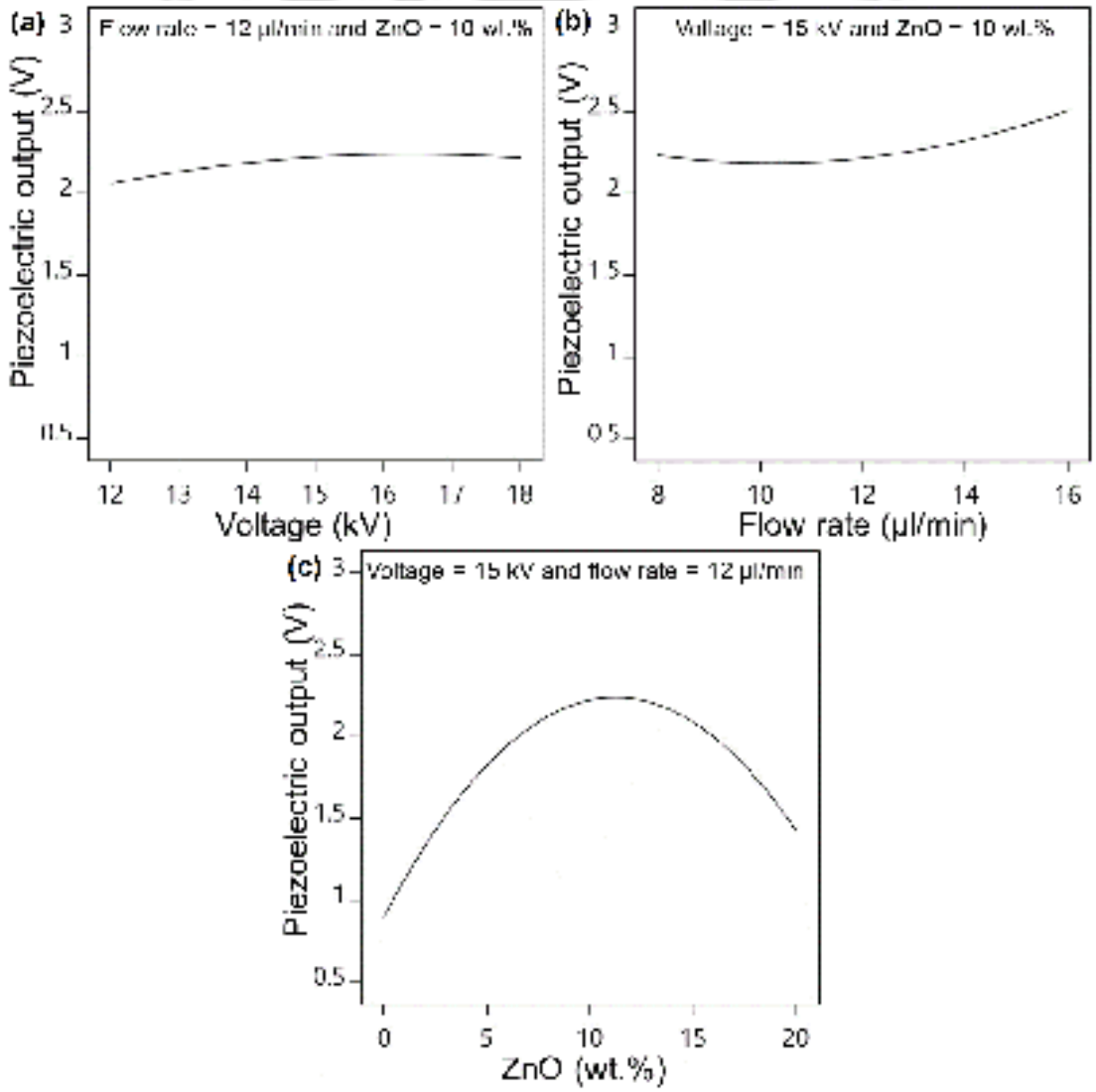

Fig. 4.16: Effect of electrospinning parameters (a) voltage, (b) flow rate, and (c) ZnO concentration on piezoelectric output.

concentration increases from 0 to 10 wt.%, spun mats show more piezoelectric performance, while

piezoelectric output reduces, when ZnO concentration increases from 10 to 20 wt.%. The possible reason behind the decrease in piezoelectric performance is the weak interaction between the ZnO nanoparticles and P(VDF-TrFE) and decrease in electroactive β phase. The combined influence of flow rate and voltage on the PENG device for the piezoelectric output, keeping ZnO concentration constant at 10 wt.% is shown in Fig. 4.17a. Increasing the flow rate from 8 to 16 µl/min and in-

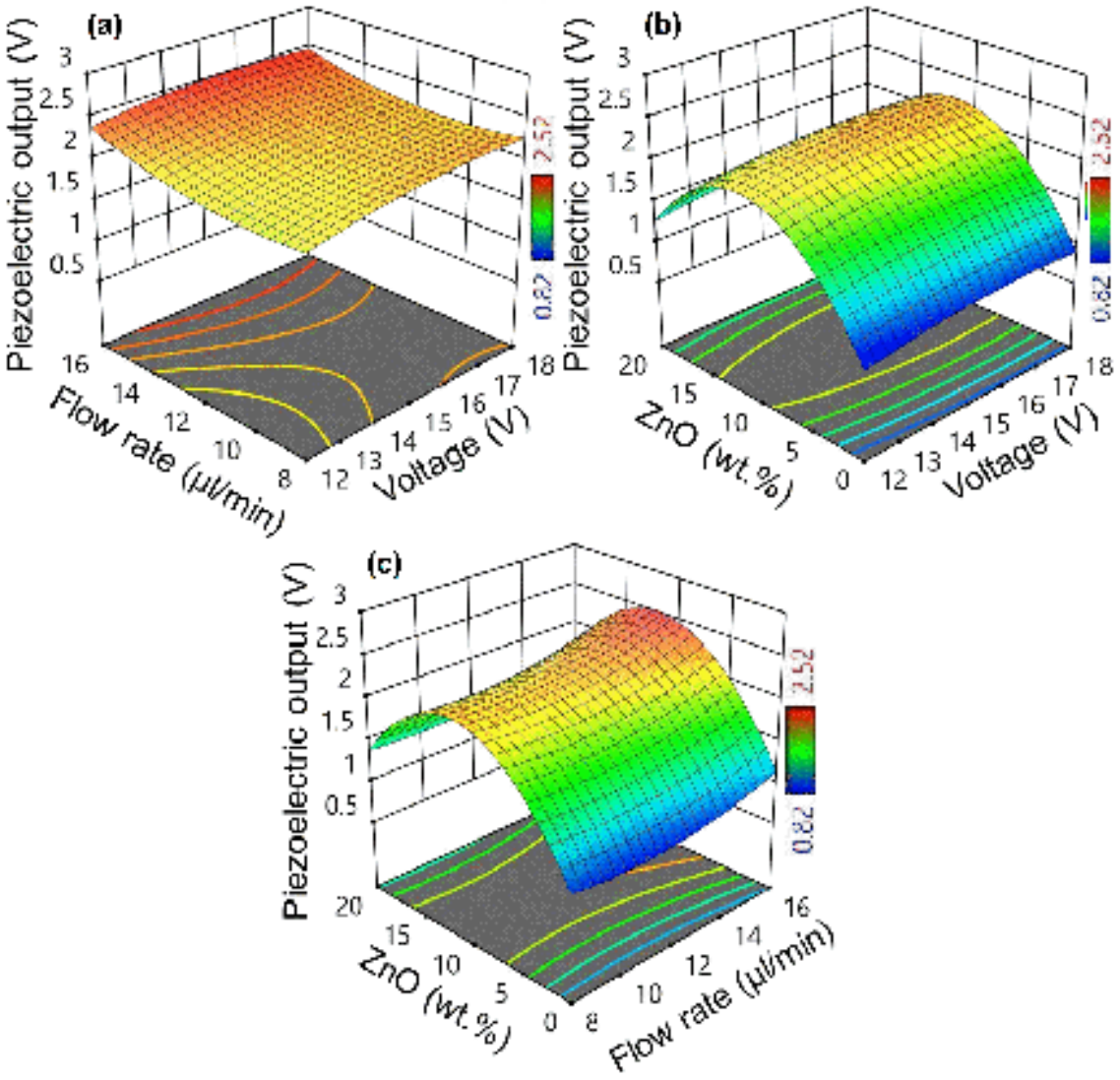

Fig. 4.17: 3D plots showing combined effect of (a) flow rate and voltage, (b) ZnO (wt.%) and voltage, and (c) ZnO (wt.%) and flow rate on piezoelectric output.

creasing the voltage up to around 17 kV, the piezoelectric output increases and attains a maximum value. Although, with further increasing the applied voltage, piezoelectric output decreases even at higher flow rate, and comparatively slower decrease in piezoelectric performance is observed at higher applied voltage. The combined impact of ZnO (wt.%) and voltage on the PENG device

for the piezoelectric output, keeping flow rate constant at 12 μl/min is shown in Fig. 4.17b. The piezoelectric output of the PENG device increases with increase in ZnO concentration and applied voltage and attains a maximum value for a ZnO concentration at 10 wt.% and voltage around 17 kV. Although, the piezoelectric output decreases slowly with applied voltage when ZnO concentration exceeds 10 wt.%. The combined impact of ZnO (wt.%) and flow rate on the PENG device for the piezoelectric output, keeping applied voltage constant at 15 KV is illustrated in Fig. 4.17c. The lowest piezoelectric output is observed at ZnO (0 wt.%) and flow rate (8 μl/min). The PENG output increases with the flow rate and ZnO concentration till 10 wt.% and then output decreases with a slow rate after the 10 wt.% of ZnO. It can be concluded that the design parameters, voltage (A), flow rate (F), and ZnO concentration (C) significantly affect the piezoelectric output (P_a) of the PENG device and the dependency of P_a on the ZnO (wt.%) and flow rate (F) is found to be quadratic while for the voltage (A), the relationship is almost linear.

4.3.11 Optimal Design Parameters for Higher Piezoelectric Output of the Nanocomposite Mats

After realizing the tunable piezoelectric properties of synthesized nanocomposite mats, an optimal combination of design parameters for achieving higher piezoelectric performance is investigated in this section. Therefore, a single-objective optimization approach is incorporated and the resulting optimization problem can be formulated as:

$$\text{Maximize piezoelectric output} \quad (P_a) = f(A, F, C) \tag{4.4}$$

$$\text{subject to} \quad 12 \leq A \leq 18 \tag{4.5}$$

$$8 \leq F \leq 16 \tag{4.6}$$

$$0 \leq C \leq 20 \tag{4.7}$$

To achieve optimization, each response has a low and high value, as represented by above objective function and constraints and the desirability approach is used to solve it. Fig. 4.18 (a-c) presents the desirability plot of the optimum solution considering the three design variables as parameters. The optimal solution appears to lie close to the highest value of A and F and close to the middle value of C. Table 4.8 shows the optimal solution predicted by the model with the higher desirability

(0.95). In order to compare the performance of the optimal modified nanocomposite film, the final

Table 4.8: Experimental validation of the RSM model at optimized parameter conditions.

Electrospinning parameters		Piezoelectric output		Error (%)
Input parameters	Value	predicted value	Experimental value	
Applied voltage	18			
Flow rate	16	2.78	2.62	6.1
ZnO concentration	9			

design is electrospun and tested as described in Table 4.8. The nanocomposite film fabricated with the same process parameter is considered for benchmarking.

4.3.12 Effect of ZnO Nanofiller on Piezoelectric Output of P(VDF-TrFE) Fiber and its Composite

The voltage and current output of the piezoelectric nanogenerators (PENG) under the direct piezoelectric effect are shown in Fig. 4.19. The peak to peak voltage under different conditions are tabulated in Table 4.9. Five PENG's are taken for further analysis, which is having higher fraction

Table 4.9: Peak to peak voltage measured of P(VDF-TrFE) and P(VDF-TrFE)/ZnO at different condition.

Sample no.	Softly bending	Softly tapping	PENG
SA-8	440 mV	1.04 V	1
SA-11	560 mV	2.52 V	2
SA-3	540 mV	2.40 V	3
SA-16	480 mV	2.30 V	4
SA-17	500 mV	1.78 V	5

of beta phase. Pure P(VDF-TrFE) film gives 440 mV and 1.04 V after subjected to bending and tapping load through human hand. These load is allowed to subjected on the PENG device for the energy scavenging applications. The nanogenerators are subjected to tapping and bending softly. The sample fabricated with 10 wt.% concentration of ZnO gives more electrical output than others

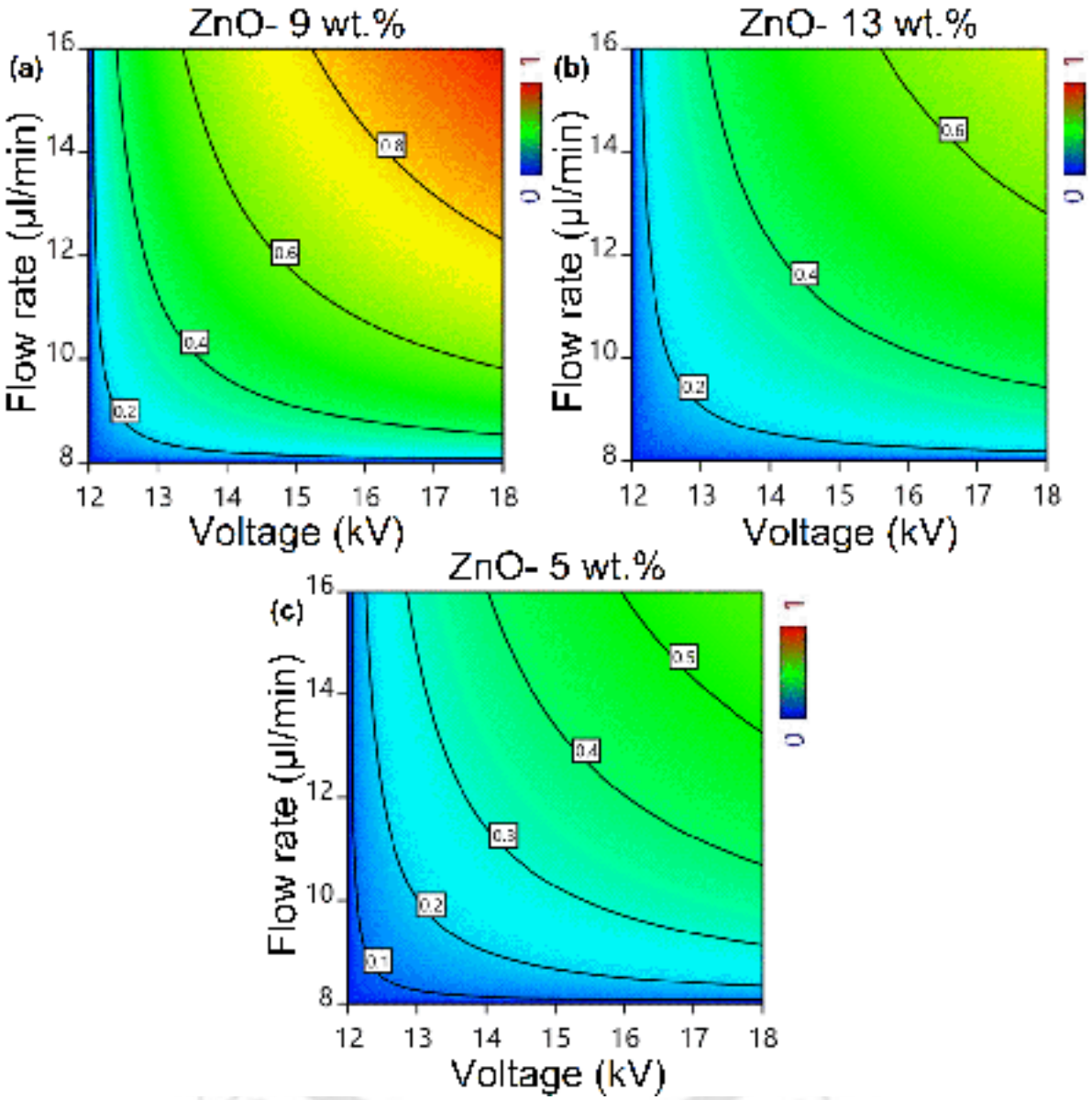

Fig. 4.18: : Desirability plot of the optimum solution (a) effect of voltage and flow rate at ZnO- 9 wt.%, (b) effect of voltage and flow rate at ZnO- 13 wt.%, and (c) effect of voltage and flow rate at ZnO- 5 wt.%.

due to having more electroactive beta phase content. The higher voltage is obtained from all the PENG under tapping condition. The reason might be that tapping has more load experience than bending. The current for P(VDF-TrFE) nanofiber (SA-8) and P(VDF-TrFE)/ZnO-10 wt.% (SA-11) are measured 12.8 µA and 20.8 µA Fig. 4.18 (c,d) when the external load is applied of 1000 ohm (Ω) with the electrical circuit.

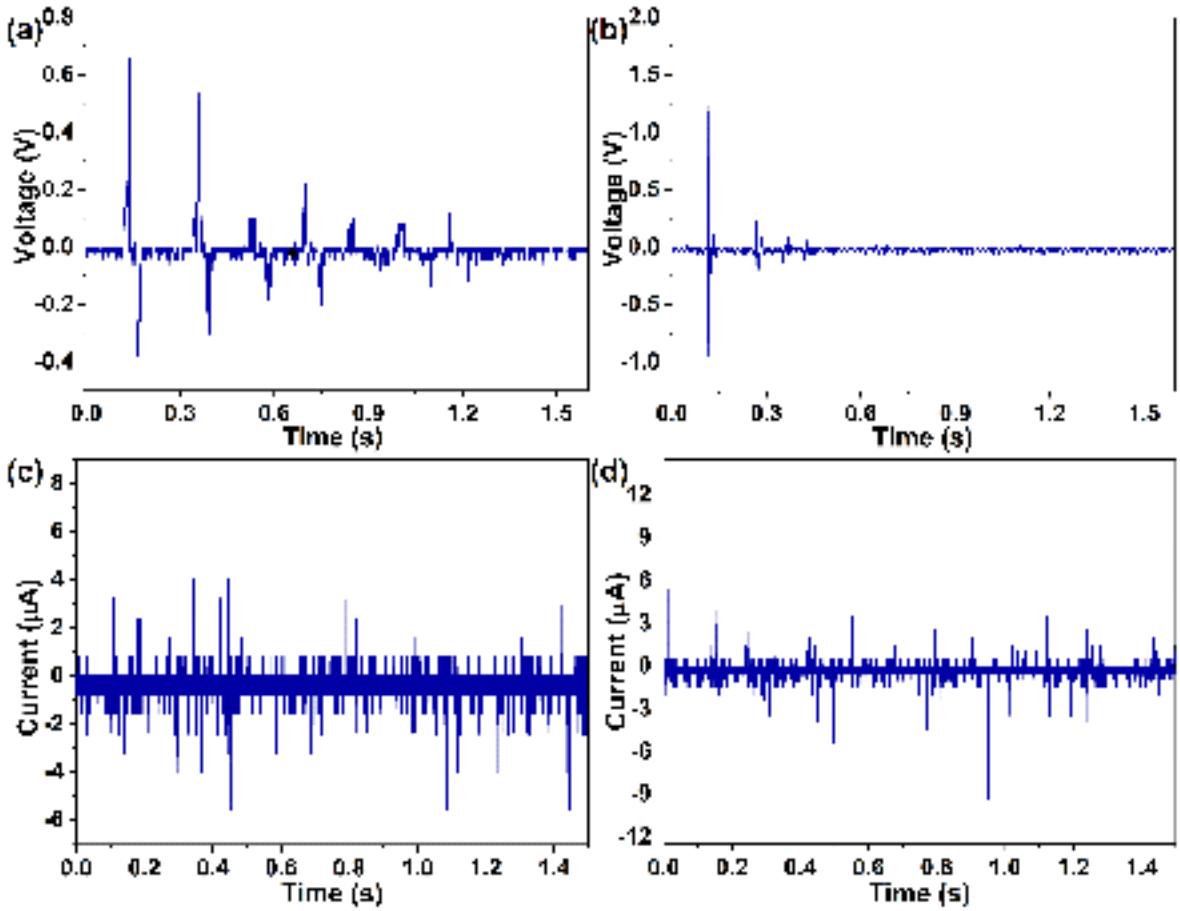

Fig. 4.19: Voltage output of (a) SA-8, (b) SA-11 and current output of (c) SA-8, (d) SA-11 generated by PENG device under tapping load condition.

4.4 SUMMARY

A set of electrospun mats made of P(VDF-TrFE) with ZnO nanopowder are fabricated using the far-field electrospinning technique. The effect of voltage, flow rate and weight percentage of ZnO nanopowder on the electrospun fibers are investigated in detail. The operating parameters of electrospinning process has been optimized using statistical design of experiments. The ANOVA model is validated at optimized process parameter conditions. It has been observed that the fraction of beta phase is enhanced at 10% of nanopowder. However, stress and strain are decreased with the addition of nanofiller. The specific surface area, rheological properties and dynamic modulus are significantly enhanced with the ZnO nanofiller. The Piezoelectric nanogenerator (PENG) based on P(VDF-TrFE)/ZnO nanocomposite showed higher electrical output than the pristine P(VDF-TrFE) nanofiber. The electrical voltage and current are measured with a higher value

under finger tapping condition. This PENG device capable of energy harvesting with enhanced piezoelectric output may give simple, cost-effective, useful, and flexible access to the self-powering of microelectronics devices for many applications. This study has led to the following inferences:

(i) The results reveal that the nanofiber composite is formed defect-free at specific electrospinning conditions.

(ii) The β crystalline phase, specific surface area, rheological properties and dynamic modulus are significantly improved after the addition of nanofiller.

(iii) It has been observed that voltage output increased with the increment of ZnO weight percentage up to 10 and then decreases.

(iv) The ANOVA study of basic electrospinning process parameters reveal that all three parameters, namely voltage, flow rate, and ZnO concentration are having percentage contributions of 1.45%, 4.36%, and 94.03%, respectively, on piezoelectric output.

(v) The optimized parameters that provide the best piezoelectric effect are 18 kV aplied voltage, 16 µl/min, and 9 wt.% of ZnO, which offers the best piezoelectric output of 2.62 V.

(vi) A maximum error of 8.28% is observed between predicted (calculated from regression equation) and experimental piezoelectric output values, which confirm the effectiveness of the DOE model.

(vii) The piezoelectric voltage and current of the piezoelectric nanogenerator device based on fiber composite is found 2.52 V and 20.8 µA whereas 1.04 V and 12.8 µA for the pristine P(VDF-TrFE) nanofiber under finger tapping conditions.

(viii) Under finger tapping load condition, the piezoelectric performance of the PENG is superior to that of bending.

Chapter 5

Electrospun functionally graded PVDF/$BaTiO_3$ based nanogenerators

5.1 INTRODUCTION

In this chapter, flexible piezoelectric functionally graded PVDF/$BaTiO_3$ electrospun film based device has been fabricated for enrgy harvesting applications. Electrospun films have gained widespread attention due to their ability to convert mechanical energy into electrical energy. Pure PVDF has low output while single film based nanogenerators with high concentration of $BaTiO_3$ gives good output but brittle and further issue of agglomeration become more dominant. Therefore, electrospun functionally graded films are synthesized using the electrospinning method to design the nanogenerator device. The material selection, fabrication of pure PVDF fiber, PVDF/$BaTiO_3$ composite, functionally graded PVDF/$BaTiO_3$ structures, nanogenerator device, and characterization through various instruments have been presented in Sec. 5.2. Electrospun functionally graded film has concentration of $BaTiO_3$ increases from bottom to top layer. The bottom most layer is pure PVDF while topmost contains 8 wt.% of $BaTiO_3$. Four types of functionally graded samples are prepared comprising of two to five layers of PVDF polymer and $BaTiO_3$ ceramic. The detail discussion of electrospun fiber mats and functionally graded films are presented in Sec. 5.3. It includes morphological study, elemental analysis, crystalline phase identification, β phase variation, optical, and mechanical properties. These studies have been accomplished using the different instruments. Further, the piezoelectric performance of nanocomposite mats and functionally graded film based nanogenerator device have been presented. The voltage output of nanogenerators have been measured using digital storage oscilloscope under different loading conditions at room tem-

perature. A systematic and detailed analysis has been carried out to assess the influence of $BaTiO_3$ nanoparticle and number of layers on the piezoelectric performance. The various manual activities, including palm tapping, wrist tapping, and elbow hitting are subjected to extract the energy from the PENG device. The PENG with external load 1 MΩ resistor generated peak to peak voltage of 8.22 V, current of 3.36 A and instantaneous power of 0.14 mW/cm^2. Compared to monolayer films, functionally graded films exhibit greater piezoelectric performance as the number of nanofiber layers increases. The piezoelectric output of PENGs device is validated using Comsol Multiphysics software, which has been presented in Sec. 5.3. This work offers an excellent alternative to powering small electronic devices from simple daily activities by developing functionally graded film-based nanogenerators.

5.2 EXPERIMENTAL

5.2.1 Materials

PVDF polymer and ceramic $BaTiO_3$ powder are procured from Sigma-Aldrich manufacturer. The molecular weight (M_w) of piezoelectric polymer and ceramic powder is 534,000 and 233.19 g/mol. The average particle size of $BaTiO_3$ nanopowder is 100 nm provided by the supplier. Sigma-Aldrich supplied DMF (N, N Dimethylformamide) with anhydrous 98% molecular weight (73.09 g/mol) has been used as solvent. All the base materials (PVDF and $BaTiO_3$) are used without any processing.

5.2.2 Fabrication of Functionally Graded PVDF/$BaTiO_3$ Film Structure

Electrospinning operation is performed with the electrospinning setup provided by E-spin Nanotech (Model- SUPER ES-2, India). Functionally graded PVDF/$BaTiO_3$ film structure and nanofiber composite are manufactured using the E-spin unit. Firstly, neat PVDF solution is prepared by the dispersion of polymer pellet with the concentration of 20% (wt./vol.) into DMF solvent and then placed on the magnetic stirrer at 55°C and 500 rpm for 6 h. As a result, the homogeneous solution is obtained. The PVDF solution is first obtained, and then $BaTiO_3$ nanopowder has been dispersed in them. Here, PVDF pellets are collected with concentrations of 18, 16, 14 and 12% (wt./vol.) and $BaTiO_3$ nanopowder with concentrations of 2, 4, 6 and 8 wt.%. Therefore, four type of solutions

are prepared having varying concentration. Again, these solutions are placed on stirrer and further sonicated for 2 h to avoid the bubbles. Finally, homogeneous solution is obtained to fabricate the electrospun film. Total nine samples have been synthesized, including pure PVDF fiber, four functionally graded films and four nanofiber composites. Electrospun functionally graded films are made by depositing the fiber layer in thickness direction with different electrospinning conditions. The electrospinning conditions have been applied as follows: the flight distance is 14 cm, applied voltage is 14-16 kV, drum collector speed is 2000 rpm, ejection rate is 16 μl/min and film deposition time has been set for 70 minutes for all fabricated fibrous membranes.

5.2.3 Fabrication of PVDF/$BaTiO_3$ Based Piezoelectric Nanogenerator

The schematic diagram and actual photo of the piezoelectric nanogenerators (PENGs) as energy harvesting device is shown in Fig. 5.1. The PENG device is like a sandwich structure to be used

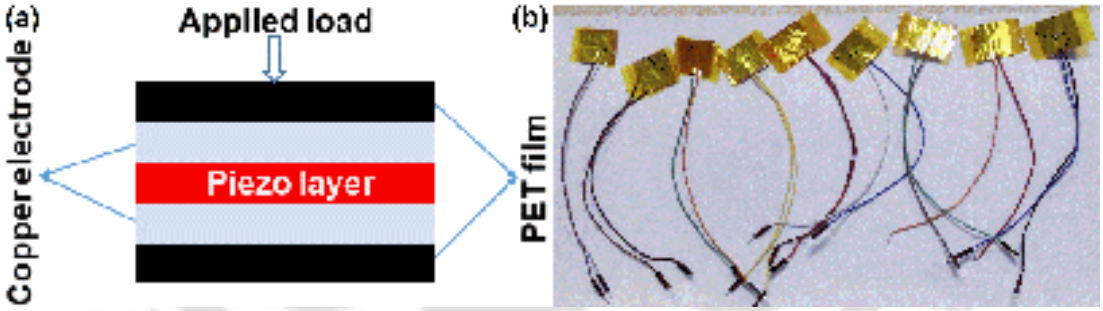

Fig. 5.1: Schematic diagram of (a) PVDF/$BaTiO_3$ film-based PENGs and (b) actual photo of PENGs.

for energy scavenging applications. The PENG device is comprised of mainly three-layer, which include an active piezo layer, electrodes and PET film. The electrically conductive two jumper wires are attached to both electrodes (top and bottom) using silver paste. The whole device is encapsulated with PET film to ensure unaffected from the external disturbance. As a final step, piezoelectric output has been measured after applying external load such as palm tapping, wrist tapping, and elbow hitting to the PENGs device.

5.2.4 Characterization and Measurement

The surface morphology of electrospun PVDF fiber, PVDF/$BaTiO_3$ based nanocomposite and functionally graded film has been characterized through field emission scanning electron microscope

(FESEM, maker: Zeiss, model: Gemini 300). This test has been carried out with accelerating voltage 6 kV and magnification 6 kX. Digital micrometer (Mitutoyo 293-240-30 micrometer) is used to measure the average thickness of fabricated samples. The presence of elements in the synthesized electrospun PVDF/$BaTiO_3$ films are characterized by energy dispersive X-ray (EDX) spectrometer (maker: Zeiss, model: Gemini SEM 500). The XRD test (X-ray diffraction) (Maker: Rigaku Technologies, Japan, model: Smartlab) has been performed for the PVDF/$BaTiO_3$ based film to obtain the crystalline structure on a diffractometer using Cu-Kα radiation 1.54 $\mathring{A}$. The samples are tested in 2θ range from 10° to 70°. FTIR (Fourier Transform Infrared) spectra of PVDF/$BaTiO_3$ nanofiber composite and functionally graded films is recorded by a spectrometer (Maker: PerkinElmer, Singapore, model: Spectrum two) in attenuated total reflection (ATR) mode over the wavenumber range of 600-2000 cm^{-1}. The crystallinity is calculated using differential scanning calorimetry (DSC) (Maker: Netzsch, model: STA449F3A00) test, which has been studied in an argon atmosphere. The test has been carried out by heating the samples from 30°C to 200°C with 10°C/min rate. The electrospun films are tested for mechanical properties using the tensile mode of 5kN Electromechanical universal testing instrument (Maker: ZwickRoell, model: Z005TN Proline) with 7 mm/min strain rate. The optical properties has been characterized using ultraviolet visible absorption spectroscopy (UVvis) (PerkinElmer Lambda 950) over the range of 200-800 nm wavelength. Digital oscilloscope (GDS-1102U-Gwin Instek Co.) has been incorporated to record the current and voltage of (PENG) with a functional area of 5 cm^2. The PENG devices are tested under external loading conditions such as wrist tapping, palm tapping and elbow hitting.

5.3 RESULTS AND DISCSSION

5.3.1 Morphological Study of Functionally Graded PVDF/$BaTiO_3$ Film

The surface morphology of electrospun functionally graded PVDF/$BaTiO_3$ structure, PVDF nanofiber and PVDF/$BaTiO_3$ nanofiber composite has been analysed by FESEM operated at voltage 6 kV and magnification 6 kX. Produced samples have been gold coated using sputter coating before scanning. The schematic diagram of electrospun functionally graded film structure containing various layer is depicted in Fig. 5.2. The samples are marked as:

1. FG-1: Functionally graded PVDF/$BaTiO_3$ film (FG-1) is comprised of two layers; one is a PVDF nanofiber film, and the other is a PVDF/$BaTiO_3$ nanocomposite film.

2. FG-2: Three layers; one layer is PVDF nanofiber, second and third layers are PVDF/$BaTiO_3$ nanocomposite.

3. FG-3: Four layer; one layer is PVDF nanofiber, second, third, and fourth layers are PVDF/$BaTiO_3$ nanocomposite.

4. FG-4: Five layer; first layer is PVDF nanofiber, second, third, fourth, and fifth layers are PVDF/$BaTiO_3$ nanocomposite. The nanocomposite film fabricated with PVDF (18%)/BTO (2%), PVDF (16%)/BTO (4%), PVDF (14%)/BTO (6%), PVDF (12%)/BTO (8%) are designated as SA-6, SA-7, SA-8, and SA-9.

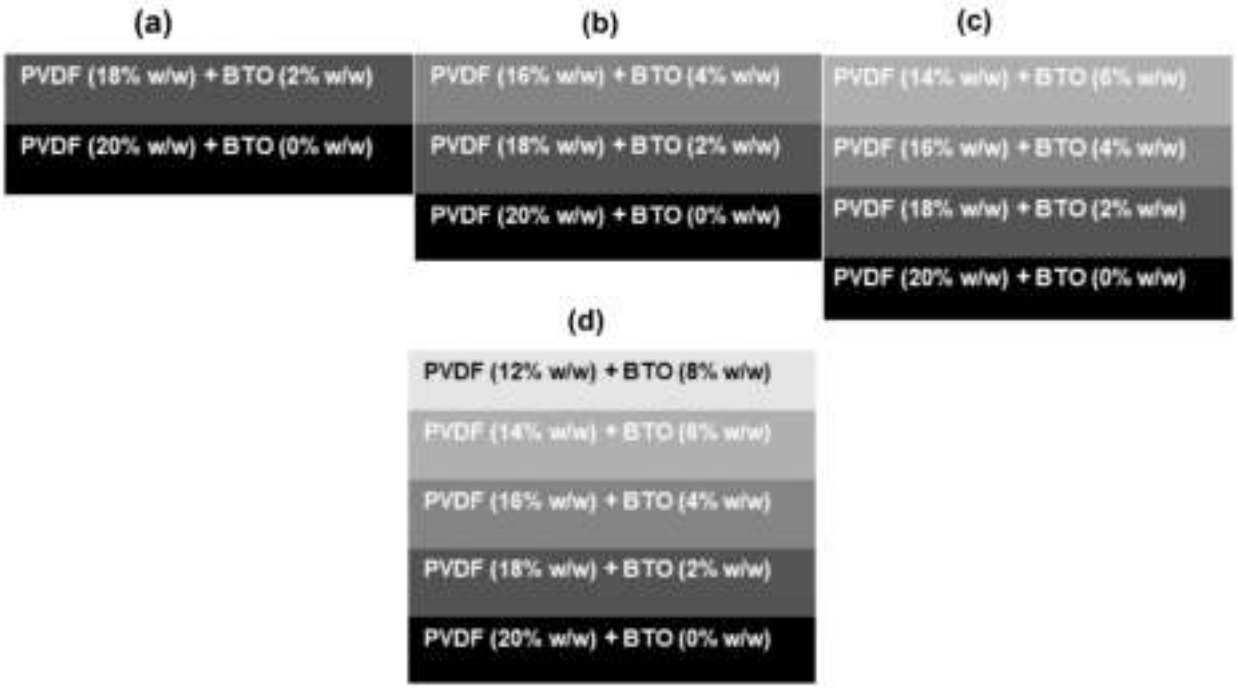

Fig. 5.2: Schematic diagram of electrospun functionally graded PVDF/$BaTiO_3$ film structure (a) FG-1, (b) FG-2, (c) FG-3, and (d) FG-4.

The gradient has been maintained by changing the concentration of matrix and reinforcement filler, which is shown in Fig. 5.2. The gradation of the electrospun film has been carried out in thickness direction in order to deposition of one layer over another layer. All the samples are successfully fabricated as can be seen through FESEM images (Fig. 5.3). However, the last

nanofiber composite is having lower thickness than other samples. This is due to reduction in solution viscosity. Fig. 5.3 represents the surface image of the fabricated sample and indicate that $BaTiO_3$ nanofiller is uniformly dispersed in the PVDF solution. The surface morphology of PVDF nanofiber and functionally graded film is presented in Fig. 5.3a and Fig. 5.3 (b-e). The surface morphology of nanocomposite membranes is shown in Fig. 5.3 (f-i). The nanocomposite film with hardly a defect or void is visible over the image, illustrating the compactness of nanocomposite.

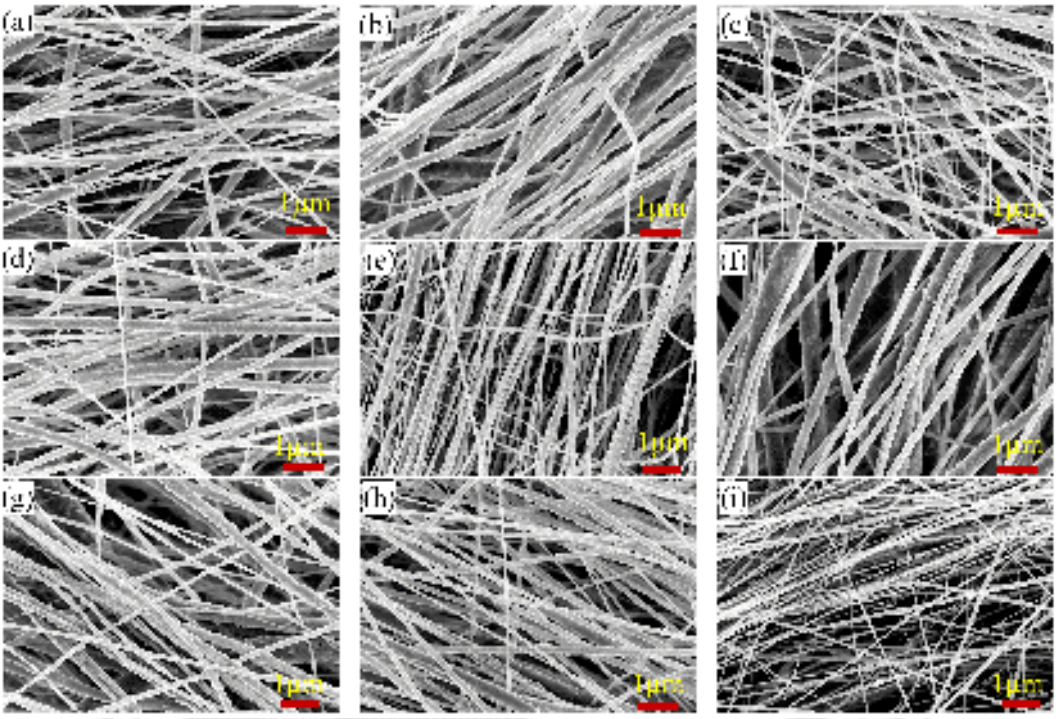

Fig. 5.3: FESEM image of (a) PVDF nanofiber (b, c, d, e) functionally graded PVDF/$BaTiO_3$ film (FG-1 to FG-4) and nanocomposite with different loading condition (f) PVDF-18% w/v, BTO- 2 wt.%, (g) PVDF-16% w/v, BTO- 4 wt.%, (h) PVDF-14% w/v, BTO- 6 wt.% (i) PVDF-12% w/v, BTO- 8 wt.%.

5.3.2 EDX Analysis

The element composition analysis of the PVDF/$BaTiO_3$ based functionally graded film structures and nanofiber composite have been characterized using energy dispersive X-Ray (EDX). This test affirmed the existence of Barium (Ba), Titanium (Ti), Carbon (C), Fluorine (F), and Oxygen (O) elements in the synthesized film and corresponding spectrum are recorded as presented in Fig. 5.4. The C, O and F elements are associated with the characteristics elements of PVDF polymer, while Ba and Ti elements are related to the composition of $BaTiO_3$ ceramic powder. The peaks are

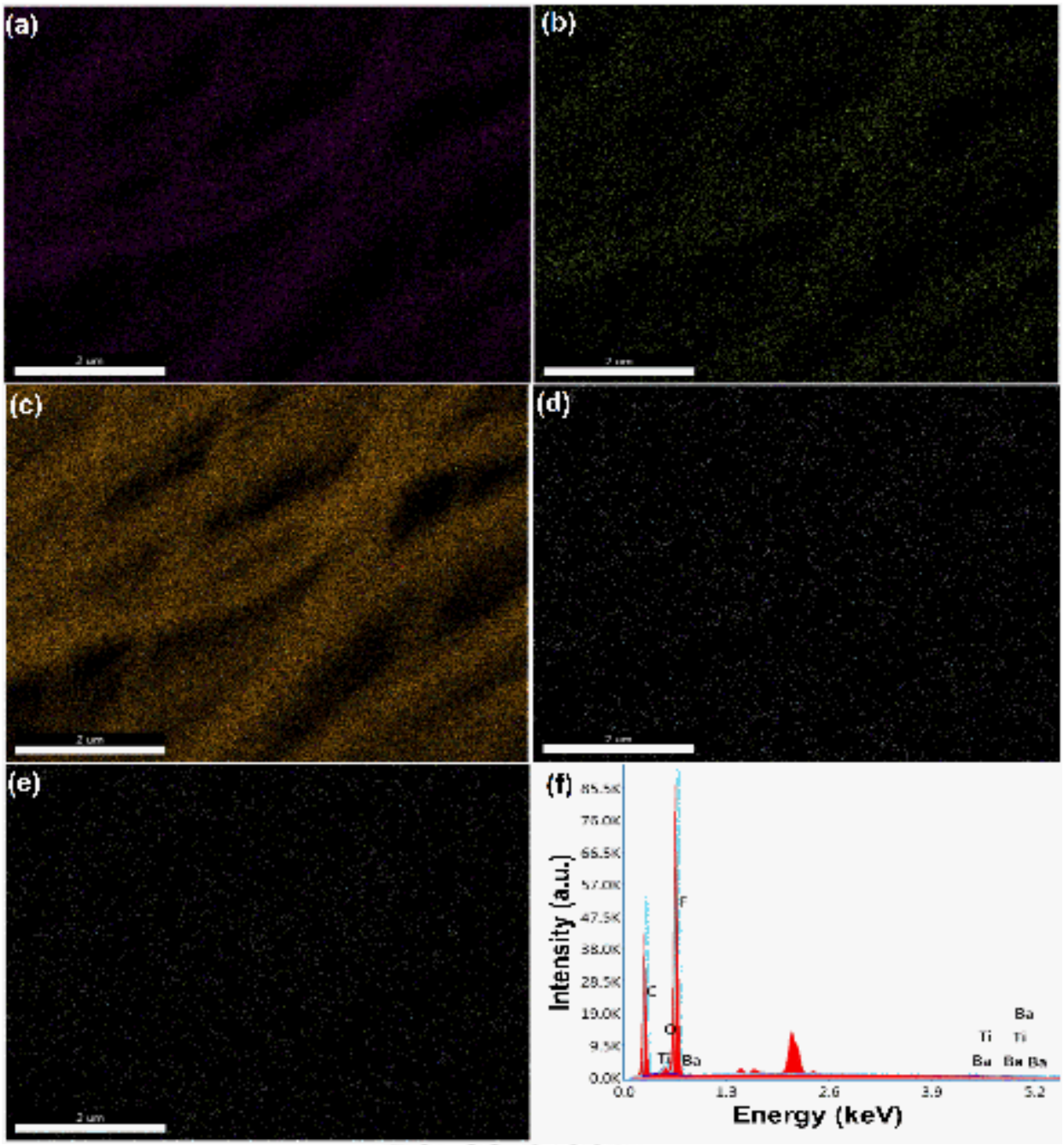

Fig. 5.4: Elemental mapping image of PVDF/$BaTiO_3$ electrospun structure: (a) C, (b) O, (c) F, (d) Ba, (e) Ti atom, and (f) EDX spectra of the electrospun functionally graded film (FG-2).

observed for the elements Carbon, Oxygen, and Fluorine at their standard energy levels 0.277 keV, 0.525 keV and 0.677 keV, respectively. As a result of the addition of $BaTiO_3$ nanoparticles in PVDF fiber membranes, more peaks are found at energy levels 0.972 KeV, 4.465 keV and 0.452, 4.5 keV, which is related to the Ba and Ti elements. All elements are uniformly dispersed in the fabricated functionally graded structures and nanocomposite film, as observed from the element

mapping (Fig. 5.4). The element distribution is studied in atomic and weight percent shown in Table 5.1.

Table 5.1: Semi quantitative EDX analysis of PVDF/$BaTiO_3$ film.

Elements	Atomic(%)	Weight(%)
CK	59.29	47.85
OK	2.71	2.92
FK	37.90	48.38
BaK	0.09	0.83
TiK	0.01	0.03

5.3.3 Crystalline Phase Identification

The XRD pattern for $BaTiO_3$ nanopowder and film fabricated with different electrospinning conditions is illustrated in Fig. 5.5. The β crystalline phase of the PVDF nanofibrous film, PVDF/$BaTiO_3$ nanocomposite film and functionally graded structure is recorded at $2\theta = 20.6°$, corresponds to the (110) and (200) crystalline plane, while the α crystalline phase observed peak at $2\theta = 18.4°$ corresponds to (020) crystal plane respectively [135]. The $BaTiO_3$ nanoparticles exhibited a peak at $2\theta = 31.57°$, 56.25° and 65.14° according to the JCPDS card no 00-003-0725. Aluminium peak is detected at $2\theta = 44.83°$ in all fabricated film due to foundation support, where samples are placed for the test. The results reveal that peak intensity is increased with the addition of $BaTiO_3$ nanopowder. The FTIR spectra analysis has been performed in attenuated total reflection (ATR) mode to characterize the chemical structure of synthesized pristine PVDF fiber film, composite film and functionally graded structure as shown in Fig. 5.6. The fraction of β phase of the fabricated film is calculated using the FTIR spectra. The characteristic peaks are detected at 840, 880, 1276, 1403 and 1431 cm^{-1}, which correspond to the all trans (TTTT) conformation of β crystalline phase of the fabricated film [142, 143, 144]. It is observed that α crystalline phase is identified at 763 cm^{-1} in pure PVDF film, but not in nanocomposite film. However, some of the film exhibits α phase with very weak intensity. The vibration peak at 840, 880, 1276, 1403 and 1431 cm^{-1}

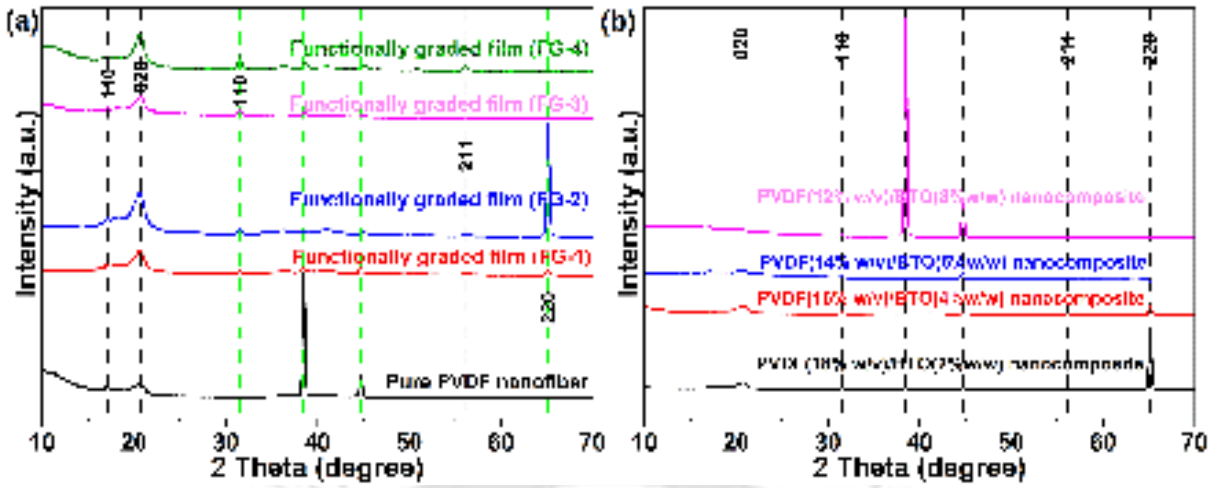

Fig. 5.5: XRD pattern of (a) pure PVDF fiber, FG-1 to FG-4 and (b) PVDF/BTO nanocomposite film with different concentrations.

assigned to β phase is recorded in all fabricated samples. This indicates that electrospinning is a viable technique for increasing polar β phase concentration. The increment in β phase content is owing to stretching, forces generated during elongation and local poling effect while the fabrication process by electrospinning that resulted in the α to β phase transformation [145]. Furthermore, rapid evaporation of the solvent and deposition of PVDF nanostructures on the collector plate may cause the non-polar phase (α) to shift to the polar phase (β). This output is consistent with the XRD result. The fraction of β phase of the pristine PVDF nanofiber, PVDF/$BaTiO_3$ functionally graded nanocomposite film could be quantitatively characterized from the absorbance intensity at 763 and 840 cm^{-1} using following equation, assuming that FTIR absorption follows LambertBeer law [144, 146].

$$F(\beta) = \frac{A_\beta}{1.26A_\alpha + A_\beta} \tag{5.1}$$

Where A_β and A_α are the absorbance at 840 and 763 cm^{-1} respectively and F(β) is fraction of polar β crystalline phase. The calculation of the fraction of β phase for the produced non-woven membranes are mentioned in Table 5.2. The F(β) value of PVDF/BTO functionally graded structure film is increased with the number of layers, whereas the F(β) magnitude of the PVDF/BTO nanocomposite decreased with the decrease in PVDF concentration and increase in $BaTiO_3$ concentration. Moreover, the fraction of β phase content of functionally graded and nanocomposite film enhanced with $BaTiO_3$ content compared to the pure PVDF nanofiber. The possible cause for

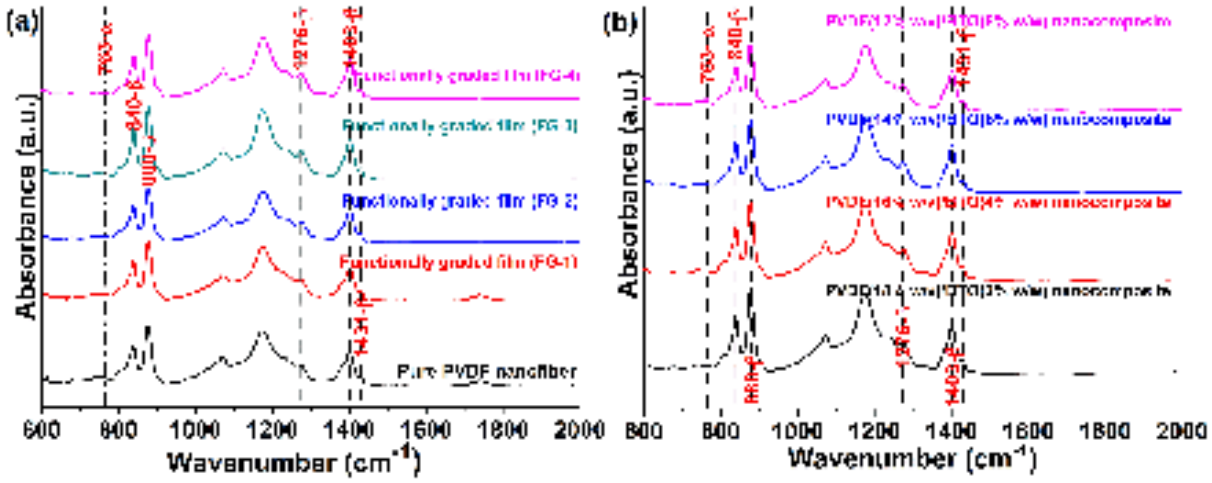

Fig. 5.6: FTIR spectra of (a) Pure PVDF nanofiber, FG-1 to FG-4 and (b) PVDF/BTO nanocomposite film with different concentrations.

Table 5.2: F(β) calculation for the various films fabricated at different conditions.

Sl. no.	Fabricated samples	PVDF (wt./vol.)	$BaTiO_3$ (wt.%)	F(β) (%)
1	PVDF nanofiber	20	0	73.9
2	FG-1	18	2	79.21
3	FG-2	16	4	81.69
4	FG-3	14	6	86.15
5	FG-4	12	8	84.23
6	PVDF/BTO	18	2	81.23
7	PVDF/BTO	16	4	80.08
8	PVDF/BTO	14	6	79.02
9	PVDF/BTO	12	8	73.25

the higher F(β) value of PVDF/$BaTiO_3$ film can be explained in the following ways. The interaction between PVDF polymer and $BaTiO_3$ nanoparticle plays a vital role in improving the polar β phase content. When an electric field is provided to a PVDF solution, it aids in the creation of all trans (TTTT) conformation and relaxing of the PVDF polymeric chain. As a result, longer trans conformer may be disturbed prior crystallization phenomena. Though, when $BaTiO_3$ nanoparticle is mixed with the PVDF solution, their dispersion can reduce the relaxation of PVDF chains that lead to the formation of long trans conformation. That is the interaction happened between them

resulting to stabilize the long trans conformation needed for crystallization.

5.3.4 Ultraviolet-Visible Spectroscopy (UV-vis) Analysis

The optical properties of the film fabricated using PVDF polymer and $BaTiO_3$ nanopowder has been carried out using UV-vis spectroscopy as shown in Fig. 5.7. This graph elucidates tauc plot of direct as well as indirect band gap of PVDF, PVDF/$BaTiO_3$ functionally graded and nanocomposite films by this equation [147]. Result showed that the lower band gap occurred for the functionally graded film and nanocomposite film compared to the pure PVDF nanofiber.

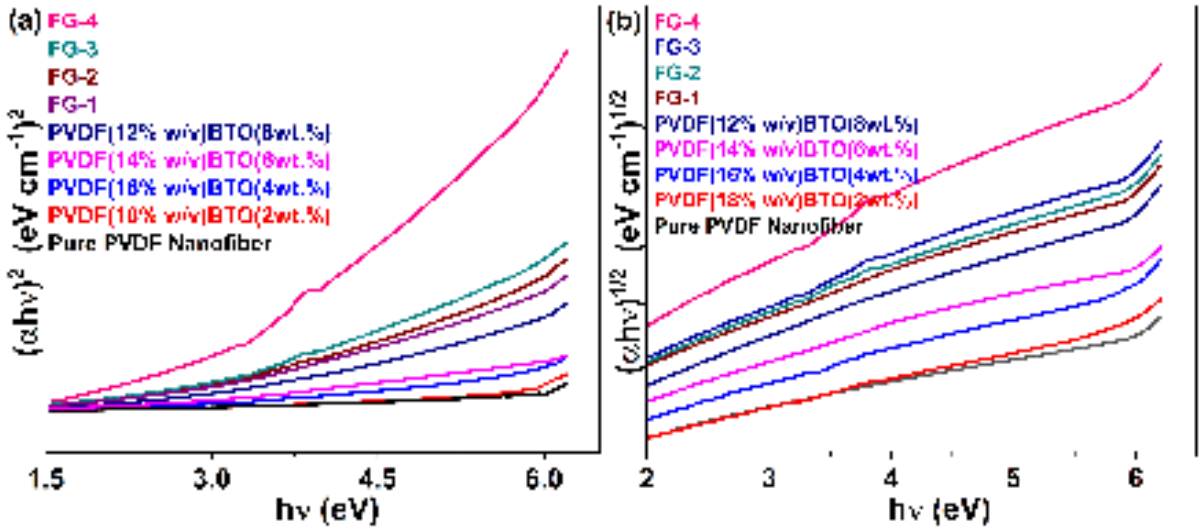

Fig. 5.7: Tauc plot for the (a) direct band gap and (b) indirect band gap of the produced membranes.

$$\alpha(\nu) = 2.303\frac{A}{t} \tag{5.2}$$

Where A and t are absorbance (a.u.) and thickness of nanofiber composite films and α is absorption coefficient.

$$\alpha(\nu) = \frac{(h\nu - E_g)^n}{h\nu} \tag{5.3}$$

Where exponent n = 0.5 is used for indirect transition and n = 2 is taken for direct transition. Hence, direct and indirect band gap of pure PVDF nanofiber and PVDF/$BaTiO_3$ nanocomposite films are obtained by Tauc plots. The optical band gap is obtained by extrapolated line which intersect the photon energy axis where the absorption coefficient (α) becomes zero. In Table 5.3, the value of each sample is listed. The result found that the band gap is reduced with the addition of

$BaTiO_3$ filler, which could be due to the defect formation led to increment in the density of localized states in the band gap and yielding in increased size of associated grains of the electrospun samples. The reduction in the band gap value of nanocomposite films increases their electrical conductivity and affects their optical properties [148].

Table 5.3: Direct and indirect band gap values for the fabricated electrospun mats.

Sl. no.	Fabricated samples	Direct band gap (eV)	Indirect band gap (eV)
1	PVDF nanofiber	5.24	4.68
2	PVDF 18% (wt./vol.)/BTO (2 wt.%)	4.99	4.27
3	PVDF 16% (wt./vol.)/BTO (4 wt.%)	4.86	4.24
4	PVDF 14% (wt./vol.)/BTO (6 wt.%)	4.72	3.84
5	FG-1	4.43	3.80
6	FG-2	4.02	3.74
7	FG-3	3.94	3.72
8	FG-4	3.55	3.63

5.3.5 Mechanical Characterization

In this study, tensile tests have been carried out on PVDF/$BaTiO_3$ fiber composites and functionally graded webs. The samples have been cut in the dimension of 11 mm×55 mm to be tested. The strain rate and gauge length are kept 7 mm/min and 40 mm. The thickness of the samples have been varied from 20 to 60 μm. The test is conducted at room temperature and dry condition. The stress versus strain curve for the fabricated electrospun fiber composite and functionally graded film is shown in Fig. 5.8. The value of tensile strength, elongation at break and Young's modulus are listed in Table 5.4. The tensile strength of nanocomposite fabricated with $BaTiO_3$ filler (6 wt.%) increased by 144 % as compared to pure PVDF nanofiber. Although, break at point continuously decreases from 52.16% to 36.68% with the dispersion of $BaTiO_3$ nanoparticles (2, 4, and 6 wt.%). The stress v_s strain graph of PVDF/$BaTiO_3$ membranes indicate that the suitable reinforcement of $BaTiO_3$ nanoparticles into PVDF tends to improve tensile strength. With increasing number of

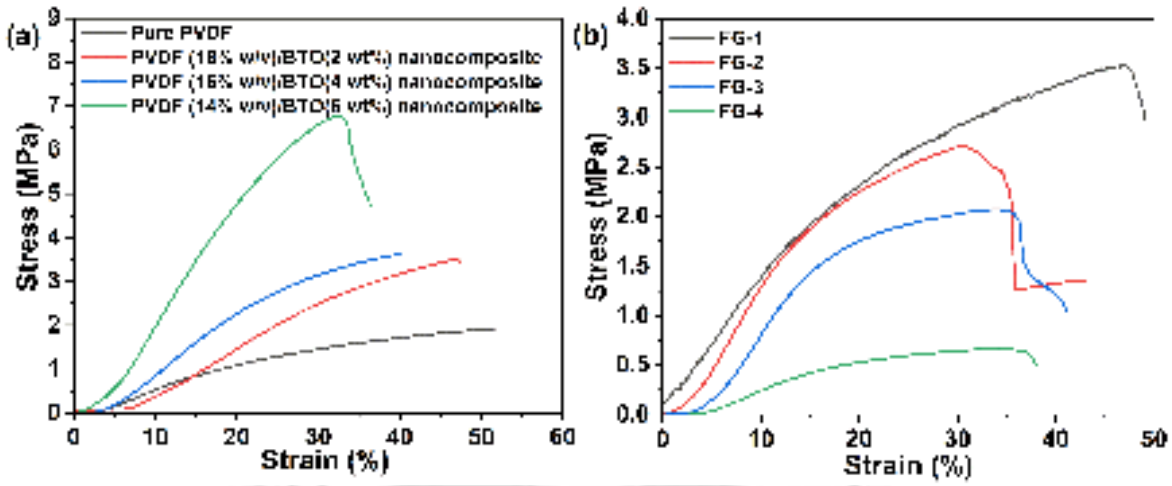

Fig. 5.8: Mechanical properties of (a) PVDF/BTO nanocomposite film with different concentrations and (b) FG-1 to FG-4.

Table 5.4: Mechanical properties of fiber composite at different concentration of nanofiller.

Sl. no.	Samples	Tensile strength (MPa)	Break at point (%)	Young's modulus (MPa)
1	PVDF nanofiber	1.93	52.16	3.9
2	FG-1	3.17	49.2	7.03
3	FG-2	2.83	43.3	9.65
4	FG-3	2.07	41.2	7.27
5	FG-4	0.53	39.33	2.24
6	PVDF-18%/BTO-2 wt.%	3.48	47.36	8.67
7	PVDF-16%/BTO-4 wt.%	3.6	40.31	10.38
8	PVDF-14%/BTO-6 wt.%	4.71	36.68	24.28

layers, functionally graded membranes demonstrated decreasing tensile stress. The possible interaction between the $BaTiO_3$ nanoparticle and the PVDF polymer is responsible for the increased film strength. The decrease in film strength may be caused by the accumulation of $BaTiO_3$ particles with a higher filler concentration. It is observed that the elastic modulus and tensile strength of the nanocomposite film enhanced by adding $BaTiO_3$ filler at 2, 4, and 6 wt.% as compared to pure PVDF nanofiber, while strain decreases at a higher concentration of filler (6 wt.%). Filler materials are generally incorporated into polymer matrix to reinforce the polymer. These data

clearly demonstrate that $BaTiO_3$ nanoparticles act as a provisional cohesive agent between PVDF matrix chains. The thin film fabricated from 12% wt./vol. PVDF and 8 wt.% $BaTiO_3$ could not be mechanically tested because of its lowest thickness.

5.3.6 Differential Scanning Calorimetry (DSC) Analysis

The thermal characterization has been performed for the synthesized nanocomposite and functionally graded film using DSC as shown in Fig. 5.9. The melting temperature, melting enthalpy and percentage crystallinity (X_C) is calculated using DSC thermogram curves. As a semi-crystalline polymer, the melting enthalpy is changing and directly related to the degree of crystallinity of fabricated samples. The degree of crystallinity (X_C) of the electrospun PVDF/$BaTiO_3$ nanocomposite and functionally graded film is quantified by the following equation [133].

$$X_C = \frac{\Delta H_f}{\Delta H_f^{\star} \times (1 - \frac{filler(wt.\%)}{100})} \times 100 \tag{5.4}$$

Where ΔH_f is the melting enthalpy of fabricated samples and $\Delta H_f^{\star}$ is melting enthalpy of sample

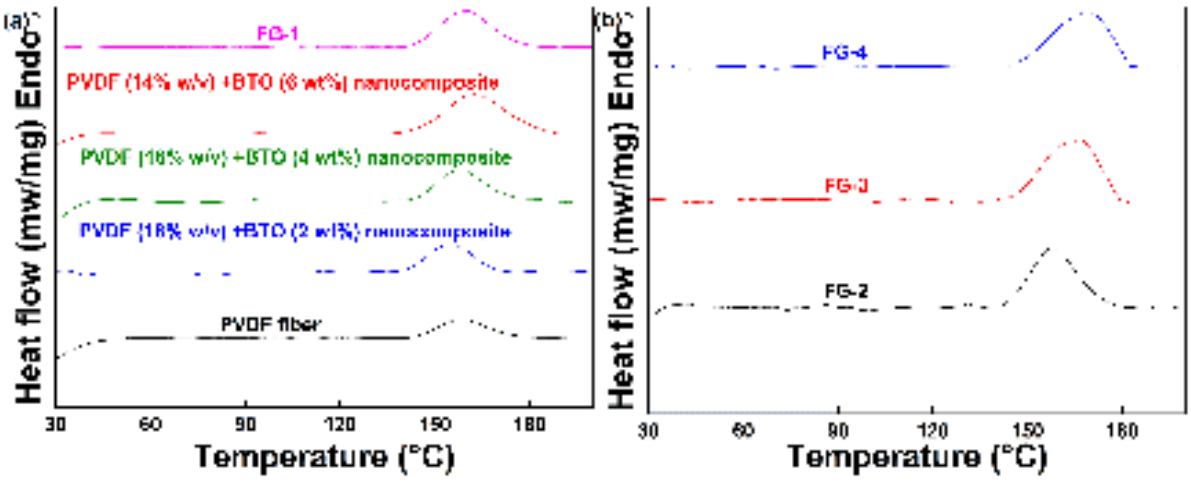

Fig. 5.9: DSC curve of (a) pure PVDF nanofiber, nanocomposite with varying BTO concentration and FG-1 (b) FG-2 to FG-4.

at 100% crystallinity, which is 104.6 J/g [134]. The values of all these parameters are listed in Table 5.5. The degree of crystallinity of functionally graded film is observed greater than PVDF fiber and composite membranes. The strong interaction between the polymer and filler likely caused the increase in crystallinity of the film.

Table 5.5: DSC analysis of synthesized nanofiber composite and functionally graded film.

Sl. no.	Fabricated samples	Melting temperature(°C)	Melting enthalpy (J/g)	Crystallinity (%)
1	PVDF nanofiber	158.34	23.49	22.45
2	PVDF-18%/BTO-2 wt.%	155.20	32.53	31.68
3	PVDF-16%/BTO-4 wt.%	157.86	37.92	37
4	PVDF-14%/BTO-6 wt.%	158.45	38.22	37.86
5	FG-1	168.84	41.28	41.98
6	FG-2	166.14	43.8	43.62
7	FG-3	160.36	47.22	46.4
8	FG-4	162.67	50.83	49.71

5.3.7 Effect of $BaTiO_3$ Nanofiller on Piezoelectric Performance

The PVDF/$BaTiO_3$ nanofiber composite and functionally graded fiber based membranes with varying content of $BaTiO_3$ nanoparticles and fibrous layer added is synthesized as piezoelectric nanogenerator to test its piezoelectric response. The working area of PENG device is 5 cm^2. The recorded peak to peak voltage and current output of the fabricated PENGs based on PVDF nanofiber, PVDF/$BaTiO_3$ nanocomposite and functionally graded film is shown in Fig. 5.10. These films are subjected external load including palm tapping, wrist tapping and elbow hitting and its piezoelectric outputs have been recorded through digital oscilloscope (DSO). In Table 5.6, different films are listed according to their piezo output. The voltage and current output recorded greater for the functionally graded film as compared to pristine PVDF nanofiber and PVDF/$BaTiO_3$ nanocomposite. The more output is found that could be ascribed to the good interaction at the interface, thickness and enhanced fraction of β phase of the electrospun functionally graded film. The thickness increases as the number of layers is added to functionally graded film. The peak to peak voltage and current output obtained for the FG-3 is 8.22 V and 3.36 A, while for the pure PVDF nanofiber is 3.22 V and 1.36 A. The piezo output obtained for the electrospun functionally graded film is 2.5 times more than pure PVDF nanofiber. The variation in voltage and current

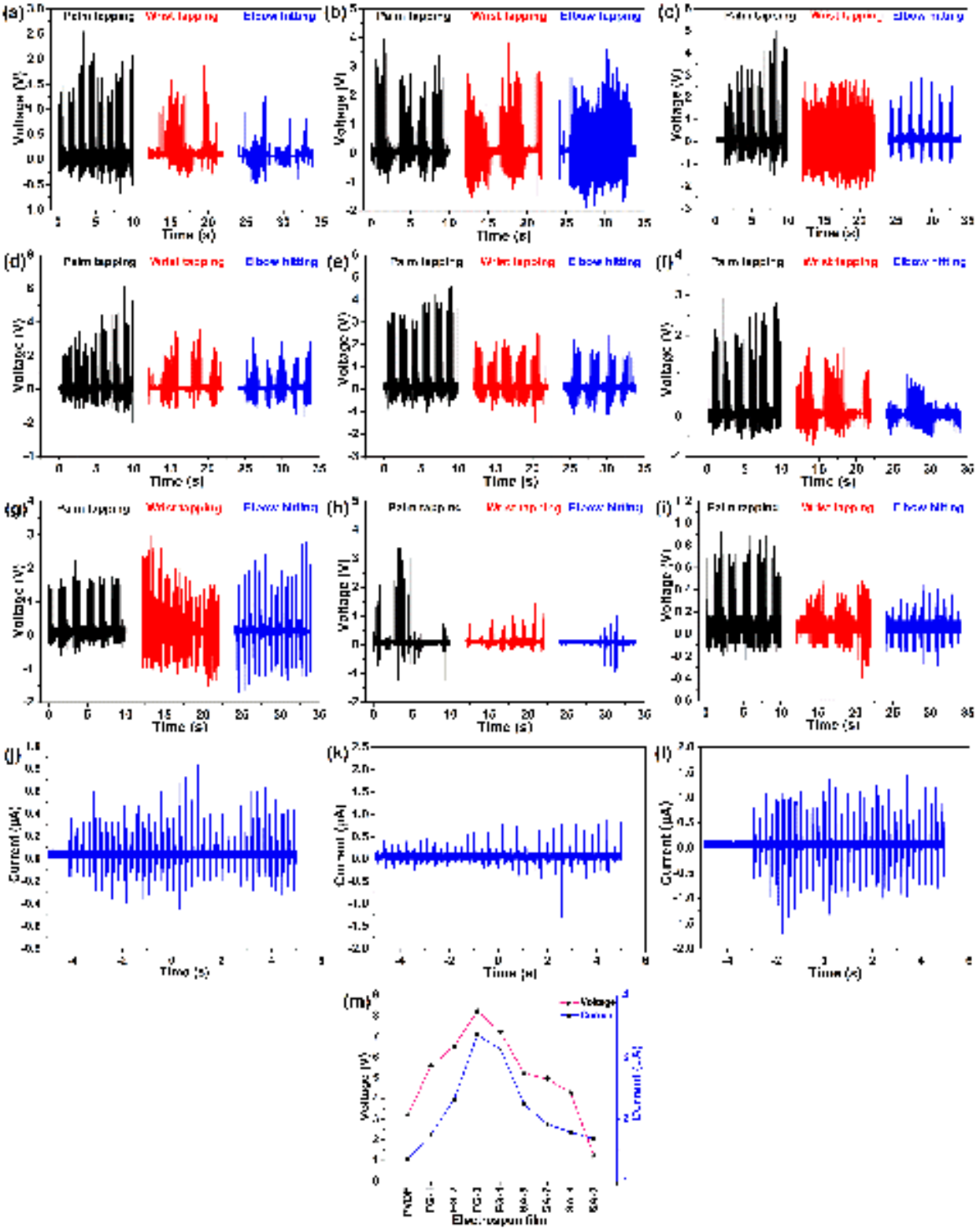

Fig. 5.10: Piezoelectric output of PENG based (a) Pure PVDF nanofiber, (b) FG-1, (c) FG-2, (d) FG-3, (e) FG-4, (f, g, h, i) PVDF/BTO nanocomposite film with varying concentrations, current output (j) Pure PVDF nanofiber, (k) FG-3, (l) FG-4, and (m) voltage and current output generated of functionally graded film and monolayer nanofiber composite membranes.

outputs of electrospun functionally graded and nanofiber composite membranes are illustrated in Fig. 5.10m. However, FG-4 showed less voltage and current than FG-3. The cause associated with them (FG-4) is more thickness and lesser fraction of β phase than FG-3. The fraction of β phase is responsible to enhance the piezoelectric output of the fabricated samples. It can be concluded from the above analysis that the piezoelectric output increases more for with four layered functionally graded film, whereas five layered functionally graded fibrous membranes shows less electric voltage.

Table 5.6: Piezoelectric output of electrospun nanofiber, composite, and functionally graded films.

Sl. no.	Samples	Voltage (V)			Current (μA)
		Palm tapping	Wrist tapping	Elbow hitting	Palm tapping
1	PVDF nanofiber	3.22	2.25	1.92	1.36
2	PVDF-18%/BTO-2 wt.%	5.21	2.44	1.92	2.24
3	PVDF-16%/BTO-4 wt.%	2.81	4.56	4.94	1.92
4	PVDF-14%/BTO-6 wt.%	4.28	1.68	1.93	1.79
4	PVDF-12%/BTO-8 wt.%	1.24	1	0.7	1.68
5	FG-1	5	5.13	5.55	1.75
6	FG-2	6.54	4.86	3.9	2.32
7	FG-3	8.22	5.64	5.04	3.36
8	FG-4	5.81	4.02	7.19	3.12

5.3.8 Simulation Analysis

Finite element method (FEM) based simulation of PENG devices using Comsol Multiphysics has been carried out for the purpose of analysing their solid mechanics and induced piezo potential. Piezoelectricity interface is used to model the entire simulation using a combination of solid mechanics and electrostatics interface with constitutive relations. The influence of multiple functionally graded layers on piezoelectric output is investigated to validate the experimental values of palm tapping mode of piezo voltage generation. Simulations are conducted using unit cell model with 30 μm width and thickness varying from 20 μm to 60 μm. $BaTiO_3$ nanoparticles are modelled with circular shape having 100 nm diameter as specified by manufacturer considering random dis-

tribution inside PVDF matrix [149]. The unit cell is fine meshed by considering triangular element. Bottom surface of the unit cell is electrically grounded and top surface is subjected to floating potential condition. The top surface of the unit cell is subjected to an external force of 10 N in vertically downward direction, while the bottom surface is mechanically fixed. The contact force calculation is carried out using the conservation of energy and momentum theory. When the PENG device is repeatedly subjected by palm tapping from an average height of 12 cm, the momentum of palm leads to charge generation. The following formula can be applied to calculate the applied contact force on the device surface;

$$mgh = \frac{1}{2}mv^2 \tag{5.5}$$

$$(F - mg).\Delta t = mv \tag{5.6}$$

Where m = mass of palm measured from electric balance, g = acceleration due to gravity, h = height from where hitting takes place, v = velocity, F = contact force applied on surface, Δt = time interval between successive two hits. Fig. 5.11 shows the 2D simulation results of pure PVDF, PVDF/$BaTiO_3$ nanocomposite film and multilayer functionally graded membranes. The experimental and simulated results are written in Table 5.7. The Hookes law and electrostatic

Table 5.7: Comparison of experimental and simulation values of PENG devices.

Fabricated samples	Experimental value	Simulation value
Pure PVDF nanofiber	3.22	3.05
PVDF-12%/BTO-8 wt.%	1.24	1.32
FG-1	5	5.401
FG-2	6.54	6.64
FG-3	8.22	8.3
FG-4	5.81	5.64

behaviour are coupled to depict piezoelectric behaviour are given below:

$$S = s^E T + d^T E \tag{5.7}$$

$$D = dT + \varepsilon^T E \tag{5.8}$$

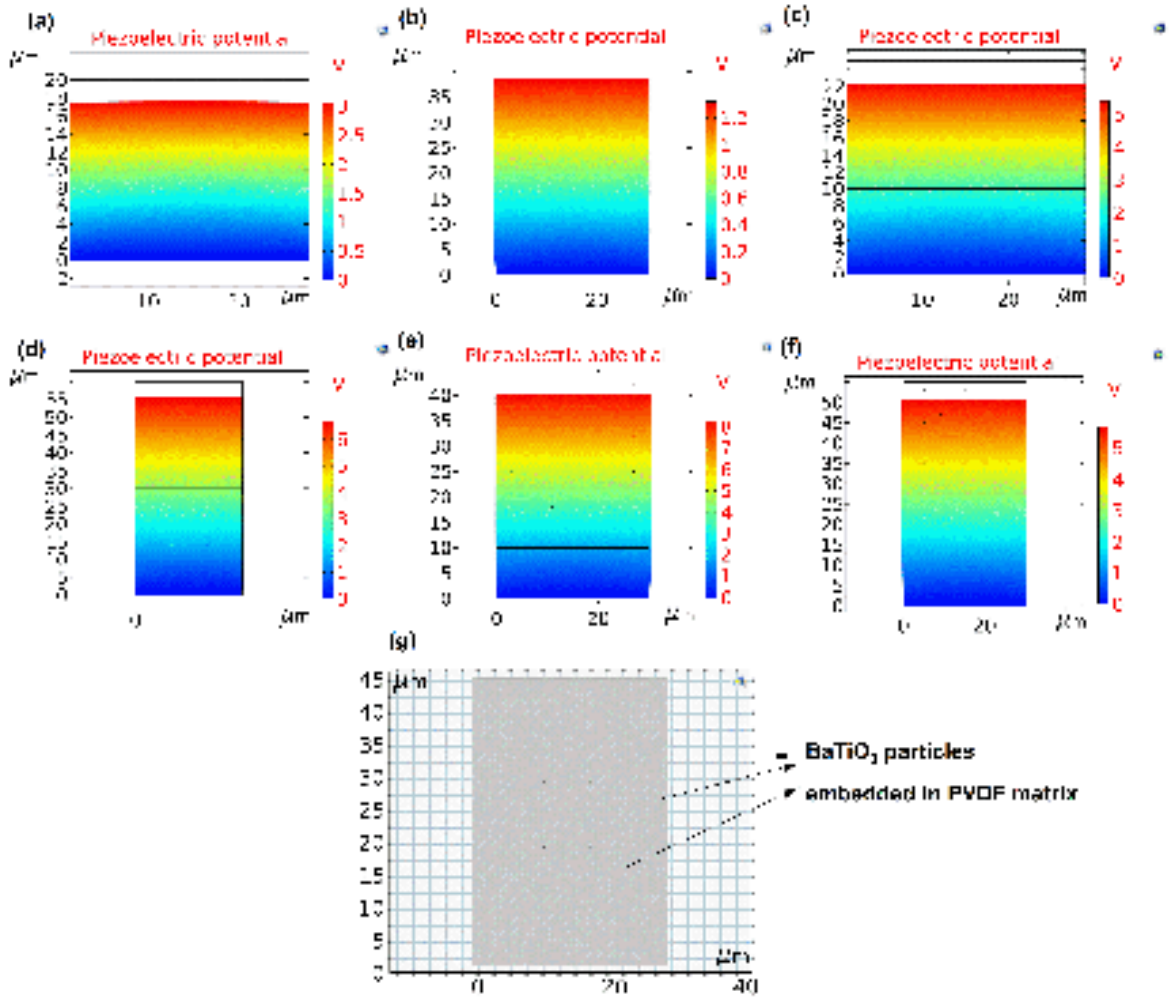

Fig. 5.11: Comsol simulation for piezoelectric potential (a) neat PVDF fiber, (b) nanocomposite (BTO-8 wt.%), (c) FG-1, (d) FG-2, (e) FG-3, (f) FG-4, and (g) simulation diagram of functionally graded (FG-4) film.

Where s is compliance, S is strain, T is stress applied, D is electric displacement, E is electric field, and ε is dielectric permittivity respectively. A maximum and minimum piezoelectric potential of 8.3 V and 1.31 V is obtained for FG-3 and PVDF (18% w/v)/BTO (2 wt.%) samples respectively. The simulation results are well in line with the experimentally found values.

5.4 SUMMARY

The PVDF/$BaTiO_3$ functionally graded and nanocomposite fibrous membranes with varying filler loading are successfully fabricated. The gradient has been maintained by changing the concentration of polymer and ceramic filler. This study has been performed to investigate the effects of $BaTiO_3$ nanoparticles and number of layers added on the surface morphology, β phase, crys-

tallinity, mechanical properties, optical properties and piezoelectric output of PVDF nanofiber, PVDF/$BaTiO_3$ nanocomposite and electrospun functionally graded membranes. The fraction of β phase and degree of crystallinity of electrospun functionally graded membranes and nanocomposite webs are enhanced with the increasing number of layers and varying the concentration of nanoparticles. The direct and indirect band gap is decreased with the addition of ceramic nanofiller and number of layers, which support to enhance the electrical properties. Mechanical properties of composite samples are enhanced, while those of functionally graded films decreased as the no. of layers increased. Furthermore, the flexible piezoelectric nanogenerators are prepared using fabricated samples. Functionally graded film shows enhanced piezoelectric output with the number of layers as compared to pure fiber and monolayer nanocomposite film. The experimental piezo outputs are validated using Comsol Multiphysics. The performance is noticeable and even higher than most piezoelectric nanogenerators fabricated by different processes. This PENG device does not only show the greater flexibility but also respond to human activity and delivers enhanced voltage output. Distinct piezoelectric signals are detected for different human activities using these devices. This device has potential applications in flexible electronics and powering small devices. This study reveals that:

(i) Pure PVDF has low output while multi-layered film based nanogenerators with high concentration of $BaTiO_3$ give more piezoelectric output.

(ii) The PENG devices have been subjected to palm tapping, wrist tapping, and elbow hitting to extract energy. The PENG generated peak to peak voltage of 8.22 V, current of 3.36 μA, and instantaneous power of 0.14 mW/cm^2.

(iii) Compared to monolayer films, functionally graded films exhibit greater piezoelectric performance as the number of nanofiber layers increases.

(iv) The nanocomposite fabricated with PVDF(12 wt.%)/$BaTiO_3$(8 wt.%) showed less piezoelectric performance as compared to other samples.

(v) The piezoelectric output of PENGs device is validated using Comsol Multiphysics software and well matched with the experimental results.

(vi) The maximum error of 6.89% is observed between the experimental piezoelectric output values and simulation result (using Comsol Multiphysics software), which confirm the effectiveness of the study.

Chapter 6

Design and synthesis of self-powered flexible P(VDF-TrFE)/ZnO/TiO_2 fiber mats as wearable device

6.1 INTRODUCTION

In this chapter, electrospun P(VDF-TrFE)/ZnO/TiO_2 hybrid nanocomposite based wearable device has been fabricated for enrgy harvesting applications. Polymer-based nanocomposite fibrous membranes are the basis of wearable flexible devices, but the application of high voltage poling, brittle material as dopants, or toxic compounds is the main challenge in the development of such devices. P(VDF-TrFE)/ZnO/TiO_2 electrospun nanofiber mats are used in here to fabricate self-poled, lead-free, and flexible piezoelectric nanogenerators as wearable device. Herein, self-poled, lead free, and flexible high performance piezoelectric nanogenerators (PENGs) are designed using the P(VDF-TrFE)/ZnO/TiO_2 electrospun fiber mats. The material selection, fabrication of pure P(VDF-TrFE) fiber, P(VDF-TrFE)/ZnO, P(VDF-TrFE)/TiO_2 composite, and P(VDF-TrFE)/ZnO/TiO_2 three phase nanocomposite, nanogenerator device, and characterization through different instruments have been presented in Sec. 6.2. Three phase nanocomposite mats with varying TiO_2 concentrations are fabricated using far-field electrospinning method. In this study, the influence of ZnO and TiO_2 nanoparticles on the viscoelastic property and piezoelectric output has been studied. The detail discussion of three phase nanocomposite mats have been presented in Sec. 6.3. This includes morphological study, elemental analysis, crystalline phase analysis, β phase variation, thermal stability, dielectric, mechanical, and DMA study. The different instruments have been used to perform these studies. In addition, three phase nanocomposite film-based

wearable device have been presented with their piezoelectric characteristics. The influence of ZnO and TiO_2 nanoparticles on piezoelectric performance has been evaluated in a systematic and detailed manner. The designed piezoelectric device generate current, voltage, and piezoelectric peak power of 4.16 A, 23 V, and 95.68 W, respectively. These piezoelectric outputs are obtained with the optimization of TiO_2 concentration and the PENG devices are subjected to elbow bending, wrist bending, and finger tapping. The piezoelectric output of three phase composite mats is almost 3.6 times higher than PENG made from P(VDF-TrFE) fiber. These device has been used to display real-time demonstrations of body movement detection and biomechanical energy harvesting to power an LED bulb. The enhanced performance and robustness of the nanogenerator make the electrospun P(VDF-TrFE)/ZnO/TiO_2 mat an excellent candidates for sensing and energy harvesting applications.

6.2 EXPERIMENTAL

6.2.1 Materials

The polymer containing vinylylidene fluoride and trifluoroethylene P(VDF-TrFE), with a molecular weight (M_w) of 3,00,000 for TrFE 25% and VDF 75%, zinc oxide (ZnO) powder (average nanoparticle size = 100 nm and M_w = 81.39 g/mol), and titanium oxide (TiO_2) nanoparticles (99.5% trace metals basis, average particle size = 100 nm) are procured from Sigma-Aldrich. In addition, Acetone (ACE) and N, N-Dimethylformamide (DMF) anhydrous, 99.8% is provided by Sigma-Aldrich, India. All chemicals are processed as received in the electrospinning process.

6.2.2 Fabrication of P(VDF-TrFE)/ZnO/TiO_2 Membranes

Three phase P(VDF-TrFE)/ZnO/TiO_2 nanocomposite membrane has been fabricated using the electrospinning (E-Spin Nanotech, India) method. The schematic diagram of electrospinning process for the fabrication of three phase nanocomposite mat is summarized in Fig. 6.1. The six distinct homogeneous solutions are prepared by adding DMF, piezoelectric polymer, and nanofiller. Initially, P(VDF-TrFE) pellets (17% w/v) are dispersed into 3 ml of DMF solvent and stirred at 500 rpm for eight hours (h) at 60°C temperature. Further, TiO_2 and ZnO nanopowder with 4

wt.% is added in the two separate polymeric P(VDF-TrFE) solution. Stirred P(VDF-TrFE)/TiO_2 and P(VDF-TrFE)/ZnO solution has been sonicated for 3 h to distribute nanopowder efficiently. At last, P(VDF-TrFE)/ZnO/TiO_2 solution is obtained by dispersing the TiO_2 nanopowder in the stirred and sonicated P(VDF-TrFE)/ZnO solution, wherein ZnO content is kept constant and TiO_2 content varied as 3%, 6%, and 10% by weight. Then, the stirring and sonication has been carried out for 5 h and 3 h respectively. The prepared solution is placed in the desiccator for 30 minutes to make bubble free solution. After that, the prepared solution is loaded into the plastic syringe and then placed in the slot adjacent to the syringe pump. In electrospinning, aluminium foil is wrapped over cylindrical drum collector and used as a substrate for deposited electrified jets. The nanocomposite fibers are synthesized using the following operational parameters, which ensured the smooth performance of electrospinning process. Throughout the process, a spinning distance of 13 cm, a flow rate of 10 μl/min, a rotational speed of 1300 rpm of the drum collector, a constant chamber temperature of 30°C, and an 18 kV applied voltage are all maintained. The ceiling fan inside the chamber has been kept running during the fabrication process of fibrous structures, which is used to remove moisture. The electrospinning current is noted 4 μA during the process. All the fibrous membranes are synthesized by depositing electrified solution jet on drum collector for three hours. The fibrous structures are peeled from the aluminum foil substrate and used to fabricate the devices. The six different fibrous mats have been synthesized with constant concentration of P(VDF-TrFE) polymer, ZnO nanofiller, and varying TiO_2. The fabricated samples are designated as follows: P(VDF-TrFE): pure nanofiber prepared with 17% w/v concentration of P(VDF-TrFE) polymer, PT: P(VDF-TrFE)/TiO_2 composite consisted of P(VDF-TrFE) 17% w/v and 4 wt.% of TiO_2, PZ: P(VDF-TrFE)/ZnO nanocomposite prepared using P(VDF-TrFE) 17% w/v and 4 wt.% of ZnO, and three different three phase nanocomposite membranes has been fabricated with various concentration of TiO_2 as x= 3 wt.% (PZT1), 6 wt.% (PZT2), and 10 wt.% (PZT3).

6.2.3 Design of P(VDF-TrFE)/ZnO/TiO_2 Naogenerator

Three phase P(VDF-TrFE)/ZnO/TiO_2 based nanogenerator is designed to power the small wearable device. The nanogenerators are made of three components: first, P(VDF-TrFE)/ZnO/TiO_2

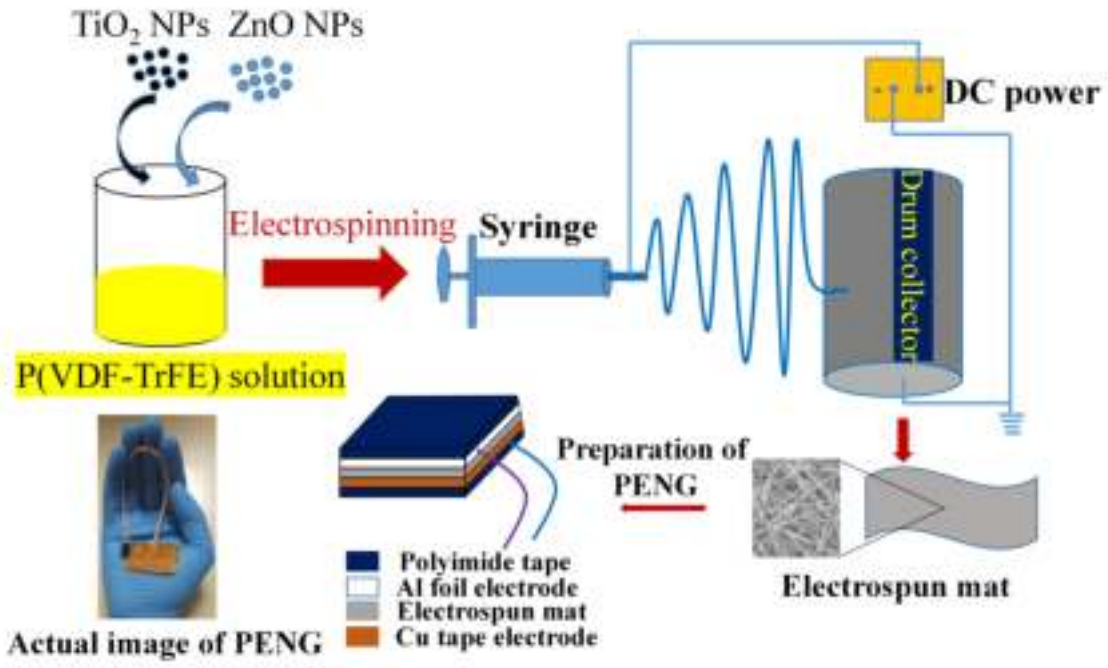

Fig. 6.1: Schematic diagram of nanofiber fabrication, piezoelectric nanogenerator (PENG) device, and actual photograph of PENG.

piezoelectric active layer, followed by two electrode layers made of conductive copper tape and aluminium foil. These conductive electrodes have been attached on both side of the fibrous membrane, which is considered as top and bottom electrodes. Copper wire is connected through the bottom and top electrodes to favour in detection of different signal using digital storage oscilloscope (DSO). The nanogenerator device is covered with polyimide tape to make them mechanically stable and prevent direct impact. The schematic diagram and actual photo of nanogenerator is depicted in Fig. 6.1.

6.2.4 Characterization and Measurements

P(VDF-TrFE)/ZnO/TiO_2 based three phase nanocomposite has been fabricated using E-spin unit procured from E-Spin Nanotech, India. The surface morphology of P(VDF-TrFE) nanofiber, P(VDF-TrFE)/ZnO, P(VDF-TrFE)/TiO_2, and three phase P(VDF-TrFE)/ZnO/TiO_2 nanocomposite membranes have been investigated using field emission scanning electron microscopy (FE-SEM) (Supplier: Zeiss, model: Gemini SEM 500). This analysis have been accomplished with an accelerating voltage of 5 kV and magnification 5 kX. The elemental composition analysis of the

fabricated fibrous membranes is studied using the energy dispersive X-ray (EDX) spectrometer, which is integrated with the same FESEM instrument. The average thickness of the electrospun mats is measured by digital micrometer (Mitutoyo 293-240-30). The X-ray diffraction (XRD) characterization has been performed to ensure the presence of crystalline structure in the fabricated fibrous membranes. The XRD pattern (Supplier: Rigaku Technologies, Japan, model: Smartlab) is observed on a diffractometer with the help of Cu-Kα radiation 1.54 $\mathring{A}$. In this study, nanocomposite membranes are scanned at 5 degree/minute in a 2θ range from 10° to 65° with a 0.02 step size. The presence of β phase in the fabricated sample has been confirmed using Fourier transform infrared (FTIR) spectra (Supplier: PerkinElmer, Singapore, model: Spectrum two). This test is conducted over the wavenumber range of 600-2400 cm^{-1} in attenuated total reflection (ATR) mode. Thermo gravimetric analysis (TGA) (Supplier: PerkinElmer, model: TGA 4000) is carried out with heating rate of 10 degree/minute and samples were heated from 30 to 700°C in nitrogen environment. The gas flow rate is supplied 19.8 ml/min to perform the TGA test. The mechanical properties of three phase nanocomposite has been characterised by 5kN Electromechanical universal testing instrument (Supplier: ZwickRoell, model: Z005TN Proline). This test has been conducted with strain rate of 5 mm/minute in tensile mode. The dielectric properties measurement is conducted using IM 3536 LCR METER (model: Hioki) from 1 kHz to 1 MHz at 25°C temperature. For this test, fiber mats are prepare into a rectangular cross-section of about (2×1.5) cm^2 followed by conductive copper tape pasted on both sides of the films. The dynamic mechanical analysis (DMA) (Physica MCR 702-Anton Paar) has been carried out to investigate the effect of ZnO and TiO_2 nanofiller on storage modulus and loss factor of three phase P(VDF-TrFE)/ZnO/TiO_2 nanocomposite in tensile mode on 3.5×1 cm^2 rectangular specimens (L×W). This study has been demonstrated for temperature sweep from -75°C to 75°C with strain rate of 0.025% and at frequency 1Hz. The preload of 0.1 N is applied to the specimen for the DMA test. The piezoelectric response of pristine P(VDF-TrFE) nanofiber and three phase electrospun nanocomposites has been recorded using digital oscilloscope (GW INSTEK GDS-2102A) under the load subjected to finger tapping, elbow, and wrist bending at ambient condition.

6.3 RESULTS AND DISCSSION

6.3.1 Morphological Study of P(VDF-TrFE), ZnO, and TiO_2 Based Fabricated Films

In this work, three phase nanocomposite P(VDF-TrFE)/TiO_2/ZnO has been fabricated by means of electrospinning method. The fabricated membranes have been cut in 5mm×5mm section, which are mounted on the FESEM sample holders and then subsequently coated with platinum. The surface morphology of P(VDF-TrFE) fiber, P(VDF-TrFE)/ZnO, P(VDF-TrFE)/TiO_2, and three phase P(VDF-TrFE)/ZnO/TiO_2 nanocomposite has been acquired using FESEM operated with accelerating voltage 5kV and magnification 5 kX. The FESEM images (Fig. 6.2) not only describe that the electrospun membranes are defect-free, but also suggest that the electrospinning parameters used are appropriate for the electrospinning method. The ZnO and TiO_2 nanoparticles in the P(VDF-TrFE) solution are agglomerated at higher concentration as seen in FESEM images. The average diameter of all the nanofiber composite is obtained using ImageJ software. The fifty different location on the FESEM images has been randomly chosen for calculating the average fiber diameter. The average diameter of pure P(VDF-TrFE) fiber, PZ, PT, PZT1, PZT2, and PZT3 composite is 333 nm, 273.5 nm, 160 nm, 146.40 nm, 132 nm, and 113 nm, respectively. The average diameter of composite membrane decreases with the addition of ZnO and TiO_2 nanofiller due to the increase in solution's conductivity. Hence, the decreased average diameter of the film membranes is observed. The average diameter of P(VDF-TrFE) is more compared to PZT3 nanocomposite. Results indicate that the nanofiber diameter decreased more with the addition of nanoparticles.

6.3.2 EDX Characterization

Energy dispersive X-ray (EDX) has been incorporated to determine the elemental composition and its weight percentage in the fabricated nanocomposite membrane samples P(VDF-TrFE), PT, PZ, and PZT1. The EDX spectra and element mapping of the fibrous membranes are shown in Fig. 6.3. The semi-qualitative and semi-quantative analysis of the EDX spectra can be performed. This characterization confirms the presence of Carbon (C), Fluorine (F), Titanium (Ti), Oxygen (O), and Zinc (Zn) elements in the fabricated membranes. The Ti, Zn, and O elements are associated with TiO_2 inorganic compound and ZnO semiconductor inorganic materials, while the C and

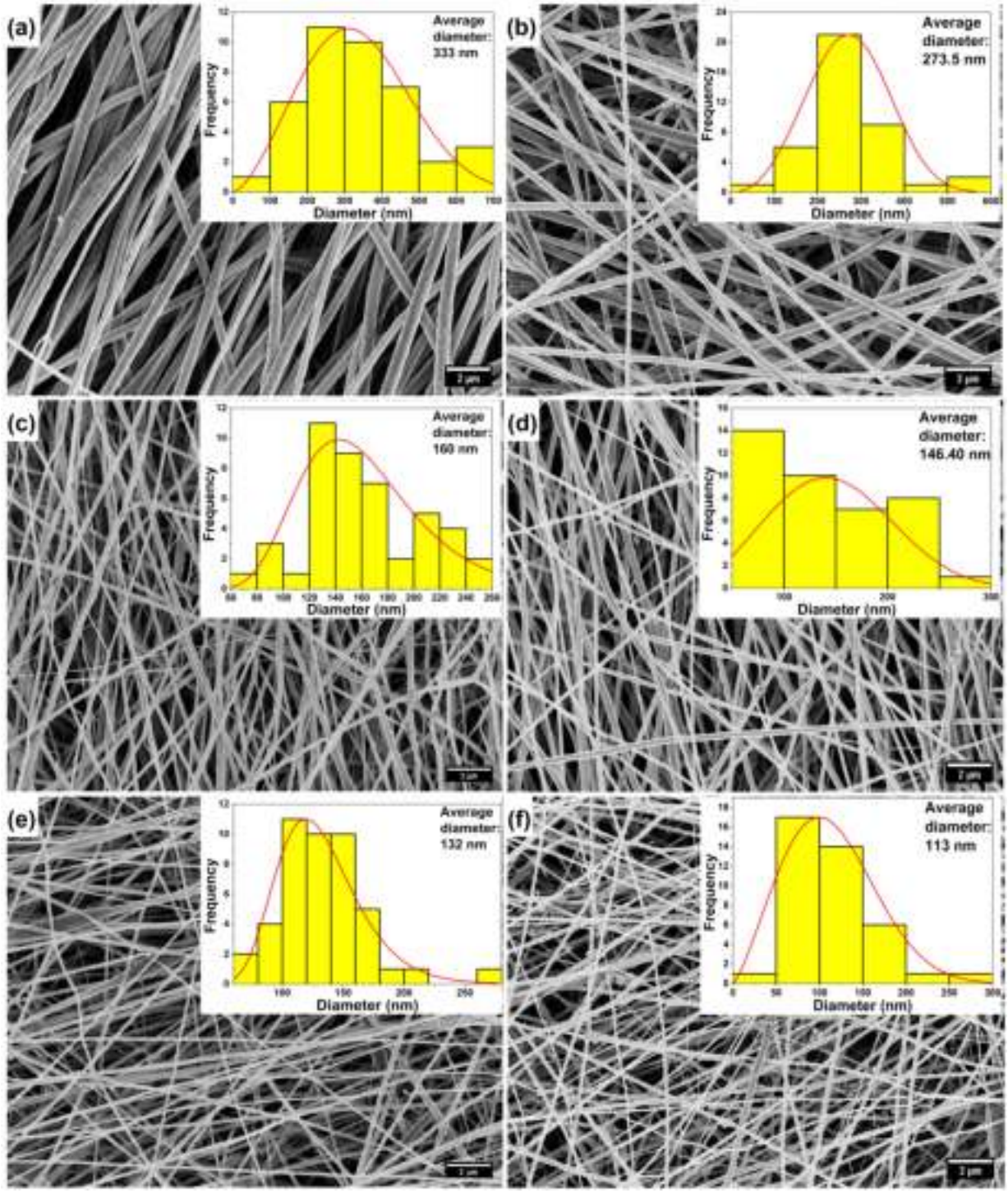

Fig. 6.2: FESEM images and fiber diameter distribution of the fabricated membranes (a) P(VDF-TrFE) nanofiber, (b) PZ, (c) PT, (d) PZT1, (e) PZT2, and (f) PZT3 nanocomposite mats.

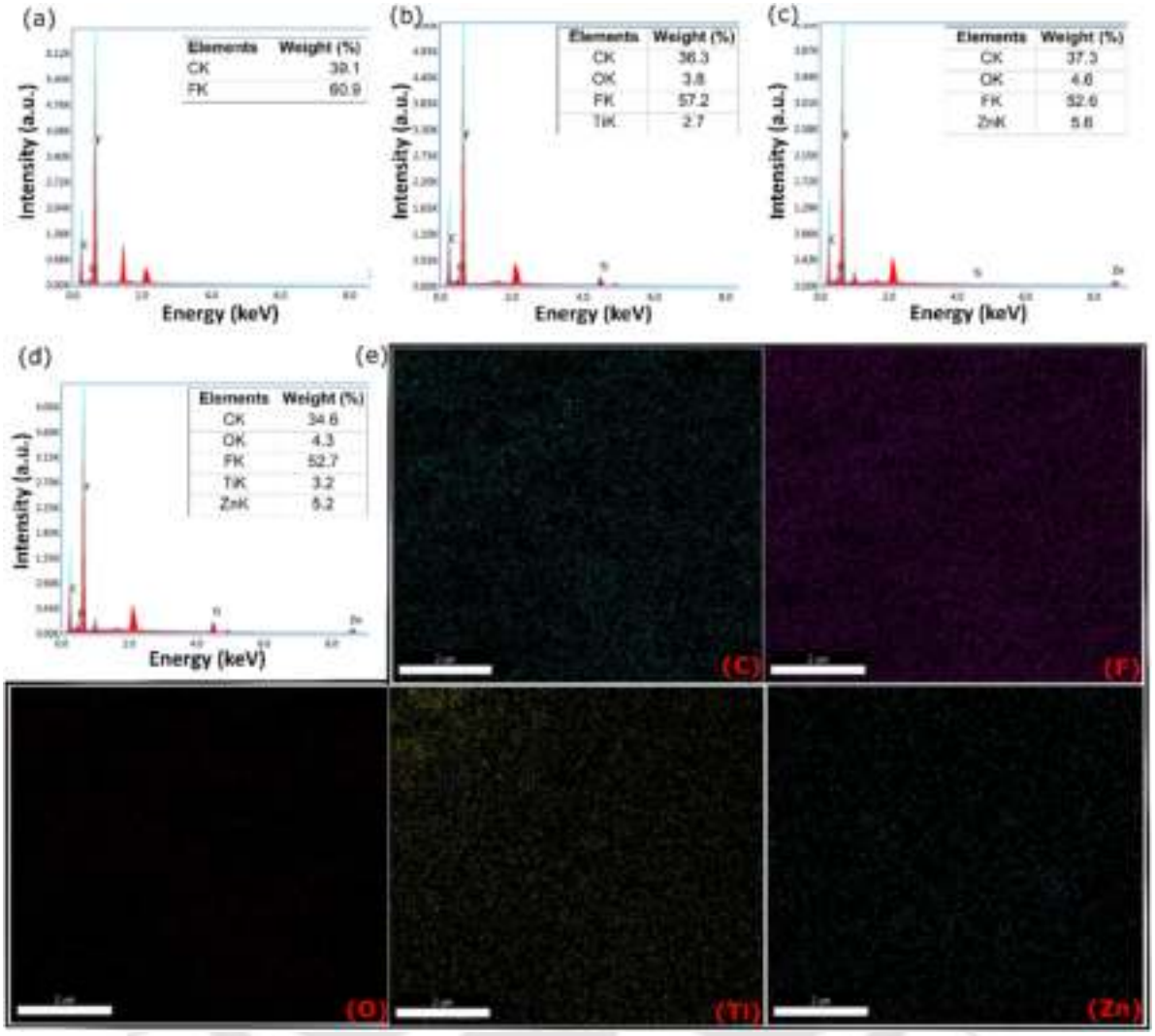

Fig. 6.3: EDX spectra for the fabricated membranes (a) P(VDF-TrFE) (b) PT (c) PZ, and (d) PZT2 nanocomposites, and element mapping of (e) C, F, O, Ti, Zn- atom.

F atoms are related to the characteristic elements of P(VDF-TrFE) polymer. Pure P(VDF-TrFE) nanofiber exhibited sharp peaks at low energy that can be assigned to the elements fluorine (Kα radiation with 0.5 keV) and carbon (Kα radiation with 0.24 keV). In the case of nanocomposite, the characteristic peaks of Ti, Zn, and O are detected at the energy level of 4.5 keV, 8.63 keV (Kα), and 0.6 keV, respectively. These peaks are well-matched with the reported results [150].

6.3.3 XRD Analysis

The XRD pattern for TiO_2, ZnO powder, and all membranes fabricated, including three phase PZT1, PZT2, PZT3 nanocomposite, and pure P(VDF-TrFE) nanofiber are depicted in Fig. 6.4. Crystallinity in polymeric materials affects its mechanical, physical, and biological properties. The

XRD characterization has been performed to reveal the presence of crystalline β phase structure, ZnO, and TiO_2 powders in the fabricated nanofiber mats. The β phase is found at 2θ = 20° (110) in the synthesized fibrous membranes as shown in the XRD pattern Fig. 6.4 [151]. When the TiO_2 and ZnO nanofiller is dispersed, the corresponding diffraction peaks of the TiO_2 and ZnO nanopowders are found at 2θ value of 27.48°, 36.26°, 41.36°, 54.45°, 56.73°, 62.89° [152] and 2θ value of 31.8°, 34.50°, 36.25°, 47.60°, 56.61°, and 62.95° as per the JCPDS card no. 00-005-0664, respectively. The diffraction peak shown at 2θ = 44.7° is for the foundation support where, the test is performed. The crystalline plane for the ZnO (black colour) and TiO_2 (pink colour) are shown in Fig. 6.4. The peak intensity of pure P(VDF-TrFE) is increased with the dispersion of ZnO and TiO_2 nanofiller. As a result of the very low concentration of ZnO and TiO_2, the peaks corresponding to these oxides have low intensity in nanocomposite samples [153].

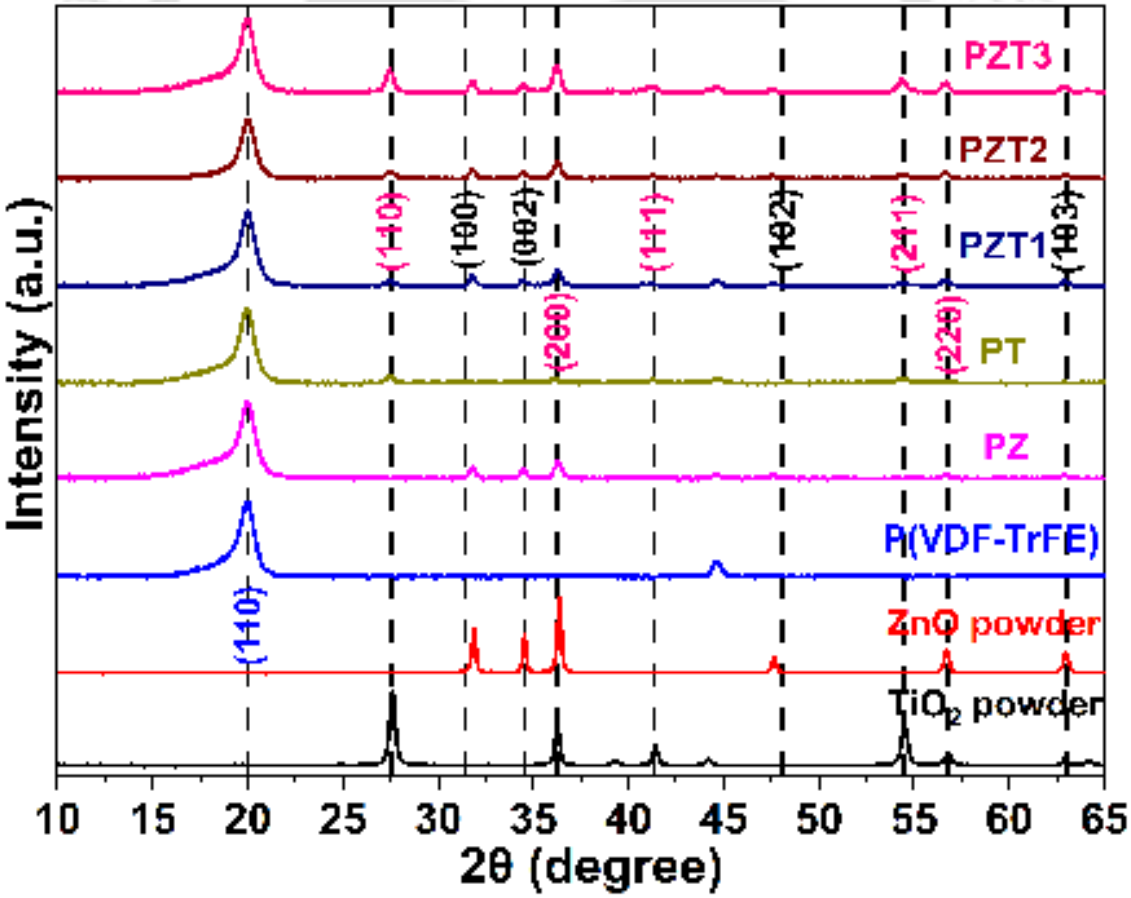

Fig. 6.4: XRD curve for the TiO_2, ZnO anopowder, and fabricated membranes P(VDF-TrFE), PZ, PT, PZT1, PZT2 and PZT3 nanocomposites.

6.3.4 FTIR Analysis

The FTIR spectra and variation in fraction of β phase of pure P(VDF-TrFE) fiber and three phase P(VDF-TrFE)/ZnO/TiO_2 composite mats with different concentration of TiO_2 are depicted in Fig. 6.5. This test has been conducted in attenuated total reflection (ATR) mode. Pure P(VDF-

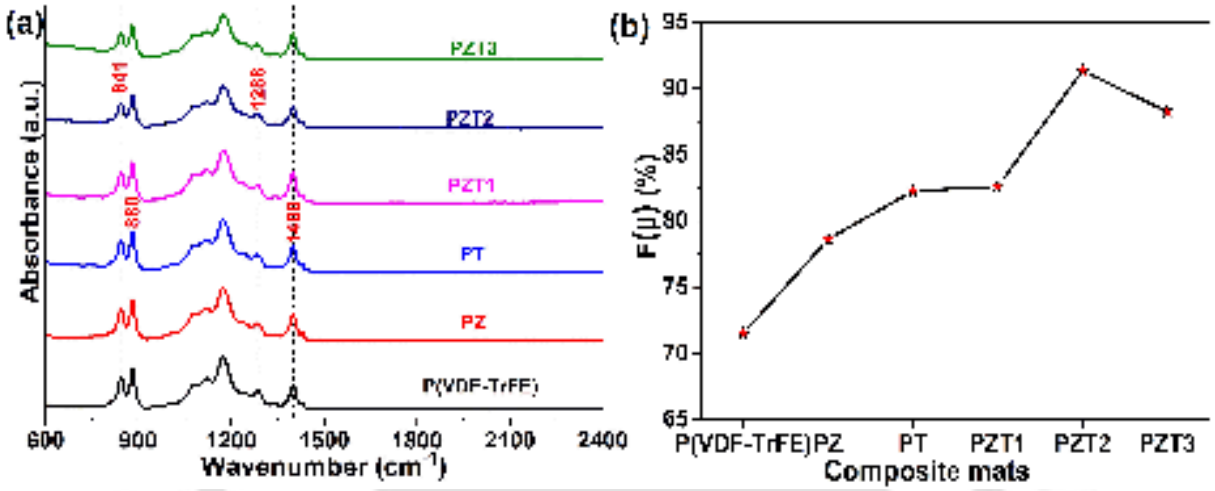

Fig. 6.5: FTIR spectra and variation in the fraction of β for the fabricated membranes P(VDF-TrFE), PZ, PT, PZT1, PZT2 and PZT3 nanocomposites.

TrFE) fiber and all composite fibrous mats are analysed by FTIR spectra to calculate their electroactive β phase content. In the scanned range (600 cm^{-1} to 2400 cm^{-1}), only P(VDF-TrFE) characteristic peaks are observed, and the intensities of ZnO and TiO_2 nanopowder are very weak because of low concentration. The peaks obtained at 841 and 1288 cm^{-1} corresponding to CF_2 symmetric stretching and 880 and 1400 cm^{-1} band relates to CH_2 rocking and wagging vibration of CH_2 of polymer [151, 154, 155]. The intensity of these peaks increases, which signify that most of the dipoles in the three phase fiber mats are aligned in parallel to the β phase. The α phase peak is not appeared in all spectra beacuse of electrospinning process, which leads to conversion from α phase to β phase and poling in the same process. The electroactive β phase [F(β)] content can be determined by the following equation.

$$F(\beta) = \frac{I_{841}}{I_{841} + (\frac{K_\beta}{K_\alpha})} \times 100 \tag{6.1}$$

Where I_{763} and I_{841} correspond to the absorbance intensities of peaks at wavenumbers 763 and 841 cm^{-1}. Kα = 6.1×10^4 cm^2/mol and Kβ = 7.7×10^4 cm^2/mol are the absorption coefficients

at 763 and 841 cm^{-1} [156]. The β phase content for P(VDF-TrFE) nanofiber, PZ, PT, PZT1, PZT2, and PZT3 nanocomposite mats are 72.51%, 78.62%, 82.25%, 83.2%, 91.33%, and 88.25%, respectively. The enhancement in β phase content may be due to the strong bonding of ZnO and TiO_2 nanoparticles in P(VDF-TrFE).

6.3.5 Thermo-gravimetric Analysis (TGA)

The thermal stability test of the three phase composite mats and P(VDF-TrFE) nanofiber has been studied from TGA curve. This test has been scanned from 30 to 700°C with the heating rate of 10°C/minute, gas flow rate of 19.8 ml/min, and gas pressure 2.0 bar under nitrogen atmosphere. The clear indication of the change in degradation temperature and the number of stages in which the samples started to degrade is shown in Fig. 6.6. The degradation of mats are completed mainly

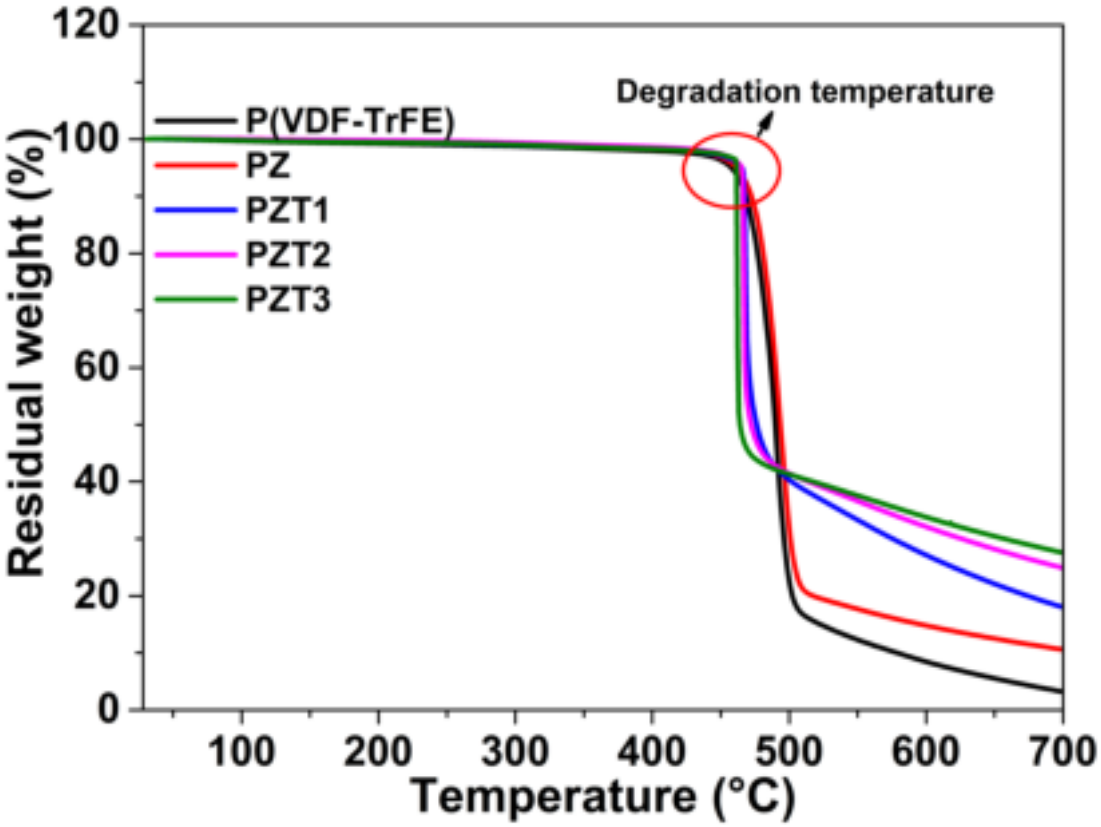

Fig. 6.6: TGA curves for fabricated three phase nanocomposite samples with varying the concentration of TiO_2 nanofiller.

in two stage in the measured temperature range. The degradation temperature varied with the samples, which can be observed from the TGA curves. The pristine P(VDF-TrFE) fiber is thermally

stable till the temperature of 430°C and then starts degraded rapidly to 506°C. The thermal stability of the mat increases with increasing TiO_2 concentration. The three phase nanocomposite mat showed greater thermal stability owing to the addition of TiO_2 and ZnO nanofiller compared to P(VDF-TrFE) nanofiber. The percentage residue mass of the electrospun mats are investigated from TGA curve. The residue mass of 3.2%, 10.6%, 18.05%, 24.93%, and 27.59% is found for the P(VDF-TrFE), PZ, PZT1, PZT2, and PZT3 composite membranes. Our results revealed that the incorporation of ZnO and TiO_2 nanoparticle significantly affected the degradation temperature and residue mass of the fabricated mats. Based on these results, it can be concluded that the prepared composite mats can be utilised in sensing higher temperature ranges and energy harvesting applications.

6.3.6 Dielectric Measurement

The dielectric properties of the fabricated P(VDF-TrFE) nanofiber, PZ, PT, PZT1, PZT2, and PZT3 nanocomposite mats with different loading conditions of fillers are measured at room temperature. The dielectric constant, dielectric loss (tanδ), and conductivity are measured in the frequency range of 1kHz to 1 MHz as shown in Fig. 6.7. It is observed that the dielectric constant (ε) increases by the loading of ZnO and TiO_2 nanofiller (Fig. 6.7a). The dielectric constant is higher in the lower frequency range, and decreases in the higher frequency range. The decrease in dielectric constant with the frequency is due to the reduction of effective dipoles [157, 158]. The dielectric constant for the P(VDF-TrFE) is around 8, while for PZT2 is 34. The enhancement in dielectric constant is more than four times after addition of ZnO and TiO_2 nanofillers in P(VDF-TrFE) matrix. The dielectric constant for the fabricated films are increases till the concentration of TiO_2 6 wt.% and decreases when TiO_2 concentration is 10 wt.%. The reduction in ε with the larger quantity of nanofiller is due to the agglomeration and the conductive channel is formed by the nanoparticles, which increased leakage current and reduced ε [159]. In Fig. 6.7b, dielectric loss (tanδ) of the prepared nanocomposite mats initially decreased and then increased with the frequency. The tanδ of the P(VDF-TrFE)/ZnO/TiO_2 composite mats showed the same trend as ε. The dielectric loss increased with the loading of nanoparticles, which can be seen in Fig. 6.7b.

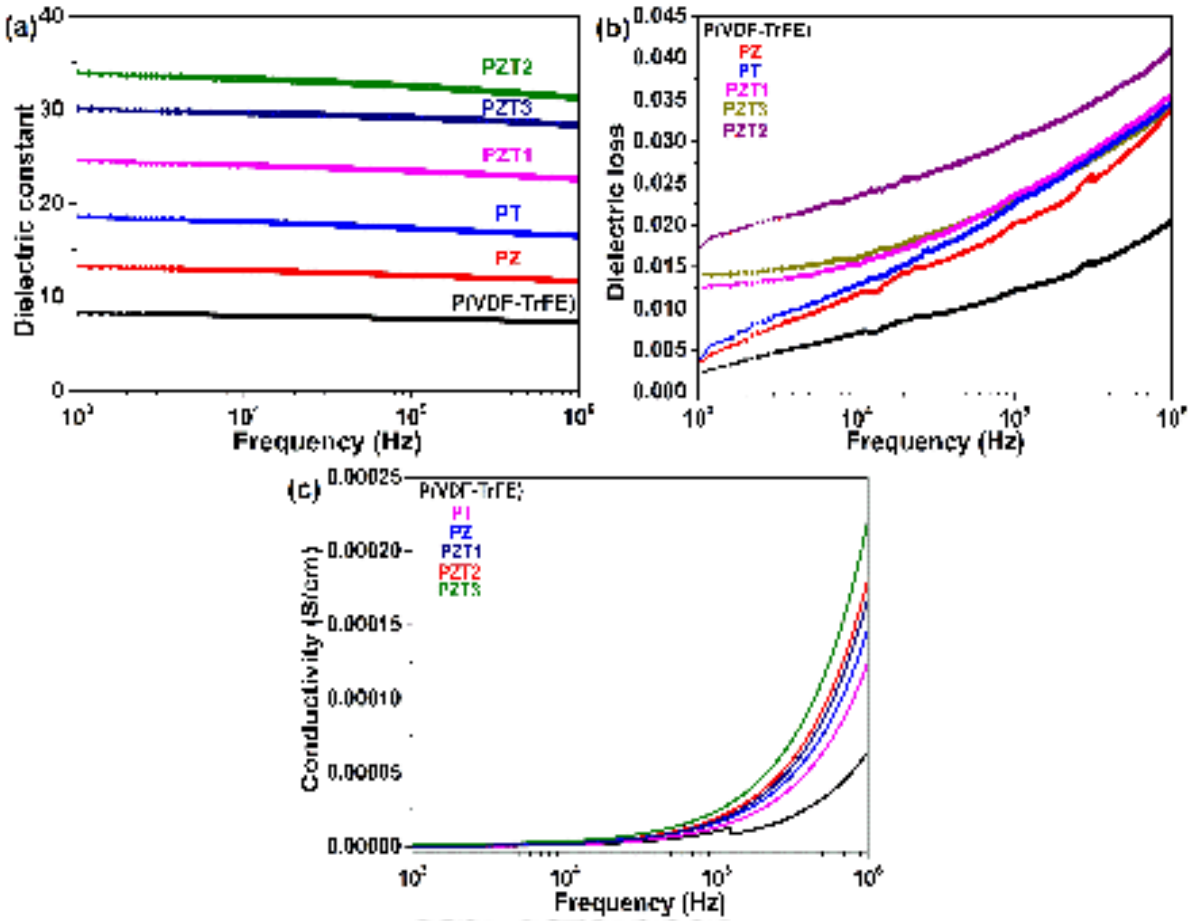

Fig. 6.7: Variation of (a) dielectric constant, (b) dielectric loss (tanδ), and (c) conductivity with frequency.

These results are clearly in agreement with those reported for nanocomposite films composed of three phases [160]. The conductivity of the composite mats increased with the frequency compared to the P(VDF-TrFE) as presented in the Fig. 6.7c. Composite mats have superior conductivity as the nanoparticles content increased compared to the pure P(VDF-TrFE) nanofibers.

6.3.7 Mechanical Characterization

The mechanical characterization has been performed for all the fabricated electrospun nanofiber and composite mats. The samples are prepared according to ASTM D882-12 standards and the test has been performed with strain rate of 5 mm/minute. The electrospun mats have been cut in 1 cm width and 5 cm length, and sand paper is glued to the lower and upper side of the mats to hold the samples tightly. Fig. 6.8a shows the stress versus strain curve for the pure P(VDF-TrFE) nanofiber, PZ, PT, and P(VDF-TrFE)/ZnO/TiO_2 three phase composite webs with different concentrations of TiO_2 nanofillers. The tensile strength and Young's modulus are calculated using the stress versus strain curve and the effect of ZnO and TiO_2 is studied for the composite mats, which can be seen in Fig. 6.8b. Generally, polymer nanocomposites with inherent stiffness, high dispersion quality, particle size, morphology, and adhesion between matrix and nanoparticles perform better in terms of mechanical properties, including Young's modulus, elongation at break, and tensile strength. The tensile strength of the P(VDF-TrFE) is 13.68 MPa which increases continuously with the addition of ZnO and TiO_2 to 24 MPa for the PZT2 sample. However, it decreases at 10 wt.% TiO_2 for the PZT3 mats. The strain of P(VDF-TrFE) is 139% and reduced to 55% with the incorporation of nanoparticles for the other mats. Young's modulus is noted to increase with the filler loading conditions for pure P(VDF-TrFE): 8.98 MPa; PZ: 12.68 MPa; PT: 26.52 MPa; PZT1: 28.42 MPa; PZT2: 30.93 MPa; PZT: 34.51 MPa. The value of tensile strength, strain, and Young's modulus are listed in Table 6.1. The enhancement in tensile strength and Young's modulus of the prepared samples with the addition of nanofillers is ascribed to the strong interaction between the P(VDF-TrFE) matrix and reinforcing components. It has been found that at 10 wt.% TiO_2 nanoparticles, mechanical properties (tensile strength and Young's modulus) of films decreases. This could be due to the agglomeration in the polymeric solution with the higher content of filler dispersion [161].

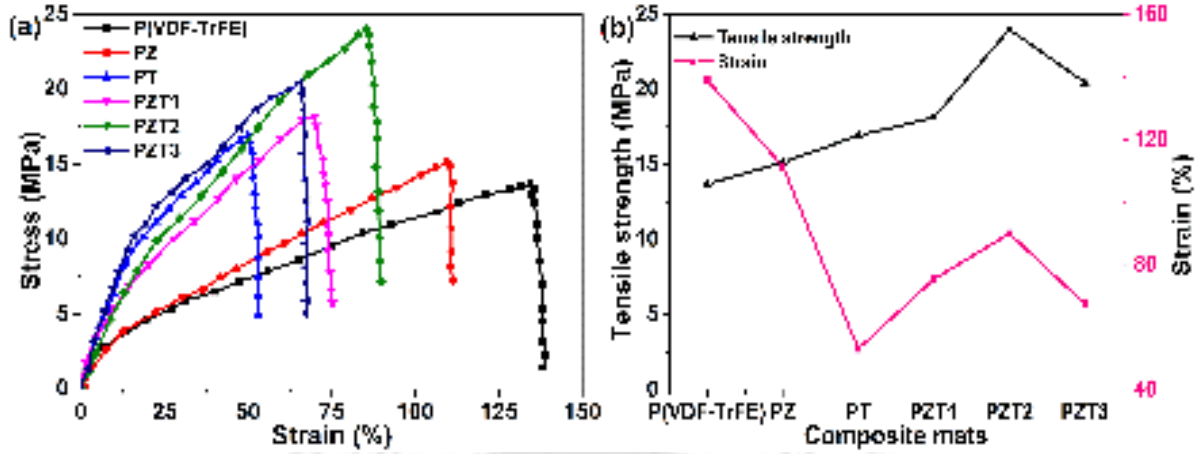

Fig. 6.8: UTM tensile test (a) stress versus strain curve, (b) tensile strength and strain variation as a function of loading conditions.

Table 6.1: Mechanical properties of three phase composite at different concentration of nanofiller.

Samples	Tensile strength (MPa)	Strain (%)	Young's modulus (MPa)
PVDF nanofiber	13.68±0.73	139±2.1	8.98±0.47
PZ	15.14±1.41	111.4±1.92	12.68±0.65
PT	16.90±1.63	55±3	26.52±1.1
PZT1	18.20±1.78	75.25±3.8	28.42±0.85
PZT2	24±1.92	90±2.83	30.93±1.4
PZT3	20.45±2.01	67.30±3.5	34.51±3

6.3.8 Dynamic Mechanical Analysis (DMA)

The DMA characterization has been conducted to assess the viscoelastic properties of the membranes and compare the difference between nanofiber mats and composite membranes in terms of their resistance to deformation or stiffness. In this test, the effect of ZnO and TiO_2 nanofiller is analyzed on storage modulus and damping factor of the fabricated nanofiber mats in tension mode. Fig. 6.9 presents the DMA test for the P(VDF-TrFE) nanofiber, PZ, PT, PZT1, PZT2, and PZT3 nanocomposite mats. As part of the test, samples were prepared in rectangular shapes measuring length of 3.5 cm and width of 1 cm, while this test has been conducted with 2.3 cm gauge length. The specimen is preloaded with 0.1 N to maintain straightness between the upper and lower jaws,

as seen in Fig. 6.9c. The PZT2 nanocomposite mats shows greater storage modulus than pure P(VDF-TrFE) nanofiber over the temperature range of -75°C to 75°C, indicating their enhanced ability to withstand stress. Here, one can observe that the storage modulus continuously improved with the increasing ZnO and TiO_2 nanoparticles content due to the uniform dispersion and strong interaction of the nanofiller with the P(VDF-TrFE) polymer. The loss factor (tanδ) of the synthesized mats is depicted in Fig. 6.9b. The damping factor increased with the increasing content of nanofillers. The peak appeared at around -43°C, assigned to the glass transition temperature (T_g) of P(VDF-TrFE), as shown in Fig. 6.9b. The Tg for nanocomposite membranes increased with ZnO and TiO2, possibly because of the good interaction between composite mat components, reducing the cooperative motion of P(VDF-TrFE) chains [162, 163].

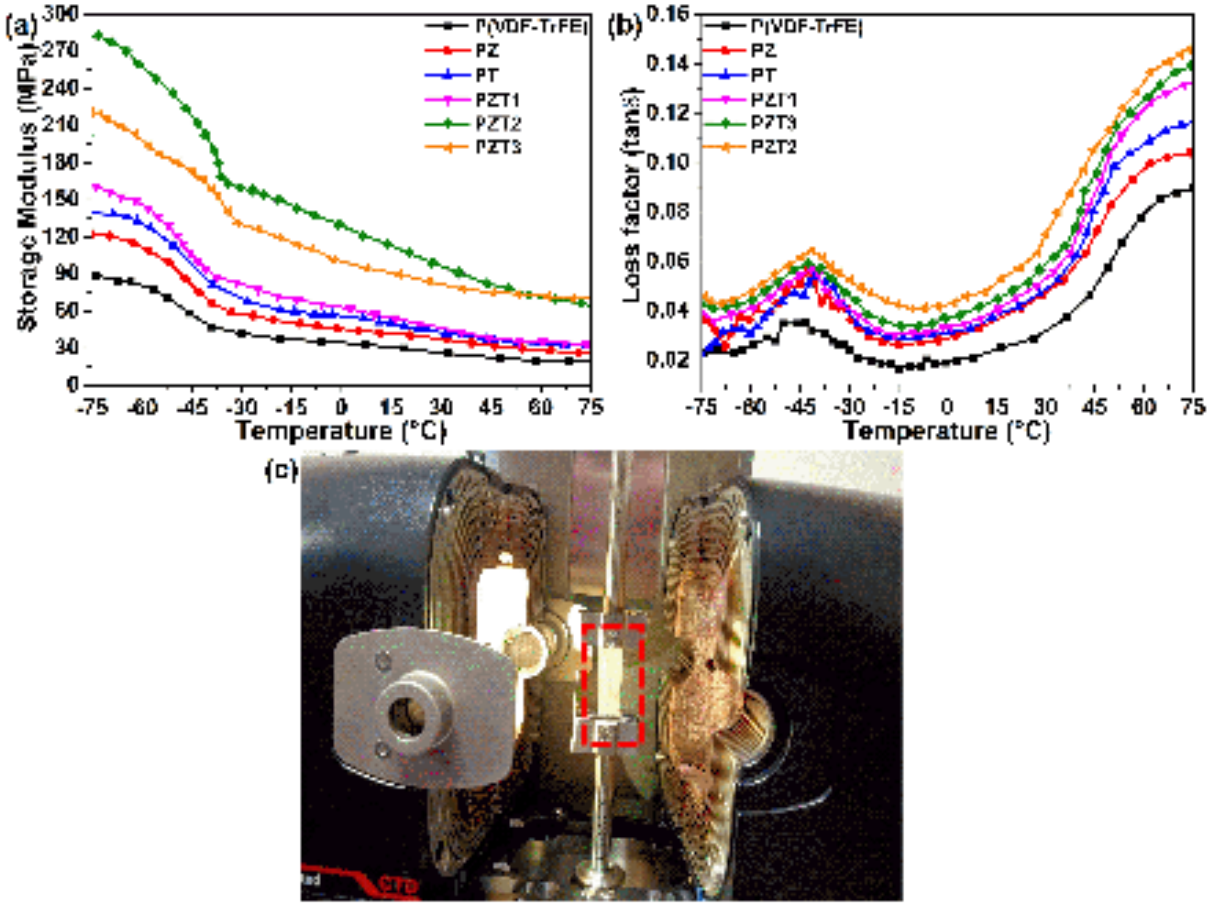

Fig. 6.9: DMA study of the fiber mats for (a) storage modulus, (b) loss factor (tan), and (c) sample in red square bracket tightly hold.

6.3.9 Piezoelectric Output Analysis

The piezoelectric properties of synthesized mats are studied under different loading conditions. The piezoelectric outputs are depicted in Fig. 6.10 for the pure nanofiber and composite mats with varying TiO_2 concentrations. The comparison between the developed device and previously developed PENGs is presented in Table 6.2. It can be found from Table 6.2 that PENGs based on P(VDF-TrFE)/ZnO/TiO_2 composite mats exhibit better piezoelectric performance. The piezoelectric nanogenerator (PENG) devices have been prepared using piezo active layer for the measurement of piezoelectric outputs. The PENG device is subjected to finger tapping, wrist, and elbow bending, and their piezoelectric voltage and currents are recorded using the digital oscilloscope (DSO). The piezoelectric voltage is obtained to be 6.52 V, 8.24 V, 8.8 V, 9.04 V, 23 V, and 11.2 V for the fabricated electrospun mats P(VDF-TrFE), PZ, PT, PZT1, PZT2, and PZT3, respectively.

Table 6.2: Comparision of piezoelectric performance of the P(VDF-TrFE)/ZnO/TiO_2 three phased based PENG designed here with existing PENGs in the literatures.

Piezoelectric materials	Fabrication methods	Peak to Peak V_{oc} (V)	Reference.
PVDF/$BiCl_3$/ZnO	Electrospinning	12	[88]
PVDF/rGO/MoS_2	Solution casting	2.4	[115]
PVDF/Cloisite-30B clay	Far-field electrospinning	4.74	[116]
(Fe-RGO)/PVDF	Solution casting	5.1	[117]
PZT/MWCNT/PVDF	Tape casting	20	[118]
P(VDF-TrFE)/ZnO/MgO	Spin coating	1.89	[119]
PVDF-HFP/$BaTiO_3$/h-BN	Solution casting	2.4	[120]
N Doped 4H-SiC Nanohole Arrays	anodic oxidation	1.35	[164]
PVDF/BTO/rGO	Solution casting	4.1	[165]
PVDF/GO	Electrospinning	16	[166]
P(VDF-HFP)/PANI/ZnS	Electrospinning	3	[167]
PVDF/MNC	Electrospinning	1.05	[168]
P(VDF-TrFE)/ZnO/TiO_2	Far-field electrospinning	23	This work

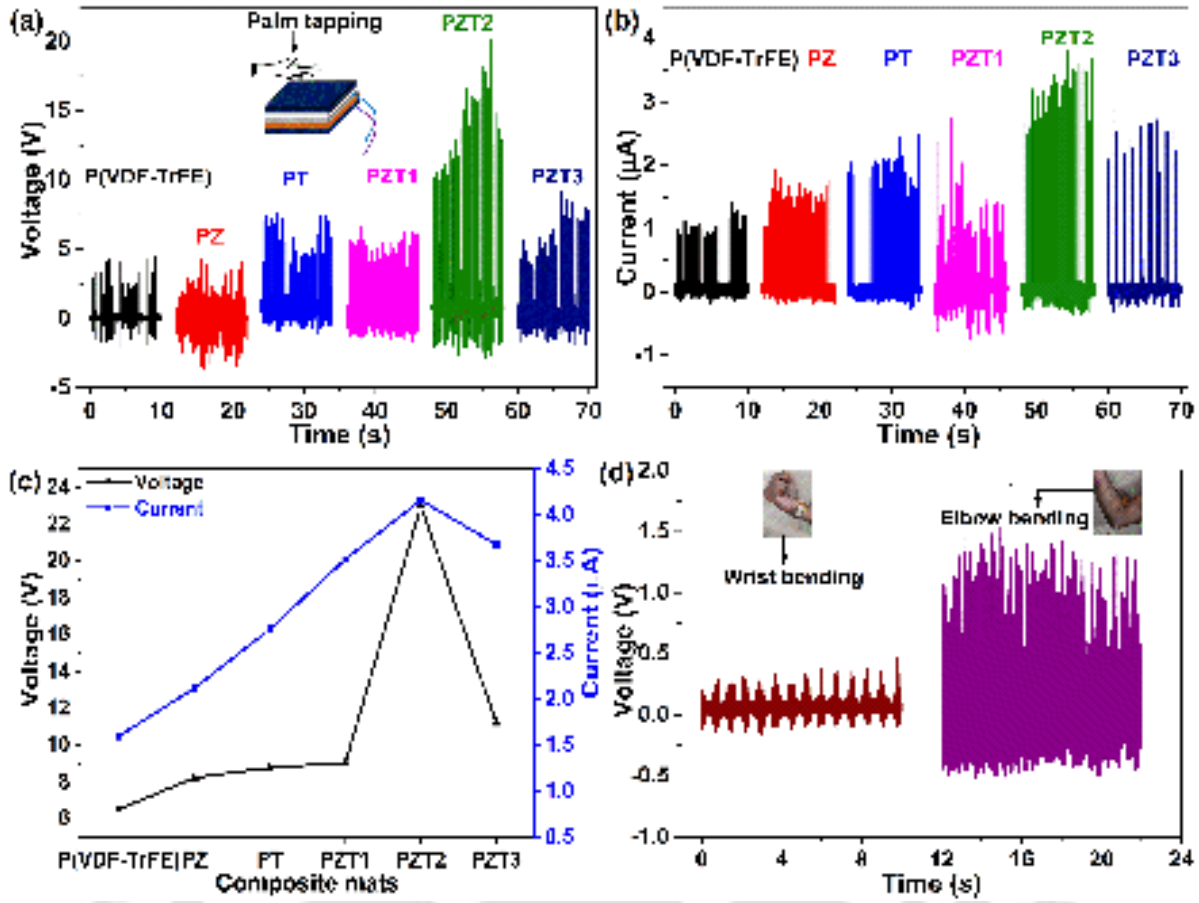

Fig. 6.10: Piezoelectric performance of the P(VDF-TrFE) nanofiber, PZ, PT, PZT1, PZT2, and PZT composite films subjected to finger tapping (a) voltage output, (b) current output, (c) comparison of voltage and current as TiO_2 varying, and (d)wrist and elbow bending.

The electrical current generated by the synthesized mats is to be 1.6 A, 2.12 A, 2.76 A, 3.52 A, 4.16 A, and 3.68 μA across the 10 MΩ resistors for the P(VDF-TrFE), PZ, PT, PZT1, PZT2, and PZT3. The piezoelectric output of the fabricated samle is shown in Table 6.3. The enhancement

Table 6.3: Piezoelectric output of fabricated matbased device .

Sl. no.	Samples	Voltage (V)	Current (μA)
1	PVDF nanofiber	6.52	1.6
2	PZ	8.24	2.12
3	PT	8.8	2.76
4	PZT1	9.24	3.52
5	PZT2	23	4.16
6	PZT3	12.2	3.68

in the piezoelectric performance is due to the synergistic effect of ZnO and TiO_2 nanoparticles with the P(VDF-TrFE) flexible matrix. The piezoelectric voltage for the PZT2 mats is almost 3.6 times greater than the other nanofiber and composite films. Although, it is noted that PZT3 mats have less piezoelectric performance than PZT2 and more than others. The decrease in piezoelectric output is due to the aggregation, which could have occurred with higher TiO_2 loading in the polymeric solution. The piezoelectric performance for the pristine P(VDF-TrFE) nanofiber under the elbow and wrist bending is found 2.80 V and 680 mV, which can be used in flexible electronics and robotics applications. The energy extracted from the PENG is used to power the LED bulb. The video recording for the energy harvesting device subjected to finger tapping, wrist, elbow bending, and led lighting have been carried out, when this device is placed at the body part.

6.4 SUMMARY

P(VDF-TrFE), PZ, PT, PZT1, PZT2, and PZT3 are successfully fabricated using far-field electrospinning method for the wearable device as energy harvesting applications. The electrospun samples are fabricated with varying the TiO_2 concentration. The material characterizations are carried out using FESEM, EDX, XRD, FTIR, UTM, TGA, and DMA. Dielectric test is carried out to study the piezoelectric characteristics of the electrospun fiber. Pure P(VDF-TrFE) fiber and three phase polymer composite are fabricated for comparison. Comparative studies have been conducted on a fabricated P(VDF-TrFE) fiber and a three phase polymer composite. The P(VDF-TrFE)/ZnO/TiO_2 polymer nanocomposite exhibit better piezoelectric property than other fiber structures. The electrospun three phase composites show higher thermal stability and better β phase without doing any electrical poling and thermal treatment. The PZT2 composite mats have greater storage modulus and damping factor compared to any other fiber structures. The energy generating devices (PENG) are designed to power the small wearable device and test the sensing ability for a different signal. Energy generation under various human activities is monitored and found to be greater voltage for the PZT2 composite mat. Fiber efficiency is enhanced by the morphological change, resulting in strong interaction and self-poling of the materials. These PENG based on nanofiber mats have the major advantage of using self-poled fibers as active layers

and flexible electrodes. Electrospun three phase nanocomposite mats are identified as excellent materials for energy harvesting and sensing applications. The analysis reveals that:

(i) The designed piezoelectric device generated current, voltage, and piezoelectric peak power of 4.16 μA, 23 V, and 95.68 μW, respectively.

(ii) The piezoelectric output of hybrid composite mats is almost 3.6 times greater than PENG made from P(VDF-TrFE) fiber, and the increment in the performance is due to the synergistic effect of ZnO and TiO_2 in the P(VDF-TrFE) polymer matrix.

(iii) The ZnO and TiO_2 nanoparticles content significantly effect the fraction of β phase, viscoelastic property and piezoelectric output.

(iv) PENG is used to display real-time demonstrations of body movement detection and biomechanical energy harvesting to power an LED bulb.

Chapter 7

High-performance flexible piezo-triboelectric hybrid nanogenerator based on P(VDF-TrFE)/TiO_2 nanocomposite

7.1 INTRODUCTION

In this chapter, piezo-triboelectric hybrid nanogenerator (HNG) is designed for enhancing energy output performance by integrating piezoelectric and triboelectric effects. The piezoelectric nanogenerator (PENG) has been comprised using the spun P(VDF-TrFE)/TiO_2 mats, while the triboelectric nanogenerator (TENG) has been designed using the Polydimethylsiloxane (PDMS) film. The hybrid nanogenerator has been incorporated as a werable device for the energy scavenging applications. The flexible nanocomposite mats are desirable for the wearable applications. These electrospun mats have been deployed as an active layer in the flexible wearable device. The material system, synthesis of pure P(VDF-TrFE) fiber, P(VDF-TrFE)/TiO_2 nanocomposite, fabrication of hybrid nanogenerator (HNG) device, and testing and measurements of the films, device testing through different instruments have been presented in Sec. 7.2. P(VDF-TrFE)/TiO_2 based nanocomposite mats are fabricated by means of electrospinning method. In this fiber fabrication, P(VDF-TrFE) has been taken 16% wt./vol. and TiO_2 is varied from 3 to 11 wt.%. The influence of TiO_2 has been studied on the perfprmance of P(VDF-TrFE)/TiO_2 nanocomposite films. The detail discussion of P(VDF-TrFE) nanocomposite mats and PDMS films have been presented in Sec. 7.3. It includes microstructural characterization, surface roughness analysis, crystalline phase analysis, thermal stability, electroactive β phase variation, tensile testing, and DMA study. The various

techniques have been incorporated to accomplish these study. Furthermore, P(VDF-TrFE)/TiO_2 nanocomposite and PDMS based hybrid nanogenerator as wearable device have been demonstrated with enhanced piezoelectric performance. The impact of TiO_2 nanofiller on the performance of hybrid nanogenerator (HNG) has been discussed in detail. This hybrid nanogenerator is capable of miniaturize the system as well as produce more energy output to power small electronic devices. In this work, TiO_2 incorporated P(VDF-TrFE) fiber membranes are deposited on aluminium foil using electrospinning to design hybrid nanogenerator for energy harvesting from simple manual activity like finger tapping. The hybrid nanogenerator device produce current of 5.36 μA across 10 MΩ resistor and voltage of 52 V, respectively. The efficiency of these nanogenerators is better than that of most nanogenerators fabricated with complex and sophisticated approaches. The performance of HNG has been compared with PENG and TENG. The enhancement in performance of P(VDF-TrFE)/TiO_2 mat based hybrid nanogenerator opens up possibilities for developing a low-cost biomechanical energy harvester and could be an excellent power source for wearable electronic devices.

7.2 EXPERIMENTAL

7.2.1 Materials

Poly(vinylidene fluoride-trifluoro ethylene) P(VDF-TrFE) polymer, molecular weight (M_w = 3,00,000), consisting VDF 75% and TrFE 25% and titanium oxide (TiO_2) nanofiller (100 nm particle size, 99.5% trace metals basis) are purchased through Sigma Aldrich. Additionally, Acetone (ACE) and N, N-Dimethylformamide (DMF) (anhydrous, 99.8%) and are supplied by Sigma Aldrich. Every single chemical is utilized in its original form in the fabrication process.

7.2.2 Synthesis of P(VDF-TrFE)/TiO_2 Nanocomposite

P(VDF-TrFE)/TiO_2 electrospun nanocomposite membranes have been synthesized through the electrospinning (Maker: E-Spin Nanotech, India) technique. Five different uniform solutions have been made using DMF, polymer P(VDF-TrFE), and ceramic (TiO_2). TiO_2 nanoparticles with 3, 5, 8, and 11 wt.% are initially added to five different beakers containing DMF solvent. This solution

has been sonicated for 60 minutes following stirring. Thereafter, 3 ml of DMF solvent is used to dissolve the P(VDF-TrFE) pellets with 16% wt./vol. concentration and then magnetic stirring has been carried out for eight hours (h), speed 500 rpm, and at 60°C temperature. Further, the stirred P(VDF-TrFE)/TiO_2 solution is homogenized through sonication for one hour. The sonicated solution is desiccated for 40 minutes to remove bubbles from the solution. The prepared solutions are filled into plastic syringes, which is then inserted into slots near the syringe pump. As part of the electrospinning process, aluminium foil is covered on cylindrical rotating collector drum, which is used as a deposition substrate of charged jets. Electrospinning for nanocomposite fiber has been carried out in accordance with the below mentioned parameters, which ensure a smooth process performance. The flight distance is set 15 cm, the flow rate is 10 µl/min, the drum speed is maintained at 1200±100 rpm, the temperature of the chamber is controlled at 28°C, and 20 kV power supply has been used constantly during the fabrication process. The ceiling fan has been kept running inside the chamber to remove moisture during fibrous structure fabrication. The current produced during electrospinning process is 3±1 µA. The fibrous mats are fabricated by the deposition of electrified jets of solution for 100 minutes on a drum collector. The free-standing fiber mats are removed from the substrate (aluminum foil) and employed in energy harvesting device fabrication. Five different nanocomposite mats are fabricated with fix content of P(VDF-TrFE) matrix and changing TiO_2 nanoparticles. The prepared test samples are referred to as follows: SA-1: pure nanofiber fabricated with 16% wt./vol. concentration of P(VDF-TrFE) polymer, SA-2: P(VDF-TrFE)/TiO_2 nanocomposite prepared with P(VDF-TrFE) 16% wt./vol. and 3 wt.% of TiO_2 nanofiller, SA-3: P(VDF-TrFE)/TiO_2 nanocomposite fabricated with P(VDF-TrFE) 16% wt./vol. and 5 wt.% of TiO_2 nanoparticles, SA-4: P(VDF-TrFE)/TiO_2 nanocomposite fabricated with P(VDF-TrFE) 16% wt./vol. and 8 wt.% of TiO_2 nanoparticles, and SA-5: P(VDF-TrFE)/TiO_2 nanocomposite fabricated with P(VDF-TrFE) 16% wt./vol. and 11 wt.% of TiO_2 nanoparticles. The quantities of P(VDF-TrFE) and TiO_2 particles used in making required solution for electrospinning process is presented in Table 7.1.

Table 7.1: Amount of matrix and nanofiller concentrations for electrospun mats.

Sample no.	Wt. of P(VDF-TrFE) (gm)	Volume of DMF (ml)	Wt. of TiO_2 (gm)
SA-1	0.42	2.6	0
SA-2	0.42	2.6	0.014
SA-3	0.42	2.6	0.023
SA-4	0.42	2.6	0.038
SA-5	0.42	2.6	0.055

7.2.3 Fabrication of P(VDF-TrFE)/TiO_2 Based Hybrid Nanogenerators

Fig. 7.1 shows the schematic diagram of the hybrid nanogenerator. Here, the P(VDF-TrFE)/TiO_2 nanocomposite is coupled with polydimethylsiloxane (PDMS) film. The silver paste is coated on both sides of the composite film to make the electrical connections. Further, silver paste is coated on one side of the polydimethylsiloxane (PDMS) film. The copper wires are fixed on the metal electrodes with the help of copper tape. The effective working area of the composite film for the nanogenerator device is 2cm×1.5cm. Mechanical vibration is applied from top surface of the device through an exciter, as presented in Fig. 7.1. In the device structure, as shown in Fig. 7.1, silver paste

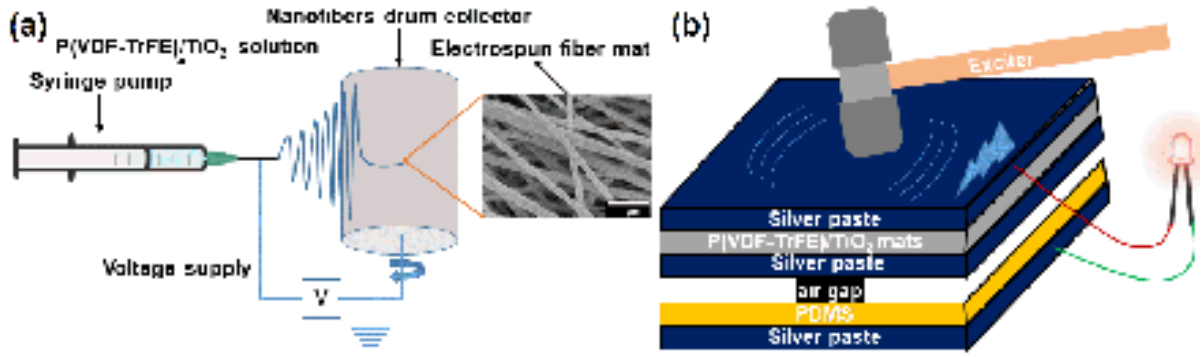

Fig. 7.1: Schematic diagram of (a) fabrication of electrospun mat and (b) hybrid nanogenerator comprised of piezo and triboelectric nanogenerator.

deposited over PDMS film and P(VDF-TrFE)/TiO_2 composite membranes gives the triboelectric output, while the silver paste coated on both sides of the nanocomposite film gives the piezoelectric output. The piezoelectric and triboelectric output is connected to two different bridge rectifiers. To get the hybrid nanogenerator's combined output, the positive and negative terminals of bridge

rectifiers are fed together using the digital storage oscilloscope.

7.2.4 Characterization and Measurements

P(VDF-TrFE)/TiO_2 nanocomposite membranes have been synthesized using E-spin setup supplied by E-Spin NANOTECH, India. The morphology of surface and structural characteristics of P(VDF-TrFE) nanofiber and P(VDF-TrFE)/TiO_2 nanocomposite mats have been investigated using field emission scanning electron microscopy (FESEM) (Gemini SEM 500, Maker: Zeiss). This characterization is conducted with a magnification of 7 kX and an accelerating voltage of 5 kV. The average thickness of the electrospun film is measured by selecting ten different locations on fabricated mats with the help of digital micrometer (293-240-30, Maker: Mitutoyo). Atomic force microscopy (AFM) (MFP-3D-BIO, Maker: Oxford Instruments) has been employed to investigate the topography and surface roughness of the P(VDF-TrFE)/TiO_2 nanocomposite films. X-ray diffraction (XRD) test has been carried out to confirm the presence of crystalline phases in the synthesized fibrous samples. The XRD pattern (Smartlab, Maker: Rigaku Technologies) is obtained on a diffractometer for nanocomposite films with the help of Cu-Kα radiation 1.54 $\mathring{A}$ scanned at 5 degree/minute with a 0.02 step size in a 2θ range from 10° to 70°. The presence of the electroactive beta (β) phase and its effect on the nanocomposite sample has been studied with the help of Fourier transform infrared (FTIR) spectra (Spectrum two, Maker: PerkinElmer). This test has been performed over the wavenumber range of 400-1600 cm^{-1} in attenuated total reflection (ATR) mode. Thermo gravimetric analysis (TGA) (STA7200, HITACHI) is performed at the rate of 10 degree/min. and test amples are subjected to temperature sweep from 25°C to 700°C. Tensile testing of these nanocomposite has been performed using Electromechanical universal testing machine (5kN) (Z005TN Proline, Maker: ZwickRoell). This test has been carried out with a cross-head speed of 5 mm/min. The dynamic mechanical analysis (DMA) (Physica MCR 702, Maker: Anton Paar) is performed to study the effect of TiO_2 nanofiller on damping factor and storage modulus of P(VDF-TrFE)/TiO_2 nanocomposite mats under tensile mode on rectangular sample (2.5×1 cm^2). This study has been analysed for temperature variation condition from -70°C to 70°C at frequency 1 Hz and strain rate of 0.025%. The preload (0.1 N) is applied for making the sample tight prior to

the test. The electrical output of spun nanocomposite based nanogenerators is measured with the aid of digital oscilloscope (GDS-2102A, Maker: GWInSTEK) under the different kind of external load at ambient conditions.

7.3 RESULTS AND DISCSSION

7.3.1 Surface Morphological Study of P(VDF-TrFE) and TiO_2 Based Electrospun Films

The morphology of P(VDF-TrFE) and P(VDF-TrFE)/TiO_2 composite with changing TiO_2 concentration is acquired using FESEM operated with magnification 7 kX and accelerating voltage 5 kV. The FESEM images for the fabricated mat are shown in Fig. 7.2. The TiO_2 nanoparticles with higher concentration in the P(VDF-TrFE) solution are accumulated as presented in FESEM images. The average diameter values of SA-1, SA-2, SA-3, SA-4, and SA-5 mats are 196.925 nm, 108.82 nm, 158.825 nm, 114.12 nm, and 150.15 nm, respectively. The diameter (average value) of nanocomposite mat reduce with the dispersion of TiO_2 nanoparticles due to the increment in conductivity of the solution. The phenomenon could be elaborated by considering the working of electrospinning technique. It works on the principle of Coulomb force (F=qE) which is exerted on the charge (q) on the fluid surface due to the applied electric field (E) [106, 169]. In the presence of an electric field of the same strength, a P(VDF-TrFE)/TiO_2 nanocomposite jet undergoes a stronger force than a P(VDF-TrFE) jet, resulting in reduced fiber diameter after TiO_2 loading.

7.3.2 Atomic Force Microscopy (AFM) Analysis

Fig. 7.3 depicts the AFM images of electrospun P(VDF-TrFE) and P(VDF-TrFE)/TiO_2 nanocomposite mats. The root mean square roughness of pure P(VDF-TrFE) and P(VDF-TrFE)/TiO_2 with changing TiO_2 content as 3, 5, 8, and 11 wt.% is calculated as 124.6, 234.5, 377.1, 539.8 and 518.2 nm. The surface roughness of P(VDF-TrFE)/TiO_2 nanocomposite films increased as against P(VDF-TrFE) due to the interaction of TiO_2 nanofillers in the P(VDF-TrFE) film. As surface roughness increases, more effective areas are available for charges to reside. This causes rise in the surface charge density of the P(VDF-TrFE) surface upon contact with other materials. Thus, the P(VDF-TrFE)/TiO_2 nanocomposite samples with rough surfaces are expected to exhibit greater

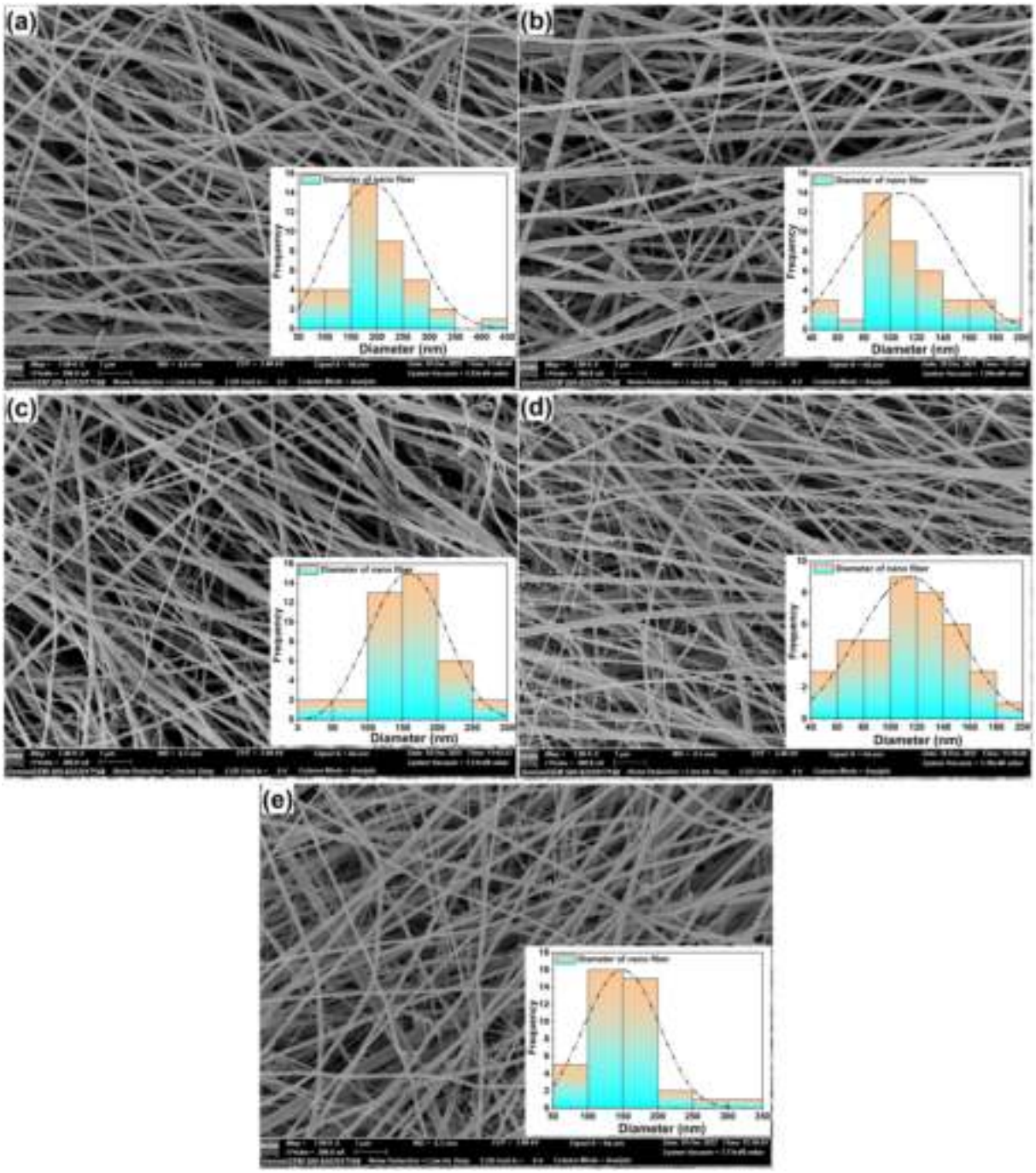

Fig. 7.2: FESEM images with fiber diameter distribution of the synthesized mats (a) P(VDF-TrFE) (b) P(VDF-TrFE)/TiO_2 nanocomposites with varying TiO_2 concentrations.

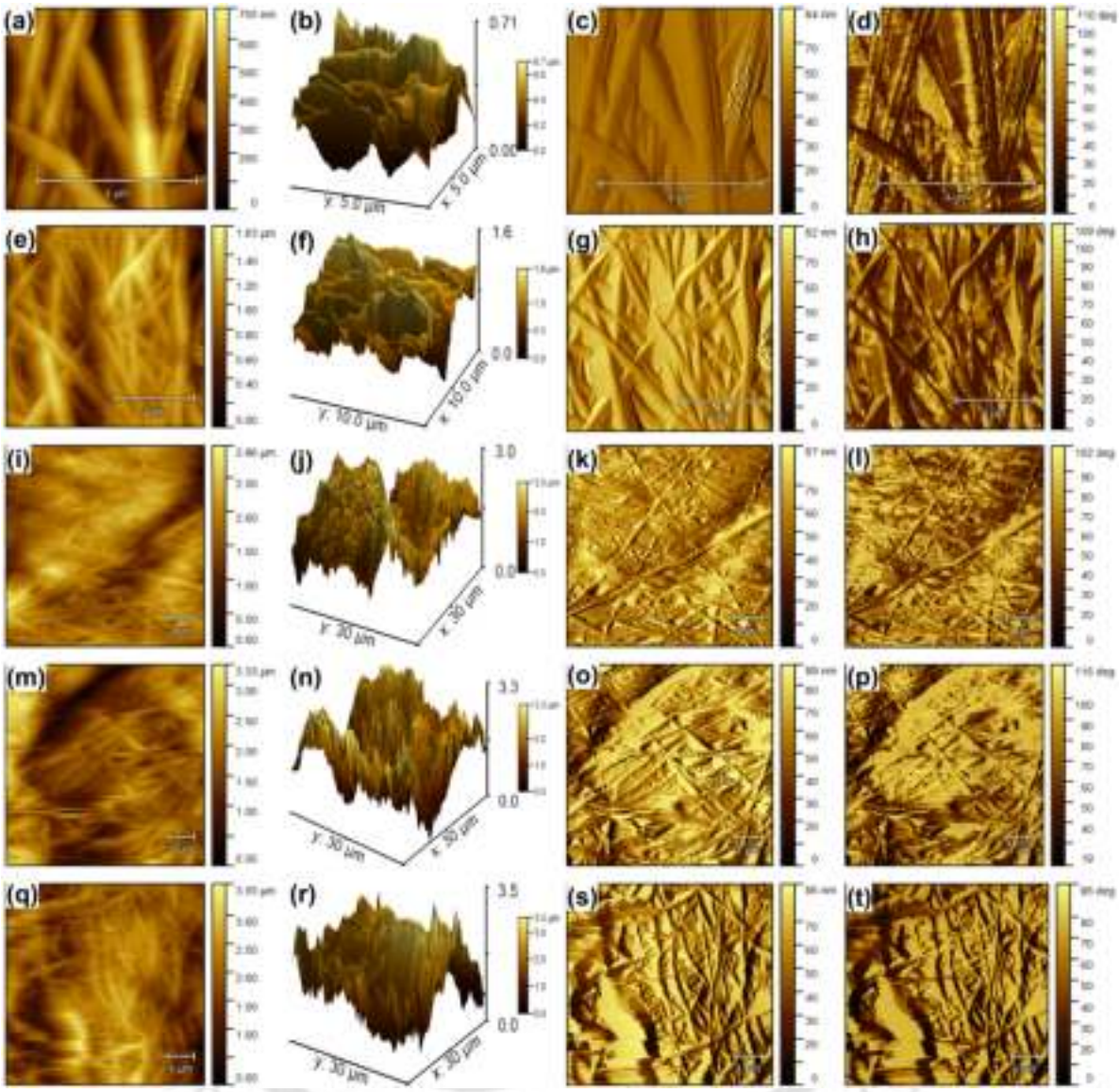

Fig. 7.3: AFM analysis of (a,e,i,m,q) height image, (b,f,j,n,r) 3D view of height image, (c,g,k,o,s) amplitude image, and (d,h,l,p,t) phase image of SA-1, SA-2, SA-3, SA-4, and SA-5.

triboelectrification than pristine P(VDF-TrFE) fiber [170].

7.3.3 XRD Analysis

XRD test has been conducted on five electrospun nanocomposite mats to confirm electroactive β phase crystal structure formation and presence of TiO_2 in P(VDF-TrFE) as shown in Fig. 7.4a. In crystalline materials, diffraction occurs due to the interaction between X-rays and their periodically aligned atoms. Three parameters characterize a diffraction peak: peak intensity, peak position, and peak profile shape. The characteristic peak at $2\theta = 19.89°$ with miller indices (200) and (110) belongs to the electroactive β phase of P(VDF-TrFE) matrix [171]. This shows that P(VDF-TrFE)

nanofibers have a dominant ferroelectric phase. Diffraction peaks occurred at $2\theta = 27.4°$, 36°, 44.1° and 56.5° represent miller indices of (110), (200), (211), and (220) respectively, which corresponds to rutile phase of TiO_2 nanoparticles [172]. Moreover, the intensity of the β phase of P(VDF-TrFE) increases first and then decreases with an increment in TiO_2 content. This effect could be attributed to molecular interaction between the polymer matrix and TiO_2 particles. Reduction in β phase peak intensity was observed when TiO_2 content reached 11 wt.%. This behavior could be due to the agglomeration effect due to excessive TiO_2 loading. These findings are direct evidence of the presence of TiO_2 in the P(VDF-TrFE) mats. It is observed that the phase of P(VDF-TrFE) matrix is not altered with the addition of TiO_2.

7.3.4 FTIR Analysis

FT-IR spectra of nanocomposite mats have been carried out to further confirm regarding existence of electroactive β phase, which is essential for piezoelectric behavior. Most of the IR vibrations of P(VDF-TrFE) most frequently observed in the range of 600 to 1500 cm^{-1} as presented in Fig. 7.4b. Absorption peaks occurred at 841, 881, 1177, 1285, and 1400 cm^{-1} belongs to β phase of P(VDF-TrFE)/TiO_2 composite membranes. Different vibrational modes present in P(VDF-TrFE) lead to specific absorption spectra. The characteristic peaks at 841, 1285, and 1400 cm^{-1} appeared due to CH_2 rocking and CF_2 anti-symmetric stretching, CF_2 anti-symmetric stretching and rocking, and CH_2 wagging and bending, respectively [173]. Moreover, the effect of TiO_2 reinforcement on the fraction of β phase content (F(β)) is studied using Gregorios relation [174]:

$$F(\beta) = \frac{I_{841}}{(\frac{K_\beta}{K_\alpha}) \times I_{763} + I_{841}} \tag{7.1}$$

Here, I_{841} and I_{763} are absorption intensities for β and α phases respectively. K_{841} and K_{763} are absorption coefficients having values 6.1×10^4 and 7.7×10^4 cm^2mol^{-1}, respectively. Fraction of electroactive β phase content of 74, 78, 81, 87 and 83% is obtained for samples SA-1, SA-2, SA-3, SA-4, and SA-5, respectively. F(β) value initially increases up to 8 wt.% of TiO_2 loading and then decreases (Fig. 7.4c). Sample SA-4 shows maximum β phase content, which is 9% more than that of P(VDF-TrFE) nanofiber mat. The β phase increment can be attributed to reduced fiber diameter and interaction between dipole and surface charge [172]. TiO_2 reinforcement has a positive impact

on the electroactive β phase fraction. However, particle aggregation and networking reduced the value at higher loading.

7.3.5 Thermo-gravimetric Analysis (TGA)

Effect of TiO_2 fillers on thermal stability of P(VDF-TrFE) and its composite has been studied using TGA test as depicted in Fig. 7.4d. This test is performed over a temperature range of 30-700°C with a heating rate of 10°C/min, gas pressure of 2 bar and gas flow rate of 19.8 ml/min in nitrogen atmosphere. Temperature corresponding to 5% loss of its original mass is called the onset of thermal degradation temperature (T_d). The thermal degradation of electrospun mats primarily occurred in two stages in the measured temperature range. Thermal decomposition of P(VDF-TRFE) nanofiber mat is observed at 452°C. 83% of the P(VDF-TrFE) mass is lost at a temperature of about 503°C. The values of T_d shows a reduction upon increasing TiO_2 reinforcement. This behavior indicates reduced thermal stability of electrospun nanocomposites as compared to P(VDF-TrFE) mat. As TiO_2 is thermally stable and does not decompose below 600°C [175]. The probable cause behind the reduction in thermal stability of electrospun nanocomposites is attributed to existence of metal oxide catalyzed oxidative decomposition pathways in the nanocomposite [176, 177]. This results in thermal degradation of an organic structure due to the thermal catalytic effect of TiO_2 [178]. However, the addition of TiO_2 nanoparticles enhanced residual mass (m_r) values. Sample SA-4 shows the maximum amount of residual mass among all the samples. This increment in m_r values is ascribed to a reaction between Ti ion chelating ligands and fluoride synthesis during backbone homolysis in the P(VDF-TrFE) decomposition, which may produce new, difficult-to-decompose products [161]. The values of T_d and m_r for electrospun composite samples are enlisted in Table 7.2.

7.3.6 Mechanical Characterization

A piezoelectric material must have excellent mechanical properties if it is to be employed in energy scavenging and self-powering devices [120]. The uniaxial stress-strain plots of P(VDF-TrFE) and P(VDF-TrFE)/TiO_2 nanocomposites are presented in Fig. 7.5. Elastic modulus, breaking strain, and tensile strength of electrospun mats are calculated using tensile testing on UTM instrument.

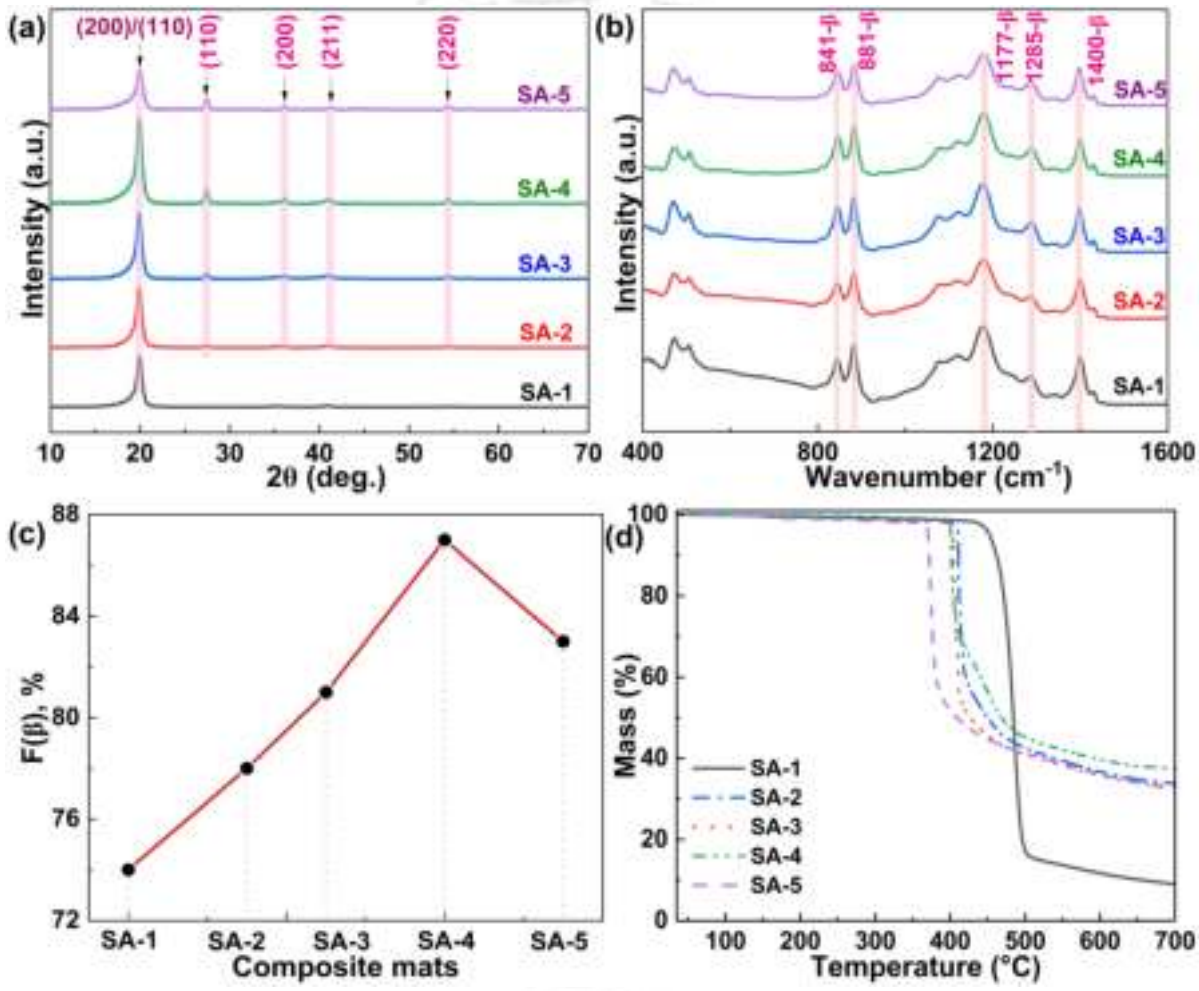

Fig. 7.4: XRD pattern of (a) nanofiber composite samples, (b) FTIR plot, (c) variation in β phase fraction content, and (d) TGA curve for the synthesized composite mats with TiO_2 loading.

Table 7.2: TGA parameters for electrospun P(VDF-TrFE) and its nanocomposites.

Sample no.	T_d (°C)	m_r (%)
SA-1	452.27	8.16
SA-2	411.31	32.26
SA-3	403.94	32.32
SA-4	400.75	35.35
SA-5	370.56	31.24

The samples for the test are prepared as per ASTM standard D882-12. Each mat is tested five times. The length and width of the prospective test sample is 55 mm and 12 mm respectively. An electrospun mat sample is fixed in upper and lower jaw of the instrument using sand paper. The stress versus strain test has been performed at room temperature condition using a fixed cross-head speed of 5 mm/min. Tensile stress and strain are recorded till the test samples are fractured. TiO_2 loading is effective in enhancing tensile strength and elastic modulus of electrospun nanocomposite mats. The tensile strength values are increased up to 8 wt.% of TiO_2 addition, but decreased beyond 8 wt.% of loading. TiO_2 nanoparticles behave as cross-link in between P(VDF-TrFE) chains and provide enhanced localized strength causing retardation of crack or cavity growth. This increases load bearing capacity of nanocomposites. When TiO_2 reaches a critical loading value, tensile strength reduces due to particle agglomeration. Nanocomposites with agglomerated particles would likely experience stress concentration due to defect generation. This results in a reduction of tensile strength [179]. Sample SA-4 showed maximum tensile strength (19.3±1.6 MPa) whereas SA-5 showed maximum elastic modulus (30.9±1.7 MPa). Reduction in breaking strain in nanocomposite mats is observed on increment in TiO_2 loading quantity. The values of tensile strength, elastic modulus and breaking strain for the fabricated films are listed in Table 7.3.

7.3.7 Dynamic Mechanical Analysis (DMA)

DMA test has been performed to examine the viscoelastic behaviour of the electrospun mats and compare the stiffness and deformation resistance of the nanofiber mats and composite membranes.

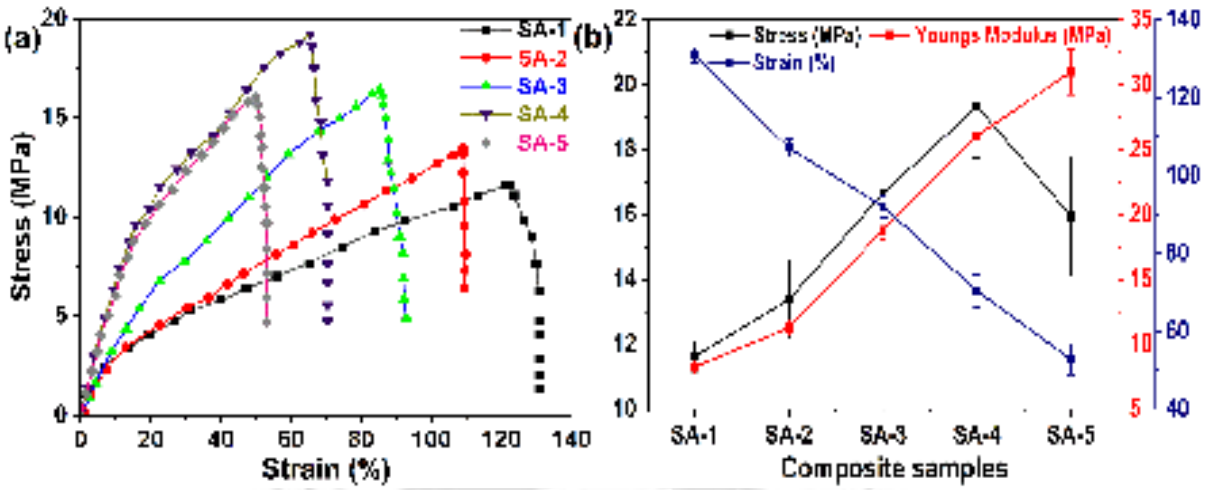

Fig. 7.5: Tensile testing of (a) fabricated nanofiber composite, (b) variation in elastic modulus, tensile strength, and strain.

Table 7.3: Tensile strength, elastic modulus, and breaking strain of spun mats at varying nanofiller concentration.

Samples	Tensile strength (MPa)	Elastic modulus (MPa)	Breaking strain (%)
SA-1	11.6±0.5	8.2±0.5	130.8±1.9
SA-2	13.4±1.2	11.2±0.6	107.1±2.1
SA-3	16.6±1.5	18.8±0.6	92±2.9
SA-4	19.3±1.6	26±0.9	70.3±4
SA-5	15.9±1.8	30.9±1.7	52.7±3.9

In this analysis, the role of TiO_2 reinforcement on damping factor and storage modulus of the electrospun membranes is analysed under tensile mode. The rectangular test samples are prepared with 25 mm length and 10 mm width, while the gauge length is 18 mm. The specimen is fixed in between lower and upper jaw of the instrument with a preload of 0.1 N. Fig. 7.6 represents the DMA test curves for samples SA-1, SA-2, SA-3, SA-4, and SA-5. Nanocomposite membranes display higher storage modulus as compared to pure P(VDF-TrFE) in the temperature range of -70°C to 70°C, demonstrating its improved capability to withstand tensile stress. Storage modulus values enhance steadily with the increasing TiO_2 concentration (Fig. 7.6a). This could be attributed to thorough dispersion and strong interaction of the nanofillers with the P(VDF-TrFE) matrix. The loss factor ($\tan\delta$) of the electrospun membranes is presented in Fig. 7.6b. The damping factor values

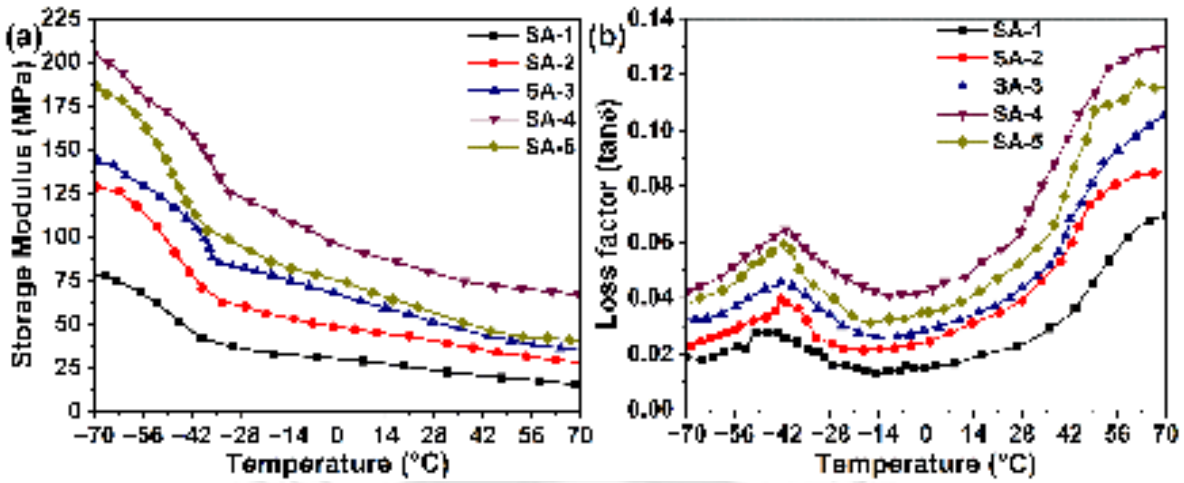

Fig. 7.6: DMA testing of electrospun fiber membranes for (a) storage modulus, (b) loss factor (tan) with varying TiO_2.

continuously enhance with increasing TiO_2 nanofiller concentrations. As per Fig. 7.6b, the peak observed at about -43°C represents the glass transition temperature (T_g) of P(VDF-TrFE). The T_g for electrospun nanocomposites enhance with TiO_2 content, which could be due to excellent interaction between nanocomposite membranes, decreasing the cooperative motion of P(VDF-TrFE) chains [162, 163].

7.3.8 Working Principle of Hybrid Nanogenerator

The schematic figure and working principle of hybrid nanogenerator is shown in Fig. 7.7. The piezoelectric output of the PENG depends on the amount of stress applied while the TENG output rely on the contact velocity and gap. Initially, air gap is maintained between the two nanogenerators (Fig. 7.7), which is used as separation gap for the triboelectric nanogenerator. Due to the contact and detachment process, both the nanogenerators create output charges that superimpose on each other, thereby increasing power output of hybrid nanogenerator. It is presented in Fig. 7.7i that there are no charges generated when the PENG and the TENG are separated. When the external load is subjected on the hybrid nanogenerator using finger tapping, a deformation of P(VDF-TrFE)/TiO_2 mat causes piezoelectric charge generation as depicted in Fig. 7.7ii. At the same instant, equivalent charges are induced on the bottom electrode of piezo active layer and the upper surface of PDMS layer. The charges on bottom electrode of P(VDF-TrFE) and bottom surface of P(VDF-TrFE) are similar as this electrode serves as a contact to accumulate the

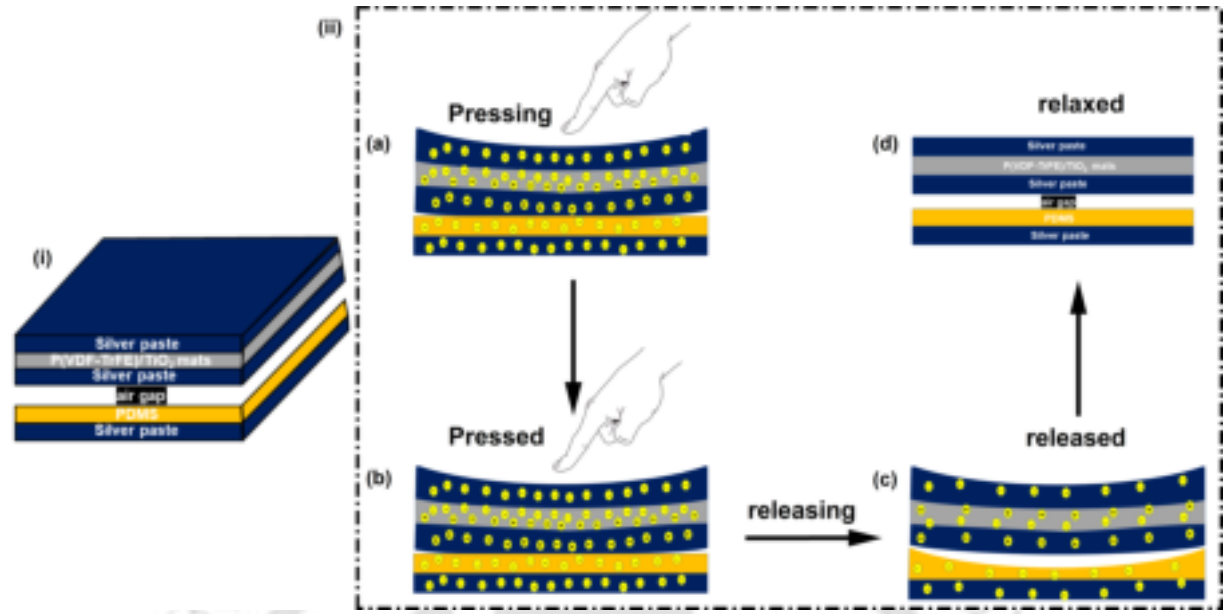

Fig. 7.7: (i) Schematic and (ii) working mechanism of the hybrid nanogenerator and distribution of charges on PENG and TENG.

charges generated on P(VDF-TrFE) mat. The bottom electrode of piezo layer and PDMS forms triboelectric nanogenerator in which negative charges are generated on PDMS layer. Thus, the piezoelectric current flows from the top electrode to bottom electrode of piezoelectric film while the triboelectric current flows from bottom electrode of PDMS to bottom electrode of P(VDF-TrFE) film. The overall charges increases when both the TENG and PENG are combined under parallel combination. As soon as the load is relieved, the hybrid nanogenerator returns to its original position, and in that case P(VDF-TrFE)/TiO_2 undergoes compressive strain, generating opposite charges compared to the load/stress process. Additionally, the neutralization of the triboelectric charges takes place, resulting the current flow in opposite direction of voltage generation. Due to the fact that piezoelectric NG and triboelectric NG are connected in parallel arrangement, the overall charges also increase in the opposite direction.

7.3.9 Piezoelectric Performance of Nanogenerators

The comparison of the piezoelectric performance of PENG, TENG, and HNG using P(VDF-TrFE)/TiO_2 membranes in varied loading conditions is presented (Fig. 7.8). The piezoelectric outputs for the PENGs are illustrated in Fig. 7.8a for the P(VDF-TrFE) nanofiber and composite membranes with varying TiO_2 (0%, 3%, 5%, 8%, 11%) weight percentage. The nanogenerators

are continuously applied stress through the finger tapping. The output voltage is obtained for the P(VDF-TrFE) based nanogenerator is 4V. To obtain more piezoelectric output, TiO_2 integrated P(VDF-TrFE) mat based PENG has been designed and its output voltage is measured as shown in Fig. 7.8a. The electrical voltage for P(VDF-TrFE)/TiO_2 are 6.16 V. 7.32 V, 12.2 V, and 10.2 V for SA-2, SA-3, SA-4, and SA-5, respectively. The piezoelectric output of P(VDF-TrFE)/TiO_2 composite film based nanogenerator increases gradually with the increase in TiO_2 content. The greater piezoelectric output is generated by the SA-4 film based nanogenerator, which is 3 times that of pure P(VDF-TrFE) film based nanogenerator. It has been observed in Fig. 7.8a that the voltage is enhanced till the 8 wt.% and then starts reducing with further increment in weight percentage. The decline in piezoelectric performance above 8 wt.% TiO_2 could be attributed to TiO_2 agglomeration in the P(VDF-TrFE) matrix, which can be observed in the FESEM images given in Fig. 7.2. The improvement in the output voltage of nanogenerators after the inclusion of TiO_2 in the flexible matrix can be due to increase in fraction of electroactive β phase content of P(VDF-TrFE). The above mentioned results are also in line with the available literature in which the piezoelectric performance is enhanced with the incorporation of nanofillers [106, 180, 181]. To further enhance the energy harvesting capability from biomechanical to electrical energy, the hybrid nanogenerators are fabricated, which is comprised of both piezoelectric and triboelectric effects. For this, fabricated electrospun mats are coupled with PDMS film in the contact separation mode as shown in Fig. 7.7i. As can be seen in Fig. 7.7i, the HNG is a amalgamation of two different nanogenerators, the top and bottom layer generates triboelectric output whereas upper layer gives piezoelectric output. Piezoelectric and triboelectric outputs are separately measured before measuring the hybrid output of the nanogenerator. The electrical voltage of PENG, TENG, and HNG are given in Table 7.4 The triboelectric output voltage for SA-1, SA-2, SA-3, SA-4, and SA-5 with PDMS layer are measured 10 V, 13 V, 16.8 V, 19.6 V, and 17.6 V, respectively (Fig. 7.8b). Piezoelectric output shows the same pattern as triboelectric output. Then output response for the hybrid nanogenerator is measured. The hybrid nanogenerator is subjected to fingertip, impact load using hammer, and their piezoelectric outputs are recorded with the help of digital oscilloscope (DSO). The output voltages obtained under finger tapping load conditions are 15.8 V, 20.2 V, 23.8 V, 35.2 V, and 30.2

V (Fig. 7.8c). Whereas the output voltage of HNG is 26.4 V, 29.6 V, 34.8 V, 52 V, and 41.5 V under hammer tapping (Fig. 7.8d). The maximum piezoelectric voltage generated for the PENG, TENG, and HNG to be 12.2 V, 19.6 V, and 52 V for the synthesized electrospun membranes P(VDF-TrFE)/TiO_2 (SA-4). The electrical current is obtained for PENG, TENG, and HNG based on manufactured mat SA-4 subjected to fingertip is found to be 1.8 μA, 2.88 μA, and 5.36 μA across the 10 MΩ resistors as presented in Fig. 7.8e. The improvement in the device performance is due to the strong interfacial interaction in between the flexible P(VDF-TrFE) matrix and TiO_2 nanoparticles. The electrical voltage for SA-4 based HNG is almost 2 times greater than HNG made from pure P(VDF-TrFE). The same enhancement is recorded for the SA-4 based PENG and TENG. Although, it is noted that SA-5 mat has less piezoelectric performance than SA-4 and more than others. The output voltage performance comparison for PENG, TENG and HNG is depicted in Fig. 7.8f. Piezoelectric output decreased due to agglomeration, which could have occurred with higher TiO_2 loadings. The results of this study are compared with previously reported PVDF-MoS2 nanocomposite based mechanical energy harvesters in Table 7.5. It is evident from the below table that the P(VDF-TrFE) based nanogenerator demonstrated a better response as compared to other mechanical energy harvesters studied. These devices are placed at the elbow, wrist, and knee, and they detect the movement of the body parts. Therefore, it can be incorporated as a wearable device.

Table 7.4: Piezoelectric output of fabricated mat based device .

Samples	PENG device	TENG device	HNG device subjected to fingertip	HNG device hammer loading
SA-1	4 V	10 V	15.8 V	26.4 V
SA-2	6.16 V	13 V	20.2 V	29.6 V
SA-3	7.32 V	16.8 V	23.8 V	34.8 V
SA-4	12.2 V	19.6 V	35.2 V	52 V
SA-5	10.2 V	17.6 V	30.2 V	41.5 V

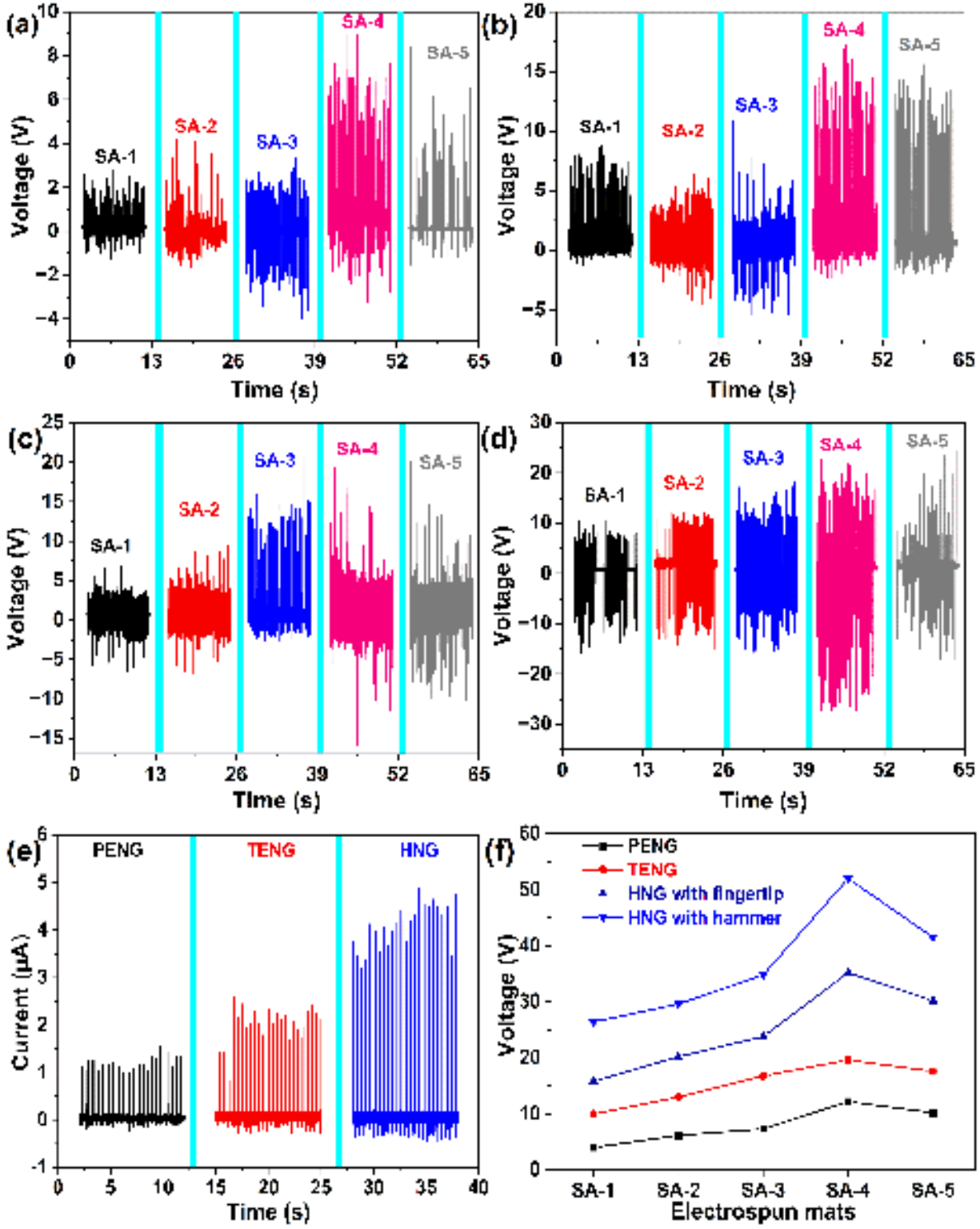

Fig. 7.8: Graphs showing the voltage output of (a) PENG, (b) TENG, (c) HNG with fingertip, (d) HNG through exciter, (e) current output comparison, and (f) voltage output comparison of PENG, TENG, and HNG.

Table 7.5: Comparison of nanogenerator's performance for P(VDF-TrFE)/TiO_2 based mechanical energy harvesters with the existing HNGs in the literatures.

Device structure	Voltage (V)	Current (μA)	Fabrication method	Reference
PVDF/TiO_2	5.45	-	Solution casting	[163]
PVDF/TiO_2	20	0.176	Electrospinning	[172]
PVDF/MoS_2	50	0.03	Electrospinning	[121]
P(VDF-TrFE)-PDMS/MWCNTs	25	-	Electrospinning	[122]
PVDF/PET	34.6	6.6	Commercially	[123]
MoS_2-PVDF/PDMS	35	20.8	Drop casting	[182]
P(VDF-TrFE)-TiO_2 /PDMS	52	5.36	Electrospinning	Present work

7.4 SUMMARY

The piezo-triboelectric hybrid nanogenerator has been developed for energy harvesting from waste biomechanical energy and convert it into the electrical energy. The high performance self-poled hybrid nanogenerators (HNGs) are fabricated successfully using the combination of P(VDF-TrFE), P(VDF-TrFE)/TiO_2, and PDMS mats. The testing and measurements of electrospun nanocomposite mats have been successfully conducted using the FESEM, AFM, XRD, FTIR, UTM (tensile testing), TGA, and DMA. In a comparison of the HNG's output voltage and current performance with its individual piezoelectric and triboelectric components, an increment in the output performance is observed. This might be the result of a synergistic effect of piezoelectricity and triboelectricity. The piezoelectric performance of TiO_2 added P(VDF-TrFE) composite film is initially compared to pristine P(VDF-TrFE), and optimum doping level of TiO_2 is obtained for the greater piezoelectric performance to be employed as a energy harvesting applications. The piezoelectric NG with optimum doping level of TiO_2 exhibits maximum output voltage and current under finger tapping. The hybrid nanogenerator containing P(VDF-TrFE)/TiO_2 with PDMS film generates higher electrical voltage as compared to the pure P(VDF-TrFE) and PDMS based HNG.

The results state that the incorporation of TiO_2 in the flexible P(VDF-TrFE) matrix promote the polar β phase content and the piezoelectric properties, which enhance the overall performance of the P(VDF-TrFE). The nanofiller dispersion enhance the surface roughness value, which increase the contact surface area and increasing the device's triboelectric output. Hybrid nanogenerators are significantly more efficient due to the combination of these factors. Further, the HNG is used to power the electronic component such as LED bulb by a finger tapping. The use of such a simpler, cost-effective process for developing HNG opens up a world of possibilities for self-powered sensors, wearable device and energy harvesting applications. The following major outputs are drawn from the study of hybrid nanogenerator:

(i) Electrospun composite mat with varying average diameter is observed from 196 nm to 108 nm, which is desirable for increasing the sensing capability of the sensor device.

(ii) The mechanical strength is also one of the factor for the device, which is to be used as energy harvester. Here, the tensile strength of the mats are increased from 11.6 MPa to 19.3 MPa, which is incorporated as a active layer in the device.

(iii) The designed hybrid nanogenerator produced voltage and current, and piezoelectric peak power of 52 V and 5.36 μA.

(iv) The piezoelectric output of hybrid nanogenerator is almost 2 times more as compared to HNG made from P(VDF-TrFE) fiber, and the enhancement in the performance is acredited to the combined effect of piezoelectric and triboelectric effect.

(v) The varying TiO_2 content significantly effect the piezoelectric output of hybrid nanogenerator.

(vi) HNG can be deployed to display real-time application for body movement detection and biomechanical energy harvesting to light up an LED bulb.

Chapter 8

Conclusions

8.1 CHAPTERWISE SYNOPTIC CONCLUSIONS FROM THE PRESENT WORK

The major outcomes of this research work and the scope for future research are summarized in this section. The major conclusions are encapsulated below.

1. P(VDF-TrFE)/ZnO nanocomposite mats are fabricated using electrospinning method by considering the effect of ZnO nanofiller concentration in terms of 18% wt./vol. and 18 wt.%. Further, the nanofiber mats are characterized using various techniques and investigated under the different load. The experimental studies have led to the following inferences:

   (i) Higher content of ZnO nanoparticles on the nanofiber mat result in agglomeration, which reduced surface area to volume ratio causes to reduce the efficiency of energy harvesting device.

   (ii) The fraction of β phase and roughness increased with the dispersion of nanoparticles as confirmed from the FTIR and AFM test.

   (iii) The viscosity, dynamic moduli of the solution are substantially enhanced with the inclusion of ZnO nanopowder while damping factor is reduced.

   (iv) ZnO with higher concentration significantly affect the fiber diameter, β phase crystalline structure, stress, strain, Young's modulus, and the piezoelectric output of the PENG device.

   (v) The findings of this study indicated that the film fabricated using the nanofiller concentration relative to the polymer is more suited for energy harvesting applications.

(vi) The piezoelectric nanogenerator under softly tapping generates more power output as compared to pressing and bending.

2. The defect free P(VDF-TrFE)/ZnO nanocomposite membranes as self powered sensor are designed for the enrgy harvesting applications. The different characterization test is used for the spun fiber mat. The influence of operational paraeter on the piezoelectric performance of the nanofiber mat is studied in detail. The following conclusions are drawn:

(i) The results reveal that the nanofiber composite is formed defect-free at specific electrospinning conditions.

(ii) The β crystalline phase, specific surface area, rheological properties and dynamic modulus are significantly improved after the addition of nanofiller.

(iii) It has been observed that voltage output increased with the increment of ZnO weight percentage up to 10 and then decreases.

(iv) The ANOVA study of basic electrospinning process parameters reveal that all three parameters, namely voltage, flow rate, and ZnO concentration are having percentage contributions of 1.45%, 4.36%, and 94.03%, respectively, on piezoelectric output.

(v) The optimized parameters that provide the best piezoelectric effect are 18 kV aplied voltage, 16 μl/min, and 9 wt.% of ZnO, which offers the best piezoelectric output of 2.62 V.

(vi) A maximum error of 8.28% is observed between predicted (calculated from regression equation) and experimental piezoelectric output values, which confirm the effectiveness of the DOE model.

(vii) The piezoelectric voltage and current of the piezoelectric nanogenerator device based on fiber composite is found 2.52 V and 20.8 μA whereas 1.04 V and 12.8 μA for the pristine P(VDF-TrFE) nanofiber under finger tapping conditions.

(viii) Under finger tapping load condition, the piezoelectric performance of the PENG is superior to that of bending.

3. Electrospun functionally graded PVDF/$BaTiO_3$ based flexible nanogenerators are prepared for the enhancement of piezoelectric performance. $BaTiO_3$ concentration increases from bottom to top. The piezoelectric output of PENGs device is validated using Comsol Multiphysics software. The effect of number of layer on the piezoelectric output of the functionally graded mat is investigated comprehensively. The experimental and simulation result leads to the following inferences:

   (i) Pure PVDF has low output while multi-layered film based nanogenerators with high concentration of $BaTiO_3$ give more output.

   (ii) The PENG devices were subjected to palm tapping, wrist tapping, and elbow hitting to extract energy. The PENG generated peak to peak voltage of 8.22 V, current of 3.36 μA, and instantaneous power of 0.14 mW/cm^2.

   (iii) Compared to monolayer films, functionally graded films exhibit greater piezoelectric performance as the number of nanofiber layers increases.

   (iv) The nanocomposite fabricated with PVDF(12 wt.%)/$BaTiO_3$(8 wt.%) showed less piezoelectric performance as compared to other samples.

   (v) The piezoelectric output of PENGs device is validated using Comsol Multiphysics software and well matched with the experimental results.

   (vi) The maximum error of 6.89% is observed between the experimental piezoelectric output values and simulation result (using Comsol Multiphysics software), which confirm the effectiveness of the study.

4. Self powered hybrid flexible P(VDF-TrFE)/ZnO/TiO_2 fiber mats as nanogenerator is fabricated for the wearable applications. The three phase nanocomposite mats are fabricated with varying the TiO_2 contents. The influence of TiO_2 concentration on the various properties including microstructural, modulus, and piezoelectric output of the hybrid composite mat is investigated thoroughly. The following results are listed below:

(i) The designed piezoelectric device generated current, voltage, and piezoelectric peak power of 4.16 μA, 23 V, and 95.68 μW, respectively.

(ii) The piezoelectric output of hybrid composite mats is almost 3.6 times greater than PENG made from P(VDF-TrFE) fiber, and the increment in the performance is due to the synergistic effect of ZnO and TiO_2 in the P(VDF-TrFE) polymer matrix.

(iii) The ZnO and TiO_2 nanoparticles content significantly effect the fraction of β phase, viscoelastic property and piezoelectric output.

(iv) PENG is used to display real-time demonstrations of body movement detection and biomechanical energy harvesting to power an LED bulb.

5. High performance flexible P(VDF-TrFE)-TiO_2/PDMS based piezo-triboelectric hybrid nanogenerator is prepared to detect the human body activity. The different hybrid nanogenerators are made using the fabricated spun mats for in-depth analysis of the piezoelectric output. The influence of various parameters on piezoelectric performance is investigated in detail. The following major outputs are drawn from the experimental study of the hybrid nanogenerator:

(i) Electrospun composite mat with varying average diameter is observed from 196 nm to 108 nm, which is desirable for increasing the sensing capability of the sensor device.

(ii) The mechanical strength is also one of the factor for the device, which is to be used as energy harvester. Here, the tensile strength of the mats are increased from 11.6 MPa to 19.3 MPa, which is incorporated as a active layer in the device.

(iii) The designed hybrid nanogenerator produced voltage and current, and piezoelectric peak power of 52 V and 5.36 μA.

(iv) The piezoelectric output of hybrid nanogenerator is almost 2 times more as compared to HNG made from P(VDF-TrFE) fiber, and the enhancement in the performance is acredited to the combined effect of piezoelectric and triboelectric effect.

(v) The varying TiO_2 content significantly effect the piezoelectric output of hybrid nanogenerator.

(vi) HNG can be deployed to display real-time application for body movement detection and biomechanical energy harvesting to light up an LED bulb.

8.2 CONTRIBUTION OF PRESENT THESIS

The salient contributions of the present thesis to overcome the hindering issues related to the electrospun composites as sensor applications are of significant engineering interest. Experimental and simulation study of spun composite films has faced hindrances due to their affecting parameters such as solution, electrospinning, and ambient parameters, controlling fiber's diameter, surface morphology complexity, design of sensor device, etc. The significant and novel contributions of the thesis are as follows:

1. The response of the sensor device depends on the thickness, effective area, electroactive phase, piezoelectric property, etc. Therefore, the fabrication of sensor devices predominantly depends on the sensor type, material selection, substrate, fabrication technique, electrode design, encapsulation, testing, and experimental cost. The choice should be made within performance, applicability, and experimental cost constraints. The current work has contributed to these domains..
2. The present work employed electrospinning technique to synthesize composite mats with enhanced sensing capability. These techniques have provided better control over the surface morphology of nanofiber membranes, resulting in increased sensor performance.
3. The present work demonstrates the potential of electrospun nanocomposites to have greater sensing characteristics than conventional sensors. The composite materials show improved sensitivity, selectivity, and response time, making them suitable for different sensing applications.
4. The present work explores the incorporation of different reinforcing nanofiller into the electrospun composites, expanding the range of sensor performance. The various reinforcing component widens the potential applications of the sensors.

5. It is noteworthy that the synthesized composite is very efficient as a biomechanical sensor for detecting the various activity of human beings. This thesis provides benchmark piezoelectric output for the hybrid nanocomposite-based sensor.
6. The electrospun functionally graded structures have been fabricated as an active layer in the sensor, which enhances the piezoelectric performance compared to the single-layered composite film.
7. The set of experiments has been conducted to optimize the electrospinning parameters to obtain better performance in the given constraints as per the statistical design of experiments. A lower to higher quantity of nanofiller has been added to the nanofiber, and their content is optimized using the same approach.
8. The electrospinning method has been employed to synthesize, which substantially reduces the cost of sensor device.
9. The present study can form the basis for the biomechanical energy harvester and development of self-powered wearable electrical systems and devices.
10. The set of experiments has been conducted to optimize the electrospinning parameters to obtain better performance in the given constraints as per the statistical design of experiments. A lower to higher quantity of nanofiller has been added to the nanofiber, and their content is optimized using the same approach.

8.3 FUTURE SCOPE OF WORK

The electrospun piezoelectric fiber composite membranes have been used as a self-powered sensor, wearable device, and energy harvesters can be extended on the following aspects for the future studies:

1. As the nanofiber diameter plays significant role in effective sensing and actuation. The influence of average diameter of electrospun mats need to be addressed through the development of model. This can be employed for accurate predictions of sensor characteristics.

2. Sensing applications rely heavily on the physical connection between piezo active layer and electrode materials. The effect of increasing the surface contact between them at the microscopic level need to be addressed through the mathematical model.
3. The electromechanical properties are not available in the open literature for further analysis. In order to carry out the further numerical and simulation work, these properties will be required.
4. The mathematical model need to be developed to predict the characteristics of the electrospun mats, which will help in experimental analysis.
5. Electrospun fiber mat based devices can be commercialized for temperature sensing and energy harvesting device.
6. The present electrospun mat can be extended to the surface acoustic wave (SAW) device to measure the physical quantities such as temperature, pressure, and humidity. As, it is used in industrial and environmental monitoring.
7. An approach to fabricating a sensor device based on bio-waste materials can be implemented using the present fabrication approach.

Bibliography

[1] Laudenslager MJ. sigmund, wm, 2012.electrospinning encyclopedia of nanotechnology, 2012.

[2] Zargham Shamim, Bazgir Saeed, Tavakoli Amir, Rashidi Abo Saied, and Damerchely Rogheih. The effect of flow rate on morphology and deposition area of electrospun nylon 6 nanofiber. *Journal of Engineered Fibers and Fabrics*, **7**(4):155892501200700414, 2012.

[3] Luzio Alessandro, Canesi Eleonora Valeria, Bertarelli Chiara, and Caironi Mario. Electrospun polymer fibers for electronic applications. *Materials*, **7**(2):906–947, 2014.

[4] Zander Nicole E. Hierarchically structured electrospun fibers. *Polymers*, **5**(1):19–44, 2013.

[5] Fong Hao, Chun Iksoo, and Reneker Darrel H. Beaded nanofibers formed during electrospinning. *Polymer*, **40**(16):4585–4592, 1999.

[6] Bae Hyun-Su, Haider Adnan, Selim KM Kamruzzaman, Kang Dong-Yoon, Kim Eun-Jin, and Kang Inn-Kyu. Fabrication of highly porous pmma electrospun fibers and their application in the removal of phenol and iodine. *Journal of Polymer Research*, **20**:1–7, 2013.

[7] Curie Jacques and Curie Pierre. Développement par compression de l'électricité polaire dans les cristaux hémièdres à faces inclinées. *Bulletin de minéralogie*, **3**(4):90–93, 1880.

[8] Lippmann Gabriel. Principe de la conservation de l'électricité, ou second principe de la théorie des phénomènes électriques. *Journal de Physique Théorique et Appliquée*, **10**(1):381–394, 1881.

[9] Mason Warren P. Piezoelectricity, its history and applications. *The journal of the Acoustical Society of America*, **70**(6):1561–1566, 1981.

[10] Birkholz Mario. Crystal-field induced dipoles in heteropolar crystals ii: Physical significance. *Zeitschrift für Physik B Condensed Matter*, **96**:333–340, 1995.

[11] Trolier-McKinstry Susan. *Crystal Chemistry of Piezoelectric Materials*. Springer US, Boston, MA, 2008.

[12] Habib Mahpara, Lantgios Iza, and Hornbostel Katherine. A review of ceramic, polymer and composite piezoelectric materials. *Journal of Physics D: Applied Physics*, **55**(42):423002, 2022.

[13] Akdogan E Koray, Allahverdi Mehdi, and Safari Ahmad. Piezoelectric composites for sensor and actuator applications. *IEEE Transactions on Ultrasonics, Ferroelectrics, and Frequency Control*, **52**(5):746–775, 2005.

[14] Kawai Heiji. The piezoelectricity of poly (vinylidene fluoride). *Japanese Journal of Applied Physics*, **8**(7):975, 1969.

[15] Harrison JS, Ounaies Zoubeida, and Bushnell Dennis M. *Piezoelectric Polymers*. 2001.

[16] Erdtman Edvin, Satyanarayana Kavitha Chelakara, and Bolton Kim. Simulation of α-and β-pvdf melting mechanisms. *Polymer*, **53**(14):2919–2926, 2012.

[17] Preston RC, Bacon DR, Livett AJ, and Rajendran K. Pvdf membrane hydrophone performance properties and their relevance to the measurement of the acoustic output of medical ultrasonic equipment. *Journal of Physics E: Scientific Instruments*, **16**(8):786, 1983.

[18] Xin Yi, Sun Hongshuai, Tian Hongying, Guo Chao, Li Xiang, Wang Shuhong, and Wang Cheng. The use of polyvinylidene fluoride (pvdf) films as sensors for vibration measurement: A brief review. *Ferroelectrics*, **502**(1):28–42, 2016.

[19] Bae Ji-Hun and Chang Seung-Hwan. Pvdf-based ferroelectric polymers and dielectric elastomers for sensor and actuator applications: a review. *Functional Composites and Structures*, **1**(1):012003, 2019.

[20] Elko G. W. and West J. E. Directional microphone systems for teleconferencing. *The Journal of the Acoustical Society of America*, **84**(S1):S67–S68, 2005.

[21] Gururaja TR, Schulze Walter A, Cross Leslie E, and Newnham Robert E. Piezoelectric composite materials for ultrasonic transducer applications. part ii: Evaluation of ultrasonic medical applications. *IEEE Transactions on Sonics and Ultrasonics*, **32**(4):499–513, 1985.

[22] Ting Robert Y. A review on the development of piezoelectric composites for underwater acoustic transducer applications. *IEEE Transactions on Instrumentation and Measurement*, **41**(1):64–67, 1992.

[23] Buzea Cristina, Pacheco Ivan I, and Robbie Kevin. Nanomaterials and nanoparticles: sources and toxicity. *Biointerphases*, **2**(4):MR17–MR71, 2007.

[24] Fahlman Bradley D. *Nanomaterials*. Springer, 2007.

[25] Roduner Emil. Size matters: why nanomaterials are different. *Chemical Society Reviews*, **35**(7):583–592, 2006.

[26] Liu Zonghua, Jiao Yanpeng, Wang Yifei, Zhou Changren, and Zhang Ziyong. Polysaccharides-based nanoparticles as drug delivery systems. *Advanced Drug Delivery Reviews*, **60**(15):1650–1662, 2008.

[27] Srinivas Goundla, Nielsen Steven O, Moore Preston B, and Klein Michael L. Molecular dynamics simulations of surfactant self-organization at a solid- liquid interface. *Journal of the American Chemical Society*, **128**(3):848–853, 2006.

[28] Evans David S. The relationship between firm growth, size, and age: Estimates for 100 manufacturing industries. *The Journal of Industrial Economics*, **35**:567–581, 1987.

[29] Subbiah Thandavamoorthy, Bhat Gajanan S, Tock Richard W, Parameswaran Siva, and Ramkumar Seshadri S. Electrospinning of nanofibers. *Journal of Applied Polymer Science*, **96**(2):557–569, 2005.

[30] Teo Wee E and Ramakrishna Seeram. A review on electrospinning design and nanofibre assemblies. *Nanotechnology*, **17**(14):R89, 2006.

[31] Eatemadi Ali, Daraee Hadis, Zarghami Nosratolah, Melat Yar Hassan, and Akbarzadeh Abolfazl. Nanofiber: Synthesis and biomedical applications. *Artificial Cells, Nanomedicine, and Biotechnology*, **44**(1):111–121, 2016.

[32] Nayl AbdElAziz A, Abd-Elhamid Ahmed I, Awwad Nasser S, Abdelgawad Mohamed A, Wu Jinglei, Mo Xiumei, Gomha Sobhi M, Aly Ashraf A, and Bräse Stefan. Review of the recent advances in electrospun nanofibers applications in water purification. *Polymers*, **14**(8):1594, 2022.

[33] Morie Asif, Garg Tarun, Goyal Amit K, and Rath Goutam. Nanofibers as novel drug carrier–an overview. *Artificial Cells, Nanomedicine, and Biotechnology*, **44**(1):135–143, 2016.

[34] Okpala Charles Chikwendu. The benefits and applications of nanocomposites. *Int. J. Adv. Eng. Tech*, **12**:18, 2014.

[35] Zeng Wei, Shu Lin, Li Qiao, Chen Song, Wang Fei, and Tao Xiao-Ming. Fiber-based wearable electronics: a review of materials, fabrication, devices, and applications. *Advanced Materials*, **26**(31):5310–5336, 2014.

[36] Okpala Charles Chikwendu. Nanocomposites–an overview. *International Journal of Engineering Research and Development*, **8**(11):17–23, 2013.

[37] Mortensen Andreas and Llorca Javier. Metal matrix composites. *Annual Review of Materials Research*, **40**:243–270, 2010.

[38] Rawal Suraj P. Metal-matrix composites for space applications. *Jom*, **53**(4):14–17, 2001.

[39] Dutta Sourav, Gupta Sanjay, and Roy Mangal. Recent developments in magnesium metal–matrix composites for biomedical applications: A review. *ACS Biomaterials Science and Engineering*, **6**(9):4748–4773, 2020.

[40] Zweben Carl. Metal-matrix composites for electronic packaging. *Jom*, **44**(7):15–23, 1992.

[41] Li Yichao, Huang Xianrong, Zeng Lijian, Li Renfu, Tian Huafeng, Fu Xuewei, Wang Yu, and Zhong Wei-Hong. A review of the electrical and mechanical properties of carbon nanofiller-reinforced polymer composites. *Journal of Materials Science*, **54**:1036–1076, 2019.

[42] Fawaz Joel and Mittal Vikas. *Synthesis of polymer nanocomposites: review of various techniques*. Wiley Online Library, 2014.

[43] Dallas Panagiotis, Sharma Virender K, and Zboril Radek. Silver polymeric nanocomposites as advanced antimicrobial agents: classification, synthetic paths, applications, and perspectives. *Advances in Colloid and Interface Science*, **166**(1-2):119–135, 2011.

[44] Tanaka Toshikatsu, Montanari GC, and Mulhaupt R. Polymer nanocomposites as dielectrics and electrical insulation-perspectives for processing technologies, material characterization and future applications. *IEEE Transactions on Dielectrics and Electrical Insulation*, **11**(5): 763–784, 2004.

[45] Wang Wenxin, Liu Yanju, and Leng Jinsong. Recent developments in shape memory polymer nanocomposites: Actuation methods and mechanisms. *Coordination Chemistry Reviews*, **320**:38–52, 2016.

[46] Wei Huige, Wang Hui, Li Ang, Cui Dapeng, Zhao Zinian, Chu Liqiang, Wei Xin, Wang Lin, Pan Duo, Fan Jincheng, and others . Multifunctions of polymer nanocomposites: environmental remediation, electromagnetic interference shielding, and sensing applications. *ChemNanoMat*, **6**(2):174–184, 2020.

[47] Thostenson Erik T, Li Chunyu, and Chou Tsu-Wei. Nanocomposites in context. *Composites Science and Technology*, **65**(3-4):491–516, 2005.

[48] Vasita Rajesh and Katti Dhirendra S. Nanofibers and their applications in tissue engineering. *International Journal of Nanomedicine*, **1**(1):15–30, 2006.

[49] Hu Xiuli, Liu Shi, Zhou Guangyuan, Huang Yubin, Xie Zhigang, and Jing Xiabin. Electrospinning of polymeric nanofibers for drug delivery applications. *Journal of Controlled Release*, **185**:12–21, 2014.

[50] Nasreen Shaik Anwar Ahamed Nabeela, Sundarrajan Subramanian, Nizar Syed Abdulrahim Syed, Balamurugan Ramalingam, and Ramakrishna Seeram. Advancement in electrospun nanofibrous membranes modification and their application in water treatment. *Membranes*, **3**(4):266–284, 2013.

[51] Stojanovska Elena, Pampal Esra Serife, Kilic Ali, Quddus Mir, and Candan Zeki. Developing and characterization of lignin-based fibrous nanocarbon electrodes for energy storage devices. *Composites Part B: Engineering*, **158**:239–248, 2019.

[52] Kang Shixiong, Zhao Kun, Yu Deng-Guang, Zheng Xiaolu, and Huang Caoxing. Advances in biosensing and environmental monitoring based on electrospun nanofibers. *Advanced Fiber Materials*, **4**(3):404–435, 2022.

[53] Reneker Darrell H and Yarin Alexander L. Electrospinning jets and polymer nanofibers. *Polymer*, **49**(10):2387–2425, 2008.

[54] Cooley John Francis. Improved methods of and apparatus for electrically separating the relatively volatile liquid component from the component of relatively fixed substances of composite fluids. *United Kingdom Patent*, **6385**:19, 1900.

[55] Sill Travis J and Von Recum Horst A. Electrospinning: applications in drug delivery and tissue engineering. *Biomaterials*, **29**(13):1989–2006, 2008.

[56] Deitzel Joseph M, Kleinmeyer James, Harris DEA, and Tan NC Beck. The effect of processing variables on the morphology of electrospun nanofibers and textiles. *Polymer*, **42**(1):261–272, 2001.

[57] Baumgarten Peter K. Electrostatic spinning of acrylic microfibers. *Journal of Colloid and Interface Science*, **36**(1):71–79, 1971.

[58] Gu SY, Ren J, and Vancso GJ. Process optimization and empirical modeling for electrospun polyacrylonitrile (pan) nanofiber precursor of carbon nanofibers. *European Polymer Journal*, **41**(11):2559–2568, 2005.

[59] Reneker Darrell H and Chun Iksoo. Nanometre diameter fibres of polymer, produced by electrospinning. *Nanotechnology*, **7**(3):216, 1996.

[60] Gee S, Johnson B, and Smith AL. Optimizing electrospinning parameters for piezoelectric pvdf nanofiber membranes. *Journal of Membrane Science*, **563**:804–812, 2018.

[61] Megelski Silke, Stephens Jean S, Chase D Bruce, and Rabolt John F. Micro-and nanostructured surface morphology on electrospun polymer fibers. *Macromolecules*, **35**(22):8456–8466, 2002.

[62] Zeleny John. The role of surface instability in electrical discharges from drops of alcohol and water in air at atmospheric pressure. *Journal of the Franklin Institute*, **219**(6):659–675, 1935.

[63] Li Zhenyu, Wang Ce, Li Zhenyu, and Wang Ce. *Effects of working parameters on electrospinning*. Springer, 2013.

[64] Reneker DH, Kataphinan W, Theron A, Zussman E, and Yarin AL. Nanofiber garlands of polycaprolactone by electrospinning. *Polymer*, **43**(25):6785–6794, 2002.

[65] Theron SA, Zussman E, and Yarin AL. Experimental investigation of the governing parameters in the electrospinning of polymer solutions. *Polymer*, **45**(6):2017–2030, 2004.

[66] Wu Chang-Mou, Hsu Ching-Hsiang, Su Ching-Iuan, Liu Chun-Liang, and Lee Jiunn-Yih. Optimizing parameters for continuous electrospinning of polyacrylonitrile nanofibrous yarn using the taguchi method. *Journal of Industrial Textiles*, **48**(3):559–579, 2018.

[67] Matabola KP and Moutloali RM. The influence of electrospinning parameters on the morphology and diameter of poly (vinyledene fluoride) nanofibers-effect of sodium chloride. *Journal of Materials Science*, **48**:5475–5482, 2013.

[68] Bhardwaj Nandana and Kundu Subhas C. Electrospinning: A fascinating fiber fabrication technique. *Biotechnology Advances*, **28**(3):325–347, 2010.

[69] Nazari Tayebe and Garmabi Hamid. The effects of processing parameters on the morphology of pla/peg melt electrospun fibers. *Polymer International*, **67**(2):178–188, 2018.

[70] Wang Tong and Kumar Satish. Electrospinning of polyacrylonitrile nanofibers. *Journal of Applied Polymer Science*, **102**(2):1023–1029, 2006.

[71] Zhang Chunxue, Yuan Xiaoyan, Wu Lili, Han Yue, and Sheng Jing. Study on morphology of electrospun poly (vinyl alcohol) mats. *European Polymer Journal*, **41**(3):423–432, 2005.

[72] Haider Sajjad, Al-Zeghayer Yousef, Ahmed Ali Fekri A, Haider Adnan, Mahmood Asif, Al-Masry Waheed A, Imran Muhammad, and Aijaz Muhammad Omer. Highly aligned narrow diameter chitosan electrospun nanofibers. *Journal of Polymer Research*, **20**:1–11, 2013.

[73] Pillay Viness, Dott Clare, Choonara Yahya E, Tyagi Charu, Tomar Lomas, Kumar Pradeep, Toit du Lisa C, and Ndesendo Valence MK. A review of the effect of processing variables on the fabrication of electrospun nanofibers for drug delivery applications. *Journal of Nanomaterials*, **2013**, 2013.

[74] Zong Xinhua, Kim Kwangsok, Fang Dufei, Ran Shaofeng, Hsiao Benjamin S, and Chu Benjamin. Structure and process relationship of electrospun bioabsorbable nanofiber membranes. *Polymer*, **43**(16):4403–4412, 2002.

[75] Doshi Jayesh and Reneker Darrell H. Electrospinning process and applications of electrospun fibers. *Journal of Electrostatics*, **35**(2-3):151–160, 1995.

[76] Sun B, Long YZ, Zhang HD, Li MM, Duvail JL, Jiang XY, and Yin HL. Advances in three-dimensional nanofibrous macrostructures via electrospinning. *Progress in Polymer Science*, **39**(5):862–890, 2014.

[77] Angammana Chitral J and Jayaram Shesha H. Analysis of the effects of solution conductivity on electrospinning process and fiber morphology. *IEEE Transactions on Industry Applications*, **47**(3):1109–1117, 2011.

[78] Choi Jae Shin, Lee Sung Won, Jeong Lim, Bae Su-Hyun, Min Bum Chan, Youk Ji Ho, and Park Won Ho. Effect of organosoluble salts on the nanofibrous structure of electrospun poly (3-hydroxybutyrate-co-3-hydroxyvalerate). *International Journal of Biological Macromolecules*, **34**(4):249–256, 2004.

[79] Lannutti J, Reneker Darrell, Ma Tea, Tomasko D, and Farson D. Electrospinning for tissue engineering scaffolds. *Materials Science and Engineering: C*, **27**(3):504–509, 2007.

[80] Kanani A Gholipour and Bahrami S Hajir. Effect of changing solvents on poly (ε-caprolactone) nanofibrous webs morphology. *Journal of Nanomaterials*, **2011**:1–10, 2011.

[81] Jarusuwannapoom Teeradech, Hongrojjanawiwat Walaiporn, Jitjaicham Sujinda, Wannatong Ladawan, Nithitanakul Manit, Pattamaprom Cattaleeya, Koombhongse Piyawit, Rangkupan Ratthapol, and Supaphol Pitt. Effect of solvents on electro-spinnability of polystyrene solutions and morphological appearance of resulting electrospun polystyrene fibers. *European Polymer Journal*, **41**(3):409–421, 2005.

[82] Huan Siqi, Liu Guoxiang, Han Guangping, Cheng Wanli, Fu Zongying, Wu Qinglin, and Wang Qingwen. Effect of experimental parameters on morphological, mechanical and hydrophobic properties of electrospun polystyrene fibers. *Materials*, **8**(5):2718–2734, 2015.

[83] Pelipenko Jan, Kristl Julijana, Janković Biljana, Baumgartner Saša, and Kocbek Petra. The impact of relative humidity during electrospinning on the morphology and mechanical properties of nanofibers. *International Journal of Pharmaceutics*, **456**(1):125–134, 2013.

[84] Park Ju-Young and Lee In-Hwa. Relative humidity effect on the preparation of porous electrospun polystyrene fibers. *Journal of Nanoscience and Nanotechnology*, **10**(5):3473–3477, 2010.

[85] De Vrieze Sander, Van Camp Tamara, Nelvig Anna, Hagström Bengt, Westbroek Philippe, and De Clerck Karen. The effect of temperature and humidity on electrospinning. *Journal of Materials Science*, **44**:1357–1362, 2009.

[86] Li Dan and Xia Younan. Electrospinning of nanofibers: reinventing the wheel? *Advanced Materials*, **16**(14):1151–1170, 2004.

[87] Mokhtari F, Shamshirsaz M, Latifi M, and Asadi S. Comparative evaluation of piezoelectric response of electrospun PVDF (polyvinilydine fluoride) nanofiber with various additives for energy scavenging application. *The Journal of the Textile Institute*, **108**(6):906–914, 2017.

[88] Zhang Dandan, Zhang Xiuli, Li Xingjia, Wang Huiping, Sang Xiaodong, Zhu Guodong,

and Yeung Yuhei. Enhanced piezoelectric performance of PVDF/$BiCl_3$/ZnO nanofiber-based piezoelectric nanogenerator. *European Polymer Journal*, **166**:110956, 2022.

[89] Jiang Jie, Tu Shijian, Fu Runfang, Li Jingjing, Hu Fei, Yan Bin, Gu Yingchun, and Chen Sheng. Flexible piezoelectric pressure tactile sensor based on electrospun $BaTiO_3$/poly(vinylidene fluoride) nanocomposite membrane. *ACS Applied Materials and Interfaces*, **12**(30):33989–33998, 2020.

[90] Augustine Robin, Sarry Frederic, Kalarikkal Nandakumar, Thomas Sabu, Badie Laurent, and Rouxel Didier. Surface acoustic wave device with reduced insertion loss by electrospinning P(VDF-TrFE)/ZnO nanocomposites. *Nano-Micro Letters*, **8**(3):282–290, 2016.

[91] Sahoo Rajesh, Mishra Suvrajyoti, Unnikrishnan Lakshmi, Mohanty Smita, Mahapatra Swapna, Nayak Sanjay Kumar, Anwar Shahid, and Ramadoss Ananthakumar. Enhanced dielectric and piezoelectric properties of fe-doped ZnO/P(VDF-TrFE) composite films. *Materials Science in Semiconductor Processing*, **117**:105173, 2020.

[92] Pan Cheng-Tang, Yen Chung-Kun, Hsieh Ming-Chun, Wang Shao-Yu, Chien Chi-Hui, Huang Jacob Chih-Ching, Lin Liwei, Shiue Yow-Ling, and Kuo Shiao-Wei. Energy harvesters incorporating silk from the taiwan-native spider nephila pilipes. *ACS Applied Energy Materials*, **1**(10):5627–5635, 2018.

[93] Pan Cheng-Tang, Yen Chung-Kun, Wang Shao-Yu, Lai Yan-Cheng, Lin Liwei, Huang JC, and Kuo Shiao-Wei. Near-field electrospinning enhances the energy harvesting of hollow PVDF piezoelectric fibers. *RSC Advances*, **5**(103):85073–85081, 2015.

[94] Pan Cheng-Tang, Yen Chung-Kun, Wu Hui-Chun, Lin Liwei, Lu Yi-Syuan, Huang Jacob Chih-Ching, and Kuo Shiao-Wei. Significant piezoelectric and energy harvesting enhancement of poly(vinylidene fluoride)/polypeptide fiber composites prepared through near-field electrospinning. *Journal of Materials Chemistry A*, **3**(13):6835–6843, 2015.

[95] Ögüt Erdem, Yördem O Sinan, Menceloğlu Yusuf Z, and Papila Melih. Poly(vinylidene fluoride)/zinc oxide smart composite material. In *Behavior and Mechanics of Multifunctional and Composite Materials 2007*, volume 6526, pages 209–218. SPIE, 2007.

[96] Meyers Frederick N, Loh Kenneth J, Dodds John S, and Baltazar Arturo. Active sensing and damage detection using piezoelectric zinc oxide-based nanocomposites. *Nanotechnology*, **24** (18):185501, 2013.

[97] Kim Tae Yeon, Anoop Gopinathan, Son Yeong Jun, Kim Soo Hyeon, Lee Eunji, and Jo Ji Young. Ferroelectric-mediated filamentary resistive switching in P(VDF-TrFE)/ZnO nanocomposite films. *Physical Chemistry Chemical Physics*, **20**(23):16176–16183, 2018.

[98] Zhang Yongming, Zou Jing, Lin Shuang, and Wang Fanghui. Effect of ZnO-Ag on dielectric properties of ZnO-Ag/P(VDF-TrFE-CTFE) composites. *International Journal of Polymer Analysis and Characterization*, **26**(2):158–168, 2021.

[99] Li Jie, Zhao Chunmao, Xia Kai, Liu Xi, Li Dong, and Han Jing. Enhanced piezoelectric output of the P(VDF-TrFE)/ZnO flexible piezoelectric nanogenerator by surface modification. *Applied Surface Science*, **463**:626–634, 2019.

[100] Rouxel Didier, Vincent Brice, Badie Laurent, Dos Santos Fabrice Domingues, Lamouroux Emmanuel, Fort Yves, and others . Influence of cluster size and surface functionalization of ZnO nanoparticles on the morphology, thermomechanical and piezoelectric properties of P(VDF-TrFE) nanocomposite films. *Applied Surface Science*, **279**:204–211, 2013.

[101] Habibur Rahaman Md, Yaqoob Usman, Muhammad Sheeraz, Uddin ASM Iftekhar, and Kim Hyeon Cheol. The effect of RGO on dielectric and energy harvesting properties of P(VDF-TrFE) matrix by optimizing electroactive β phase without traditional polling process. *Materials Chemistry and Physics*, **215**:46–55, 2018.

[102] Paik Haemin, Choi Yoon-Young, Hong Seungbum, and No Kwangsoo. Effect of Ag nanoparticle concentration on the electrical and ferroelectric properties of Ag/P(VDF-TrFE) composite films. *Scientific Reports*, **5**(1):1–7, 2015.

[103] Bhavanasi Venkateswarlu, Kumar Vipin, Parida Kaushik, Wang Jiangxin, and Lee Pooi See. Enhanced piezoelectric energy harvesting performance of flexible P(VDF-TrFE) bilayer films with graphene oxide. *ACS Applied Materials and Interfaces*, **8**(1):521–529, 2016.

[104] Luo WB, Chen LG, Meng J, Shuai Y, Wu CG, Sun XY, and Zhang WL. Enhanced pyroelectric property of PMN-PT/P(VDF-TrFE) thick film by optimizing poling temperature. *Journal of Materials Science: Materials in Electronics*, **29**(1):271–276, 2018.

[105] Sinha Nidhi, Goel Sahil, Joseph Abhilash J, Yadav Harsh, Batra Kriti, Gupta Manoj Kumar, and Kumar Binay. Y-doped ZnO nanosheets: Gigantic piezoelectric response for an ultra-sensitive flexible piezoelectric nanogenerator. *Ceramics International*, **44**(7):8582–8590, 2018.

[106] Sorayani Bafqi Mohammad Sajad, Bagherzadeh Roohollah, and Latifi Masoud. Fabrication of composite PVDF-ZnO nanofiber mats by electrospinning for energy scavenging application with enhanced efficiency. *Journal of Polymer Research*, **22**:1–9, 2015.

[107] Mansouri Soheil, Sheikholeslami Tahereh Fanaei, and Behzadmehr Amin. Investigation on the electrospun PVDF/NP-ZnO nanofibers for application in environmental energy harvesting. *Journal of Materials Research and Technology*, **8**(2):1608–1615, 2019.

[108] Jeong Chang Kyu, Baek Changyeon, Kingon Angus I, Park Kwi-Il, and Kim Seung-Hyun. Lead-free perovskite nanowire-employed piezopolymer for highly efficient flexible nanocomposite energy harvester. *Small*, **14**(19):1704022, 2018.

[109] Yaqoob Usman, Uddin ASM Iftekhar, and Chung Gwiy-Sang. A novel tri-layer flexible piezo-

electric nanogenerator based on surface-modified graphene and PVDF-$BaTiO_3$ nanocomposites. *Applied Surface Science*, **405**:420–426, 2017.

[110] Guo Wenzhe, Tan Cenxiao, Shi Kunming, Li Junwen, Wang Xiao-Xiong, Sun Bin, Huang Xingyi, Long Yun-Ze, and Jiang Pingkai. Wireless piezoelectric devices based on electrospun PVDF/$BaTiO_3$ NW nanocomposite fibers for human motion monitoring. *Nanoscale*, **10**(37): 17751–17760, 2018.

[111] Nunes-Pereira J, Sencadas Vitor, Correia Vítor, Cardoso Vanessa F, Han Weihua, Rocha José Gerardo, and Lanceros-Méndez Senentxu. Energy harvesting performance of $BaTiO_3$/poly (vinylidene fluoride–trifluoroethylene) spin coated nanocomposites. *Composites Part B: Engineering*, **72**:130–136, 2015.

[112] Wang Zhenjin, Maruyama Kohei, and Narita Fumio. A novel manufacturing method and structural design of functionally graded piezoelectric composites for energy-harvesting. *Materials and Design*, **214**:110371, 2022.

[113] Ippili Swathi, Jella Venkatraju, Eom Ji-Ho, Kim Jaegyu, Hong Seungbum, Choi Jin-Seok, Tran Van-Dang, Van Hieu Nguyen, Kim Yun-Jeong, Kim Hye-Jin, and others . An eco-friendly flexible piezoelectric energy harvester that delivers high output performance is based on lead-free masni3 films and masni3-pvdf composite films. *Nano Energy*, **57**:911–923, 2019.

[114] Veeralingam Sushmitha and Badhulika Sushmee. Bi2s3/pvdf/ppy-based freestanding, wearable, transient nanomembrane for ultrasensitive pressure, strain, and temperature sensing. *ACS Applied Bio Materials*, **4**(1):14–23, 2020.

[115] Faraz Mohd, Singh Huidrom Hemojit, and Khare Neeraj. A progressive strategy for harvesting mechanical energy using flexible PVDF-rGO-MoS_2 nanocomposites film-based piezoelectric nanogenerator. *Journal of Alloys and Compounds*, **890**:161840, 2022.

[116] Amith V, Sridhar R, Gangadhar A, and Vishnumurthy KA. Design and synthesis of PVDF-cloisite-30B nanocomposite fibers for energy harvesting applications. *Surfaces and Interfaces*, **22**:100869, 2021.

[117] Karan Sumanta Kumar, Mandal Dipankar, and Khatua Bhanu Bhusan. Self-powered flexible Fe-doped RGO/PVDF nanocomposite: an excellent material for a piezoelectric energy harvester. *Nanoscale*, **7**(24):10655–10666, 2015.

[118] Pal Avijit, Sasmal Abhishek, Manoj Bindu, Rao DSD Prasada, Haldar AK, and Sen Shrabanee. Enhancement in energy storage and piezoelectric performance of three phase PZT/MWCNT/PVDF composite. *Materials Chemistry and Physics*, **244**:122639, 2020.

[119] Arunguvai J and Lakshmi P. Flexible nano-vibration energy harvester using three-phase polymer composites. *Journal of Materials Science: Materials in Electronics*, **31**:8283–8290, 2020.

[120] Ponnamma Deepalekshmi and Al-Maadeed Mariam Al Ali. Influence of $BaTiO_3$/white graphene filler synergy on the energy harvesting performance of a piezoelectric polymer nanocomposite. *Sustainable Energy and Fuels*, **3**(3):774–785, 2019.

[121] Sahatiya Parikshit, Kannan Santhosh, and Badhulika Sushmee. Few layer MoS_2 and in situ poled PVDF nanofibers on low cost paper substrate as high performance piezo-triboelectric hybrid nanogenerator: energy harvesting from handwriting and human touch. *Applied Materials Today*, **13**:91–99, 2018.

[122] Wang Xingzhao, Yang Bin, Liu Jingquan, Zhu Yanbo, Yang Chunsheng, and He Qing. A flexible triboelectric-piezoelectric hybrid nanogenerator based on P(VDF-TrFE) nanofibers and PDMS/MWCNT for wearable devices. *Scientific Reports*, **6**(1):36409, 2016.

[123] Zhu Jie, Hou Xiaojuan, Niu Xushi, Guo Xuepei, Zhang Jing, He Jian, Guo Tao, Chou Xiujian, Xue Chenyang, and Zhang Wendong. The d-arched piezoelectric-triboelectric hybrid

nanogenerator as a self-powered vibration sensor. *Sensors and Actuators A: Physical*, **263**: 317–325, 2017.

[124] Xia Weimin, Xu Zhuo, Zhang Qiuping, Zhang Zhicheng, and Chen Yuanqing. Dependence of dielectric, ferroelectric, and piezoelectric properties on crystalline properties of P(VDF-co-TrFE) copolymers. *Journal of Polymer Science Part B: Polymer Physics*, **50**(18):1271–1276, 2012.

[125] Yogamalar Rajeswari, Srinivasan Ramasamy, Vinu Ajayan, Ariga Katsuhiko, and Bose Arumugam Chandra. X-ray peak broadening analysis in ZnO nanoparticles. *Solid State Communications*, **149**(43-44):1919–1923, 2009.

[126] Vonk Chris G. Computerization of ruland's x-ray method for determination of the crystallinity in polymers. *Journal of Applied Crystallography*, **6**(2):148–152, 1973.

[127] Mandal Dipankar, Henkel Karsten, Müller Klaus, and Schmeisser Dieter. Bandgap determination of P(VDF-TrFE) copolymer film by electron energy loss spectroscopy. *Bulletin of Materials Science*, **33**:457–461, 2010.

[128] Thakur Pradip, Kool Arpan, Hoque Nur Amin, Bagchi Biswajoy, Khatun Farha, Biswas Prosenjit, Brahma Debdip, Roy Swagata, Banerjee Somtirtha, and Das Sukhen. Superior performances of in situ synthesized ZnO/PVDF thin film based self-poled piezoelectric nanogenerator and self-charged photo-power bank with high durability. *Nano Energy*, **44**:456–467, 2018.

[129] Wu Chang-Mou, Chou Min-Hui, Chala Tolesa Fita, Shimamura Yoshinobu, and Murakami Ri-ichi. Infrared-driven poly (vinylidene difluoride)/tungsten oxide pyroelectric generator for non-contact energy harvesting. *Composites Science and Technology*, **178**:26–32, 2019.

[130] Parangusan Hemalatha, Ponnamma Deepalekshmi, and AlMaadeed Mariam Al Ali. Investigation on the effect of γ-irradiation on the dielectric and piezoelectric properties of stretchable

PVDF/Fe-ZnO nanocomposites for self-powering devices. *Soft Matter*, **14**(43):8803–8813, 2018.

[131] Cai Xiaomei, Lei Tingping, Sun Daoheng, and Lin Liwei. A critical analysis of the α, β and γ phases in poly (vinylidene fluoride) using FTIR. *RSC Advances*, **7**(25):15382–15389, 2017.

[132] Jiang Xubo, Zhao Xiaojia, Peng Guirong, Liu Wenpei, Liu Ke, and Zhan Zaiji. Investigation on crystalline structure and dielectric relaxation behaviors of hot pressed poly (vinylidene fluoride) film. *Current Applied Physics*, **17**(1):15–23, 2017.

[133] Zhang Yunchong, Jiang Yang, Han Lei, Wang Bijia, Xu Hong, Zhong Yi, Zhang Linping, Mao Zhiping, and Sui Xiaofeng. Biodegradable regenerated cellulose-dispersed composites with improved properties via a pickering emulsion process. *Carbohydrate Polymers*, **179**: 86–92, 2018.

[134] Benz Marcel and Euler William B. Determination of the crystalline phases of poly (vinylidene fluoride) under different preparation conditions using differential scanning calorimetry and infrared spectroscopy. *Journal of Applied Polymer Science*, **89**(4):1093–1100, 2003.

[135] Zaarour Bilal, Zhu Lei, Huang Chen, and Jin Xiangyu. Enhanced piezoelectric properties of randomly oriented and aligned electrospun PVDF fibers by regulating the surface morphology. *Journal of Applied Polymer Science*, **136**(6):47049, 2019.

[136] Bicy K, Suriyakumar Shruti, Anu AS, Kalarikkal Nandakumar, Stephen Arul Manuel, Geethamma VG, Rouxel Didier, Thomas Sabu, and others . Highly lithium ion conductive, Al_2O_3 decorated electrospun P(VDF-TrFE) membranes for lithium ion battery separators. *New Journal of Chemistry*, **42**(24):19505–19520, 2018.

[137] Vijayan Thirukonda Anandamoorthy, Chandramohan Rathinam, Valanarasu Santiyagu, Thirumalai Jagannathan, Venkateswaran Sivasuriyan, Mahalingam Thaiyan, and Srikumar

Subbiah Ramachandran. Optimization of growth conditions of ZnO nano thin films by chemical double dip technique. *Science and Technology of Advanced Materials*, **9**(3):035007, 2008.

[138] Choi Yoon-Young, Hong Jongin, Leem Dong-Seok, Park Moonkyu, Song HanWook, Sung Tae-Hyun, and No Kwangsoo. Spin-coated ultrathin poly (vinylidene fluoride-co-trifluoroethylene) films for flexible and transparent electronics. *Journal of Materials Chemistry*, **21**(13):5057–5061, 2011.

[139] Zhang Yunxiang, Zuo Min, Song Yihu, Yan Xueping, and Zheng Qiang. Dynamic rheology and dielectric relaxation of poly (vinylidene fluoride)/poly (methyl methacrylate) blends. *Composites Science and Technology*, **106**:39–46, 2015.

[140] Gondim Fernanda Fabbri, Tienne Lucas Galhardo Pimenta, Cruz Macena da Barbara de Salles, Chaves Erica Gervasoni, Carvalho Peres de Augusto Cesar, and Marques Maria de Fatima Vieira. Poly (vinylidene fluoride) with zinc oxide and carbon nanotubes applied to pressure sheath layers in oil and gas pipelines. *Journal of Applied Polymer Science*, **138** (14):50157, 2021.

[141] Arjunan Arun, Zahid Suhaib, Baroutaji Ahmad, and Robinson John. 3D printed auxetic nasopharyngeal swabs for COVID-19 sample collection. *Journal of the Mechanical Behavior of Biomedical Materials*, **114**:104175, 2021.

[142] Martins P, Lopes AC, and Lanceros-Mendez S. Electroactive phases of poly (vinylidene fluoride): Determination, processing and applications. *Progress in Polymer Science*, **39**(4): 683–706, 2014.

[143] Khalifa Mohammed and Anandhan S. PVDF nanofibers with embedded polyaniline–graphitic carbon nitride nanosheet composites for piezoelectric energy conversion. *ACS Applied Nano Materials*, **2**(11):7328–7339, 2019.

[144] Ahn Yongjin, Lim Jun Young, Hong Soon Man, Lee Jaerock, Ha Jongwook, Choi Hyoung Jin, and Seo Yongsok. Enhanced piezoelectric properties of electrospun poly (vinylidene fluoride)/multiwalled carbon nanotube composites due to high β-phase formation in poly (vinylidene fluoride). *The Journal of Physical Chemistry C*, **117**(22):11791–11799, 2013.

[145] Yu Hao, Huang Tao, Lu Mingxia, Mao Mengye, Zhang Qinghong, and Wang Hongzhi. Enhanced power output of an electrospun PVDF/MWCNTs-based nanogenerator by tuning its conductivity. *Nanotechnology*, **24**(40):405401, 2013.

[146] Sencadas Vitor, Gregorio Jr Rb, and Lanceros-Méndez Senentxu. α to β phase transformation and microestructural changes of PVDF films induced by uniaxial stretch. *Journal of Macromolecular Science®*, **48**(3):514–525, 2009.

[147] Indolia Ajay Pal and Gaur MS. Optical properties of solution grown PVDF-ZnO nanocomposite thin films. *Journal of Polymer Research*, **20**:1–8, 2013.

[148] Mathai C Joseph, Saravanan S, Anantharaman MR, Venkitachalam S, and Jayalekshmi S. Effect of iodine doping on the bandgap of plasma polymerized aniline thin films. *Journal of Physics D: Applied Physics*, **35**(17):2206, 2002.

[149] Zhang Ranran, Li Lili, Long Shaojun, Lou Hanyu, Wen Fei, Hong Hui, Shen Yuncong, Wang Gaofeng, and Wu Wei. Enhanced energy storage performance of PVDF composite films with a small content of $BaTiO_3$. *Journal of Materials Science: Materials in Electronics*, **32**: 24248–24257, 2021.

[150] Hu Yu-Chih, Dai Ching-Liang, and Hsu Cheng-Chih. Titanium dioxide nanoparticle humidity microsensors integrated with circuitry on-a-chip. *Sensors*, **14**(3):4177–4188, 2014.

[151] Cherumannil Karumuthil Subash, Prabha Rajeev Sreenidhi, Valiyaneerilakkal Uvais, Athiyanathil Sujith, and Varghese Soney. Electrospun poly (vinylidene fluoride-

trifluoroethylene)-based polymer nanocomposite fibers for piezoelectric nanogenerators. *ACS Applied Materials and Interfaces*, **11**(43):40180–40188, 2019.

[152] Joni IM, Nulhakim L, and Panatarani C. Characteristics of TiO_2 particles prepared by simple solution method using $TiCl_3$ precursor. In *Journal of Physics: Conference Series*, volume 1080, page 012042. IOP Science, 2018.

[153] Muduli Sakti Prasanna, Veeralingam Sushmitha, and Badhulika Sushmee. Interface induced high-performance piezoelectric nanogenerator based on a electrospun three-phase composite nanofiber for wearable applications. *ACS Applied Energy Materials*, **4**(11):12593–12603, 2021.

[154] Arrigoni Alessia, Brambilla Luigi, Bertarelli Chiara, Serra Gianluca, Tommasini Matteo, and Castiglioni Chiara. P(VDF-TrFE) nanofibers: structure of the ferroelectric and paraelectric phases through ir and raman spectroscopies. *RSC Advances*, **10**(62):37779–37796, 2020.

[155] Zhai Wenchao, Lai Qingsong, Chen Lei, Zhu Laipan, and Wang Zhong Lin. Flexible piezoelectric nanogenerators based on P(VDF-TrFE)/GeSe nanocomposite films. *ACS Applied Electronic Materials*, **2**(8):2369–2374, 2020.

[156] Ghosh Sujoy Kumar, Xie Mengying, Bowen Christopher Rhys, Davies Philip R, Morgan David J, and Mandal Dipankar. A hybrid strain and thermal energy harvester based on an infra-red sensitive Er^{3+} modified poly (vinylidene fluoride) ferroelectret structure. *Scientific Reports*, **7**(1):16703, 2017.

[157] Bharath R Sundararam, Chakraborthy Tirthankar, Nhalil Hariharan, Masin B, Ashok K, Sreemoolanadhan H, Oommen Charlie, and Elizabeth Suja. Synthesis and evaluation of PVDF–$MgTiO_3$ polymer–ceramic composites for low-k dielectric applications. *Journal of Materials Chemistry C*, **7**(15):4484–4496, 2019.

[158] Wang Yifei, Cui Jin, Yuan Qibin, Niu Yujuan, Bai Yuanyuan, and Wang Hong. Significantly enhanced breakdown strength and energy density in sandwich-structured barium titanate/poly (vinylidene fluoride) nanocomposites. *Advanced Materials*, **27**(42):6658–6663, 2015.

[159] Dang Zhi-Min, Yuan Jin-Kai, Zha Jun-Wei, Zhou Tao, Li Sheng-Tao, and Hu Guo-Hua. Fundamentals, processes and applications of high-permittivity polymer–matrix composites. *Progress in Materials Sience*, **57**(4):660–723, 2012.

[160] Zhao Yang, Zhang Yongming, He Zemin, Zhang Huimin, Wang Haiyang, and Zhao Yuzhen. Enhanced dielectric properties of PVDF-based composite film with $BaTiO_3$@ $SrTiO_3$ nanoparticles. *New Journal of Chemistry*, **46**(22):10577–10583, 2022.

[161] Li Wei, Li Hong, and Zhang Yong-Ming. Preparation and investigation of PVDF/PMMA/TiO_2 composite film. *Journal of Materials Science*, **44**:2977–2984, 2009.

[162] Khodaparast P and Ounaies Zoubeida. On the impact of functionalization and thermal treatment on dielectric behavior of low content TiO_2/PVDF nanocomposites. *IEEE Transactions on Dielectrics and Electrical Insulation*, **20**(1):166–167, 2013.

[163] Kulkarni Nikhil Dilip and Kumari Poonam. Development of highly flexible PVDF-TiO_2 nanocomposites for piezoelectric nanogenerator applications. *Materials Research Bulletin*, **157**:112039, 2023.

[164] Zhou Linlin, Zhu Laipan, Yang Tao, Hou Xinmei, Du Zhengtao, Cao Sheng, Wang Hailong, Chou Kuo-Chih, and Wang Zhong Lin. Ultra-stable and durable piezoelectric nanogenerator with all-weather service capability based on N doped 4H-SiC nanohole arrays. *Nano-Micro Letters*, **14**:1–10, 2022.

[165] Kulkarni Nikhil Dilip and Kumari Poonam. Role of rGO on mechanical, thermal, and piezo-

electric behaviour of PVDF-BTO nanocomposites for energy harvesting applications. *Journal of Polymer Research*, **30**(2):79, 2023.

[166] Yang Jie, Zhang Yihe, Li Yanan, Wang Zhihao, Wang Wenjiang, An Qi, and Tong Wangshu. Piezoelectric nanogenerators based on graphene oxide/PVDF electrospun nanofiber with enhanced performances by in-situ reduction. *Materials Today Communications*, **26**:101629, 2021.

[167] Parangusan Hemalatha, Bhadra Jolly, and Al-Thani Noora. Flexible piezoelectric nanogenerator based on P(VDF-HFP)/PANI-ZnS electrospun nanofibers for electrical energy harvesting. *Journal of Materials Science: Materials in Electronics*, **32**:6358–6368, 2021.

[168] Ponnan Sathiyanathan, Schmidt Thomas Walter, Li Tianyuan, Gunasekaran Harini Bhuvaneswari, Ke Xixian, Huang Yajing, Mubarak Suhail, Anand Prabu Arun, Weng Zixiang, and Wu Lixin. Electrospun poly (vinylidene fluoride)–magnesiochromite nanofiber-based piezoelectric nanogenerator for energy harvesting applications. *ACS Applied Polymer Materials*, **3**(10):4879–4888, 2021.

[169] Maity Kuntal, Mahanty Biswajit, Sinha Tridib Kumar, Garain Samiran, Biswas Anirban, Ghosh Sujoy Kumar, Manna Smarajit, Ray Samit K, and Mandal Dipankar. Two-dimensional piezoelectric MoS_2-modulated nanogenerator and nanosensor made of poly (vinlydine fluoride) nanofiber webs for self-powered electronics and robotics. *Energy Technology*, **5**(2): 234–243, 2017.

[170] Singh Huidrom Hemojit and Khare Neeraj. Flexible ZnO-PVDF/PTFE based piezo-tribo hybrid nanogenerator. *Nano Energy*, **51**:216–222, 2018.

[171] Liew Weng Heng, Mirshekarloo Meysam Sharifzadeh, Chen Shuting, Yao Kui, and Tay Francis Eng Hock. Nanoconfinement induced crystal orientation and large piezoelectric coefficient in vertically aligned P(VDF-TrFE) nanotube array. *Scientific Reports*, **5**(1):1–7, 2015.

[172] Alam Md Mehebub, Sultana Ayesha, and Mandal Dipankar. Biomechanical and acoustic energy harvesting from TiO_2 nanoparticle modulated PVDF nanofiber made high performance nanogenerator. *ACS Applied Energy Materials*, **1**(7):3103–3112, 2018.

[173] Wang Zhuo, Li Yanxin, Li Yinbo, Yi Zhihui, and Kong Menglei. Enhanced polarization of PVDF composite films by trace $BiFeO_3$ fiber filler. *Journal of Materials Science: Materials in Electronics*, **32**(14):19703–19712, 2021.

[174] Shepelin Nick A, Glushenkov Alexey M, Lussini Vanessa C, Fox Phillip J, Dicinoski Greg W, Shapter Joseph G, and Ellis Amanda V. New developments in composites, copolymer technologies and processing techniques for flexible fluoropolymer piezoelectric generators for efficient energy harvesting. *Energy and Environmental Science*, **12**(4):1143–1176, 2019.

[175] Feng Wei, Sun Enhai, Fujii Akihiko, Wu Hongcai, Niihara Koichi, and Yoshino Katsumi. Synthesis and characterization of photoconducting polyaniline-TiO_2 nanocomposite. *Bulletin of the Chemical Society of Japan*, **73**(11):2627–2633, 2000.

[176] Sawada Takashi and Ando Shinji. Synthesis, characterization, and optical properties of metal-containing fluorinated polyimide films. *Chemistry of Materials*, **10**(11):3368–3378, 1998.

[177] Rancourt JD and Taylor LT. Preparation and properties of surface-conductive polyimide films via in situ codeposition of metal salts. *Macromolecules*, **20**(4):790–795, 1987.

[178] Falconer John L and Magrini-Bair Kimberley A. Photocatalytic and thermal catalytic oxidation of acetaldehyde on Pt/TiO_2. *Journal of Catalysis*, **179**(1):171–178, 1998.

[179] Jian Li and Chilan Cai. The preparation and tribological properties of $PVDF/TiO_2$ nanocomposites. *Polymer-Plastics Technology and Engineering*, **49**(7):643–647, 2010.

[180] Kumar Mukesh and Kumari Poonam. P(VDF-TrFE)/ZnO nanocomposite synthesized by

electrospinning: effect of ZnO nanofiller on physical, mechanical, thermal, rheological and piezoelectric properties. *Polymer Bulletin*, **20**:1–20, 2022.

[181] Wankhade Shivaji H, Tiwari Shivam, Gaur Anupama, and Maiti Pralay. PVDF-PZT nanohybrid based nanogenerator for energy harvesting applications. *Energy Reports*, **6**:358–364, 2020.

[182] Singh Vishal and Singh Bharti. MoS_2-PVDF/PDMS based flexible hybrid piezo-triboelectric nanogenerator for harvesting mechanical energy. *Journal of Alloys and Compounds*, **941**: 168850, 2023.

Appendix A

A.1 MATERIAL PROPERTY OF PVDF

Finite element method (FEM) based simulation of sensor device using Comsol Multiphysics has been carried out to analyze its solid mechanics and induced piezo potential. For this, the material property is required to study the piezoelectric performance of the sensor device. The material properties are as follows:

Density = 1780 kg/m^3

Relative permittivity

$$\epsilon_r = \begin{bmatrix} 7.4 & 0 & 0 \\ 0 & 7.4 & 0 \\ 0 & 0 & 7.4 \end{bmatrix} \tag{A.1}$$

Elastic matrix (Pa)

$$[C] = \begin{bmatrix} 3.8e+09 & 1.9e+09 & 0.9e+09 & 0 & 0 & 0 \\ 1.9e+09 & 3.8e+09 & 0.9e+09 & 0 & 0 & 0 \\ 0.9e+09 & 0.9e+09 & 1.2e+09 & 0 & 0 & 0 \\ 0 & 0 & 0 & 7e+08 & 0 & 0 \\ 0 & 0 & 0 & 0 & 9e+08 & 0 \\ 0 & 0 & 0 & 0 & 0 & 9e+08 \end{bmatrix} \tag{A.2}$$

Coupling coefficient matrix (C/N)

$$[d] = \begin{bmatrix} 0 & 0 & 0 & 0 & 0 & 0 \\ 0 & 0 & 0 & 0 & 0 & 0 \\ 1.358e-11 & 1.476e-12 & -3.38e-11 & 0 & 0 & 0 \end{bmatrix} \tag{A.3}$$

Compliance matrix (1/Pa)

$$[C] = \begin{bmatrix} 3.781e-10 & -1.482e-10 & -1.724e-10 & 0 & 0 & 0 \\ -1.482e-10 & 3.781e-10 & -1.724e-10 & 0 & 0 & 0 \\ -1.724e-10 & -1.724e-10 & 3.781e-10 & 0 & 0 & 0 \\ 0 & 0 & 0 & 3.781e-10 & 0 & 0 \\ 0 & 0 & 0 & 0 & 3.781e-10 & 0 \\ 0 & 0 & 0 & 0 & 0 & 3.781e-10 \end{bmatrix} \tag{A.4}$$

A.2 MATERIAL PROPERTY OF $BaTiO_3$

The $BaTiO_3$ nanoparticles are incorporated to fabricate the piezoelectric sensor device. The material properties are required to study for the simulation using the FEM-based software. The material constants are given as:

Density = 6020 kg/m^3

Relative permittivity

$$\epsilon_r = \begin{bmatrix} 1976.8 & 0 & 0 \\ 0 & 1976.8 & 0 \\ 0 & 0 & 111.7 \end{bmatrix} \tag{A.5}$$

Elastic matrix (Pa)

$$[C] = \begin{bmatrix} 2.75121e+11 & 1.78967e+11 & 1.51555e+11 & 0 & 0 & 0 \\ 1.78967e+11 & 2.75121e+11 & 1.51555e+11 & 0 & 0 & 0 \\ 1.51555e+11 & 1.51555e+11 & 1.6486e+11 & 0 & 0 & 0 \\ 0 & 0 & 0 & 5.43478e+10 & 0 & 0 \\ 0 & 0 & 0 & 0 & 5.43478e+10 & 0 \\ 0 & 0 & 0 & 0 & 0 & 1.13122e+11 \end{bmatrix} \tag{A.6}$$

Coupling coefficient matrix (C/m^2)

$$[d] = \begin{bmatrix} 0 & 0 & 0 & 0 & 21.3043 & 0 \\ 0 & 0 & 0 & 21.3043 & 0 & 0 \\ -2.69289 & -2.69289 & 3.65468 & 0 & 0 & 0 \end{bmatrix} \tag{A.7}$$

Compliance matrix (1/Pa)

$$[C] = \begin{bmatrix} 8.05e-12 & -2.35e-12 & -5.24e-12 & 0 & 0 & 0 \\ -2.35e-12 & 8.05e-12 & -5.24e-12 & 0 & 0 & 0 \\ -5.24e-12 & -5.24e-12 & 1.57e-11 & 0 & 0 & 0 \\ 0 & 0 & 0 & 1.84e-11 & 0 & 0 \\ 0 & 0 & 0 & 0 & 1.84e-11 & 0 \\ 0 & 0 & 0 & 0 & 0 & 8.84e-12 \end{bmatrix} \quad \text{(A.8)}$$

Brief Biodata of the Author

The author, Mukesh Kumar, was born in the town Begusarai situated in Bihar State, India. He graduated with B.Tech in Mechanical Engineering from College of Engineering Bhubaneswar (COEB), Bhubaneswar, Odisha in the year 2011. Subsequently, in 2012, he secured admission for his M.Tech degree in Industrial Design at the Maulana Azad National Institute of Technology (MANIT) Bhopal, Madhya Pradesh, based on his performance in the GATE (All India Graduate Aptitude Test in Engineering) mechanical engineering paper. Then, he joined E-max Group of Institutions (Ambala) in the same year to work as a Assistant Professor in the Department of Mechanical Engineering for almost three yeras. Again after qualifying the GATE in 2015, he joined the Ph.D. program at the Department of Mechanical Engineering, IIT Guwahati in July 2017 and this research work is carried out during this period.

List of Publications from the Thesis

List of Publications in International Journals

List of Publications

Peer reviewed Journal Publications

1. Kumar, M., Kumari, P., 2022. P(VDF-TrFE)/ZnO nanocomposite synthesized by electrospinning: effect of ZnO nanofiller on physical, mechanical, thermal, rheological and piezoelectric properties. Polymer Bulletin, 1-20.

2. Kumar, M., Kumari, P., Sahatiya, P., 2022. P(VDF-TrFE)/ZnO nanofiber composite based piezoelectric nanogenerator as self-powered sensor: fabrication and characterization. Journal of Polymer Research 29, 1-16.

3. Kumar, M., Kumari, P., 2023. Design and fabrication of self-powered flexible P(VDF-TrFE)/ZnO/TiO_2 fiber mats as nanogenerator for wearable applications. Materials Science in Semiconductor Processing, 107429.

4. Kumar, M., Kulkarni, N., Kumari, P. (*Under review*). Piezoelectric performance enhancement of electrospun functionally graded PVDF/$BaTiO_3$ based flexible nanogenerators. Material Research Bulletin.

5. Kumar, M., Kulkarni, N., Saha, A., Kumari, P. (*Under review*). Design and fabrication of self-powered flexible P(VDF-TrFE)/ZnO/TiO_2 fiber mats as nanogenerator for wearable applications. Composites Part A: Applied Science and Manufacturing.

6. Kumar, M., Kumari, P. (under preparation). Modeling and optimization of electrospinning parameter for P(VDF-TrFE)/ZnO nanocomposite as biomechanical sensor.

Book Chapter

1. Kumari, P., **Kumar, M.**, 2020. Piezoelectric materials and their application. Nikhil Publishers, ISBN: 978-93-87697-80-5, 190-197.

International Conference Publication

1. Kumar, M., Verma, D., Kumari, P., 2019. The Synthesis, Characterization and performance of Piezoelectric P(VDF-TrFE) Electrospun Nanofibers. *International Conference on Precision, Meso, Micro and Nano Engineering (COPEN 2019)*, December 12-14, 2019 IIT Indore, India.

2. Kumar, M., Kumari, P., 2021. Fabrication, Characterization, and Enhanced Piezoelectric output of Electrospun P(VDF-TrFE)/ZnO Nanocomposite. *The 7th Asian Conference on Mechanics of Functional Materials and Structures (ACMFMS 2020+1)*, March 13-15, 2021 Virtually at Tohoku University, Japan. (Best Presentation Award)

3. Kumar, M., Kumari, P., 2021. The effect of reciprocating motion of drum collector on electrospun PVDF nanofiber for energy harvesting application. *The 4th World Congress on Micro and Nano Manufacturing (WCMNM 2021)*, September 20-23, 2021 Virtually at IIT Bombay, India. (Student Award)

4. Kumar, M., Kulkarni, N., Kumari, P., 2022. Fabrication and characterization of PVDF/$BaTiO_3$ nanocomposite for energy harvesting application. *1st International Conference on Advances in Mechanical Engineering and Material Science (ICAMEMS-22)*, January 22-24, 2022 Virtually at VIT AP, India, Materials Today: Proceedings 56 (2022): 1151-1155.

5. Kumar, M., Kumari, P., 2022. Synthesis and Characterization of Electrospun PVDF nanofibers for Energy harvesting: Effect of solvent ratio. *International Conference on Advances in Chemical and Materials Sciences (ACMS-2022)*, February 24-26, 2022 Virtually at HIT Kolkata, India.

6. Kulkarni. N., **Kumar, M.**, Kumari, P., 2022. PVDF/RGO based piezoelectric nanocomposite films for enhanced mechanical and dielectric properties. *International Conference on Advances in Chemical and Materials Sciences (ACMS-2022)*, February 24-26, 2022 Virtually at HIT Kolkata, India, Materials Today: Proceedings (2022).

7. Kumar, M., Kulkarni, N., Kumari, P., 2022. Enhanced performance of PVDF-based piezo-

electric nanogenerators for energy harvesting applications. *8th Asian Conference on Mechanics of Functional Materials and Structures (ACMFMS 2022)*, December 11-14, 2022 IIT Guwahati, India.

8. Kulkarni. N., **Kumar, M.**, Kumari, P., 2023. Development of flexible PVDF-Graphene piezoelectric nanocomposites for smart sensing applications. *International Conference on Graphene, Semiconductors and 2D Materials (Graphene 2023)*, March 20-21, 2023 City Seasons Hotel, Dubai, UAE.

9. Kumar, M., Kumari, P., 2023. Hybrid nanocomposite mat-based nanogenerator with enhanced performance for energy harvesting application. *International Conference on Materials for Advanced Technologies (ICMAT-2023)*, June 26-30, 2023 at Suntec, Singapore.